ISSN 2458-973X

JSCMT

Journal of Sustainable Construction Materials and Technologies

Volume 9
Number 3
Year 2024

YTÜ PRESS

www.jscmt.yildiz.edu.tr

ISSN 2458-973X

JSCMT

Journal of Sustainable Construction Materials and Technologies

Volume 9 Number 3 Year 2024

ISSN 2458-973X

JSCMT

Journal of
Sustainable Construction
Materials and Technologies

Volume 9 Number 3 Year 2024

CONTENTS

Journal of Sustainable Construction Materials and Technologies
Web page info: https://jscmt.yildiz.edu.tr
DOI: 10.47481/jscmt.1554284

JSCMT
Journal of Sustainable Construction Materials and Technologies

Research Article

Sustainable geopolymer concrete for pavements: Performance evaluation of recycled concrete aggregates in fly ash-based mixtures

B. Naga Malleswara RAO, Chereddy Sonali Sri DURGA*, Chava VENKATESH, T. Muralidhara RAO

Department of Civil Engineering, CVR College of Engineering, Telangana, India

ARTICLE INFO

Article history
Received: 19 May 2024
Revised: 06 August 2024
Accepted: 14 September 2024

Key words:
Compressive strength, fly ash, geopolymer concrete, pavement, recycled aggregates

ABSTRACT

This study investigates the feasibility of incorporating recycled concrete aggregates (RCA) into fly ash-based geopolymer concrete for sustainable pavement applications. The research evaluates RCA's physical and mechanical properties compared to virgin coarse aggregates (VCA) and assesses the performance of geopolymer concrete mixtures with up to 40% RCA replacement. Aggregate characterization revealed that RCA exhibited higher water absorption (4.39%), crushing value (20.9%), impact value (28.2%), and abrasion value (26.1%) compared to VCA, yet these values remained within acceptable limits for pavement applications. Geopolymer concrete specimens were tested for compressive strength, water absorption, abrasion resistance, and chloride ion permeability. Results indicated that increasing RCA content led to a gradual decrease in compressive strength, from 40.16 MPa to 33.52 MPa, while water absorption increased from 5.2% to 6.8%. Abrasion resistance declined as RCA content rose, and chloride ion penetrability increased from 1687 to 2196 coulombs. However, mixtures with up to 20% RCA replacement met the strength and durability criteria required for pavement construction. This study demonstrates the potential for utilizing RCA in geopolymer concrete pavements, offering a sustainable solution for waste management and resource conservation in the construction industry.

Cite this article as: Rao, B. N. M., Durga, C.S.S., Venkatesh, C., & Rao, T. M. (2024). Sustainable geopolymer concrete for pavements: Performance evaluation of recycled concrete aggregates in fly ash-based mixtures. *J Sustain Const Mater Technol*, 9(3), 211–220.

1. INTRODUCTION

Using recycled concrete aggregates (RCA) in pavement construction has emerged as a crucial strategy to address the growing environmental concerns and resource scarcity in the construction industry [1]. With global concrete production exceeding 10 billion tons annually, construction and demolition waste poses significant ecological challenges [2, 3]. Simultaneously, the depletion of natural aggregate resources has become a pressing issue in many regions [4]. In this context, incorporating RCA in pavement construction offers a sustainable solution that addresses waste management and resource conservation [5]. The use of RCA in pavements also aligns with circular economy principles, reducing the carbon footprint associated with aggregate production and transportation [6]. Tam et al. [7] estimated that incorporating RCA in pavement construction could reduce CO_2 emissions by up to 20% compared to conventional methods.

On the other hand, Geopolymer concrete has emerged as a promising alternative to traditional Portland cement concrete in pavement construction, offering significant environmental and performance benefits [8, 9]. This innovative

*Corresponding author.
*E-mail address: chereddysony@gmail.com

Table 1. Physical and chemical characteristics of binders

	SiO_2	CaO	Al_2O_3	Fe_2O_3	Na_2O	MgO	SO_3	LOI	Specific gravity	Specific surface area (m^2/g)
Fly ash	58.32	4.08	25.71	5.27	0.37	1.04	0.92	4.29	2.39	5.12
GGBFS	34.16	44.25	12.23	1.02	0.78	3.61	0.73	3.22	2.86	6

material, which utilizes industrial by-products such as fly ash or ground granulated blast furnace slag as binders activated by alkaline solutions, can reduce CO_2 emissions by up to 80% compared to ordinary Portland cement concrete [10]. Geopolymer concrete exhibits superior durability, including enhanced resistance to chemical attack, freeze-thaw cycles, and chloride ion penetration, critical factors in pavement longevity [11]. It also offers rapid strength gain, allowing for faster construction and earlier traffic opening, and demonstrates better performance under extreme temperature conditions.

Geopolymer concrete has the combined advantages of a lower carbon footprint binder system based on industrial waste fly ash, with an opportunity to incorporate another waste stream as aggregate [12]. Work on RCA recycled into non-geopolymer concrete shows that at high replacement levels, RCA affects concrete properties such as lower density, higher water absorption, lower mechanical strength, more significant shrinkage, and lower durability compared to natural aggregates (NA) [13]. In terms of compressive strength, de Juan and Gutiérrez [14] observed up to 5–30% lower strength when replacing NA with 25–100% coarse RCA due to RCA's higher porosity and water absorption. Other studies [15, 16] have also found the rate of strength gain of RCA concrete to be slower than that of NA concrete. Research indicates substitution limits of 20–30% coarse RCA are suitable for structural concrete applications [17].

Regarding durability, Pepe et al. [18] reported that up to 100% replacement of NA by coarse or fine RCA had negligible effects on freeze-thaw resistance. Corrosion resistivity was also similar, with up to 30% replacement levels [19]. Permeability and diffusion testing showed higher chloride ingress rates with higher RCA replacement ratios [20]. Drying shrinkage strains were found to be 10–25% higher with RCA incorporation [21].

In particular, geopolymer concrete derived from industrial by-products, serving as a sustainable construction material alternative to traditional Portland cement concrete, has not undergone substantial investigations evaluating the incorporation of RCAs. Additionally, earlier RCA research is predominantly limited to the impacts on compressive strength and essential durability characteristics like sorptivity and acid/sulfate resistances. Evaluating longevity indicators such as volumetric abrasion loss and rapid chloride permeability, which better quantify actual concrete pavement performance, can support extending RCAs to road infrastructure where durability against water/chloride ingress is vital. Therefore, a research gap exists in applying learnings from RCA use in standard concrete to geopolymer concrete for structural applications. This study assesses the effects of coarse RCA content on the core mechanical strength and various relevant durability metrics of fly ash-based geopolymer. Outcomes can support preliminary standardization for greener concretes using waste and by-product-sourced materials. With this research gap in mind, this study evaluates the use of crushed recycled concrete aggregates (RCA) to replace natural coarse aggregates in fly ash-based geopolymer concrete partially. The research experimentally evaluates geopolymer concrete incorporating up to 40% replacement of natural coarse aggregate with RCA. Strength, abrasion resistance, water absorption, and chloride permeability are tested to gauge detrimental effects. This study aims to establish a framework for utilizing waste concrete in next-generation sustainable pavements, addressing environmental concerns and structural performance needs by determining optimal RCA replacement levels that maintain required engineering properties.

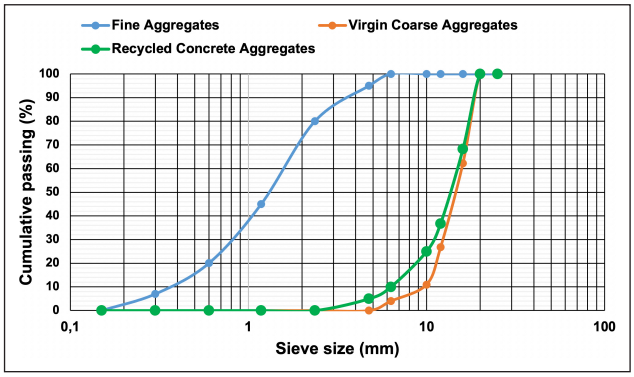

Figure 1. Particle size distribution of aggregates.

2. MATERIALS AND METHODS

2.1. Materials

In the present study, Fly ash (FA) and ground granulated blast furnace slag (GGBFS) were used as geopolymer binders, conforming to ASTM C618-08 [22] and ASTM C989-18 [23] respectively (Table 1). FA was sourced from a local coal-fired thermal power plant, while GGBFS was obtained commercially (JSW Cements Ltd., India). Sodium silicate (Na_2SiO_3) and sodium hydroxide (NaOH) were used as alkaline activators, procured from local chemical suppliers. The Na_2SiO_3 had a composition by weight of Na_2O 14.5%, SiO_2 29.6% and water 55.9%. Locally sourced granite stone and river sand provided the coarse and fine aggregates conforming to ASTM C33 [24] and BS 882 grading requirements [25]. The coarse aggregate was sieved into 20 mm and 12 mm fractions while the fine aggregate passed through a 4.75 mm sieve, as shown in Figure 1. A NaOH: Na_2SiO_3 ratio of 1:2.5 was used for

Table 2. Mix Calculations (kg/m^3)

Mix	FA	GGBFS	Aggregates			NaoH	Na_2SiO_3	S/B
			Fine	VCA	RCA			
RA0	336	84	570	1140	–	108.57	43.43	0.40
RA10	336	84	570	1026	114	108.57	43.43	0.40
RA20	336	84	570	912	228	108.57	43.43	0.40
RA30	336	84	570	798	342	108.57	43.43	0.40
RA40	336	84	570	684	456	108.57	43.43	0.40

the alkaline activator based on previous work [12, 26]. The 8M NaOH solution was prepared 24 hrs before mixing and cooled in an ice bath [2], and its preparation process is shown in Figure 2.

2.2. Preparation of Recycled Aggregates

Recycled concrete aggregates (RCA) were produced from previously tested concrete samples in our laboratory. The process involved crushing the concrete samples using a laboratory jaw crusher and washing them to remove dust and fine particles. The washed aggregates were oven-dried at 105 °C for 24 hours [27, 28]. Finally, the dried aggregates were sieved to match the grading of the natural aggregates used in this study. The present study did not follow a specific standard for this process, and this method is similar to those described in ASTM C33 [24] and BS EN 12620 [29] for processing recycled aggregates.

2.3. Mix Design and Curing

Geopolymer concrete mixes were designed as per IS 10262-2019 (Table 2) [30–32], with RCA replacing 0%, 10%, 20%, 30%, and 40% of the coarse aggregate by volume. Additionally, 20% of GGBFs was used to replace the fly ash in all mixes. Dry components were pre-mixed for 2–3 minutes before adding the alkaline activator and mixing for 5–6 minutes. The geopolymer concrete specimens were cured under ambient conditions for 28 days. In this investigation, 160 specimens (i.e., 80 cubes for compressive strength and water absorption, 40 cylinders for the abrasion resistance test, and 40 disc specimens for the rapid chloride permeability test) were prepared and tested throughout the experimentation.

2.4. Experimental Methods

2.4.1. Aggregate Tests

The aggregate impact test was carried out as per IS 2386 Part 4 [33]. The aggregate sample was first oven-dried at 100 °C to 110 °C and allowed to cool. It was then filled in the cylindrical steel cup of the impact testing machine to overflow and was tamped 25 times with a tamping rod. The weight (W1) of aggregates was determined before subjecting the cup fixed in position to 15 blows of hammer rotated from a height of 380 mm. The crushed aggregate was removed and sieved through a 2.36 mm IS sieve. The fraction passing the 2.36 mm sieve (W2) was weighed, and the aggregate impact value was calculated using Eq.1.

$$\text{Aggregate impact value (\%)} = ((W1 - W2)/W1) \times 100 \quad \text{Eq.1}$$

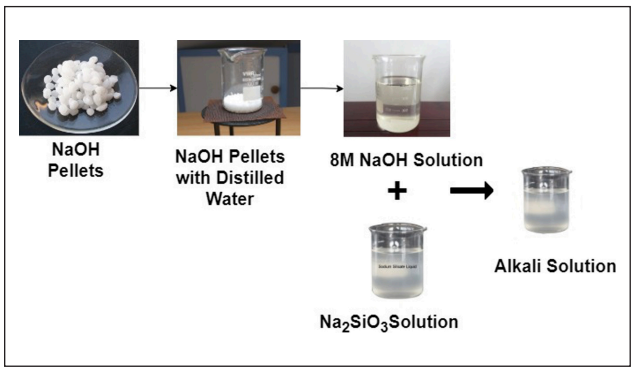

Figure 2. Geopolymer solution preparation [2].

The aggregate crushing strength test was performed per IS 2386 Part 4 [33]. The oven-dried aggregate sample was sieved through 12.5 mm and 10 mm IS sieves. Aggregates passing a 12.5 mm sieve and retained on a 10 mm sieve were selected. Three test specimens were prepared by mixing aggregates of different sizes to get an aggregate weight of approximately 100 g in each case. The specimens were placed in compression testing machines one by one, and load was applied at a uniform rate of 40 tonnes/minute until failure occurred. The crushing load for all three specimens was noted, and their average was taken as the aggregate crushing strength.

The abrasion test was carried out as per IS 2386 Part 4 [33]. The coarse aggregate sample was oven-dried and then divided into 6 equal parts, mixing them thoroughly. The one-part sample was taken and was sieved through a 1.7 mm IS sieve. The fraction passing was discarded. The retained sample was placed in an abrasion testing machine cylinder in 5 layers, tamping each layer 25 times. The sample was then subjected to 100 revolutions in an abrasion testing machine. After that, the abraded aggregate was sieved through a 1.7 mm IS sieve, and the fraction passing through the sieve was weighed. The percentage of wear due to abrasion was then calculated.

As per IS 2386 Part 3 [34], the water absorption test was performed by oven drying the aggregates to constant mass first. The dried aggregates were then immersed in water for 24 hours, taken out, wiped to remove traces of water, and weighed (W1). The aggregates were again submerged in water for 72 hours, removed, surface wiped, and weighed (W2). The water absorption was calculated using the Eq.2.

$$\text{Water absorption (\%)} = ((W2 - W1)/W1) \times 100 \quad \text{Eq.2}$$

Figure 3. Compressive strength setup.

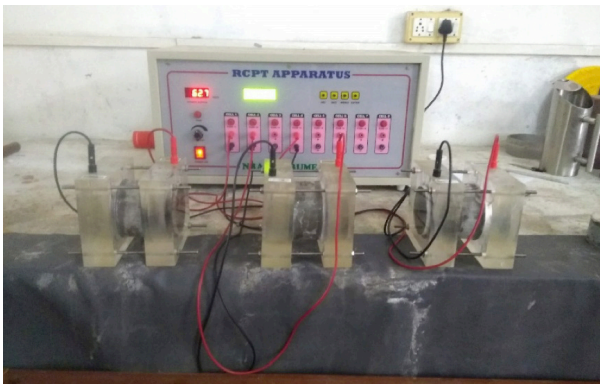

Figure 4. Rapid chloride permeability test setup.

Figure 5. Water absorption test setup.

2.4.2. Compressive Strength

The concrete compressive strength test was carried out as per IS 516 [35–38] by casting three 150mm concrete cubes, demolding after 24 hours, curing by immersion in water for 28 days, wiping the cubes dry, placing them in compression testing machine one by one, aligning blocks properly, and applying load uniformly at a rate of approximately 140 kg/sq cm per minute until failure occurred. The maximum load divided by the cross-sectional area gave the compressive strength. Figure 3 shows the experimental setup of the compressive strength.

2.4.3. Abrasion Resistance Test

The abrasion resistance test was performed as per IS 1237 [39] by casting concrete into 140 mm diameter and 60mm height cylinders in steel molds, demolding after 24 hours, curing by immersion in water for 28 days, and then oven drying. The specimens were set up in the abrasion testing machine wearing a test rig rotated at 30–33 rpm and subjected to abrasive action of 200 revolutions wearing a path of 52mm length uniformly before weighing percentage wear. The abrasion resistance was calculated using the Eq.3.

Abrasion resistance = ((Initial weight-Final weight)/Initial weight)x100 Eq.3

Where;

Initial weight = Weight of specimen before the test; Final weight = Weight of specimen after the test.

2.4.4. Rapid Chloride Permeability Test

The rapid chloride permeability test was conducted as per ASTM C1202 [40–43] by casting 100mm diameter and 50mm height concrete specimens, demolding after 24 hours, and curing by immersion in water for 28 days. The test apparatus containing the vacuum-saturated specimen was connected to a 60V DC source for 6 hours, during which the passed electrical charge was monitored periodically before calculating chloride permeability. Figure 4 shows the experimental photograph of the Rapid chloride permeability test setup.

2.4.5. Water Absorption

The water absorption test was performed as per IS 1199 [44–47] by casting concrete cubes of 150mm size, demolding after 24 hours, and curing by immersion in water for 28 days. The cured specimens were dried in an oven at 100–105 °C to constant mass. After cooling, the cubes were immersed in water for 72±2 hours. The specimens were then weighed in water and after surface drying to determine water absorption using the percentage increase in mass. Figure 5 shows the experimental setup of the water absorption test.

Table 3. Physical and mechanical properties of Virgin and Recycled aggregates

	Specific gravity	Density (kg/m³)	Water absorption (%)	Aggregate crushing value (%)	Aggregate impact value (%)	Abrasion value (%)
VCA	2.64	1542	1.75	17.2	16.78	14.3
RCA	2.51	1366	4.39	20.9	28.2	26.1
IS 2386 Limits for pavements	2.5–3.0	1500–1700	<2%	<30%	<30%	<30%

3. RESULTS AND DISCUSSION

3.1. Physical and Mechanical Properties of Recycled Coarse Aggregates

Table 3 presents the physical and mechanical properties of Virgin Coarse Aggregates (VCA) and Recycled Concrete Aggregates (RCA) in comparison with the IS 2386 limits for pavements. The results reveal notable differences between VCA and RCA across all measured parameters. The specific gravity of RCA (2.51) is lower than that of VCA (2.64), consistent with the previous studies. This reduction aligns with findings by Verian et al. [48], who reported specific gravity values for RCA ranging from 2.35 to 2.58. The lower specific gravity of RCA can be attributed to the presence of adhered mortar, which is less dense than the original aggregate (McNeil and Kang, 2013) [49]. The density of RCA (1366 kg/m³) is substantially lower than VCA (1542 kg/m³), further confirming the increased porosity. While the VCA density falls within the IS 2386 limits for pavements (1500–1700 kg/m³), the RCA density is slightly below this range, which may require consideration in mix design for pavement applications.

The RCA exhibits significantly higher water absorption (4.39%) compared to VCA (1.75%), exceeding the IS 2386 limit of <2% for pavements. This increased absorption is consistent with studies by Saravanakumar et al. [50], who reported water absorption values for RCA between 4.5% and 7.0%. The higher absorption is primarily due to the porous nature of the adhered mortar in RCA. This characteristic can lead to workability issues in fresh concrete and potential long-term durability concerns in hardened concrete. To mitigate these effects, special consideration may be needed in mix design, potentially including using water-reducing admixtures or pre-saturation techniques for RCA (Verian et al. [48]).

Aggregation impact and crushing tests determine the Resistance against externally applied loads. Impact value signifies the ability to resist sudden shocks while crushing value indicates the capacity to sustain gradual compressive loads without excessive breakdown. Owing to the attached porous old mortar phase on RCA particles, both impact and crushing values are higher than VCA. Both the crushing value (20.9%) and impact value (28.2%) of RCA are higher than those of VCA (17.2% and 16.78%, respectively). These results align with findings by Wang et al. (2017) [51], who observed crushing values for RCA between 24% and 35%. The increased crushing and impact values indicate lower resistance to mechanical stresses, which can be attributed to the weaker adhered mortar and potential micro-cracks in RCA resulting from the crushing process (Xiao et al., [52]). All values are within the IS 2386 limit (<30%), suggesting better quality RCA than previous studies.

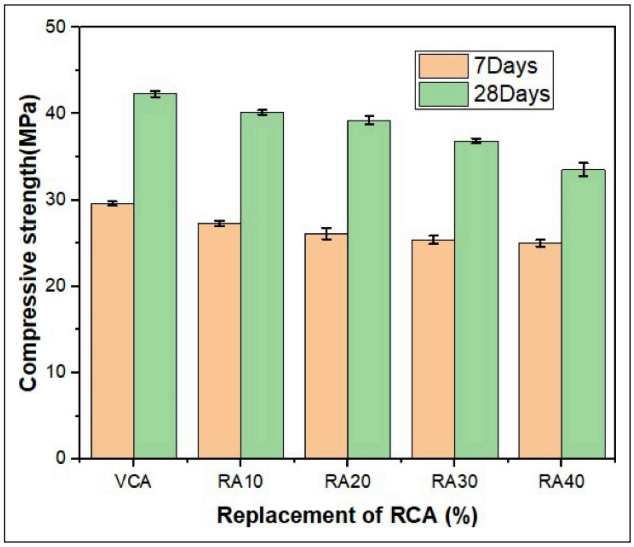

Figure 6. Compressive strength of RCA-based geopolymer concrete.

The abrasion value empirically quantifies wear and tear from rubbing/grinding actions through standard attrition test methods. Abrasion induces progressive particle disintegration, influencing concrete structures' long-term strength and stability. The RCA demonstrates a higher abrasion value (26.1%) compared to the VCA (14.3%), but both are within the IS 2386 limit of <30%. This aligns with the work by Silva et al. [53], who reported abrasion values for RCA ranging from 30% to 44%. The current results show lower abrasion values for both VCA and RCA than the previous studies, indicating better wear resistance.

These new results suggest that the RCA used in this study is of higher quality than the previous studies, with improved mechanical properties. This could lead to better performance in pavement applications. However, the higher water absorption and slightly lower mechanical strength of RCA compared to VCA may still necessitate adjustments in mix design, potentially including the use of supplementary cementitious materials or chemical admixtures to mitigate adverse effects on workability and long-term durability (Verian et al., [48]), with this concern these aggregates were partially replaced in the Virgin Coarse Aggregates used in geopolymer concrete for the pavement applications.

3.2. Compressive Strength

Figure 6 outlines the 28-day compressive strength exhibited by geopolymer concrete containing varying replacement percentages of natural aggregates via recycled concrete aggregates (RCA). Assessment of strength de-

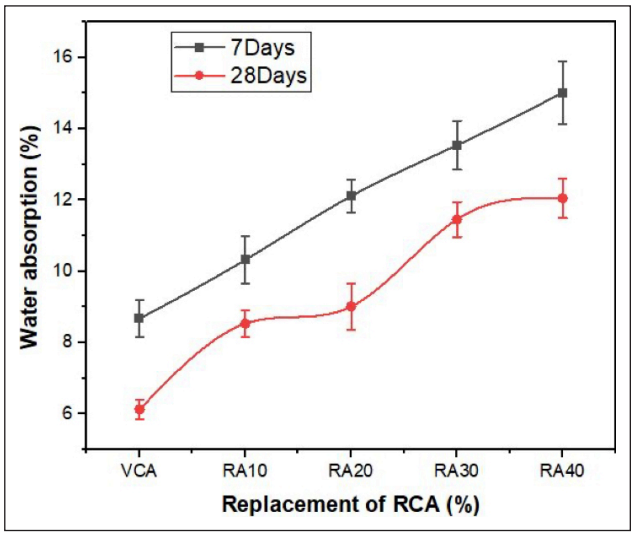

Figure 7. Water absorption of RCA-based Geopolymer concrete.

velopment is imperative to determine the feasibility of achieving standard structural requirements when utilizing recycled aggregate mixes. It is evident that progressively increasing the RCA percentage as a substitute for virgin coarse aggregates results in the gradual decline of compressive strength in the hardened geopolymer concrete from 40.16MPa to 33.52MPa. However, the concrete mixes with 10% and 20% RCA comfortably satisfy the target mean strength of 35MPa at 28 days for M35 grade concrete intended for pavement applications.

The noticeable drop in strength ensues due to the inherent disparity between natural aggregates' properties and recycled aggregates discussed earlier. The porous, weak zones emerging from old adhered mortar on RCA particles generate discontinuities in what would be a monolithic microstructure with only VCA [54]. Moreover, the higher water absorption capacity interferes with efficient particle packing, increasing the voids ratio. Both phenomena provoke more significant defect sites in the hardened concrete composite, allowing failure under loading to initiate and propagate through weaker zones across the RCA interfacial pockets [55]. Additionally, rapid strength development associated with pure geopolymer systems gets marginally deferred in the presence of RCA, where the aggregates possess lower strength characteristics that translate to the bulk matrix. However, over extended periods, the geopolymerization process aids strength gain by forming stable three-dimensional binder structures enveloping the aggregates [56]. Compatibility between the geopolymer gel and RCA improves with curing, mitigating the negative trends seen during the early stages. The nature of the bulk paste-aggregate interface impacts load transfer efficiency and measured strength performance. Hence, the CA percentage must be restricted, and suitable admixtures must be adopted to boost interfacial bonding, densification, and longer-term strength development to attain reliable structural quality geopolymer concrete containing recycled aggregates.

3.3. Water Absorption

Figure 7 represents the water absorption exhibited by geopolymer concrete mixes containing increasing percentages of recycled concrete aggregates (RCA) as replacements for natural aggregates after 28 days of curing. Evaluating sorptivity behavior is necessary to ensure the permeation properties are not adversely altered in RCA-based concrete, which can undermine durability against environmental exposure during service life. The results show that as the RCA replacement ratio is enhanced incrementally from 0% to 40%, the water absorption values of the geopolymer concrete increase gradually from 5.2% to 6.8%. However, all the mixes demonstrate water absorption within the specified limit of 7% for structural concrete applications. The visible escalating trend is anticipated and is attributed primarily to the higher individual absorption capacity of the recycled aggregates arising from the porous adhered old mortar on particles that retain additional moisture [57].

When recycled aggregates are integrated into the concrete matrix, the networks of existing fine pores in the weaker RCA phase translate into the hardened cement paste, producing increased microstructural voids. Moreover, the interfacial transition zone (ITZ) between RCA particles and geopolymer paste tends to weaken, allowing localized penetrability [56]. During mixing, higher absorption by RCA reduces free moisture that can interfere with effective dispersion and encourage flocculation. These factors collectively provoke an escalation in sorptivity [58]. However, specific self-sealing mechanisms emerge over longer-term curing periods as geopolymeric gels diffuse into available pores within RCA, achieving densification.

Moreover, enhanced moisture gets nullified in many practical exposure conditions through drying/evaporation effects preventing saturation except in situations of continuous water contact [59]. Proper air entrainment measures further offset risks from higher absorption capacity. Hence, with a restricted RCA percentage to balance absorption effects, structural stability and durability performance against water penetration remain within the permissible range for RCA-based concretes implied by the test data. However, conservative limits are necessary for universal standardization, warranting significant focus on appropriate curing to control water ingress risks in RCA-integrated concretes.

3.4. Abrasion Resistance of RCA-Based Geopolymer Concrete

Figure 8 represents abrasion resistance evaluated through weight loss in geopolymer concrete mixes incorporating increasing replacement percentages of natural aggregates via recycled concrete aggregates (RCA) after 28 days of standard curing. Determining abrasion behavior is vital to assure surface integrity against progressive material disintegration from friction/impact damage during the service life of concrete structures like pavements. The test results demonstrate that when the RCA content is elevated, the abrasion resistance characterized by the density of concrete lost from the specimen surface declines gradually. The reference mix without RCA exhibits the lowest volume removal of 10.82 cm^3/50

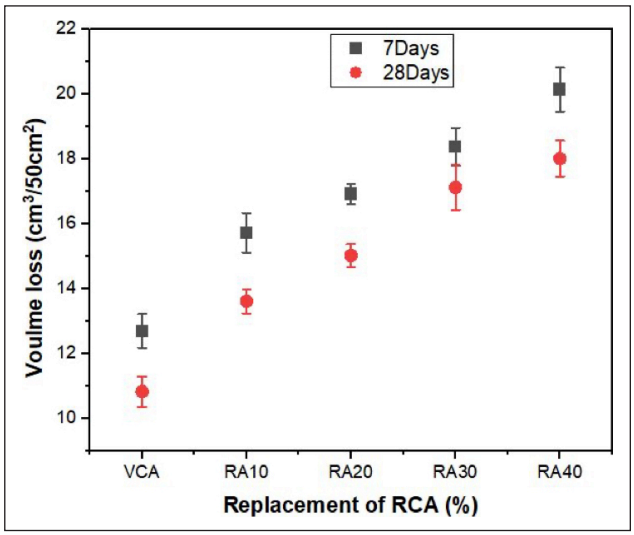

Figure 8. Abrasion resistance of RCA-based Geopolymer concrete.

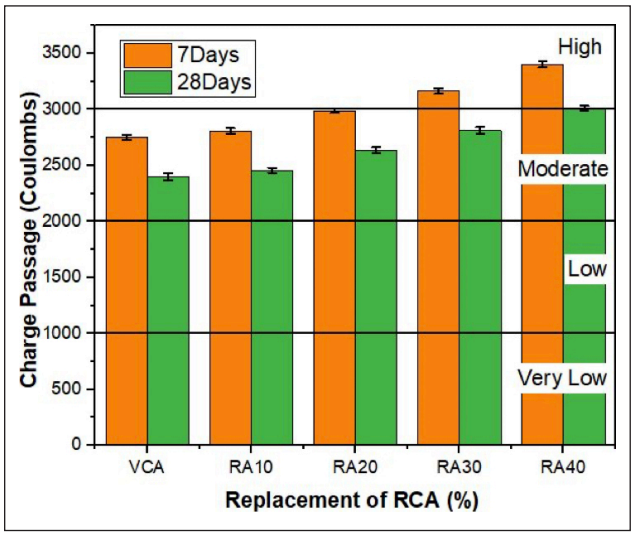

Figure 9. Chloride ions passage of RCA-based Geopolymer concrete.

cm², aligning with high-strength performance concretes. As RCA substitution is enhanced to 40%, the abrasion value rises to 18.01 cm³/50 cm², implying that surface integrity becomes more vulnerable to wearing mechanisms but is still within limits for concrete pavement application.

A noticeable reduction in abrasion resistance ensues because the recycled concrete aggregates themselves display inferior surface hardness compared to natural gravels, resulting from the porous, weak zones emerging from old adhered mortar on particles [48, 50]. When loads are applied, these softer sites become prominent locations for crack initiation, which exponentially leads to material failure and breakdown [60]. Moreover, due to higher porosity, the interfacial bonding between RCA particles and geopolymeric paste remains poor, allowing dislodgement of particles under abrasion and exacerbating weight loss [50, 60]. However, upon prolonged moist curing, the geopolymer concrete matrix develops enhanced consolidation as the gel permeates into available voids through the pozzolanic effect, diminishing flaws otherwise present around RCA zones [61]. However, the individual lower hardness characteristics translate proportionally into bulk concrete composite behavior depending on the replacement ratio. Structured optimization of RCA percentage coupled with incorporating abrasion-resistant admixtures like silicon carbide can aid in attaining strength, and abrasion attributes service life for geopolymer concrete containing recycled aggregates.

3.5. Chloride Ion Permeability of RCA-Based Geopolymer Concrete

Figure 9 represents the resistance to chloride ion penetration assessed through total charge passed during accelerated migration testing in geopolymer concrete specimens with up to 40% coarse aggregates replaced via recycled concrete aggregates (RCA). Analyzing chloride diffusivity is imperative to evaluate durability against the ingress of harmful salts, which can initiate rebar corrosion in structurally reinforced concrete. It is discernible that charge passed, which serves as an index of chloride penetrability, rises progressively with an increase in RCA replacement levels from 1687 coulombs for reference mix to 2196 coulombs for 40% RCA mix after 28 days of standard moist curing. However, as per ASTM 1202 classification, all four concrete variations demonstrate low chloride ion permeability, implying appreciable resistance against chloride ingress and corresponding corrosion risks.

The noticeable rise in chloride diffusivity is anticipated. It is a consequence of the relatively more porous and permeable microstructure introduced by the recycled aggregates having weaker interfacial bonding with the geopolymeric paste, which acts as transport paths aiding the migration of chlorides [62]. Moreover, RCA's higher moisture absorption capacity leads to more excellent solution saturation, causing increased chloride transportation compared to only natural aggregates. Nonetheless, over longer durations, densification occurs through secondary geopolymerization infilling pores within the composite transition zones, resulting in the refinement of permeability [63]. Adding mineral admixtures like Metakaolin or GGBFS optimizes packing, leading to narrowed pores that restrain fluid transport. Finer RCA fractions also demonstrate superior chloride resistance than coarser particles, mitigating the negative impacts. Overall, with controlled RCA proportions, geopolymer concretes can achieve adequacy in permeability properties for assured durability, as the test data indicates. Optimization of mix design coupled with modified curing can address the implications of marginally elevated chloride penetrability in sustainable concretes containing recycled concrete aggregates.

4. CONCLUSIONS

Based on the results presented in the attachment, here are specific conclusions for this study:

- Recycled concrete aggregates (RCA) exhibited inferior properties compared to virgin coarse aggregates (VCA), with higher water absorption (4.39% vs. 1.75%), aggre-

gate crushing value (20.9% vs. 17.2%), aggregate impact value (28.2% vs 16.78%), and abrasion value (26.1% vs 14.3%). However, these values still fall within acceptable limits for pavement applications.

- Increasing the RCA replacement ratio in geopolymer concrete resulted in a gradual decline in 28-day compressive strength from 40.16 MPa (0% RCA) to 33.52 MPa (40% RCA). Notably, up to 20% RCA substitution achieved the minimum stipulated strength for pavement applications.
- Water absorption of geopolymer concrete increased from 5.2% to 6.8% as RCA content increased from 0% to 40%. All mixes demonstrated water absorption within the specified limit of 7% for structural concretes.
- Abrasion resistance, evaluated through the density of concrete lost, declined with increasing RCA content from 10.82 $cm^3/50cm^2$ for the control mix to 18.01 $cm^3/50cm^2$ for 40% RCA mix. However, all abrasion values remained within acceptable limits for pavement-quality concrete.
- Chloride ion penetrability, assessed through total charge passed, increased with rising RCA proportions from 1687 to 2196 coulombs. Despite this increase, all geopolymer concrete variations exhibited low chloride permeability, indicating adequate durability.
- With the RCA percentage restricted to 20%, the strength, abrasion resistance, and permeability requirements for pavement construction were fulfilled, substantiating the feasibility of using recycled aggregates in geopolymer concrete for this application.

These conclusions highlight the potential for using RCA in geopolymer concrete for pavement applications while acknowledging the trade-offs in performance as RCA content increases. The study suggests that up to 20% RCA replacement can be effectively used without compromising essential properties required for pavement construction.

ETHICS

There are no ethical issues with the publication of this manuscript.

DATA AVAILABILITY STATEMENT

The authors confirm that the data that supports the findings of this study are available within the article. Raw data that support the finding of this study are available from the corresponding author, upon reasonable request.

CONFLICT OF INTEREST

The authors declare that they have no conflict of interest.

FINANCIAL DISCLOSURE

The authors declared that this study has received no financial support.

USE OF AI FOR WRITING ASSISTANCE

Not declared.

PEER-REVIEW

Externally peer-reviewed.

REFERENCES

[1] Tuladhar, R., Marshall, A., & Sivakugan, N. (2020). Use of recycled concrete aggregate for pavement construction. In *Advances in construction and demolition waste recycling* (pp. 181–197). Woodhead Publishing. [CrossRef]

[2] Durga, C. S. S., Chava, V., Priyanka, M., Chaitanya, B. K., Rao, B. N. M., & Rao, T. M. (2021). Synergistic effects of GGBFS addition and oven drying on the physical and mechanical properties of fly ash-based geopolymer aggregates. *J Sustain Constr Mater Technol, 9*(2), 93–105. [CrossRef]

[3] Ningampalli, R., Rao, M. S., & Desai, V. B. (2021). Flexural and cracking behavior of reinforced lightweight self-compacting concrete beams made with LECA aggregate. *J Sustain Constr Mater Technol, 9*(2), 159–169. [CrossRef]

[4] Chaitanya, B. K., Sivakumar, I., Madhavi, Y., Cruze, D., Venkatesh, C., Naga Mahesh, Y., & Sri Durga, C. S. (2024). Microstructural and residual properties of self-compacting concrete containing waste copper slag as fine aggregate exposed to ambient and elevated temperatures. *Infrastructures, 9*(5), 85. [CrossRef]

[5] Nwakaire, C. M., Yap, S. P., Onn, C. C., Yuen, C. W., & Ibrahim, H. A. (2020). Utilisation of recycled concrete aggregates for sustainable highway pavement applications; a review. *Constr Build Mater, 235*, 117444. [CrossRef]

[6] Reza, F., Wilde, W. J., & Izevbekhai, B. (2018). Sustainability of using recycled concrete aggregates as coarse aggregate in concrete pavements. *Transp Res Rec, 2672*(27), 99–108. [CrossRef]

[7] Tam, V. W., Soomro, M., & Evangelista, A. C. J. (2018). A review of recycled aggregate in concrete applications (2000–2017). *Constr Build Mater, 172*, 272–292. [CrossRef]

[8] Bellum, R. R., Venkatesh, C., & Madduru, S. R. C. (2021). Influence of red mud on performance enhancement of fly ash-based geopolymer concrete. *Innov Infrastruct Solut, 6*(4), 215. [CrossRef]

[9] Zhang, B. (2024). Durability of sustainable geopolymer concrete: A critical review. *Sustain Mater Technol*, e00882. [CrossRef]

[10] Bellum, R. R., Al Khazaleh, M., Pilla, R. K., Choudhary, S., & Venkatesh, C. (2022). Effect of slag on strength, durability and microstructural characteristics of fly ash-based geopolymer concrete. *J Build Pathol Rehabil, 7*(1), 25. [CrossRef]

[11] Wasim, M., Ngo, T. D., & Law, D. (2021). A state-of-the-art review on the durability of geopolymer concrete for sustainable structures and infrastructure. *Constr Build Mater, 291*, 123381. [CrossRef]

[12] Bellum, R. R., Muniraj, K., & Madduru, S. R. C. (2020). Exploration of mechanical and durability characteristics of fly ash-GGBFS based green geopolymer concrete. *SN Appl Sci, 2*(5), 919. [CrossRef]

[13] Mas, B., Cladera, A., Bestard, J., Muntaner, D., López, C. E., Piña, S., & Prades, J. (2012). Concrete with mixed recycled aggregates: Influence of the type of cement. *Constr Build Mater, 34*, 430–441. [CrossRef]

[14] De Juan, M. S., & Gutiérrez, P. A. (2009). Study on the influence of attached mortar content on the properties of recycled concrete aggregate. *Constr Build Mater, 23*(2), 872–877. [CrossRef]

[15] Kou, S. C., & Poon, C. S. (2010). Properties of concrete prepared with PVA-impregnated recycled concrete aggregates. *Cem Concr Compos, 32*(8), 649–654. [CrossRef]

[16] Letelier, V., Tarela, E., Muñoz, P., & Moriconi, G. (2017). Combined effects of recycled hydrated cement and recycled aggregates on the mechanical properties of concrete. *Constr Build Mater, 132*, 365–375. [CrossRef]

[17] Ozbakkaloglu, T., Gholampour, A., & Xie, T. (2018). Mechanical and durability properties of recycled aggregate concrete: Effect of recycled aggregate properties and content. *J Mater Civ Eng, 30*(2), 04017275. [CrossRef]

[18] Pepe, M., Toledo Filho, R. D., Koenders, E. A., & Martinelli, E. (2014). Alternative processing procedures for recycled aggregates in structural concrete. *Constr Build Mater, 69*, 124–132. [CrossRef]

[19] Stambaugh, N. D., Bergman, T. L., & Srubar III, W. V. (2018). Numerical service-life modeling of chloride-induced corrosion in recycled-aggregate concrete. *Constr Build Mater, 161*, 236–245. [CrossRef]

[20] Liang, C., Ma, H., Pan, Y., Ma, Z., Duan, Z., & He, Z. (2019). Chloride permeability and the caused steel corrosion in the concrete with carbonated recycled aggregate. *Constr Build Mater, 218*, 506–518. [CrossRef]

[21] Silva, S., Evangelista, L., & De Brito, J. (2021). Durability and shrinkage performance of concrete made with coarse multi-recycled concrete aggregates. *Constr Build Mater, 272*, 121645. [CrossRef]

[22] ASTM C 618. (2008). *Standard specification for coal FA and raw or calcined natural pozzolan for use in concrete*. ASTM International, West Conshohocken.

[23] ASTM C989, C989M-18a. (2018). *Standard specification for slag cement for use in concrete and mortars*. ASTM International, West Conshohocken.

[24] ASTM C 33. (2023). *Standard specification for concrete aggregates*. ASTM International, West Conshohocken.

[25] BS 882. (1992). *Standard specification for aggregates from natural sources for concrete*.

[26] Mukkala, P., Venkatesh, C., & Habibunnisa, S. (2022). Evaluation of mix ratios of lightweight concrete using geopolymer as binder. *Mater Today Proc, 52*, 2053–2056. [CrossRef]

[27] Wu, L., Sun, Z., & Cao, Y. (2024). Modification of recycled aggregate and conservation and application of recycled aggregate concrete: A review. *Constr Build Mater, 431*, 136567. [CrossRef]

[28] Nune, S., Murthy, N. D., & Rao, M. S. (2021, November). Studies on impact resistance of self-compacting concrete with mechanically treated recycled coarse aggregate. In *IOP Conf Ser Mater Sci Eng* (Vol. 1197, No. 1, p. 012051). IOP Publishing. [CrossRef]

[29] BSI. (2008). BS EN 12620: *Aggregates for concrete*. BSI, Milton Keynes, UK.

[30] BIS 10262. (2019). *Standard specification for concrete mix design*. Bureau of Indian standards, New Delhi.

[31] Durga, C. S. S., Venkatesh, C., Muralidhararao, T., Bellum, R. R., & Rao, B. N. M. (2023). Estimation of durability properties of self-healing concrete influenced by different Bacillus species. *Res Eng Struct Mater, 9*(4), 1489–1505. [CrossRef]

[32] Durga, C. S. S., Venkatesh, C., Muralidhararao, T., & Bellum, R. R. (2023). Crack healing and flexural behaviour of self-healing concrete influenced by different Bacillus species. *Res Eng Struct Mater, 9*(4), 1477–1488. [CrossRef]

[33] IS 2386 (Part 4). (2002). *Standard specification for method of tests for aggregates for concrete: Aggregate impact value test, aggregate crushing strength test, and abrasion test*. Bureau of Indian standards, New Delhi, India.

[34] IS 2386 (Part 3). (2002). *Standard specification for method of tests for aggregates for concrete: Water absorption*. Bureau of Indian standards, New Delhi, India.

[35] IS 516-1959. (1959). *Methods of tests for strength of concrete*. Bureau of Indian Standards, New Delhi, India.

[36] Durga, C. S. S., Venkatesh, C., Bellum, R. R., Chaitanya, B. K., Rao, B. N. M., & Rao, T. M. (2024). Influence of Bacillus species on mechanical and microstructural properties of concrete. *Multiscale Multidiscip Model Exp Des, 2024*, 1–17. [CrossRef]

[37] Chava, V., & Chereddy, S. S. D. (2023). Effect of calcination on the physical, chemical, morphological, and cementitious properties of red mud. *J Sustain Constr Mater Technol, 8*(4), 297–306. [CrossRef]

[38] Rao, T. M., Mahesh, K., Venkatesh, C., Durga, C. S. S., Reddy, B. R., Tejaswi, P. S., & Charandeepneelesh, R. (2023). Influence of magnetization of water on mechanical and durability properties of fly ash concrete. *Mater Today Proc, 2023*, 1–8.

[39] IS 1237-2012. (2012). *Methods of tests for abrasion resistance of concrete flooring*. Bureau of Indian Standards, New Delhi, India.

[40] ASTM C 1202. (2012). *Standard test method for electrical indication of concrete's ability to resist chloride ion penetration*. ASTM International, West Conshohocken, PA.

[41] Ruben, N., Venkatesh, C., Durga, C. S. S., & Chand, M. S. R. (2021). Comprehensive study on performance of glass fibers-based concrete. *Innov Infrastruct Solut, 6*(2), 112. [CrossRef]

[42] Venkatesh, C., Nerella, R., & Chand, M. S. R. (2021). Role of red mud as a cementing material in concrete: A comprehensive study on durability behavior. *Innov Infrastruct Solut, 6*(1), 13. [CrossRef]

[43] Venkatesh, C., Nerella, R., & Chand, M. S. R. (2020). Experimental investigation of strength, durability, and microstructure of red-mud concrete. *J Korean Ceram Soc, 57*(2), 167–174. [CrossRef]

[44] BIS, IS 1124-1974. (1974). *Specification for water absorption for concrete*. Bureau of Indian Standards, New Delhi.

[45] Anirudh, M., Rekha, K. S., Venkatesh, C., & Nerella, R. (2021). Characterization of red mud-based cement mortar; mechanical and microstructure studies. *Mater Today Proc, 43*, 1587–1591. [CrossRef]

[46] Venkatesh, C., Sri Rama Chand, M., Ruben, N., & Sonali Sri Durga, C. (2020). Strength characteristics of red mud and silica fume based concrete. In *Smart technologies for sustainable development: Select proceedings of SMTS 2019* (pp. 387–393). Springer Singapore. [CrossRef]

[47] Venkatesh, C., Mallikarjuna, V., Rao, G. M., Patil, S. K., Yashwanth, M. K., Venkata Siva Rama Prasad, C., & Sree Lakshmi Devi, G. (2024). Synergistic effects of graphene oxide and limestone calcined clay cement on mechanical properties and durability of concrete. *J Build Pathol Rehabil, 9*(2), 1–14. [CrossRef]

[48] Verian, K. P., Ashraf, W., & Cao, Y. (2018). Properties of recycled concrete aggregate and their influence in new concrete production. *Resour Conserv Recycl, 133*, 30–49. [CrossRef]

[49] McNeil, K., & Kang, T. H. K. (2013). Recycled concrete aggregates: A review. *Int J Concr Struct Mater, 7*, 61–69. [CrossRef]

[50] Saravanakumar, P., Abhiram, K., & Manoj, B. (2016). Properties of treated recycled aggregates and its influence on concrete strength characteristics. *Constr Build Mater, 111*, 611–617. [CrossRef]

[51] Wang, Z., & He, W. (2017). Regional energy intensity reduction potential in China: A non-parametric analysis approach. *J Clean Prod, 149*, 426–435. [CrossRef]

[52] Xiao, J., Li, W., Fan, Y., & Huang, X. (2012). An overview of study on recycled aggregate concrete in China (1996–2011). *Constr Build Mater, 31*, 364–383. [CrossRef]

[53] Silva, R. V., De Brito, J., & Dhir, R. K. (2014). Properties and composition of recycled aggregates from construction and demolition waste suitable for concrete production. *Constr Build Mater, 65*, 201–217. [CrossRef]

[54] Wang, R., Yu, N., & Li, Y. (2020). Methods for improving the microstructure of recycled concrete aggregate: A review. *Constr Build Mater, 242*, 118164. [CrossRef]

[55] Tam, V. W., Wattage, H., Le, K. N., Butera, A., & Soomro, M. (2021). Methods to improve microstructural properties of recycled concrete aggregate: A critical review. *Constr Build Mater, 270*, 121490. [CrossRef]

[56] Pawluczuk, E., Kalinowska-Wichrowska, K., Jimenez, J. R., Fernández-Rodríguez, J. M., & Suescum-Morales, D. (2021). Geopolymer concrete with treated recycled aggregates: Macro and microstructural behavior. *J Build Eng, 44*, 103317. [CrossRef]

[57] Joseph, M., Boehme, L., Sierens, Z., & Vandewalle, L. (2015). Water absorption variability of recycled concrete aggregates. *Mag Concr Res, 67*(11), 592–597. [CrossRef]

[58] Quattrone, M., Cazacliu, B., Angulo, S. C., Hamard, E., & Cothenet, A. (2016). Measuring the water absorption of recycled aggregates, what is the best practice for concrete production? *Constr Build Mater, 123*, 690–703. [CrossRef]

[59] Belin, P., Habert, G., Thiery, M., & Roussel, N. (2014). Cement paste content and water absorption of recycled concrete coarse aggregates. *Mater Struct, 47*, 1451–1465. [CrossRef]

[60] Nikmehr, B., & Al-Ameri, R. (2022). A state-of-the-art review on the incorporation of recycled concrete aggregates in geopolymer concrete. *Recycling, 7*(4), 51. [CrossRef]

[61] Kumar, G., & Mishra, S. S. (2022). Effect of recycled concrete aggregate on mechanical, physical and durability properties of GGBS–fly ash-based geopolymer concrete. *Innov Infrastruct Solut, 7*(4), 237. [CrossRef]

[62] Koushkbaghi, M., Alipour, P., Tahmouresi, B., Mohseni, E., Saradar, A., & Sarker, P. K. (2019). Influence of different monomer ratios and recycled concrete aggregate on mechanical properties and durability of geopolymer concretes. *Constr Build Mater, 205*, 519–528. [CrossRef]

[63] Lim, Y. Y., & Pham, T. M. (2021). Effective utilisation of ultrafine slag to improve mechanical and durability properties of recycled aggregates geopolymer concrete. *Clean Eng Technol, 5*, 100330. [CrossRef]

Journal of Sustainable Construction Materials and Technologies
Web page info: https://jscmt.yildiz.edu.tr
DOI: 10.47481/jscmt.1536060

JSCMT
Journal of Sustainable Construction Materials and Technologies

Research Article

Sustainability beyond the surface: Evaluating the long-term environmental and energy performance of selected cladding materials for housing retrofits

Mark ALEGBE*[1], Nasiru HAMMED[2]

[1]*Department of Architectural Technology, Auchi Polytechnic, Edo State, Nigeria*
[2]*Department of Architecture, Bells University of Technology, Ogun State, Nigeria*

ARTICLE INFO

Article history
Received: January 06 2024
Revised: 18 March 2024
Accepted: 15 July 2024

Key words:
Building embodied carbon, cladding, gravel stone, ranking system, sustainable façade

ABSTRACT

External walls, constituting the largest exposed surface area of the building envelope, face heightened susceptibility to environmental influences. In this study location, aesthetic considerations often overshadow environmental impact and comfort requirements in selecting exterior cladding materials. This paper investigates the energy performance, global warming potential, and thermal comfort aspects of carefully selected cladding materials, informed by an exhaustive literature review, for application in retrofit projects in Abuja, Nigeria. Energy consumption, carbon emissions, and temperature distributions were simulated using materials in a hypothetical single-floor residential building finished with cement-sand plaster. The findings show that gravel stone exhibits the most negligible environmental impact. In contrast, aluminum and lightweight metal cladding panels contribute significantly to the embodied carbon of the building despite ranking as the most expensive materials. Insulating the test building with polyurethane boards yields substantial energy savings of up to 9% in cooling electricity, averting the need for added cladding. This study emphasizes the significance of adopting a multi-criterion approach in selecting façade cladding materials, prioritizing environmental and thermal considerations over aesthetic and cost benefits. The implications extend beyond mere emissions reduction, shedding light on the vital interplay between material choices on comfort and energy efficiency in building design.

Cite this article as: Alegbe, M., & Hammed, N. (2024). Sustainability beyond the surface: Evaluating the long-term environmental and energy performance of selected cladding materials for housing retrofits. *J Sustain Const Mater Technol*, 9(3), 221–238.

1. INTRODUCTION

In building design, a noticeable conflict has emerged between the pursuit of aesthetic ideals and the imperatives of sustainability [1]. The allure of cultural values and visual appeal often precedes the crucial energy efficiency considerations in buildings. In the contemporary landscape, marked by an energy crisis, the separation of structural and cladding functions in buildings has posed challenges to architects, demanding a delicate balance between durability and the fundamental properties of external finishes [2]. Recognizing the urgency of sustainability, architects are transcending the confines of mere artistic expression. Collaborating with diverse professionals, they now strive for a holistic sustainability approach [3, 4]. This drift is particularly evident in treating wall claddings, which fulfill multiple roles—providing protection, enhancing aesthetic appeal, and regulating building thermal conditions. The building envelope, a cor-

***Corresponding author.**
*E-mail address: alegbemark@gmail.com

nerstone of structural integrity, is connected to the exterior sphere and constantly influences dynamic environmental factors [5]. Evaluating the sustainability performance of cladding materials within this complex context involves addressing uncertainties related to quantification and the complex interplay of various parameters [6].

The symbiotic relationship between the building envelope and the surrounding environment is pivotal, with implications for occupants, structural integrity, and the global climate. However, when designed in harmony with nature, the impact of cladding materials on these aspects becomes negligible [7]. Balaji et al. [8] accentuate the significance of wall configuration in achieving superior thermal performance. Factors such as the coefficient of thermal conductivity, wall thickness, and mortar thickness play a fundamental role in determining the heat transfer rates of cladding materials [9]. Materials with higher thermal conductivity transfer heat more readily than those with lower conductivity. In the context of building cladding materials, as used by the author, materials with a higher coefficient of thermal conductivity will allow heat to pass easily through the cladding materials, leading to increased heat transfer rates through the wall components. Similarly, it was found using Gray theory analysis that the coefficient of thermal conductivity of wall materials and wall and mortar thicknesses are influencing factors that correlate with the wall heat transfer coefficient. However, the climatic conditions of the building's location significantly influence their effectiveness [5], making considerations for time lag and decrement factors paramount in tropical regions [8].

In the contemporary built environment industry, a paramount concern is the reduction of buildings' energy consumption. Various factors, including material properties, building size, geographical location, and environmental conditions, collectively shape the energy performance of buildings according to Atashbar and Noorzai [10] and Balaji et al. [8]. A global imperative for sustainable buildings to mitigate emissions and address climate change has shifted the focus from aesthetics [11] to a more comprehensive evaluation encompassing quality, cost, and environmental impact [12, 13]. Therefore, beyond satisfying thermal requirements, cladding selection necessitates considering physical qualities, ecological impact, and financial implications [2]. A holistic understanding of a material's sustainability, as advocated by Takano et al. [14], demands a lifecycle approach.

The global trend of housing retrofit in the construction industry seeks to enhance the energy efficiency of existing housing stock [15]. Modifying wall fabrics, glazing, or incorporating thermal insulators can significantly impact energy savings and influence the sizing of HVAC systems [16–18]. As part of this trend, cladding systems emerge as crucial contributors to sustainable energy performance, albeit with challenges during selection. The decision-making matrix balances cost, embodied carbon, aesthetics, thermal properties, maintenance, and lifecycle impact [14]. Regional preferences further complicate the scenario, with Northern Europe favoring local timber for cladding, while the UK leans towards rendered concrete blocks and brick for their external visual appeal [19]. Cost considerations, however, are driving a shift away from traditional materials [12].

The choice of cladding materials is inherently complex and necessitates a case-by-case examination [20]. On the other hand, Dodge and Liu [21] encourages selecting environmentally friendly materials to minimize adverse environmental impacts, emphasizing their effects on the user's comfort, the building's lifespan, and maintenance considerations [22]. When viewed through a building's microclimate lens, cladding performance takes precedence over efficacy. Building practitioners must refrain from focusing solely on cost reduction, recognizing that the most cost-effective materials may not always align with environmental sustainability requirements. Hence, a delicate equilibrium between ecological considerations and the practicalities of design function and economy should guide the selection and use of building materials [23].

While many building materials claim environmental friendliness based on a specific aspect of the lifecycle [21], the efficacy of cladding materials extends beyond reducing carbon emissions. Considerations like life expectancy and maintenance values should also factor into material choices [13]. As construction becomes more intricate and material options proliferate, the responsibility of material selection may extend beyond architects due to knowledge gaps or project complexity [24]. Enhancing existing housing stock, especially external walls, to adapt to changing climates and meet carbon emissions reduction targets is becoming crucial [4]. Yet, public resistance persists as long as sustainability efforts seem technical and aesthetically unpleasant. However, while integral to architectural sustainability, aesthetics should not define the concept; it encompasses broader considerations, including social equity, environmental impact, and the preservation of cultural values [25].

This study proposes an approach for selecting external cladding materials in existing buildings or retrofit projects in Nigeria. Focused on a test building with a conventional cement-sand plaster exterior, the investigation involves remodeling using various cladding materials through computer simulations. The study presents a ranking system based on embodied carbon, electricity for cooling, building energy per conditioned area, and operative temperature on the South-facing wing. The results aim to enlighten practitioners on the multifaceted aspects of cladding selection, offering guidance in decision-making processes.

2. LITERATURE REVIEW

Green architecture has reached a critical juncture where careful considerations ensure that a building's façade remains visually appealing without compromising essential sustainability values [3]. However, a study reveals that climate conditions and material performance often take a backseat in material selection, with a predominant focus on cost, aesthetics, and societal influence. Craig et al. [19] further emphasizes a preference for external cladding materials' "traditional" look over novel alternatives. The challeng-

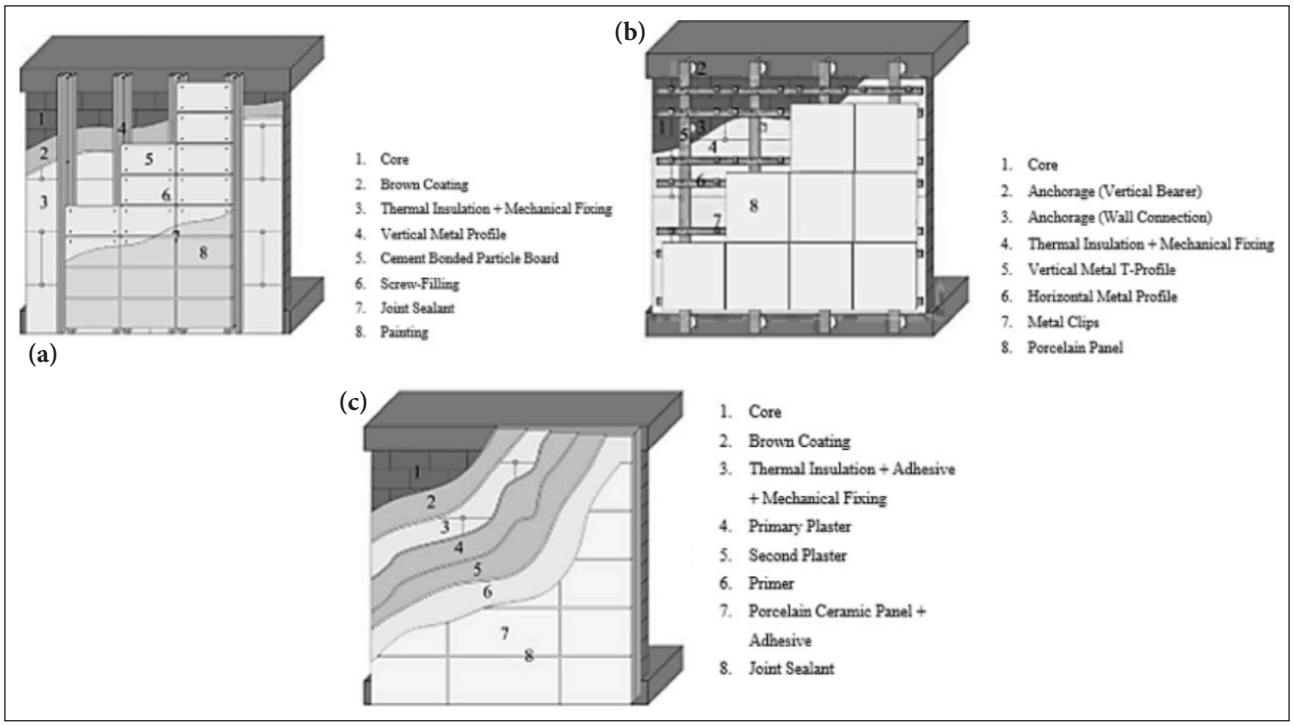

Figure 1. Cladding construction techniques- **(a)** screwed system, **(b)** fixed system, **(b)** bonded system [36].

es associated with modern materials, including weathering (patina), durability, and assembly, have been highlighted Slaton [26]. While modern materials demonstrate reduced susceptibility to water leakage or mold growth compared to traditional masonry wall construction, concerns persist regarding strength loss and anchorage deterioration, especially in modern thin claddings. Dissanayake et al. [27] argue that any building material utilizing waste materials or minimizing natural resource consumption holds promise for sustainability.

Moreover, studies show that cladding material choices evolve due to technological advances and contemporary material inventions meeting functional requirements. Historical trends in the US residential construction industry have witnessed shifts in the last decade, exemplified by using wood, aluminum siding, fiber cement, and vinyl for external wall cladding [12]. Notably, fiber cement boards have garnered interest from developers as a façade cladding material [6]. In urban space design, ceramic cladding emerges as a potentially transformative sustainable architectural material for the 21st century [7].

Over the years, the efficacy of different cladding materials has been extensively investigated across various regions globally, considering their application, selection and performance based on energy savings [15, 17, 28], environmental impact [11, 15, 21], cost [22, 29] and thermal comfort [20, 30]. Similarly, these materials have been researched worldwide in various climates, with some options considered in this study. Notable cladding materials investigated in prior research include aluminium [21], wood [31], polystyrene [27], terracotta [32], marble, stone [33], Ceramic [7], boards [34, 35], resin panels [26], recycled waste [6], concrete [28], plaster [20] and Date Palm Midribs (DPM) [15].

2.1. Cladding Construction Techniques

According to Metin and Tavil [36], the facade cladding construction techniques encompass three primary methods: the screwed system, the fixed system, and the bonded system (Fig. 1). The choice among these methods depends on material type, desired aesthetics, application cost, specific building requirements, and cladding location. Claddings can be installed directly onto the structural building system, the core of the external wall, or over the core of the external wall. When choosing between facade cladding construction techniques, architects must consider various factors to ensure the selected approach aligns with the building project's requirements, budget, aesthetics, and performance objectives. They must therefore:

I. Understand the properties and characteristics of the available cladding material.
II. Assess how the chosen cladding material and construction technique contribute to the visual appearance of the building facade.
III. Determine whether the cladding system needs to accommodate additional features or functionalities such as integrated solar panels, ventilation systems, or rainwater management solutions.
IV. Assess the long-term performance and durability of the chosen cladding materials and construction techniques.
V. Evaluate the cost implication of different cladding materials and construction techniques.

2.1.1. Screwed System

The screwed system, also known as the "rivet system" [37] or "screw face" fixing, is a cost-effective way of installing facade cladding that works well with various material types. Cladding panels in this system are mechanically attached to

the building using screws. While this system offers several advantages, such as ease of installation and cost-effectiveness, it also presents potential challenges. Here are some of the challenges, along with possible mitigation strategies.

Thermal Bridging: Screws or fasteners used in this system can create thermal bridges, where heat is transferred through the fasteners, leading to energy loss and reduced thermal performance of the building envelope. To avoid this, the authors suggest the use of thermal break materials or isolators between the fasteners and the cladding panels to minimize heat transfer or the use of screws with lower thermal conductivity in conjunction with insulating gaskets.

Visual Appeal: The presence of visible screws on the facade may detract from the aesthetic appeal of the building, especially for projects with sleek or minimalist design intentions. To mitigate this challenge, it is advisable to conceal screws within the joints or seams of the cladding panels where possible or incorporate design elements or features that strategically integrate the fasteners into the overall facade design, turning them into intentional design elements rather than distractions.

Corrosion and Maintenance: Exposing metal fasteners to weather elements and moisture can lead to corrosion of screws over time, potentially compromising the structural integrity of the cladding system, thus, increasing maintenance requirements. To avoid this, it is suggested to use corrosion-resistant materials such as stainless steel or galvanized steel for screws.

2.1.2. Fixed System

The fixed system relies on hidden mechanisms to provide a seamless appearance to the building façade. Studies indicate that the fixed system contributes the most to the sustainability of the construction process [36]. This system poses challenges while contributing to better thermal performance due to a complex installation process that can increase construction and maintenance costs.

2.1.3. Bonded System

The bonded system employs adhesive or bonding agents to attach the cladding material to the building structure. This approach offers the advantage of a monolithic appearance for the external facade, enhanced durability, and reduced thermal bridging compared to the screwed system. However, costs may increase where specific skills and adhesives are needed.

2.2. Cladding Choice on Building's Performance

The escalating demand for quality housing is projected to increase energy usage [27]. Atashbar and Noorzai [10] demonstrated that optimal material selection for residential building facades can lead to a 40% reduction in annual average energy consumption. For example, opaque materials have been shown to have a short time lag and can decrease indoor temperature by approximately 9 ^{0}C [30]. Pekdogan and Basaran [17] also assert that opaque materials, such as stone cladding, contribute to significant energy savings. A study investigating various materials for a traditional single-family home in Ohio, USA, found that vinyl siding was the most environmentally friendly and cost-efficient option despite limited recycling potential and shorter service life. Similar investigations in the hot climate of the UAE favored stone cladding systems for their exceptional performance, closely followed by aluminum cladding panels (ACP) and plaster systems. As Hamoush et al. [33] suggested, engineered stone contributes to substantial energy savings, reducing the cooling load in the UAE by 4% compared to ACP and 1.5% compared to plaster.

Moreover, using locally sourced or industrial waste materials for cladding, such as Date Palm Midribs (DPM), has demonstrated significant energy savings, as highlighted by Darwish et al. [15] achieving a 13% reduction in cooling and 4% in total energy consumption. Specifically, DPM fibers have been recognized as a sustainable and energy-efficient material for cladding and construction due to the inherent properties of the fiber, which can be processed into strips and fiber boards. They have natural insulating properties that can help regulate indoor temperatures by reducing heat transfer through the building envelope. The production process of DPM involves minimal energy input compared to many industrial waste materials. Since they are harvested from agricultural waste or by-products of date palm cultivation, they have low embodied energy, meaning they need less energy for extraction, processing, and manufacturing than conventional building materials.

Further, the adoption of locally produced timber for cladding, driven by cost considerations and a commitment to improving housing sustainability, is gaining traction [19]. However, comparative cost analyses by Mac-Barango [29] and Alegbe [38] on concrete blocks against timber indicate that timber cladding can significantly increase construction costs. While timber is valued for its ecological advantages, such as carbon storage [39], it is not without challenges, particularly its interaction with moisture. This can lead to issues like timber discoloration in specific climates [12, 31]. Prevailing wind direction can also influence timber discoloration, especially in tropical monsoon climates [40]. It is, thus, worthwhile to undertake a condensation analysis to ascertain the possibility of mold growth when wood-based materials define the facade of buildings.

Taylor et al. [11] compared to the global warming potential of different cladding materials, they revealed that plywood and masonry wall cladding had the lowest carbon emissions. Conversely, reinforced concrete foundations were associated with the highest global warming potential. The buildings studied were different in size and design, which may have influenced the outcome of carbon emissions. Investigations by Özel [28] in Elazığ, Türkiye, highlighted the highest peak load and maximum temperature swings for concrete walls among various materials. Concrete, metal, and brick were identified as the top three exterior wall cladding emitters. Reducing carbon emissions in a building depends on factors such as the building system, operational schedule, and the source of electricity [13]. In conclusion, the literature review highlights various pivotal factors that shape the choice of cladding materials. These encompass differences in material availability and usage depending on location, the

continuous evolution of cladding materials, and the complex interaction between numerous factors influencing the energy performance of these materials.

3. MATERIALS AND METHODS

3.1. Cladding Materials Selection Process

This research adopted a comparative and experimental design to examine the energy performance of 19 carefully selected cladding materials derived from an extensive literature review in contrast to widely used cement-sand plaster on a test building. The selection of cladding materials for the study followed a systematic process to ensure the representation of diverse materials commonly used in building construction within tropical regions. Three primary criteria guided the selection process:

I. Commonly Used Materials: Cladding materials were chosen based on their prevalence in tropical construction projects, ensuring that the selected materials were representative of those encountered in practice. For example, materials such as clay and stone are commonly used in tropical climates due to their durability and thermal properties.
II. Material Diversity: Selection criteria encompassed a wide range of material types, including natural materials (e.g., straw, clay, gravel stone), synthetic materials (e.g., PVC tiles, aluminum panels), and composite materials (e.g., resin-bonded fibreboard, polyurethane cellular board). This diversity facilitated a comprehensive comparison of material properties and performance characteristics relevant to tropical construction environments.
III. Availability and Accessibility: Priority was given to cladding materials that are readily available in the market and commonly used in construction projects. This consideration ensured the practical relevance and applicability of the study findings to real-world scenarios in tropical regions, especially Nigeria.

The search for relevant literature employed a rigorous approach leveraging reputable academic databases such as Scopus, Web of Science, and Google Scholar. A targeted search strategy was utilized using keywords, Boolean operators, and explicit vocabulary terms (e.g., 'cladding materials,' 'building envelope,' 'tropics'). Articles published from 2010 onwards were selected to ensure relevance to current construction practices within tropical climates, with reports, books, and theses excluded to prioritize peer-reviewed research. Retrieved articles underwent screening based on title, abstracts, and full text to assess their relevance and eligibility for inclusion in the literature review. This ensured a robust and all-inclusive analysis of the selected cladding materials.

The primary focus of this study is to evaluate these materials' environmental performance, energy consumption, and cost implications, aiming to suggest a basis for cladding selection for retrofit projects in Nigeria through a multi-criterion ranking system. Contemporary EnergyPlus (EPW) weather files specific to Abuja were generated using Meteonorm (V 8.0.3), ensuring a precise representation of real-world environmental conditions. These weather files were imported into the DesignBuilder (V 6.1.0.6) energy simulation program, facilitating an all-inclusive building performance analysis.

3.2. Simulation Environment Setup and Parameters

Detailed attention was paid to various parameters across categories to establish a robust simulation environment. For instance, residential spaces were modeled in the Activity system settings using the "Domestic Bedroom" template to reflect typical occupancy patterns accurately. Moreover, all zones within the test building were included in thermal and radiance daylight calculations, allowing for a holistic understanding of environmental dynamics. Occupancy density was fixed at 0.0229 persons/m² with a metabolic factor of 0.90, ensuring a precise representation of human heat gains for a maximum of two users in all occupied areas. Additionally, scheduled-based clothing was defined to align with typical clothing behaviors. Thermal calculations were also conducted annually, with cooling setpoints configured at 25^{0}C for comfort conditions and a setback temperature of 28^{0}C to optimize energy efficiency.

Furthermore, construction boundary parameters utilized the Uninsulated Heavyweight template to represent the building's initial construction characteristics accurately. Model infiltration was set at 1.0 air changes per hour (ac/h), simulating realistic air exchange rates peculiar to residential buildings in the study location. Window openings had two layers of 3mm generic clear glass with two horizontal dividers. In contrast, vertical dividers were omitted to simplify the simulation while capturing essential building envelope characteristics. Also, exterior lighting schedules were established with an absolute power setting of 100 watts, designed to turn off during daylight hours to conserve energy automatically. For HVAC operations, mechanical systems were exclusively employed for cooling, with electricity sourced from the grid as the primary fuel. Furthermore, humidity control settings were configured for dehumidification to address prevalent high humidity levels recorded in the location.

3.3. Base Model Calibration and Validation of Simulation Parameters

To ensure the accuracy and reliability of the simulation results, rigorous steps were taken to validate the parameters of the simulation environment. Firstly, the input data, including weather files and building geometry, were carefully cross-referenced with data from the Nigerian Meteorological Agency (NIMET) and benchmarked against historical data to verify their consistency and accuracy. Furthermore, a sensitivity analysis was conducted using the initial setup to identify critical factors influencing energy consumption in the base model, revealing that occupancy level, wall thickness, and insulation are the primary drivers of energy use intensity. These factors guided the alterations needed for the building simulations.

The model underwent detailed iterative calibration to align simulation results with benchmarked empirical data and improve accuracy. Initially set at 0.1187 persons per square meter (equivalent to 8 occupants), the occupancy

level was adjusted to 0.0229 persons per square meter (2 occupants) to reflect better the actual usage scenario appropriate for the hypothetical building's area. Each adjustment involved recalculating energy consumption, highlighting that varying the number of occupants significantly affected the building's energy usage. The wall thickness and insulation levels were also iteratively adjusted to optimize thermal performance. The initial model included a 150mm wall without insulation, yielding a U-value of 1.385 W/m²K. Increasing the wall thickness to 225mm reduced the U-value to 1.054 W/m²K. Adding a 35mm PUR insulation further improved the U-value to 0.436 W/m²K. However, it was observed that increasing the insulation thickness to 75mm led to higher energy consumption, likely due to over-insulation effects.

Moreover, thicker insulations always increase the overall costs of the building project [41]. Therefore, 35mm PUR insulation was selected as the optimal thickness, balancing energy efficiency and the potential for introducing cladding materials for further energy performance experiments. This iterative process of adjusting parameters ensured the model's thermal properties aligned with real-world performance metrics in the tropics. A better alignment between real-world scenarios and simulation parameters is necessary to reduce the prediction gap of results [42].

The test building, featuring a cross-shaped form (Fig. 2) and encompassing a total floor area of 71.85 m², was in the first simulation stage, modeled using 225mm concrete hollow blocks and finished with 35mm cement-sand plaster on the exterior and interior surfaces. Occupying a single floor level, the building consists of equal units on all orientations (North, South, West, and East), with a central space providing access to all four spaces.

The building plan is hypothetical, and the size does not indicate retrofit projects in Nigeria, as this can vary in length and scale. The adopted plan, however, reflects standard features in a typical project with rooms flanked towards different orientations. The building represents real-world scenarios with manageable spaces for conducting experiments in a controlled environment. The cladding application followed the screwed, fixed, or bonded system, depending on the suitability of each cladding material with the construction system. A combination of these systems was employed to suit the unique properties of each material. The study method provides a foundation for future research in cladding selection when dealing with large and complex retrofit buildings.

In the first investigation stage, multiple simulations were conducted by cladding the original wall with each cladding material, generating comprehensive data on energy consumption, environmental impact, and cost implications. Simulations were carried out simultaneously on the north, south, west, and east sides to discern potential variations in energy impact. During the second phase of the experiment, a 35mm diffusion light polyurethane board insulator was uniformly applied to all the materials. This insulator, with a conductivity of 0.0260 W/m-K, density of 35 kg/m³, and an embodied carbon of 3.0 $KgCO_2$/Kg, was added to assess the impact of insulation on the selected materials.

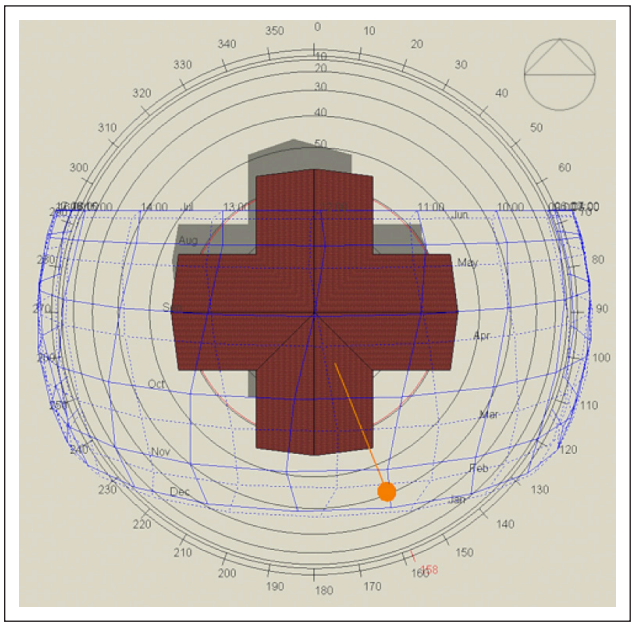

Figure 2. Top view of test building with sun path in DesignBuilder.

An analytical comparison of the simulation results with data from relevant literature was conducted to validate the simulation model. This approach is particularly suitable for simulations not incorporating field measurement data [43]. The energy consumption results for the hypothetical building, both with and without insulation, were compared against values reported in benchmark studies. These studies were chosen based on their relevance to the energy performance of insulated and non-insulated buildings and their alignment with the findings of this research. The selected benchmarks include energy performance data for residential and tertiary building stock in Spain [44, 45], public and commercial buildings in China [46, 47], public buildings in Malaysia [48], and residential buildings in Libya and Nigeria [49, 50]. These studies provided diverse energy consumption data to validate the simulation results.

3.4. Data Analysis and Visualization

Statistical analysis and visualization of the simulation results were conducted using a combination of Microsoft Excel and Tableau (version 2018.3). Initial data exploration and analysis were performed using the Data Analysis ToolPak add-in in Excel, facilitating a comprehensive statistical assessment. Descriptive statistics were employed to characterize the data's dispersion and distribution, including measures of central tendency such as mean and median and measures of variability such as standard deviation and range. Graphical representations, including histograms and radar charts, were used to visualize the distribution and identify any outliers or patterns within the data. To enhance the clarity and quality of data visualization, Tableau was employed to create high-quality visual representations that effectively depict statistical findings, easing a clearer understanding of data trends and distributions.

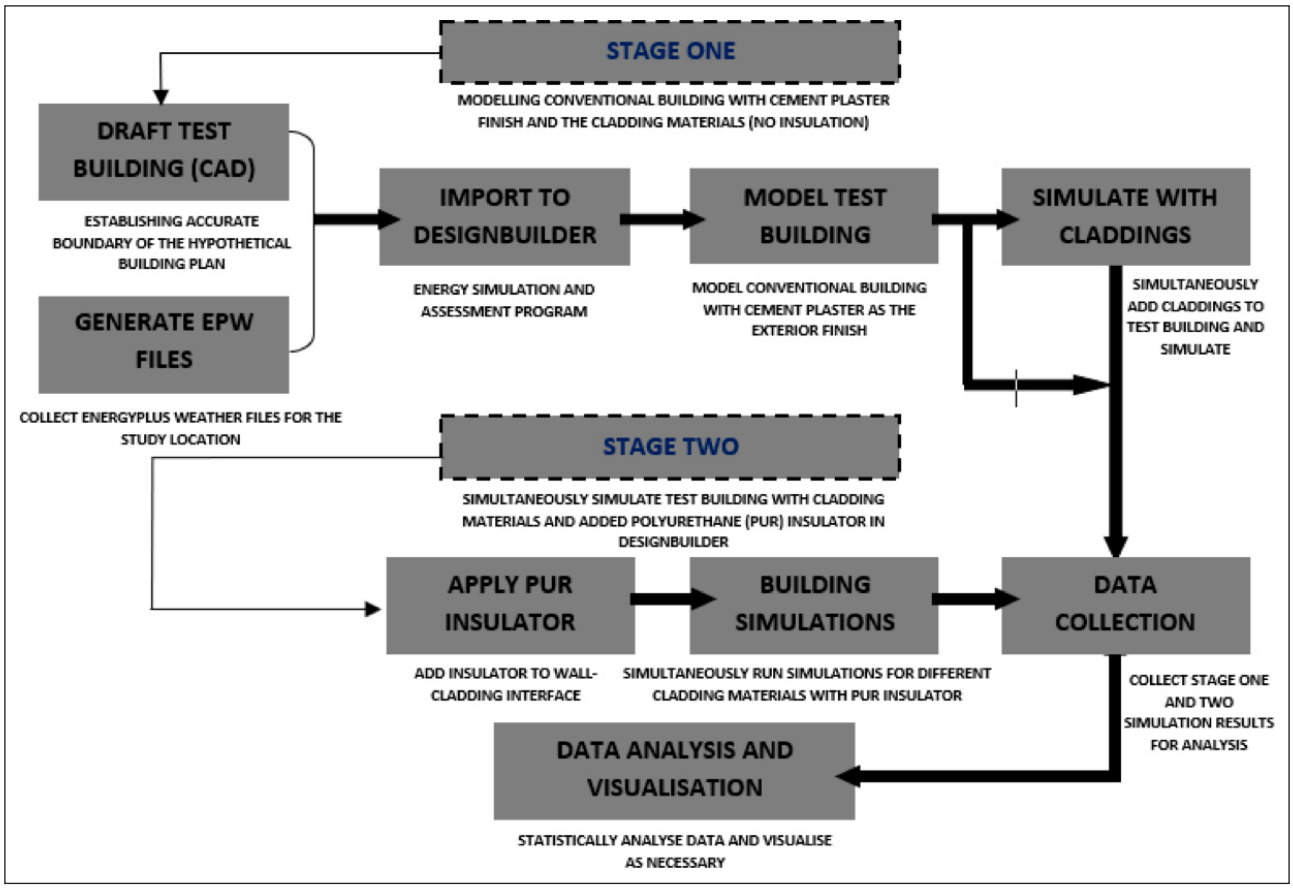

Figure 3. Methodology framework.

In addition to descriptive statistics, inferential statistical techniques were employed to investigate relationships and differences within the dataset. Analysis of Variance (ANOVA) was used to assess differences in energy performance among the various cladding materials. This allowed for a comparison of means across multiple groups and provided insights into the impact of different materials on energy consumption. Furthermore, a t-test analysis was conducted to compare specific variables, such as embodied carbon and cost, between distinct groups or conditions. These tests provided valuable insights into the significance of differences observed within the dataset. Regression analysis was also employed to explore the relationship between key variables, such as cladding material properties and their influence on energy performance. The combination of these tools enabled a comprehensive analysis of the simulation data, providing helpful information into the performance of different cladding materials and their implications for building energy efficiency and sustainability.

Several key performance metrics were carefully considered to broadly evaluate the cladding materials' environmental sustainability, energy efficiency, and cost-effectiveness. These metrics were chosen to provide a holistic assessment of the materials' performance across various dimensions. The impact of the materials' embodied carbon on the building's total global warming potential throughout its lifecycle was a primary consideration in assessing environmental sustainability. The materials' contributions to reducing indoor temperature and cooling loads were also evaluated to determine the building's energy efficiency.

Furthermore, the cost of implementing different cladding options was analyzed to ascertain the most cost-effective alternative. This included upfront costs and potential long-term savings or expenses associated with maintenance, repairs, and energy consumption. By examining these key metrics, cladding materials that offer optimal environmental sustainability, energy efficiency, and cost-effectiveness were identified, informing decision-making in building design and construction.

Building fabric insulation plays a vital role in improving the thermal performance of buildings [51–53]; thus, adding insulation offered valuable insights in the context of the experiments. The framework of the methodology is depicted in Figure 3.

4. RESULTS AND DISCUSSIONS

Selecting an appropriate cladding material for existing cement-sand plastered buildings is a complex undertaking, influenced by factors such as thickness, material density, embodied carbon, and conductivity, as shown in Table 1. A regression analysis explored the relationship between several factors, including the embodied carbon of cladding materials and the building's total embodied carbon. The study revealed a moderate to strong relationship between the embodied carbon of the cladding materials and the building's

Table 1. Thermophysical properties of experimented cladding materials

S/No	Cladding materials	Density (Kg/m^3)	Conductivity (W/mk)	Material's embodied carbon ($KgCO_2/Kg$)	Wall's U-value (W/m^2k)
1	Conventional Cement Plaster	1860	0.720	0.19	1.054
2	Straw Fireboard	300	0.100	0.53	0.770
3	Plate Glass	2710	0.760	0.85	0.883
4	Aluminium Panels (With Air Gap)	7680	45	8.55	0.855
5	Expanded Impregnated Cork Board	150	0.043	0.19	0.567
6	Polyvinylchloride (PVC) Tiles	1200	0.190	2.41	0.973
7	Clay Tiles	1120	0.520	0.46	1.033
8	Burnt Brick Tiles	1890	0.800	0.46	1.033
9	Cement-bonded Particle Board	1200	0.230	0.60	0.986
10	Vermiculite Insulating Brick	700	0.270	0.44	0.927
11	Gravel Stone	1840	0.360	0.02	0.956
12	Polyurethane Cellular Board	24	0.023	3.00	0.405
13	Hardboard Solid wood	600	0.080	0.89	0.635
14	Resin-Bonded Fibre Board	240	0.042	0.59	0.561
15	Flax Shive Resin Bonded Board	500	0.012	0.51	0.259
16	Particle Board	640	0.0129	0.51	0.458
17	Foil-Laced, Glass Fibre-Reinforced Polyisocyanurate Board	32	0.019	0.58	0.358
18	Perlite Plaster	400	0.080	0.12	0.721
19	Expanded Rigid Rubber Board	70	0.032	3.51	0.490
20	Lightweight Metallic panels	1250	0.290	8.55	0.859

total embodied carbon (R^2=0.462). The implication is that the materials' embodied carbon influences the building's total embodied carbon. Additionally, the analysis yielded a statistically significant F-value of 0.000974 (F<0.005), indicating the variables' significance.

Among the materials examined, boards demonstrate promise as effective cladding materials, particularly when insulated. Insulated walls are crucial in reducing peak loads on interior surfaces [28]. However, gravel stone cladding is the most consistent material considering energy efficiency, cooling load, embodied carbon, and thermal comfort. Introducing cladding to the test building results in an overall cost increase and a surge in embodied carbon. In the experimental setup, the simulated cost increase is attributed to material expenses and labor costs, including geographical-based labor rates. Adding an extra layer to a building inevitably increases these associated costs. In the case of cladding, compared to conventional plaster, the increase in cost is due to the cladding material and installation costs. For instance, cladding with hardboard solid wood resulted in a negligible cost increase of 0.02%, while using aluminum cladding panels incurred the highest cost increase of 6.26%.

Concerning embodied carbon, buildings with cladding exhibit higher levels than those with conventional plaster, primarily due to the added materials, energy, and resources needed for production, transportation, and installation. The choice of cladding material significantly influences the magnitude of this increase. The conventional cement-plaster wall finishes with 0.19 $KgCO_2$/kg of embodied carbon contribute to the building's total embodied carbon, amounting to 25,869.80 $KgCO_2$. As illustrated in the ranking schedule in Table 2, the test building with conventional plaster shows the lowest embodied carbon and cost, primarily because no additional cladding was incorporated.

In contrast, the aluminum cladding panel, with an embodied carbon of 8.55 $KgCO_2$/kg, elevates the total building's carbon footprint to 267,829.20 $KgCO_2$, representing a 90.34% increase. These figures underscore the substantial impact of a material's embodied carbon on a building's overall sustainability profile.

It is important to note that while cladding may entail higher upfront costs and embodied carbon, it offers long-term benefits such as improved energy efficiency, enhanced durability, and aesthetic appeal. These benefits can justify the initial investments associated with cladding, especially when considering the building's lifecycle. Additionally, advancements in sustainable cladding materials and construction practices continue to drive improvements in environmental performance, mitigating the environmental impacts associated with cladding installations.

4.1. Energy Performance

The greenness of individual components within a building directly influences the overall sustainability of the building structure, its operation, and its energy efficiency [7]. The energy performance of the cladding materials was

Table 2. Performance-based ranking of uninsulated cladding materials

S/No	Energy per total building area (Kwh/m²)	Cooling electricity (Kwh/m²)	Building's embodied carbon ($KgCO_2$)	Cost	Building's mean annual operative temperature (^0C)	Hours above 28 ^0C (South-facing wing)
1	Gravel Stone	Gravel Stone	Conventional Cement Plaster	Conventional Cement Plaster	Gravel Stone	Flax Shive Resin Bonded Board
2	Particle Board	Lightweight Metallic panels	Particle Board	Hardboard Solid wood	Lightweight Metallic panels	Foil-Laced, Glass Fibre-Reinforced Polyisocyanurate Board
3	Lightweight Metallic panels	Flax Shive Resin Bonded Board	Foil-Laced, Glass Fibre-Reinforced Polyisocyanurate Board	Resin-Bonded Fibre Board	Plate Glass	Polyurethane Cellular Board
4	Flax Shive Resin Bonded Board	Foil-Laced, Glass Fibre-Reinforced Polyisocyanurate Board	Expanded Impregnated Cork Board	Particle Board	Flax Shive Resin Bonded Board	Expanded Rigid Rubber Board
5	Foil-Laced, Glass Fibre-Reinforced Polyisocyanurate Board	Polyurethane Cellular Board	Gravel Stone	Polyvinylchloride (PVC) Tiles	Perlite Plaster	Particle Board
6	Polyurethane Cellular Board	Perlite Plaster	Perlite Plaster	Straw Fireboard	Foil-Laced, Glass Fibre-Reinforced Polyisocyanurate Board	Resin-Bonded Fibre Board
7	Perlite Plaster	Expanded Rigid Rubber Board	Polyurethane Cellular Board	Perlite Plaster	Polyurethane Cellular Board	Expanded Impregnated Cork Board
8	Expanded Rigid Rubber Board	Resin-Bonded Fibre Board	Resin-Bonded Fibre Board	Vermiculite Insulating Brick	Expanded Rigid Rubber Board	Hardboard Solid wood
9	Resin-Bonded Fibre Board	Expanded Impregnated Cork Board	Clay Tiles	Expanded Rigid Rubber Board	Resin-Bonded Fibre Board	Perlite Plaster
10	Expanded Impregnated Cork Board	Particle Board	Straw Fireboard	Cement-bonded Particle Board	Expanded Impregnated Cork Board	Straw Fireboard
11	Hardboard Solid wood	Hardboard Solid wood	Expanded Rigid Rubber Board	Expanded Impregnated Cork Board	Hardboard Solid wood	Lightweight Metallic panels
12	Plate Glass	Plate Glass	Flax Shive Resin Bonded Board	Flax Shive Resin Bonded Board	Straw Fireboard	Plate Glass
13	Straw Fireboard	Straw Fireboard	Cement-bonded Particle Board	Clay Tiles	Particle Board	Aluminium Panels (With Air Gap)
14	Conventional Cement Plaster	Conventional Cement Plaster	Vermiculite Insulating Brick	Foil-Laced, Glass Fibre-Reinforced Polyisocyanurate Board	Aluminium Panels (With Air Gap)	Gravel Stone
15	Polyvinylchloride (PVC) Tiles	Aluminium Panels (With Air Gap)	Burnt Brick Tiles	Polyurethane Cellular Board	Vermiculite Insulating Brick	Vermiculite Insulating Brick

Table 2 (cont). Performance-based ranking of uninsulated cladding materials

S/No	Energy per total building area (Kwh/m^2)	Cooling electricity (Kwh/m^2)	Building's embodied carbon (KgCO_2)	Cost	Building's mean annual operative temperature (^{0}C)	Hours above 28 ^{0}C (South-facing wing)
16	Vermiculite Insulating Brick	Vermiculite Insulating Brick	Hardboard Solid wood	Plate Glass	Polyvinylchloride (PVC) Tiles	Polyvinylchloride (PVC) Tiles
17	Aluminium Panels (With Air Gap)	Polyvinylchloride (PVC) Tiles	Polyvinylchloride (PVC) Tiles	Gravel Stone	Burnt Brick Tiles	Cement-bonded Particle Board
18	Cement-bonded Particle Board	Cement-bonded Particle Board	Plate Glass	Burnt Brick Tiles	Cement-bonded Particle Board	Burnt Brick Tiles
19	Clay Tiles	Clay Tiles	Lightweight Metallic panels	Lightweight Metallic panels	Clay Tiles	Clay Tiles
20	Burnt Brick Tiles	Burnt Brick Tiles	Aluminium Panels (With Air Gap)	Aluminium Panels (With Air Gap)	Conventional Cement Plaster	Conventional Cement Plaster

assessed across three key energy parameters: energy per building area, total electricity consumption, and cooling electricity. Analysis of Variance (ANOVA) test was conducted to evaluate the impact of cladding material choice on these energy metrics and shed light on the factors influencing the overall energy efficiency of the building. The results of the tests revealed significant variations in energy performance among the different cladding materials investigated. Across all three parameters, the choice of cladding material exerted a discernible effect on energy efficiency ($F(2, 57)=1285.59$, $p<0.05$). Specifically, the between-groups variance (SS=400067.0165) significantly exceeded the within-groups variance (SS=8869.009755) for all three energy parameters, showing notable disparities in energy performance across the range of cladding materials tested. The calculated F-statistic of 1285.59, coupled with a p-value of 3.82176E-48, highlights the statistical significance of these findings. Notably, with an alpha value of 0.05, the probability of observing such substantial differences in energy performance by random chance alone is exceedingly low.

The findings further reveal that gravel stone, occurring naturally as loose aggregates of rock fragments, exhibits the lowest energy consumption as a cladding material. In comparison, the building with cement-sand plaster has a total building energy per normalized floor area of 258.20 kWh/m^2. However, the Energy Use Intensity (EUI) decreased by 8% when clad with gravel stone. The energy savings achieved by gravel stone cladding are synonymous with similar investigations conducted by those who gained significant energy savings through cladding materials inclusion in the building envelope. It is essential to note that adding cladding does not entirely reduce energy consumption. For instance, materials such as polyvinyl chloride (PVC) tiles, vermiculite insulating brick, aluminum panels (with air gap), cement-bonded particle board, clay tiles, and burnt brick tiles all increased the EUI of the building (Fig. 4). Burnt brick tiles, for example, increased the energy use of the building by 2%.

Nevertheless, when insulation was attached to these cladding materials on the exterior of the test building, results differed. Remarkably, simply cladding the cement-plaster building with a polyurethane insulating board reduces the energy consumption of the building by 6%, offering the most substantial energy savings without further cladding (Fig. 5). Several factors contribute to this phenomenon, including variations in insulation effectiveness against the cladding materials, thermal bridging, air leakage, and interstitial condensation. This is evident from the condensation analysis conducted in the experimental setup, which produced the Glaser diagrams for aluminum cladding panels, clay brick, and PVC tiles cladding shown in Figure 6. These diagrams illustrate how adding cladding can inadvertently introduce thermal bridges or compromise the airtightness of the building envelope, thereby offsetting the intended energy-saving benefits.

Furthermore, certain cladding materials' inherent properties may result in poor thermal resistance or inadequate insulation, leading to increased heat transfer through the

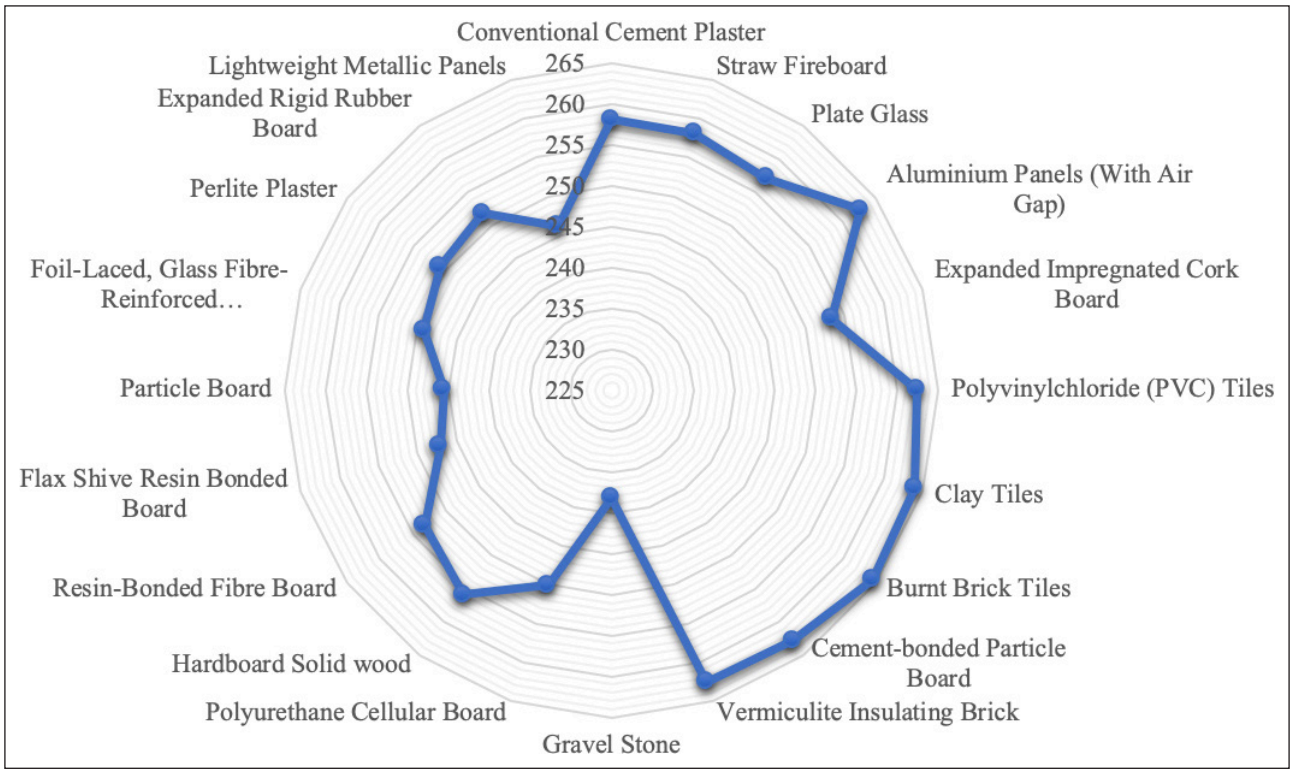

Figure 4. Energy consumption of uninsulated cladding materials.

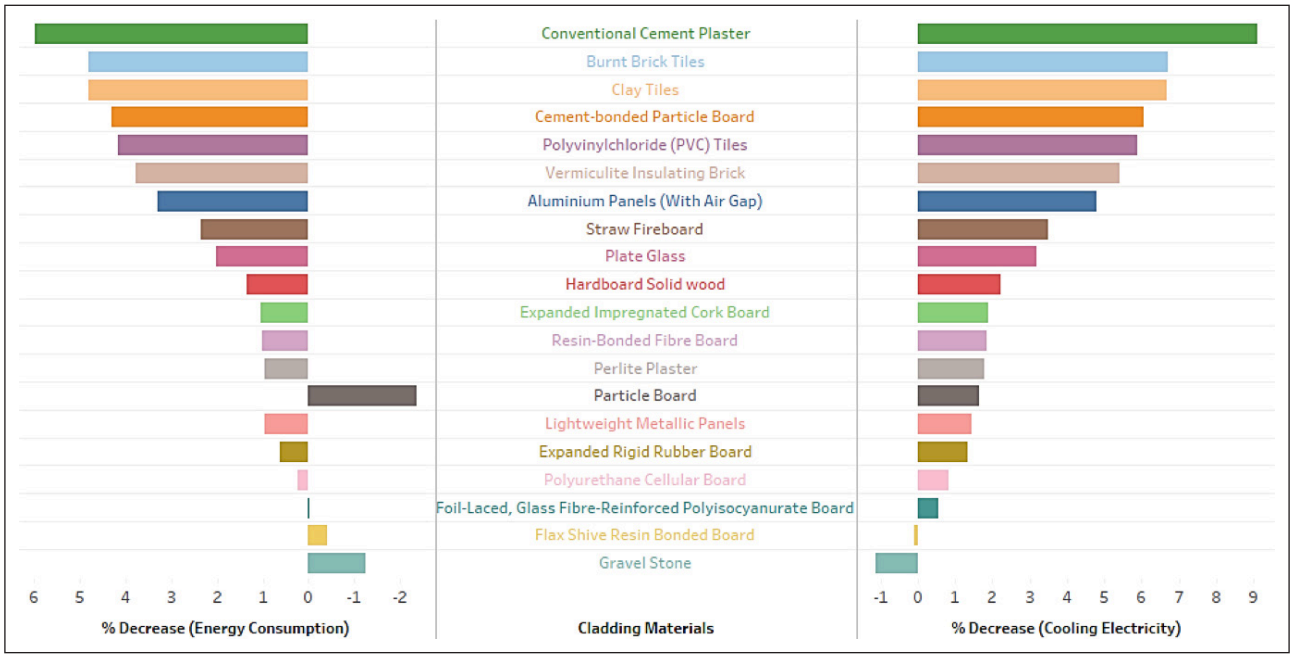

Figure 5. Energy savings on insulated cladding materials.

building envelope. Additionally, cladding installation and construction technique variations, which depend on the material type and design considerations, can further impact energy efficiency outcomes.

While Insulation can enhance the thermal performance of cladding systems by reducing heat loss or gain through the building envelope, its effectiveness may be influenced by interactions with other building components, such as windows, doors, and HVAC systems. In scenarios where insulation is added to cladding materials, the energy consumption of dissimilar materials can be affected differently. Materials with inherently poor insulation properties may experience minimal improvements in energy efficiency despite adding insulation. Conversely, materials with better insulation properties may benefit more from insulation additions, reducing energy consumption. Figure 7 compares the energy consumption of the cladding materials with and without insulation. The cement-plaster building exhibited

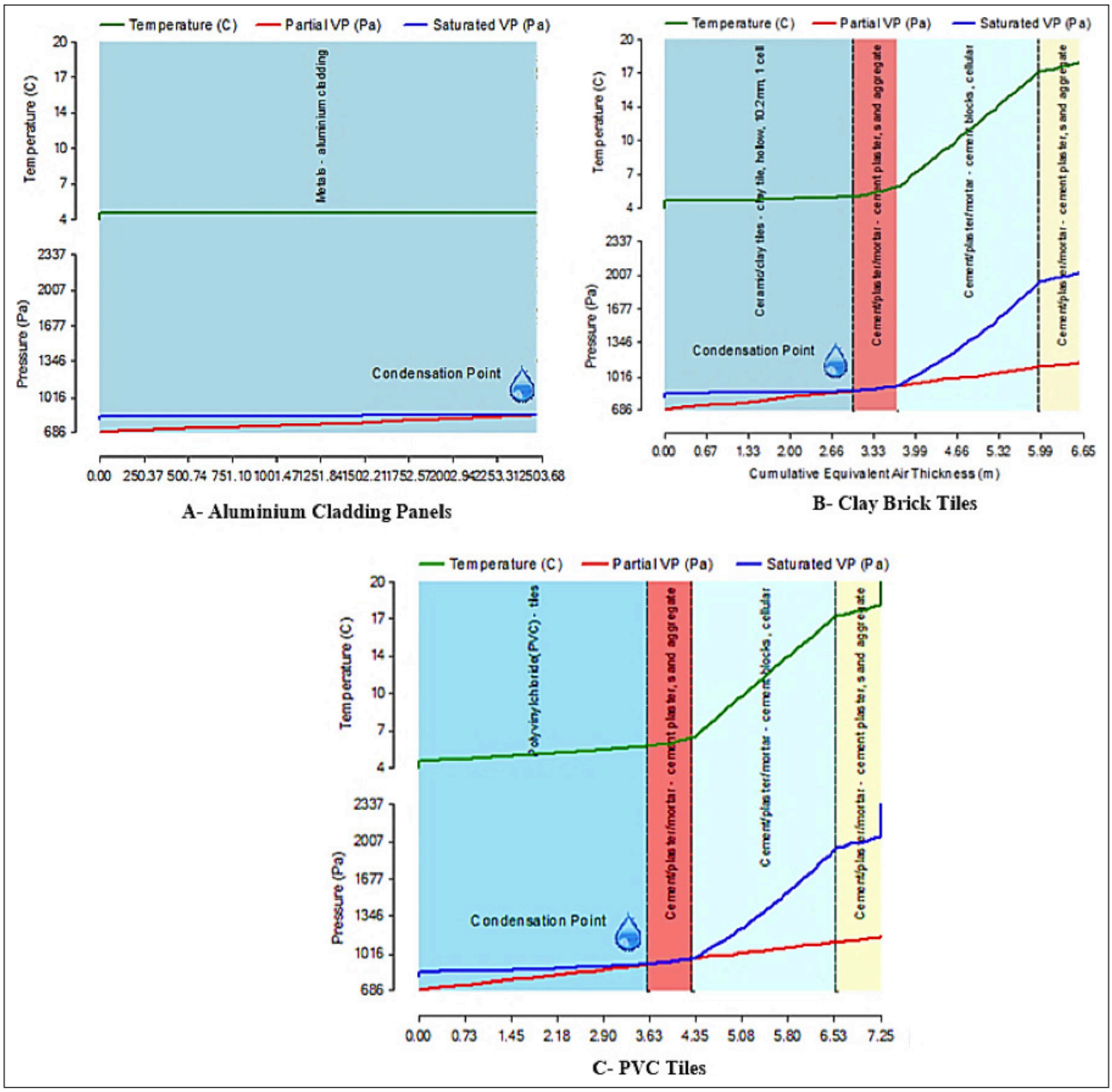

Figure 6. Glaser diagrams- Interstitial condensation on aluminum cladding panels **(a)**, clay brick tiles **(b)**, and PVC tiles **(c)**.

a notably higher energy consumption of 258.20 kWh/m² than the insulated scenario, where energy consumption decreased to 242.75 kWh/m². This considerable difference underscores the significant impact of insulation on building energy efficiency. The observed dramatic difference, particularly for the cement-plaster building, can be attributed to the insulation's ability to mitigate heat transfer through the building envelope. Insulation helps retain conditioned air within the building, reducing the need for cooling and thus lowering overall energy consumption. Additionally, the variation in energy consumption across different cladding materials further contributes to the range of values depicted in the figure.

While gravel stone maintains the lowest energy consumption for insulated buildings, it does not integrate well with the insulator used, resulting in an approximately 1% increase in EUI. The thickness of the insulation layer may not have been sufficient to provide adequate thermal resistance to mitigate heat transfer through the building envelope, leading to increased energy consumption. Certain cladding materials may exacerbate heat transfer or moisture issues, counteracting the intended benefits of the insulation layer.

Other materials in the top 25% with the least EUI in this study include particle board, lightweight metallic panels, flax shive resin-bonded board, and foil-laced glass fiber-reinforced polyisocyanurate board (Table 2). These materials show a comparative energy reduction of 5% in the case of particle board cladding and 3.5% in foil-laced polyisocyanurate board. On the other hand, cooling loads vary for these materials despite having a low EUI. Precisely, unlike other materials in the top 25%, the cooling load for particle board

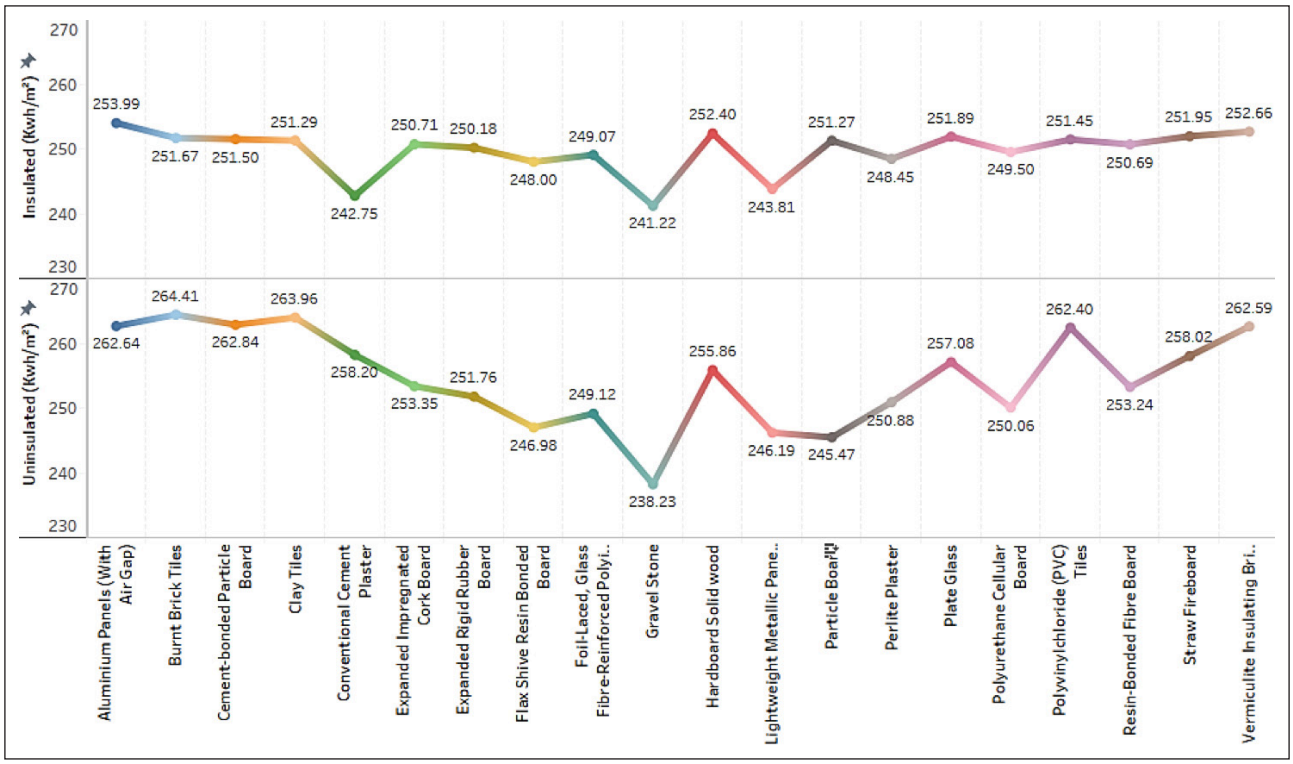

Figure 7. Energy consumption of cladding materials.

does not align with its reduced energy consumption. In the ranking of materials based on cooling load, polyurethane cellular board makes the list of the top 25%.

Gravel stone, without insulation, has the most significant savings on cooling energy, with an 11% reduction in electricity for cooling, compared to conventional buildings (Fig. 7). The potential of gravel stone to reduce indoor temperature was emphasized by Mediastika and Hariyono [30] and Hamoush et al. [33], who achieved a cooling load reduction of 4%. Conversely, materials at the bottom of the energy ranking include vermiculite insulating brick, aluminum panels (with air gap), cement-bonded particle board, clay tiles, and burnt brick tiles. Similar to an investigation by Taylor et al. [11], concrete, metal, and brick negatively impacted building performance. Their densities and conductivities may influence the energy performance of these materials. While aluminum cladding panels are proven effective in reducing energy consumption in hot climates [33], they increase energy consumption. Notwithstanding, lightweight metallic panels decreased energy consumption by approximately 5%. The selection of materials requires careful consideration, as their inherent properties can significantly impact thermal performance.

4.2. Cost and Embodied Carbon

The relative cost of building construction varies even within the same geographical region. The cost analysis presented in this study provides an overview of how cladding materials costs impact a building's budget. Choosing materials solely based on cost may have unintended environmental consequences. As highlighted by Takano et al. [14], an expensive building material can exhibit lower environmental impacts and offer high aesthetic quality. The findings of this investigation identify hardboard solid wood, resin-bonded fiberboard, particleboard, polyvinyl chloride (PVC) tiles, and straw fireboard as the top 25% most cost-effective materials.

Interestingly, only one of these materials, particle board, also ranks at the top regarding the most minor energy consumption, as discussed in section 5.1. This suggests that an inexpensive material can still positively impact a building's energy performance. Conversely, gravel stone, burnt brick tiles, lightweight metallic panels, and aluminum panels contribute to an increased building cost. To illustrate, while hardboard solid wood only marginally increases the building cost by 0.02%, adding aluminum cladding panels raises the building cost by approximately 6%.

The embodied carbon of a material plays a crucial role in a building's carbon emissions. The data collected for embodied carbon in this study excludes emissions arising from electricity consumption, as it was treated separately to assess specific impact areas. Table 1 shows that aluminum cladding and lightweight metal panels exhibit the highest embodied carbon (8.55 $KgCO_2/Kg$). The carbon data collected for buildings with these metal panels show a significant increase in embodied carbon, with about 37.88% and 90.34% increases for lightweight metallic and aluminum cladding panels, respectively. Materials with the least embodied carbon on the ranking table include particle board, foil-laced glass fiber-reinforced polyisocyanurate board, expanded impregnated cork board, and gravel stone. While particle board increases the test building's carbon by 0.2%, gravel stone adds to the building's carbon by 0.9%. Particle board presents the most minor carbon emission to the building, although it is not the material with the least in-

herent embodied carbon. The impact of cost on a building's embodied carbon shows that the most expensive materials also contribute to an increased building's embodied carbon. However, this should not be a primary criterion for selecting a cladding material, as a costly material can still reduce a building's carbon footprint. Gravel stone, for example, is ranked as one of the most expensive materials in this study but does not significantly increase the building's carbon emissions.

Notably, a t-test analysis conducted to compare the building's embodied carbon and associated cost revealed a statistically significant difference between the mean values of the two variables. The calculated t-statistic of -10.805 shows a substantial difference between the means, with the mean cost significantly lower than the mean embodied carbon. Furthermore, the p-value obtained for both one-tailed (7.44981E-10) and two-tailed (1.48996E-09) tests is extremely small, well below the used significance level of 0.05. This shows compelling evidence against the null hypothesis, supporting the assertion of a significant difference between the means. Practically, these results imply that while some materials may offer lower initial costs, they may entail higher environmental costs in terms of embodied carbon. Conversely, materials with lower embodied carbon may have a higher financial expense. This trade-off necessitates careful consideration during the material selection process to balance environmental sustainability and economic viability in building projects.

4.3. Indoor Comfort Level

The simulations conducted in this study were performed under-regulated indoor HVAC conditions. The choice of cladding material and system had minimal impact on the average indoor operative temperature of the building annually. Despite the test building with cement-sand plaster exhibiting the highest mean annual operative temperature, no cladding material achieved a reduction of 1°C. Nevertheless, gravel stone emerged as the cladding material, providing the best average yearly temperature for the building, which was 27.32°C. Gravel stone has a unique combination of properties that contribute to its effectiveness in enhancing indoor comfort levels. Its high thermal inertia enables it to absorb heat during the day and release it gradually at night, promoting temperature stability within indoor spaces.

Additionally, gravel stone exhibits exceptional heat absorption and radiation characteristics, complemented by its natural insulation properties. Studies have proven that the opaque nature of gravel stone also helps maintain lower indoor temperatures, further enhancing comfort levels. The exceptional performance of stone cladding in hot climates is further corroborated by Hamoush et al. [33], who suggested that the uniqueness of stone for indoor comfort and energy savings can be further harnessed when engineered.

Despite these advantages, the research uncovered unexpected findings regarding the performance of wood-based cladding materials on the south-facing wing, which is the most exposed part of the building on a typical sunny day. Specifically, resin-bonded, polyisocyanurate, and polyurethane boards showed slightly fewer discomfort hours annually than gravel stone (Fig. 8). This divergence can be attributed to the lower surface temperatures exhibited by wood-based products when exposed to direct sunlight.

Adding insulation with these claddings further enhanced indoor comfort for these materials. Initially, the range of discomfort hours the materials without insulation provided varied from 6.5°C (Flax Shive Resin-Bonded Board) to 23°C (Clay Tiles). But, with insulation added to the cladding materials and the cement-plaster building, the range narrowed to 6.5°C (Cement-Plaster Building) and 7.0°C (Lightweight Metallic Panels), emphasizing the significance of insulating buildings. The challenge of solar gains on the south-facing wing can be effectively controlled by retrofitting solar shading mechanisms to block the sun's rays [54, 55], enhancing energy efficiency. It is worth noting that while these measures can contribute to increased operational costs for retrofit projects [56, 57], they offer valuable solutions for managing solar gains and improving overall building performance.

4.4. Implications for Nigeria's Built Environment Sector

Nigeria aims to achieve net-zero emissions by 2060, as declared during the COP26 Climate Summit. The country was the 25th largest global emitter of greenhouse gasses in 2019, with the potential to meet 59% of its energy consumption needs by 2050 [58] through sustainable building practices with renewable energy integration. Significant benefits will ensue if the necessary building stakeholders embrace critical aspects of the research findings, including a reduction in carbon emissions within the built environment and a notable shift towards achieving net-zero carbon and emission reduction targets. Sustainable building practices with local materials foster better environments and reduce dependence on imported materials. Moreover, these practices could prompt government investment in more sustainable and low-carbon materials research, laying the groundwork for a resilient and eco-friendly built environment.

The research findings also shed light on the complexities of sustainable materials for projects within the Nigerian built environment industry, emphasizing the intricate considerations involved in material selection and building energy performance enhancement. This holistic perspective goes beyond surface aesthetics to address long-term environmental impact and sustainability. Amidst the dynamic landscape of sustainable building construction, industry stakeholders must balance the allure of aesthetically pleasing materials with the imperative to prioritize ecological performance. While initial costs may pose significant challenges, as expounded previously, the enduring cost-effectiveness and return on investment of green technologies offer promising opportunities to reshape Nigeria's construction sector.

With Nigeria's urban population projected to double its current figure by 2067 [59], the demand for sustainable housing solutions becomes increasingly urgent. Em-

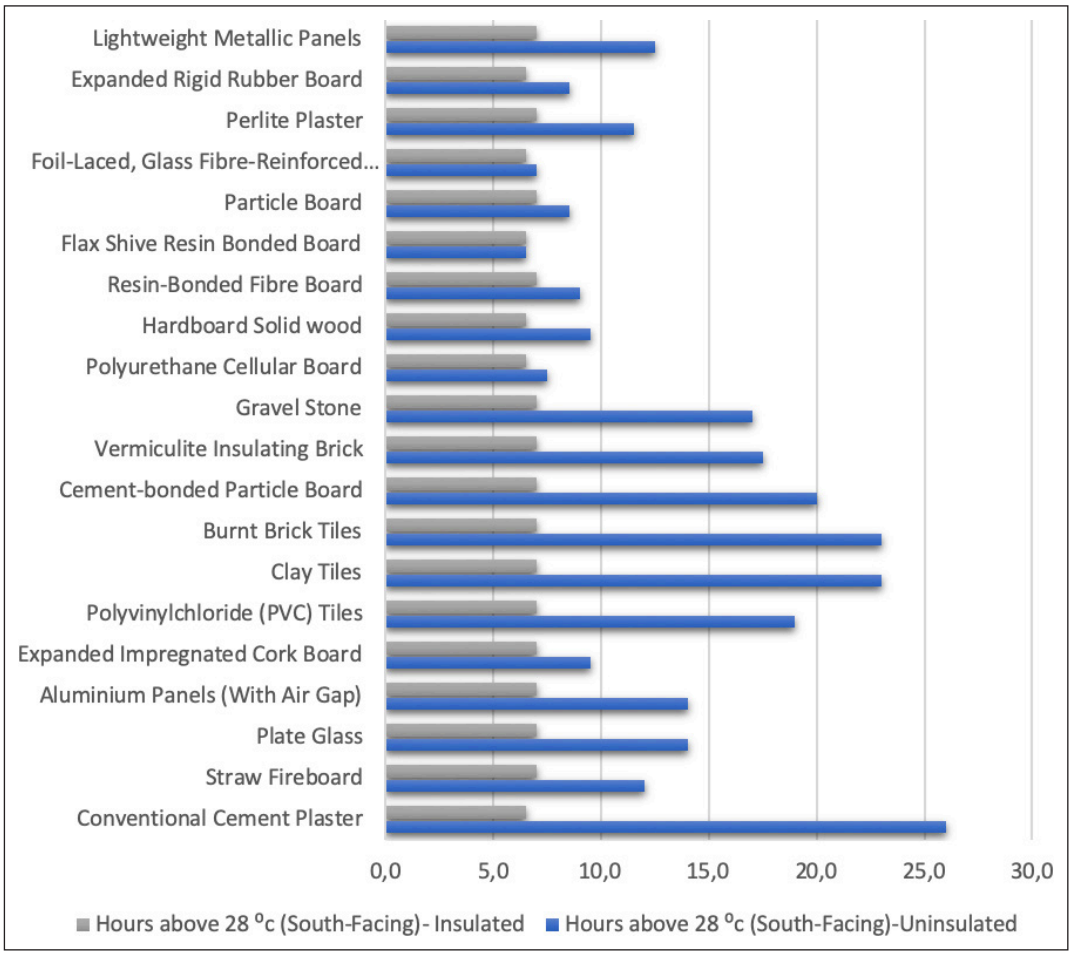

Figure 8. Discomfort hours generated by cladding materials.

bracing environmentally conscious materials in building design reduces operational costs, enhances property values, and drives job creation. Adopting green building initiatives aligns seamlessly with Nigeria's emissions reduction targets and climate resilience goals. However, realizing the full economic potential of sustainable practices requires proactive measures, including establishing green building policies and standards by policymakers and industry stakeholders [60–62]. Integrating renewable energy systems and locally sourced materials can strengthen Nigeria's energy security and resilience, reducing dependency on imported resources. Collaboration across governmental, industrial, and academic sectors is essential to overcome barriers such as financing constraints and technical expertise gaps. In light of projections indicating that future buildings in Nigeria may face extreme outdoor temperature shifts [16], adherence to the research findings reduces expenses for retrofitting future buildings. Early incorporation of sustainable measures can pre-empt costly adjustments down the line.

Additionally, these practices enhance estate values for buildings, as environmentally conscious designs and materials increasingly appeal to investors and occupants, aligning with the growing demand for sustainable and resilient structures. In embracing sustainable building practices, stakeholders can attract foreign investment, foster innovation, and stimulate local industries. By conscientiously evaluating the environmental performance of materials and adopting sustainable practices, Nigeria can chart a path toward economic prosperity, environmental stewardship, and climate resilience.

5. CONCLUSION AND RECOMMENDATION

In an era marked by energy crises, practitioners in the building industry face the daunting task of mitigating the environmental impact of buildings, known as significant contributors to global warming. Sadly, there is no one-size-fits-all solution to address the energy challenges faced by the industry. Ongoing studies cover a spectrum of sustainability, from building fabrics and microenvironments to renewable energy sources and building user control measures, all aimed at enhancing building energy efficiency, especially in the tropics.

This research significantly contributes to the evolving knowledge base on building sustainability, specifically by exploring the environmental impact and indoor comfort benefits of various cladding materials on a hypothetical building in Nigeria's temperate dry climate. Foreseeing substantial future investments by the government to enhance the building energy performance of the existing housing stock, this paper provides an experiential back-

ground for future research. It offers a comprehensive guide for cladding selection in the region, particularly for retrofit projects involving cement and plastered walls. Recognizing that a single criterion cannot decide the most environmentally friendly cladding materials, this study considered multiple factors, including energy user intensity (EUI), material and building embodied carbon, cooling load, and thermal comfort.

Using a ranking system for 19 cladding materials selected based on availability and feasibility in the region, compared to the cement-sand plaster building, simulation results reveal that only a few materials consistently reduce the EUI, embodied carbon, cooling load, and overheating hours of the building. In particular, gravel stone, particle board, and lightweight metallic cladding panels are the most energy-efficient in terms of energy consumed per building area. Gravel stone's superior performance can be attributed to its high thermal inertia, excellent heat absorption and radiation characteristics, and natural insulation properties. These properties allow gravel stone to stabilize indoor temperatures, reducing energy consumption and improving thermal comfort. On the other hand, particle boards and lightweight metallic cladding panels demonstrate energy efficiency and thermal comfort due to their inherent insulation properties, which help regulate temperature fluctuations and minimize heat transfer through the building envelope. Additionally, the reflective properties of metallic panels contribute to lower solar heat gain, further enhancing their performance in reducing cooling loads and overheating hours.

Concerning cooling load, gravel stone, lightweight metallic cladding panels, and flax shive resin-bonded board require the least electricity for cooling. Furthermore, gravel stone, lightweight metallic cladding panels, and plate glass provide the best operative temperature for the building annually. However, it is worth noting that these top-performing cladding materials can be costly, all making the list of expensive materials. Likewise, the simulations show that metals increased building costs and contributed to an increase in the building's embodied carbon by up to 90% compared to the test building with cement and plaster.

Significantly, gravel stone stands out as the most environmentally friendly material, whether or not the building structure is insulated. Nonetheless, adding a polyurethane board insulator to the exterior of the cement-sand plaster building shows promise for energy efficiency and thermal comfort, calling for further investigations. The insulating board might serve as an external fabric without added cladding, reducing the building's embodied carbon and comparative costs.

One limitation of this study is its geographical specificity to Abuja, Nigeria. Climate variations across different regions of the country may affect the generalisability of findings to locations with different climates. Nevertheless, the outcomes of this investigation provide a valuable trajectory for future researchers and building practitioners, emphasizing the need to look beyond the aesthetic and cost attributes in selecting façade cladding materials.

ACKNOWLEDGMENTS

The authors acknowledge the support of Federal Polytechnic, Auchi, Nigeria, for providing the research facilities necessary to complete this work.

ETHICS

There are no ethical issues with the publication of this manuscript.

DATA AVAILABILITY STATEMENT

The authors confirm that the data that supports the findings of this study are available within the article. Raw data that support the finding of this study are available from the corresponding author, upon reasonable request.

CONFLICT OF INTEREST

The authors declare that they have no conflict of interest.

FINANCIAL DISCLOSURE

The authors declared that this study has received no financial support.

USE OF AI FOR WRITING ASSISTANCE

Not declared.

PEER-REVIEW

Externally peer-reviewed.

REFERENCES

[1] Abusafieh, S. (2020). The conflict between aesthetics and sustainability: Empowering sustainable architecture with aesthetics to enhance people's lifestyle and sustainable behavior. In A. Sayigh (Ed.), *Renewable energy and sustainable buildings: Selected papers from the world renewable energy congress WREC 2018* (pp. 653–664). Springer. [CrossRef]

[2] Georgiou, M. D. (2006). *An environmental guide for selecting wall cladding materials for architects* [Master's thesis, University College London]. Bartlett School of Graduate Studies, University College London.

[3] Abdi, M. Y., & Virányi, Z. (2010). Aesthetics in sustainability [Technical Report]. VIA University College, Denmark.

[4] Kupatadze, I. (2014). Ethics vs. aesthetics in sustainable architecture. *WIT Trans Built Environ, 142*, 553–562. [CrossRef]

[5] Jannat, N., Hussien, A., Abdullah, B., & Cotgrave, A. (2020). A comparative simulation study of the thermal performances of the building envelope wall materials in the tropics. *Sustainability (Basel), 12*(12), 4892. [CrossRef]

[6] Sadrolodabaee, P., Hosseini, S. A., Claramunt, J., Ardanuy, M., Haurie, L., Lacasta, A. M., & de la Fuente, A. (2022). Experimental characterization of comfort performance parameters and multi-criteria sustainability assessment of recycled textile-reinforced cement facade cladding. *J Clean Prod, 356*, 131900. [CrossRef]

[7] Toplicic-Curcic, G., Grdic, D., Ristic, N., & Grdic,

Z. (2016). Ceramic facade cladding as an element of sustainable development. *Facta Univ Ser Archit Civ Eng, 13*(3), 219–231. [CrossRef]

[8] Balaji, N., Mani, M., & Reddy, B. V. (2013). *Thermal performance of the building walls*. Preprints of the 1st IBPSA Italy conference, Free University of Bozen-Bolzano.

[9] Diao, R., Sun, L., & Yang, F. (2018). Thermal performance of building wall materials in villages and towns in hot summer and cold winter zone in China. *Appl Therm Eng, 128*, 517–530. [CrossRef]

[10] Atashbar, H., & Noorzai, E. (2023). Optimization of exterior wall cladding materials for residential buildings using the non-dominated sorting genetic algorithm II (NSGAII) based on the integration of building information modeling (BIM) and life cycle assessment (LCA) for energy consumption: A case study. *Sustainability, 15*(21), 15647. [CrossRef]

[11] Taylor, C., Roy, K., Dani, A. A., Lim, J. B. P., De Silva, K., & Jones, M. (2023). Delivering sustainable housing through material choice. *Sustainability, 15*(4), 3331. [CrossRef]

[12] Bradtmueller, J. P., & Foley, S. P. (2014). *Historical trends of exterior wall materials used in US residential construction*. 50th ASC annual international conference proceedings, Kentucky, USA.

[13] Radhi, H. (2010). On the optimal selection of wall cladding system to reduce direct and indirect CO2 emissions. *Energy, 35*(3), 1412–1424. [CrossRef]

[14] Takano, A., Hughes, M., & Winter, S. (2014). A multidisciplinary approach to sustainable building material selection: A case study in a Finnish context. *Build Environ, 82*, 526–535. [CrossRef]

[15] Darwish, E. A., Eldeeb, A. S., & Midani, M. (2023). Housing retrofit for energy efficiency: Utilizing modular date palm midribs claddings to enhance indoor thermal comfort. *Ain Shams Eng J, 15*, 102323. [CrossRef]

[16] Alegbe, M., & Mtaver, G. (2023). Climate resilience and energy performance of future buildings in Nigeria based on RCP 4.5 and 8.5 scenarios. *J Des Resil Arch Plan, 4*(3), 354–371. [CrossRef]

[17] Pekdogan, T., & Basaran, T. (2017). Thermal performance of different exterior wall structures based on wall orientation. *Appl Therm Eng, 112*, 15–24. [CrossRef]

[18] Alegbe, M., Chukwuemeka, L., Lekwauwa Kalu, J., & Eke-Nwachukwu, A. (2023). Building optimisation vis-à-vis solar shading for improved comfort and energy efficiency in classrooms. *Dimensi J Architect Built Environ, 50*(2), 53–68. [CrossRef]

[19] Craig, A., Abbott, L., Laing, R., & Edge, M. (2017). *Assessing the acceptability of alternative cladding materials in housing: Theoretical and methodological challenges*. In Housing, space and quality of life (pp. 59–69). Routledge. [CrossRef]

[20] Abu Dabous, S., Ibrahim, T., Shareef, S., Mushtaha, E., & Alsyouf, I. (2022). Sustainable façade cladding selection for buildings in hot climates based on thermal performance and energy consumption. *Results Eng, 16*, 100643. [CrossRef]

[21] Dodge, B., & Liu, R. (2018). *Comparing exterior wall finishes using life-cycle assessment*. 7th International Building Physics Conference, IBPC 2018, Syracuse, NY, USA. [CrossRef]

[22] Folorunso, C., Akingbohungbe, D., & Ogunruku, M. (2017). Choice prediction factors in building exterior finishes' selection in Lagos, Nigeria: Clients' perspective. *Int J Res Eng Soc Sci, 7*(1), 14–20.

[23] Efthymiou, E., Cöcen, Ö. N., & Ermolli, S. R. (2010). Sustainable aluminium systems. *Sustainability, 2*(9), 3100–3109. [CrossRef]

[24] Brookes, A. J., & Meijs, M. (2008). *Cladding of buildings* (4th ed.). Taylor & Francis. [CrossRef]

[25] Grazuleviciute-Vileniske, I., Viliunas, G., & Daugelaite, A. (2021). The role of aesthetics in building sustainability assessment. *Spatium, 45*, 79–89. [CrossRef]

[26] Slaton, D. (2017). Challenges of modern materials: Assessment and repair. *J Archit Conserv, 23*(1-2), 47–61. [CrossRef]

[27] Dissanayake, D. M. K. W., Jayasinghe, C., & Jayasinghe, M. T. R. (2017). A comparative embodied energy analysis of a house with recycled expanded polystyrene (EPS) based foam concrete wall panels. *Energy Build, 135*, 85–94. [CrossRef]

[28] Ozel, M. (2011). Thermal performance and optimum insulation thickness of building walls with different structure materials. *Appl Therm Eng, 31*(17), 3854–3863. [CrossRef]

[29] Mac-Barango, D. (2017). Comparative cost analysis of wall cladding materials. *Int J Econ Financ Manage, 2*, 20–33.

[30] Mediastika, C. E., & Hariyono, J. (2017). Wall cladding effects and occupants' perception of indoor temperature of typical student apartments in Surabaya, Indonesia. *Environ Climate Technol, 20*(1), 51–66. [CrossRef]

[31] Hill, C., Kymäläinen, M., & Rautkari, L. (2022). Review of the use of solid wood as an external cladding material in the built environment. *J Mater Sci, 57*(20), 9031–9076. [CrossRef]

[32] Metin, B., & Tavil, A. (2014). *Environmental assessment of cladding construction: A case study of residential buildings*. Proceedings of the 3rd International Environment and Design Congress, Istanbul, Turkey. [CrossRef]

[33] Hamoush, S., Abu-Lebdeh, T., Picornell, M., & Amer, S. (2011). Development of sustainable engineered stone cladding for toughness, durability, and energy conservation. *Constr Build Mater, 25*(10), 4006–4016. [CrossRef]

[34] Tiwari, R., Boháč, V., Réh, R., Lo Giudice, V., Todaro, L., Vretenár, V., Štofanik, V., & Kristak, L. (2023). Investigation of thermophysical properties of Turkey oak particleboard for sustainable building envelopes. *Dev Built Environ, 16*, 100228. [CrossRef]

[35] Zhu, Z., Jin, X., Li, Q., & Meng, Q. (2015). Experimental study on the thermal performance of ventilation wall with cladding panels in hot and humid area. *Procedia Eng, 121*, 410–414. [CrossRef]

[36] Metin, B., & Tavil, A. (2010). *Sustainability of the construction process of the cladding systems*. Proceedings of the ICBEST 2010-International Conference on Building Envelope Systems and Technologies,

Vancouver, Canada.
[37] Hassinen, P., Misiek, T., & Naujoks, B. (2011). *Cladding systems for sandwich panels - refurbishment of walls and roof*. Eurosteel 2011 / Proceedings of the 6th European Conference on Steel and Composite Structures, Budapest, Hungary.
[38] Alegbe, M. (2022). *Comparative analysis of wall materials toward improved thermal comfort, reduced emission, and construction cost in tropical buildings*. 11th Masters Conference: People and Buildings, University of Westminster, London, United Kingdom.
[39] Brischke, C. (2019). Timber. *In Long-term performance and durability of masonry structures* (pp. 129–168). Elsevier. [CrossRef]
[40] Okuda, S., Corpataux, L., & Wei, K. H. (2023). *Timber cladding discolouration in tropical monsoon climates*. World Conference on Timber Engineering, Oslo, Norway. [CrossRef]
[41] Orzechowski, T., & Orzechowski, M. (2018). Optimal thickness of various insulation materials for different temperature conditions and heat sources in terms of economic aspect. *J Build Phys, 41*(4), 377–393. [CrossRef]
[42] Marshall, A., Fitton, R., Swan, W., Farmer, D., Johnston, D., Benjaber, M., & Ji, Y. (2017). Domestic building fabric performance: Closing the gap between the in situ measured and modelled performance. *Energy Build, 150*, 307–317. [CrossRef]
[43] Tayari, N., & Nikpour, M. (2023). Investigating DesignBuilder simulation software's validation in terms of heat gain through field measured data of adjacent rooms of courtyard house. *Iranica J Energy Environ, 14*(1), 1–8. [CrossRef]
[44] Aunión-Villa, J., Gómez-Chaparro, M., & García-Sanz-Calcedo, J. (2021). Study of the energy intensity by built areas in a medium-sized Spanish hospital. *Energy Effic, 14*(3), 26. [CrossRef]
[45] Gangolells, M., Casals, M., Forcada, N., Macarulla, M., & Cuerva, E. (2016). Energy mapping of existing building stock in Spain. *J Clean Prod, 112*, 3895–3904. [CrossRef]
[46] Kong, X., Lu, S., Gao, P., Zhu, N., Wu, W., & Cao, X. (2012). Research on the energy performance and indoor environment quality of typical public buildings in the tropical areas of China. *Energy Build, 48*, 155–167. [CrossRef]
[47] Xu, P., Huang, J., Shen, P., Ma, X., Gao, X., Xu, Q., Jiang, H., & Xiang, Y. (2013). Commercial building energy use in six cities in southern China. *Energy Policy, 53*, 76–89. [CrossRef]
[48] Mohsenzadeh, M., Marzbali, M. H., Tilaki, M. J. M., & Abdullah, A. (2021). Building form and energy efficiency in tropical climates: A case study of Penang, Malaysia. *City Braz J Urban Manage, 13*, e20200280. [CrossRef]
[49] Alkali, M. A., Jie, L., Dalibi, S. G., Danja, I. I., Nasir, M. H., Inuwa Labaran, U., Umar, A. M., & Adamu, K. (2021). Optimizing building orientation for reduced cooling load in Northeast Nigeria's residential architecture. *IOP Conf Ser Earth Environ Sci, 793*(1), 012028. [CrossRef]
[50] Umbark, M. A., Alghoul, S. K., & Dekam, E. I. (2020). Energy consumption in residential buildings: Comparison between three different building styles. *Sustain Dev Res, 2*(1), p1. [CrossRef]
[51] Alvarez-Feijoo, M. Á., Orgeira-Crespo, P., Arce, E., Suárez-García, A., & Ribas, J. R. (2020). Effect of insulation on the energy demand of a standardized container facility at airports in Spain under different weather conditions. *Energies, 13*(20), 5263. [CrossRef]
[52] Tong, Y., Yang, H., Bao, L., Guo, B., Shi, Y., & Wang, C. (2022). Analysis of thermal insulation thickness for a container house in the Yanqing Zone of the Beijing 2022 Olympic and Paralympic Winter Games. *Int J Environ Res Public Health, 19*(24), 16417. [CrossRef]
[53] Wang, R., Lu, S., Zhai, X., & Feng, W. (2022). The energy performance and passive survivability of high thermal insulation buildings in future climate scenarios. *Build Simul, 15*(7), 1209–1225. [CrossRef]
[54] Arman, H. (2019). Assessment of solar shading strategies in low-income tropical housing: The case of Uganda. *Proc Inst Civ Eng Eng Sustain, 172*(6), 293–301. [CrossRef]
[55] Bazazzadeh, H., Świt-Jankowska, B., Fazeli, N., Nadolny, A., Safar Ali Najar, B., Hashemi Safaei, S. S., & Mahdavinejad, M. (2021). Efficient shading device as an important part of daylightophil architecture; a designerly framework of high-performance architecture for an office building in Tehran. *Energies, 14*(24), 8272. [CrossRef]
[56] Chandrasekaran, C., Sasidhar, K., & Madhumathi, A. (2023). Energy-efficient retrofitting with exterior shading device in hot and humid climate – case studies from fully glazed multi-storied office buildings in Chennai, India. *J Asian Archit Build Eng, 22*(4), 2209–2223. [CrossRef]
[57] Venegas, T. P., Espinosa, B. A., Cataño, F. A., & Vasco, D. A. (2023). Impact assessment of implementing several retrofitting strategies on the air-conditioning energy demand of an existing university office building in Santiago, Chile. *Infrastructures, 8*(4), 80. [CrossRef]
[58] Dunne, D. (2020). *The carbon brief profile: Nigeria*. Carbon Brief Ltd.
[59] Macrotrends. (2022). *Nigeria population growth rate 1950–2024*. https://www.macrotrends.net/global-metrics/countries/NGA/nigeria/population-growth-rate
[60] Abisuga, A. O., & Okuntade, T. F. (2020). The current state of green building development in Nigerian construction industry: Policy and implications. In Z. Gou (Ed.), *Green building in developing countries: Policy, strategy and technology* (pp. 129–146). Springer International Publishing. [CrossRef]
[61] Atanda, J. O., & Olukoya, O. A. P. (2019). Green building standards: Opportunities for Nigeria. *J Clean Prod, 227*, 366–377. [CrossRef]
[62] Chukwu, D. U., Anaele, E. A., Omeje, H. O., & Ohanu, I. B. (2019). Adopting green building constructions in developing countries through capacity building strategy: Survey of Enugu State, *Nigeria. Sust Build, 4*, 4. [CrossRef]

Journal of Sustainable Construction Materials and Technologies
Web page info: https://jscmt.yildiz.edu.tr
DOI: 10.47481/jscmt.1555157

JSCMT
Journal of Sustainable Construction Materials and Technologies

Research Article

A study on the influence of material gradient index on bending and stress responses of FGM rectangular plates using the Finite Element Method

Masihullah NOORI*, Ayça BİLGİN, Hamza DIALLO, Mohammad Omar AL ROUSAN, Ahmad Reshad NOORI

Department of Civil Engineering, İstanbul Gelişim University, İstanbul, Türkiye

ARTICLE INFO

Article history
Received: 19 June 2024
Revised: 30 August 2024
Accepted: 03 September 2024

Key words:
Bending, deflection, finite element method, FGM rectangular plate, stresses

ABSTRACT

Functionally graded materials (FGMs) are advanced materials designed to achieve specific property gradients. The unique characteristic of these materials—variations in spatial dimensions—allows for integrating the advantages of different materials within a single component, where a combination of properties, such as mechanical strength, thermal resistance, and others, is needed. This paper utilizes finite element analysis to examine the deflection and stress responses of FGM rectangular plates with different material gradient profiles. Various boundary conditions, including clamped, simply supported, and free edges in different configurations, are considered. The plates are subjected to uniformly distributed, sinusoidally distributed, and concentrated loads. The study investigates the effects of boundary and loading conditions, along with the impact of the material gradient, on the deflections and stress responses of FGM rectangular plates. The results indicate variations in deflection and stress values for different material gradients, under varying boundary and loading conditions.

Cite this article as: Noori, M., Bilgin, A., Diallo, H., Al Rousan, M. O., & Noori, A. R. (2024). A study on the influence of material gradient index on bending and stress responses of FGM rectangular plates using the Finite Element Method. *J Sustain Const Mater Technol*, 9(3), 239–254.

1. INTRODUCTION

Functionally graded materials (FGMs) are advanced composite materials with structural characteristics that provide customized mechanical, thermal, and chemical properties. The gradual variation in the composition or microstructure of these materials across spatial dimensions makes it possible to manipulate their properties based on practical needs [1]. Although FGMs have attracted significant attention owing to their potential applications in diverse engineering fields, including structural, aerospace, automotive, and biomedical engineering, future applications also demand materials that are readily available at reasonable costs and do not compromise environmental concerns [2].

Torelli et al. [3] comprehensively analyzed Functionally Graded Concrete (FGC), focusing on structural applications, design methods, and production procedures. Keeping in mind that the industrial production of cement, the critical constituent of concrete, accounts for approximately 5% of global human-made carbon emissions, they showed through their results that material savings of up to 40% are possible through the functional gradation of concrete. In their sustainability analysis, Chan et al. [4] investigated FGC made of recycled aggregates reinforced with fibers. They concluded that a reduction in the total volume of steel fibers, resulting from a decreased ratio of reinforced layer height to total height, minimized the total embodied CO2 and cost of concrete.

***Corresponding author.**
*E-mail address: masihullahnoori12@gmail.com

Sustaining energy demands for the current generation can pose significant environmental challenges for upcoming generations. Although progress in this field seems gradual, it aligns with innovations in materials, equipment, and environmental considerations [5]. The concept of FGMs dates back to the late 20th century, with initial conceptualizations emerging during a space plane project in Japan in the 1980s [6]. Advancements in material processing techniques during the 1990s and early 2000s, such as powder metallurgy and sol-gel methods, facilitated the manufacturing of FGM structures with greater control over material properties. Today, producing graded structures can be considered the next step in the development of composite materials [7].

Academic researchers have conducted comprehensive studies on the behavior of structural elements composed of FGMs in different applications, illustrating their mechanical, thermal, and chemical responses. Chaabani et al. [8] studied the buckling and post-buckling behavior of porous FGM plates using High Order Continuation based on the Asymptotic Numerical Method in conjunction with the Finite Element Method (FEM) to model the nonlinear behavior of a Porous Functionally Graded Material (PFGM) plate. Several plates with different porosity distributions under various types of transverse loads were analyzed, and they concluded that an increase in the porosity coefficient of PFGM plates causes more significant deflections, thereby diminishing plate stiffness and reducing critical buckling loads.

Moita et al. [9] investigated higher-order finite element models for the static linear and nonlinear response of FGM plate-shell structures. Their study revealed that the gradient index can determine the mechanical behavior of FGM plates. They also highlighted the influence of high temperatures on the predictability of these responses. Afzali et al. [10] conducted a study to investigate the thermal buckling response of FGM plates with temperature-dependent properties. Their findings revealed that using the actual temperature distribution instead of assumed ones can lead to more precise results in thermal buckling analysis. Kazemzadeh-Parsi et al. [11] analyzed the thermoelasticity of FGMs using Proper Generalized Decomposition (PGD), primarily focusing on material gradation in one, two, and three directions. They reduced high-dimensional problems to one-dimensional problems, contributing to the simplicity of the solution and design procedure.

Kargarnovin et al. [12] investigated the thermal buckling behavior of FGM rectangular plates using the Classical Plate Theory (CPT) and the Galerkin method. They concluded that plate geometry and material properties can influence the critical buckling temperature. Saad and Hadji [13] studied different parameters affecting the critical buckling temperature of thick FGM plates. They presented numerical results derived from thermal buckling analyses on FGM plates subjected to uniform, linear, and non-linear thermal loading conditions. Using the four-variable higher-order shear Deformation Theory (HSDT), they underscored the validity of the proposed shear theory in resolving the buckling behavior of PFGM plates under varied thermal loading conditions.

Slimani et al. [14] used the seemingly 3D refined HSDT to investigate the static bending with two distinct types of porosity dispersal in FGM plates. The results showed that the E-FGM (exponential function) yielded larger deflection values, normal stresses, and shear stresses than the P-FGM (power-law function). Rebai et al. [15] investigated an analytical approach based on micromechanical models to analyze the static deflection behavior of sandwich FGM plates subjected to thermal loads. A comparative outcome stated that while various micromechanical models affect the deflection behavior, their overall impact on the deflection behavior is relatively small.

Hamza and Bouderba [16], using an efficient and straightforward refined plate theory, analyzed the buckling of FGM plates subjected to different load conditions. They explored the effects of uniaxial and biaxial compression loads, alongside simply supported boundary conditions, on rectangular FGM plates. Their results confirmed that the application of uniaxial and biaxial compressive loads, coupled with transverse shear loading, stabilizes the shear buckling phenomenon of FGM plates subjected to combined shear and directional loading.

Hong [17] studied static bending and free vibration analysis of bidirectional FGM plates using FEM and third-order shear deformation theory. He concluded that increased deformation and load intensity applied to the structure leads to conflicts arising from linear and nonlinear problems. Talha and Singh [18] conducted free vibration and static analysis of square and rectangular FGM plates based on HSDT in conjunction with FEM. A special modification was made to the transverse displacement. An increase in frequency parameter was observed and confirmed, resulting from increased plate aspect ratio and smaller side-to-thickness ratio.

Singh and Gupta [19] used HSDT to investigate the effects of porosity integration and geometric flaws on the vibrational frequency of sandwich functionally graded material (SFGM) plates under both usual and unusual boundary conditions. They found that due to a reduction in metallic content, the non-dimensional frequency parameter (NDFP) decreases as the volume fraction index (n) decreases from metal to ceramic, reducing the overall stiffness of the SFGM plate. While HSDT can be more accurate than the four-variable shear deformation theory (FVSDT), FVSDT strikes a balance between accuracy and computational efficiency, making it suitable for various applications involving moderate thicknesses and shear deformation effects. Alghanmi and Aljaghthami [20] utilized FVSDT to investigate the effects of nonuniform heterogeneous parameters, aspect ratios, side-to-thickness ratios, and changing porosities on the sandwich plates' static bending behavior. They found that higher porosity leads to greater deflections. This may also be known as the elasticity modulus deterioration resulting from excessive porosities, which causes the plate's bending stiffness to decline. Because the plate bending stiffness is reduced at greater side-to-thickness and lower aspect ratio, the center deflection is amplified even more.

Nguyen et al. [21] investigated the buckling properties of variable thickness functionally graded porous (FGP) plates with sinusoidal porosity distribution. They achieved this by integrating ES-MITC3 with First Order Shear Deformation Theory (FSDT). They discovered that since the ES-MITC3 is built on traditional triangular elements, meshing elements with complicated geometries is simpler. The FGP plate rigidity decreases with a rise in the power-law index, which lowers the critical load. Elkafrawy et al. [22] investigated the elastic buckling of FGM thin plates with circular, square, and diamond-shaped openings using FEM. Their analysis revealed that enlarging the opening and adjusting the aspect ratio reduced the critical buckling load for the FGM plate.

Alashkar et al. [23] studied the buckling analysis of FGM thin plates with various circular cutout arrangements using FEM. They concluded that the critical buckling load increases as the plate thickness decreases and the circular cutout diameter increases. In a separate study, they investigated the elastic buckling characteristic of skew FGM thin plates with a circular opening using FEM. They found that the critical buckling load also increases as the skew angle rises. Furthermore, the critical buckling load declines as the opening moves from the plate's border toward its center [24].

Kumar et al. [25] presented the modified Radial Basis Function (RBF)-based mesh-free method for the initial buckling analysis of elastically supported rectangular FGM plates subjected to various in-plane loading conditions. A thin plate spline RBF method was implemented. They found that the critical buckling load generally decreases as the aspect ratio increases for all loading arrangements. Shehab et al. [26] investigated the free vibration analysis of intact and cracked FGM plates using experimental and numerical methods. The results showed that when the FGM gradient index is less than 3, it significantly affects the plate's natural frequency, while higher gradient indexes have no significant effect on both cracked and intact plates.

Hu et al. [27] proposed the Symplectic Superposition Method (SSM) as an analytical method to solve the free vibration problem of non-Lévy type porous FGM rectangular plates. Their study highlighted that SSM doesn't need pre-defined solution forms, paving the way for obtaining rapidly convergent frequency results with high accuracy. Peng et al. [28] found that the fundamental frequency of the stiffened FGM plates resting on the Winkler foundation varies with variations in the power-law exponent. Lim et al. [29] investigated a sophisticated, multilayered modeling approach, likely based on FEM, for the static analysis of porous FGM cooling plates with cutouts. By considering various conventional and unconventional boundary conditions, they discovered that the location of clamped edges significantly impacts the deflection, with a specific configuration (BC3) exhibiting the lowest deflection. Ramu and Mohanty [30] coded an FGM plate program in MATLAB to determine its natural frequencies and mode shapes using FEM. It was observed that increasing the power-law index value (n) reduced the first five natural frequencies under various boundary conditions in their study.

In their study, Srivastava et al. [31] analyzed Radial Basis Functions (RBFs) with modified radial distance for the vibration analysis of FGM rectangular plates using HSDT. Their findings showed that increasing grading and porosity indexes causes a decrease in normalized natural frequency. Kumar [32], in his free transverse vibration analysis of a thin isotropic FG rectangular plate with porosity effects based on CPT, concluded that the frequencies of isotropic simply supported plates are proportional to those of merely supported homogeneous isotropic plates. Kumaravelan [33], in his thesis, studied the axisymmetric bending of FGM circular plates under uniformly distributed transverse mechanical, thermal, and combined mechanical-thermal loads using the Element Free Galerkin (EFG) method. He concluded that adding a metal or ceramic plate to one face of a tapered FGM plate decreases the induced stresses. Therefore, in cases where the FGM plate does not have sufficient strength for a particular application, a metal or ceramic plate can be bonded to the FGM plate.

Smaine et al. [34] investigated the volumetric proportion of the FGM concept in the Fiber-Matrix mixing laws in UD composites using the ABAQUS calculation code and FEM. They noticed that the suggested graded composite exhibited overcapacity of resistance as indicated by the grading index (n) or their locations. The fibers C1 and C2 contributed to optimizing this capacity. Asemi and Salami [35] extended a numerical approach for the low-velocity impact analysis of rectangular FGM plates based on the 3D theory of elasticity. They concluded that applying 3D-graded elements to analyze the plates eliminates the discontinuities in the stress distribution that are present in conventional FE results. Rani et al. [36] developed the Extended Finite Element Method (XFEM) and the level set method for modeling and analyzing stresses around rounded rectangular inclusions enclosed with an FGM layer. They demonstrated that the FGM layer significantly reduces the stress concentration and identified optimal FGM properties for minimizing it.

Yildirim [37] investigated hydrogen-induced stresses in FGM circular members using the two-dimensional theory of elasticity. Through his simple and efficient procedure, he concluded that radial stress is more affected by the material model selection than hoop stress. Feri et al. [38] studied the 3D bending behavior of an intelligent plate consisting of a viscoelastic FGM layer sandwiched between piezoelectric layers under electric field and pressure. The analysis used a state-space technique and Fourier series expansion to solve the governing equations in the Laplace domain. Based on the numerical results, it was demonstrated that the viscoelastic properties strongly affect the bending behavior of the FGM plate.

Bendenia et al. [39] studied the static and free vibration behavior of nanocomposite sandwich plates reinforced with carbon nanotubes. It was found that functionally graded carbon nanotube face sheet-reinforced sandwich plates have high resistance against deflections compared to other reinforcements. Several other structural elements, such as beams, arches, columns, domes, etc., composed of functionally

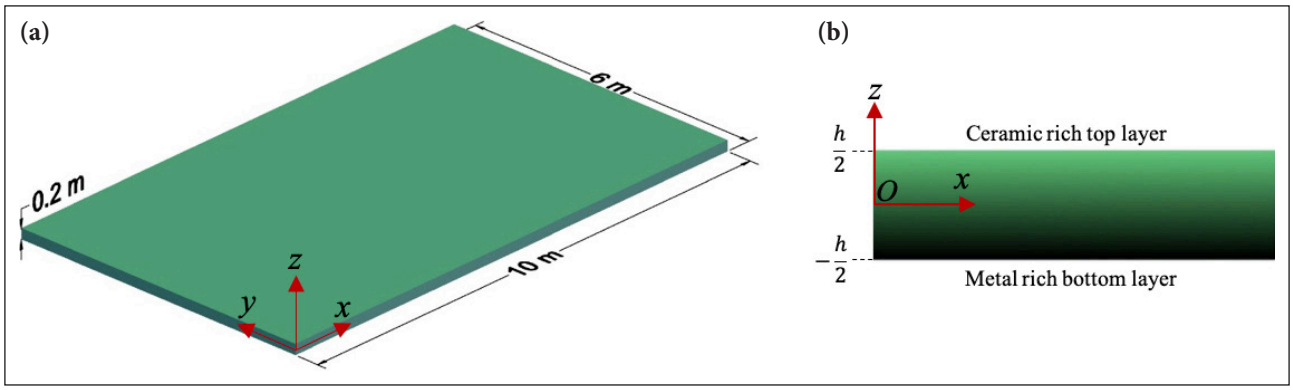

Figure 1. **(a)** FGM rectangular plate; **(b)** Cross section of FGM rectangular plate.

graded materials, have also been investigated by researchers, shedding light on various behavioral aspects of FGMs in diverse applications [40–48]. Researchers have utilized a wide range of analytical models to solve these problems.

Menasria et al. [49] ensured the zero-shear stresses at the free surfaces of functionally graded sandwich plates without introducing any correction factor by proposing a refined shear deformation theory with fewer unknowns. Through verification studies, Rabhi et al. [50] confirmed that their three-unknown shear deformation theory is comparable with other higher-order shear deformation theories in solving problems related to the buckling and vibration responses of exponentially graded sandwich plates.

Matouk et al. [51] investigated the free vibration responses of functionally graded nano-beams using integral Timoshenko beam theory. Their model has three variable unknowns and requires the introduction of a shear correction factor due to uniformly varied shear stress in the thickness direction. In finite element analysis, mesh density is an essential concept that closely relates to the accuracy of finite element models while directly determining their complexity level.

Hassan and Kurgan [52] modeled and analyzed the buckling of rectangular plates using the ANSYS software package, emphasizing selecting an appropriate number of elements in FEM. A large number of elements leads to more computational time without a significant gain in accuracy, while too few elements can produce incorrect solutions. Extensive research studies have been conducted to explore the impact of mesh refinement in both static and dynamic analyses. A consensus is present among all the conducted studies that the fineness of the mesh can significantly influence the obtained results [53, 54].

This paper analyzes FGM plates with various material gradients in the thickness direction using the finite element package program ANSYS Mechanical APDL [55]. The effects of material gradients, boundary conditions, and load types on the deflection and stress responses of FGM plates are investigated. The study aims to illustrate how increasing the power-law index, which introduces more steel constituents into the mix, can affect the bending and stress responses of FGM plates. Additionally, the influence of constraints at the edges of the plates on bending and stress formation within the FGM plates is studied. A convergence study also discusses the optimal number of layers and mesh density for discretizing these plates.

2. MATERIALS AND METHODS

In this paper, an FGM rectangular plate, as shown in Figure 1, with various types of boundary conditions subjected to three distinct load forms, is studied using the FEM. For this study, the dimensions of the rectangular plate were arbitrarily selected without any specific rationale. The length and width of the plate are considered to be 10 and 6 meters with a thickness (h) of 20 centimeters. The Cartesian coordinate system $Oxyz$, where O is the origin of the coordinate system, is located at the left corner of the mid-plane of the plate, in which x, y, and z are the planer in-plane and vertical out-of-plane coordinates, respectively. Functionally gradation of materials in the thickness direction of the plate is shown in Figure 1.

Young's modulus of elasticity E is assumed to be a function of spatial coordinate z in the thickness direction and can vary linearly or non-linearly. Thus, the material properties of the FGM plate can be obtained by the rule of mixture as follows [56]:

$$V_c+V_m=1 \quad (1)$$

$$E(z)=E_c V_c+E_m V_m=(E_c-E_m)\, V_c+E_m \quad (2)$$

V_c and V_m are volume fractions, and E_c and E_m are Young's modulus of elasticity for the FGM ceramic and metal components, respectively. The volume fraction of ceramic as a function of the thickness z coordinate can be determined by a power-law function [56]:

$$V_c = \left(\frac{1}{2}+\frac{z}{h}\right)^n,\ n \geq 0 \quad (3)$$

Where z is the dimensionless coordinate in the thickness direction, h is the total thickness of the plate, and n is the power-law index, which indicates the material variation profile in the thickness direction. At the top ceramic-rich layer ($z=h/2$), $n=0$ leads Eq. 2 to $E(z)=E_c$, and at the bottom metal-rich layer ($z=-h/2$), $n=\infty$ leads Eq. 2 to $E(z)=E_m$. Delale and Erdogan investigated the effect of Poisson's ratio on the deformation of plates [57]. They concluded that Poisson's ratio had a much lower impact on deformation than Young's modulus. Thus, the Pois-

Table 1. Material properties

Material	Young's modulus (GPa)	Poisson ratio
Ceramic - Alumina (Al_2O_3)	380	0.3
Steel	200	0.3

son's ratio of the plate is assumed to be constant. Alumina and steel are considered ceramic and metal materials in this study, and their properties are presented in Table 1. Variations of Young's modulus of elasticity in the thickness direction of the plate for different power-law indexes (n) are shown in Figure 2.

The plates were analyzed using the finite element package program ANSYS Mechanical APDL, and a 3D element SHELL281 [58] was selected for discretization. SHELL281 is appropriate for the analysis of thin to moderately thick shell structures. This element is based on first-order shear deformation theory, which governs the accuracy of modeling composite or sandwich structures. It is also well-suited for linear applications involving large rotations and/or strain nonlinearities. This finite element has eight nodes, each with six degrees of freedom: translations along the x, y, and z axes and rotations around the x, y, and z axes. The geometric configuration of SHELL281 is shown in Figure 3.

Shape functions of 3D 8-node SHELL281 element are presented through Eqs. (4–9) [58].

$$u = \frac{1}{4}\left(u_I(1-s)(1-t)(-s-t-1) + u_J(1+s)(1-t)(s-t-1) + u_K(1+s)(1+t)(s+t-1) + u_L(1-s)(1+t)(-s+t-1)\right) + \frac{1}{2}\left(u_M(1-s^2)(1-t) + u_N(1+s)(1-t^2) + u_O(1-s^2)(1+t) + u_P(1-s)(1-t^2)\right) \quad (4)$$

$$v = \frac{1}{4}\left(v_I(1-s)(1-t)(-s-t-1) + v_J(1+s)(1-t)(s-t-1) + v_K(1+s)(1+t)(s+t-1) + v_L(1-s)(1+t)(-s+t-1)\right) + \frac{1}{2}\left(v_M(1-s^2)(1-t) + v_N(1+s)(1-t^2) + v_O(1-s^2)(1+t) + v_P(1-s)(1-t^2)\right) \quad (5)$$

$$w = \frac{1}{4}\left(w_I(1-s)(1-t)(-s-t-1) + w_J(1+s)(1-t)(s-t-1) + w_K(1+s)(1+t)(s+t-1) + w_L(1-s)(1+t)(-s+t-1)\right) + \frac{1}{2}\left(w_M(1-s^2)(1-t) + w_N(1+s)(1-t^2) + w_O(1-s^2)(1+t) + w_P(1-s)(1-t^2)\right) \quad (6)$$

$$\theta_x = \frac{1}{4}\left(\theta_{x_I}(1-s)(1-t)(-s-t-1) + \theta_{x_J}(1+s)(1-t)(s-t-1) + \theta_{x_K}(1+s)(1+t)(s+t-1) + \theta_{x_L}(1-s)(1+t)(-s+t-1)\right) + \frac{1}{2}\left(\theta_{x_M}(1-s^2)(1-t) + \theta_{x_N}(1+s)(1-t^2) + \theta_{x_O}(1-s^2)(1+t) + \theta_{x_P}(1-s)(1-t^2)\right) \quad (7)$$

$$\theta_y = \frac{1}{4}\left(\theta_{y_I}(1-s)(1-t)(-s-t-1) + \theta_{y_J}(1+s)(1-t)(s-t-1) + \theta_{y_K}(1+s)(1+t)(s+t-1) + \theta_{y_L}(1-s)(1+t)(-s+t-1)\right) + \frac{1}{2}\left(\theta_{y_M}(1-s^2)(1-t) + \theta_{y_N}(1+s)(1-t^2) + \theta_{y_O}(1-s^2)(1+t) + \theta_{y_P}(1-s)(1-t^2)\right) \quad (8)$$

$$\theta_z = \frac{1}{4}\left(\theta_{z_I}(1-s)(1-t)(-s-t-1) + \theta_{z_J}(1+s)(1-t)(s-t-1) + \theta_{z_K}(1+s)(1+t)(s+t-1) + \theta_{z_L}(1-s)(1+t)(-s+t-1)\right) + \frac{1}{2}\left(\theta_{z_M}(1-s^2)(1-t) + \theta_{z_N}(1+s)(1-t^2) + \theta_{z_O}(1-s^2)(1+t) + \theta_{z_P}(1-s)(1-t^2)\right) \quad (9)$$

Where u, v, and w are displacement components, θ_x, θ_y, and θ_z are rotation components in x, y, and z directions, respectively, and s and t are local coordinates within the finite element.

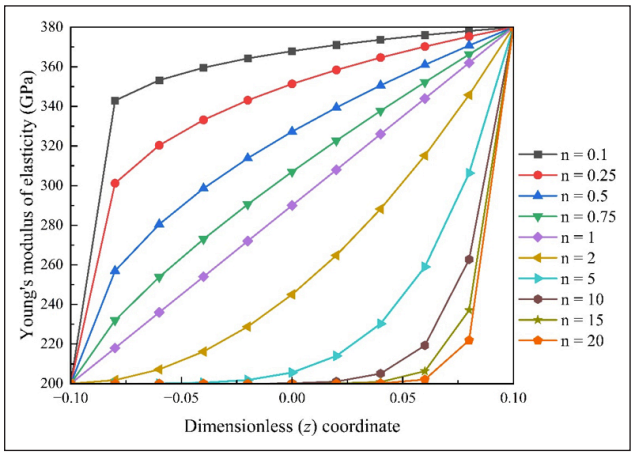

Figure 2. Young's modulus of elasticity in the thickness direction for different values of n.

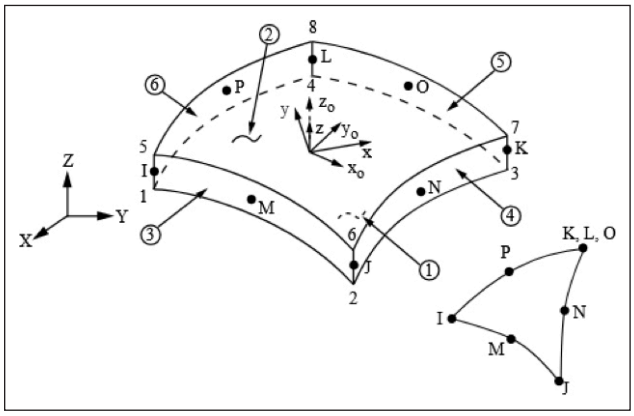

Figure 3. SHELL281 geometry [58].

2.1. Convergence Study

A convergence study was conducted to model the FGM plates in ANSYS Mechanical APDL and determine the appropriate number of layers and mesh size for discretization. Singha et al. [56] used a high-precision plate bending element based on first-order shear deformation theory to analyze the deflection and stresses of FGM plates under distributed transverse load. In their study, the formulation realistically accounted for the neutral surface position and the shear correction factors. Different boundary conditions with uniformly and lateral sinusoidal distributed loads were examined. For this study, only the results obtained in their research for the non-dimensional central displacement of clamped thin square alumina/aluminum FGM plates with power law indexes 0, 1, 2, 3, 4, 5, 10, and ∞ under uniformly distributed load were selected and compared with the results of the present study. The results of the present study and their study exhibit substantial agreement, affirming the reliability of the findings and validating the methodology used in this research. Comparisons of non-dimensional central displacement values of FGM plates with varying numbers of layers and mesh sizes are tabulated in Table 2 and Table 3, respectively.

As presented in Table 2, one layer is qualifying enough to obtain reliable results in the case of isotropic homoge-

Table 2. Non-dimensional central displacement of FGM plates with varying number of layers

Number of layers	Power-law index (n)							
	0	1	2	3	4	5	10	∞
1	0.001267	–	–	–	–	–	–	0.006890
11	–	0.002638	0.003229	0.003480	0.003584	0.003654	0.003828	–
21	–	0.002589	0.003243	0.003515	0.003654	0.003758	0.004002	–
31	–	0.002575	0.003250	0.003549	0.003689	0.003793	0.004071	–
41	–	0.002565	0.003250	0.003549	0.003689	0.003793	0.004106	–
51	–	0.002561	0.003254	0.003549	0.003723	0.003793	0.004141	–
61	–	0.002558	0.003254	0.003549	0.003723	0.003828	0.004141	–
71	–	0.002558	0.003254	0.003549	0.003723	0.003828	0.004176	–
81	–	0.002554	0.003257	0.003584	0.003723	0.003828	0.004176	–
91	–	0.002554	0.003257	0.003584	0.003723	0.003828	0.004176	–
101	–	0.002551	0.003257	0.003584	0.003723	0.003828	0.004176	–
201	–	0.002547	0.003257	0.003584	0.003723	0.003828	0.004211	–
Singha et al. [56]	0.001267	0.002542	0.003258	0.003580	0.003746	0.003854	0.004233	0.006881

Table 3. Non-dimensional central displacement of FGM plates with different mesh sizes

Power-law index (n)	Mesh sizes						Singha et al. [56]
	5 x 5	10 x 10	20 x 20	30 x 30	40 x 40	50 x 50	
0	0.000936	0.001267	0.001267	0.001267	0.001267	0.001267	0.001267
1	0.001837	0.002544	0.002547	0.002547	0.002547	0.002547	0.002542
2	0.002380	0.003250	0.003257	0.003257	0.003257	0.003257	0.003258
3	0.002666	0.003584	0.003584	0.003584	0.003584	0.003584	0.003580
4	0.002822	0.003723	0.003723	0.003723	0.003723	0.003723	0.003746
5	0.002930	0.003828	0.003828	0.003828	0.003828	0.003828	0.003854
10	0.003243	0.004211	0.004211	0.004211	0.004211	0.004211	0.004233
∞	0.005081	0.006855	0.006890	0.006890	0.006890	0.006890	0.006881

Table 4. Transitional and rotational restraints of supports

Type of support	Restraints
Clamped (C)	Ux = Uy = Uz = Rotx = Roty = Rotz = 0
Simply supported (S)	At x = 0 and 10, Uy = Uz = 0, At y = 0 and 6, Ux = Uz = 0
Free (F)	–

neous thin plates. In the FGM plates, the results converged as the number of layers in the thickness direction was increased. No significant change was observed in non-dimensional central displacement values of FGM plates after adding more than 201 layers. In Table 3, the values of non-dimensional central displacements for all plates were the same for finer meshes after 20 x 20. Although the non-dimensional central displacements of an isotropic homogeneous ceramic plate are the same after a 10 x 10 mesh size, in the case of an isotropic homogeneous metal plate, the results converged after a 20 x 20 mesh size. These findings suggest the sufficiency of 201 layers and 20 x 20 mesh size in solving thin to moderately thick FGM plates, yielding acceptable results while minimizing computational time. They also indicate a high degree of consistency and validation across both studies. The modeling and analyzing procedure of the present study is shown through a flowchart in Figure 4.

3. RESULTS AND DISCUSSION

This paper investigates deflections and stress responses of FGM plates with different boundary conditions subjected to three types of loads. All FGM plates have 201 layers in the thickness direction, with each layer having its distinct material properties calculated by using Eq. 2. The variations of these material properties are based on the considered power-law indexes (0, 0.1, 0.25, 0.5, 0.75, 1, 2, 5, 10, 15, and 20). A mesh size of 20 x 20 is used for discretization. Seven different boundary conditions are taken into account. The

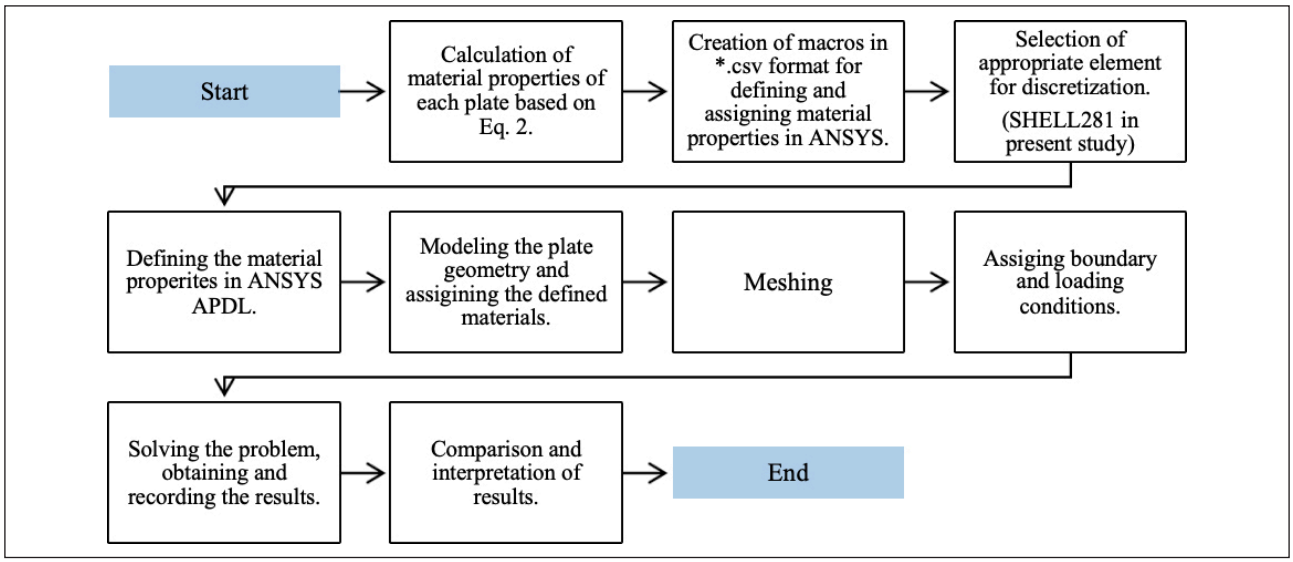

Figure 4. Modeling and analyzing procedure.

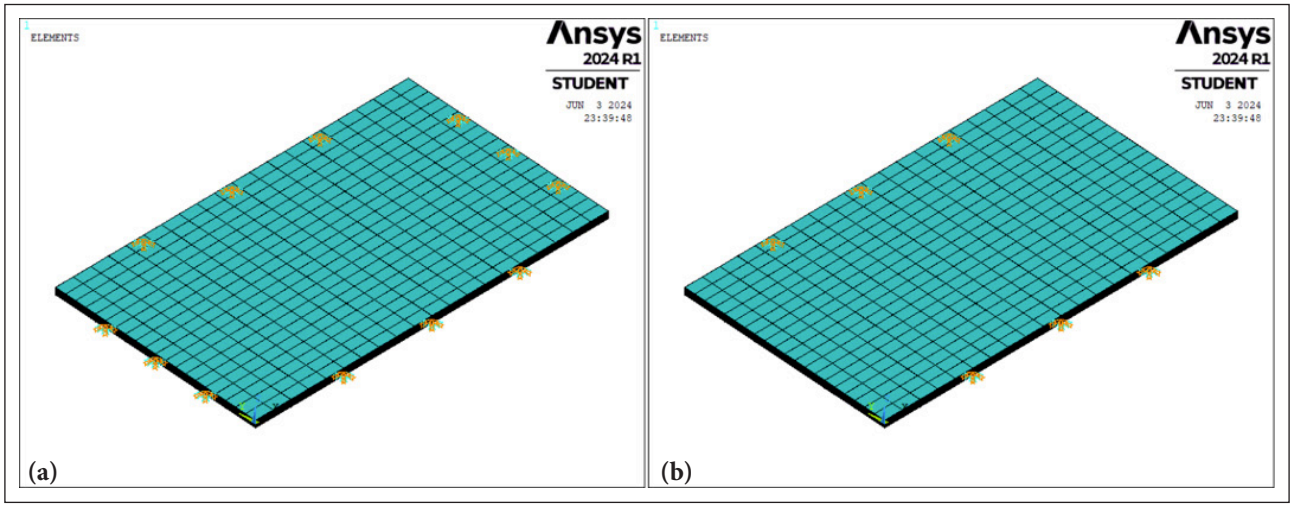

Figure 5. Meshed FGM rectangular plates with **(a)** CCCC and **(b)** CCFF boundary conditions.

transitional and rotational restraints of the supports are presented in Table 4. The configuration of the boundary conditions is such that from the left side, the first two letters represent the bottom and top, and the last two letters represent the left and right edges of the plate. Figure 5 shows meshed FGM rectangular plates with CCCC and CCFF boundary conditions.

10 FGM plates with distinct material properties are modeled and analyzed with seven boundary conditions and three different load types. A concentrated point load is assigned at the center point of the top ceramic-rich face. Uniformly and sinusoidal distributed loads were assigned on the top ceramic-rich face of the plate. The function of sinusoidal load is presented in Eq. 10.

$$P = p_0 \sin\left(\frac{\pi x}{a}\right) \sin\left(\frac{\pi y}{b}\right) \tag{10}$$

Where P is the sinusoidal load, a and b represent the length and width of the plate, respectively, and p_0 The magnitude of uniformly distributed load is assumed to be *10 kN* per square meter. It is worth mentioning that there is no specific reason for assigning this magnitude of load on the plate, and it is selected completely arbitrarily for this study. Maximum deflections of different FGM plates under uniformly distributed load, sinusoidal distributed load, and concentrated point loads with various boundary conditions are obtained and tabulated in Tables 5–7 and are compared in Figures 6–8, respectively. The results corresponding to the isotropic homogeneous ceramic and metal plates are included only in the tables to provide a wider scope of comparison.

As is evident from Figures 6–8, the smallest deflections were obtained in the case of sinusoidal and uniformly distributed loads, respectively, while the highest deflections were observed when the plates were subjected to concentrated point load. This is a result of the nature of the loading. Sinusoidal load varies smoothly and gradually across the plate, peaking at the center and reducing towards the edges in an illustrative manner, which paves the way for a more evenly spread out of stress and strain over the surface of the plate. This smooth distribution causes minimum local stress concentration and deflection. Uniformly distributed

Table 5. Maximum deflections (m) of isotropic homogeneous and FGM rectangular plates under uniformly distributed load

Power-law index (n)	Boundary conditions						
	CCCC	SSSS	CCSS	CSCS	CCCF	SSSF	CCFF
0	0.000112	0.000412	0.000121	0.000206	0.000139	0.000702	0.000139
0.1	0.000119	0.000439	0.000128	0.000220	0.000148	0.000747	0.000148
0.25	0.000127	0.000469	0.000137	0.000235	0.000159	0.000800	0.000158
0.5	0.000138	0.000509	0.000149	0.000255	0.000172	0.000868	0.000172
0.75	0.000145	0.000538	0.000157	0.000269	0.000182	0.000916	0.000181
1	0.000151	0.000558	0.000163	0.000279	0.000188	0.000950	0.000188
2	0.000162	0.000598	0.000175	0.000300	0.000202	0.001019	0.000202
5	0.000173	0.000638	0.000187	0.000320	0.000216	0.001086	0.000215
10	0.000182	0.000672	0.000197	0.000337	0.000227	0.001144	0.000226
15	0.000188	0.000693	0.000203	0.000347	0.000234	0.001180	0.000234
20	0.000192	0.000708	0.000207	0.000354	0.000239	0.001205	0.000238
∞	0.000212	0.000783	0.000229	0.000392	0.000265	0.001333	0.000264

Table 6. Maximum deflections (m) of isotropic homogeneous and FGM rectangular plates under sinusoidal distributed load

Power-law index (n)	Boundary conditions						
	CCCC	SSSS	CCSS	CSCS	CCCF	SSSF	CCFF
0	0.0000819	0.000263	0.0000863	0.000139	0.0000844	0.000306	0.0000867
0.1	0.0000872	0.000280	0.0000919	0.000148	0.0000899	0.000326	0.0000923
0.25	0.0000934	0.000299	0.0000983	0.000158	0.0000962	0.000349	0.0000988
0.5	0.0001010	0.000325	0.0001070	0.000171	0.0001040	0.000379	0.0001070
0.75	0.0001070	0.000343	0.0001130	0.000181	0.0001100	0.000400	0.0001130
1	0.0001110	0.000355	0.0001170	0.000188	0.0001140	0.000415	0.0001170
2	0.0001190	0.000381	0.0001250	0.000201	0.0001230	0.000445	0.0001260
5	0.0001270	0.000406	0.0001340	0.000215	0.0001310	0.000474	0.0001340
10	0.0001340	0.000428	0.0001410	0.000226	0.0001380	0.000499	0.0001410
15	0.0001380	0.000442	0.0001450	0.000233	0.0001420	0.000515	0.0001460
20	0.0001410	0.000451	0.0001480	0.000238	0.0001450	0.000526	0.0001490
∞	0.0001560	0.000499	0.0001640	0.000264	0.0001600	0.000582	0.0001650

Table 7. Maximum deflections (m) of isotropic homogeneous and FGM rectangular plates under concentrated point load

Power-law index (n)	Boundary conditions						
	CCCC	SSSS	CCSS	CSCS	CCCF	SSSF	CCFF
0	0.000576	0.001269	0.000585	0.000787	0.000581	0.001347	0.000585
0.1	0.000613	0.001351	0.000662	0.000838	0.000618	0.001434	0.000623
0.25	0.000656	0.001445	0.000666	0.000896	0.000661	0.001534	0.000666
0.5	0.000712	0.001568	0.000722	0.000972	0.000717	0.001665	0.000723
0.75	0.000751	0.001655	0.000762	0.001026	0.000757	0.001757	0.000763
1	0.000779	0.001717	0.000791	0.001065	0.000786	0.001823	0.000792
2	0.000838	0.001844	0.000850	0.001144	0.000844	0.001957	0.000851
5	0.000895	0.001967	0.000908	0.001221	0.000902	0.002087	0.000909
10	0.000943	0.002072	0.000957	0.001286	0.000950	0.002198	0.000957
15	0.000972	0.002137	0.000987	0.001326	0.000980	0.002266	0.000987
20	0.000992	0.002181	0.001007	0.001353	0.001000	0.002314	0.001007
∞	0.001095	0.002411	0.001112	0.001495	0.001104	0.002559	0.001112

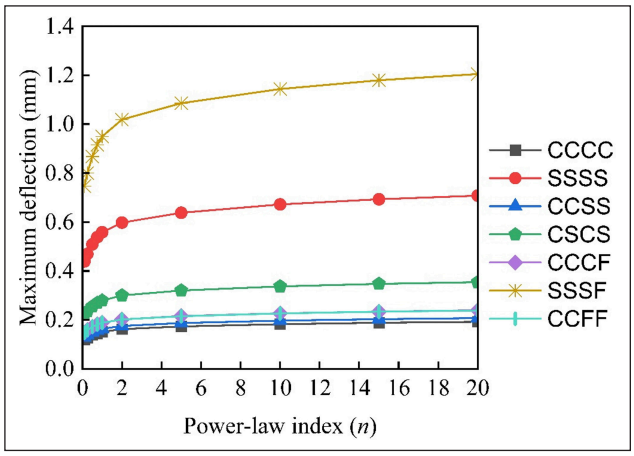

Figure 6. Maximum deflections of FGM rectangular plates under uniformly distributed load.

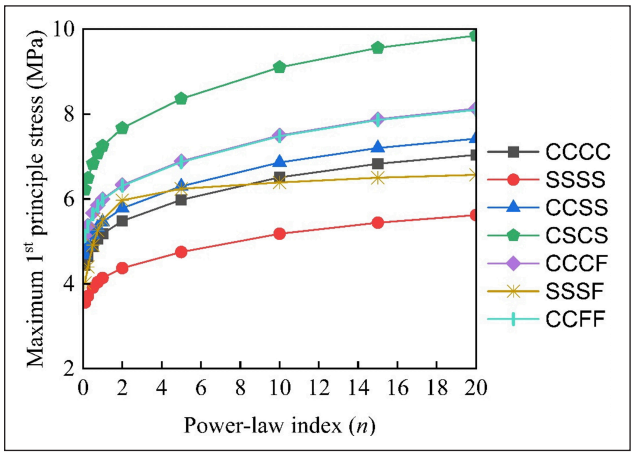

Figure 9. Maximum 1st principle stresses of FGM rectangular plates under uniformly distributed load.

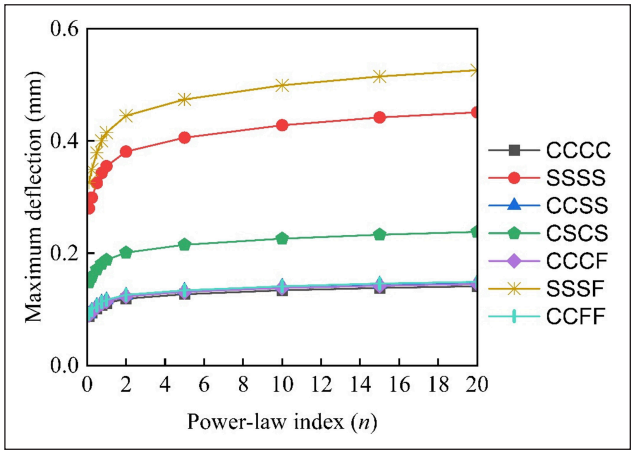

Figure 7. Maximum deflections of FGM rectangular plates under sinusoidal distributed load.

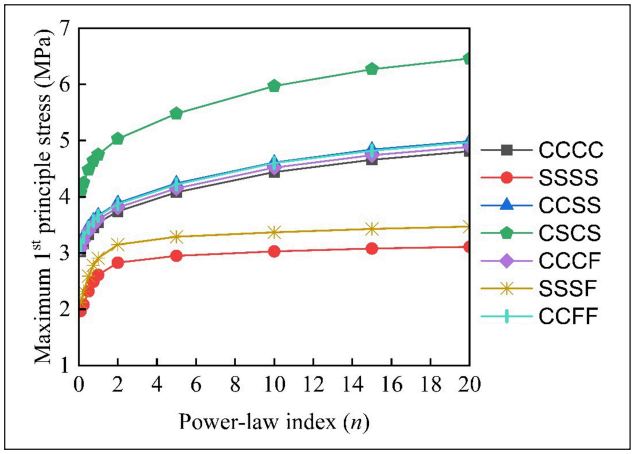

Figure 10. Maximum 1st principle stresses of FGM rectangular plates under sinusoidal distributed load.

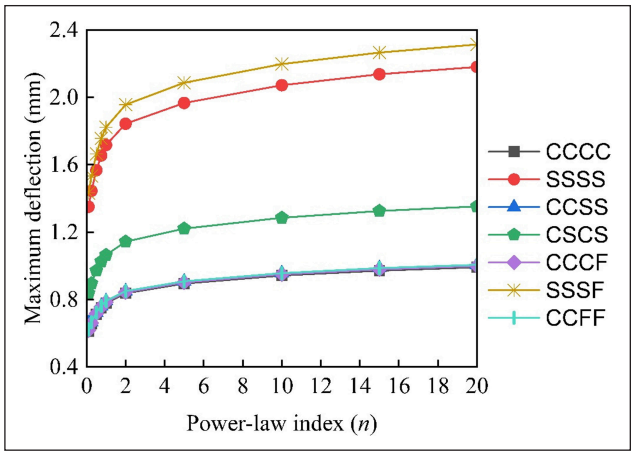

Figure 8. Maximum deflections of FGM rectangular plates under concentrated point load.

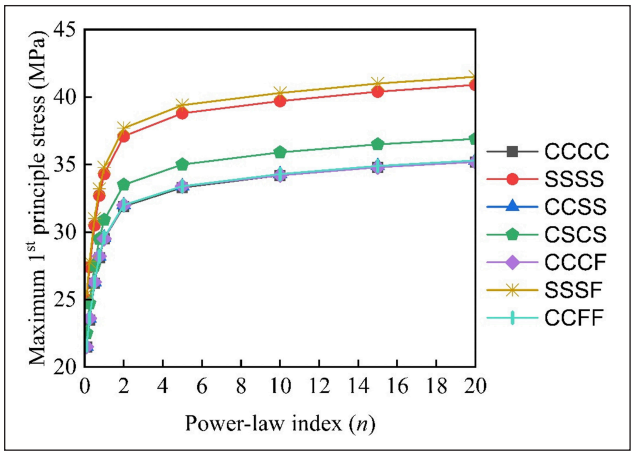

Figure 11. Maximum 1st principle stresses of FGM rectangular plates under concentrated point load.

load resulted in slightly higher deflections due to the constant magnitude over the entire face of the plate. Point Load, on the other hand, exhibited the highest deflections in FGM plates due to high-stress concentration at the point of application. The effect of boundary conditions on the deflection values of the FGM plates can be observed, too. In all three cases, SSSF, SSSS, and CSCS-type boundary conditions resulted in higher deflections than the others. Plates with SSSF boundary conditions have higher deflections because the free edge allows maximum movement, and simply support-

Table 8. Maximum 1st principle stresses (MPa) of isotropic homogeneous and FGM rectangular plates under uniformly distributed load

Power-law index (n)	Boundary conditions						
	CCCC	SSSS	CCSS	CSCS	CCCF	SSSF	CCFF
0	4.27	4.91	4.50	5.98	4.94	7.01	4.92
0.1	4.44	3.56	4.68	6.22	5.14	4.02	5.13
0.25	4.64	3.71	4.89	6.49	5.37	4.40	5.35
0.5	4.88	3.91	5.15	6.83	5.67	4.91	5.64
0.75	5.06	4.04	5.33	7.07	5.85	5.26	5.83
1	5.18	4.14	5.46	7.25	6.00	5.51	5.98
2	5.48	4.37	5.78	7.67	6.33	5.97	6.31
5	5.98	4.75	6.30	8.36	6.89	6.24	6.87
10	6.51	5.18	6.86	9.10	7.50	6.39	7.48
15	6.83	5.44	7.20	9.56	7.88	6.50	7.86
20	7.04	5.62	7.42	9.85	8.13	6.57	8.10
∞	4.27	4.91	4.50	5.98	4.94	7.01	4.92

Table 9. Maximum 1st principle stresses (MPa) of isotropic homogeneous and FGM rectangular plates under sinusoidal distributed load

Power-law index (n)	Boundary conditions						
	CCCC	SSSS	CCSS	CSCS	CCCF	SSSF	CCFF
0	2.92	3.32	3.03	3.92	2.97	3.70	3.02
0.1	3.03	1.97	3.15	4.08	3.09	2.12	3.14
0.25	3.17	2.08	3.29	4.25	3.22	2.32	3.28
0.5	3.33	2.32	3.46	4.48	3.39	2.59	3.45
0.75	3.45	2.49	3.58	4.64	3.51	2.78	3.57
1	3.54	2.61	3.67	4.75	3.60	2.91	3.66
2	3.74	2.83	3.89	5.03	3.81	3.15	3.87
5	4.08	2.95	4.24	5.48	4.15	3.29	4.22
10	4.44	3.03	4.61	5.97	4.52	3.37	4.60
15	4.66	3.08	4.84	6.27	4.74	3.43	4.82
20	4.81	3.11	4.99	6.46	4.89	3.47	4.97
∞	2.92	3.32	3.03	3.92	2.97	3.70	3.02

ed edges allow rotation, contributing to more considerable deflections than the clamped conditions. The effect of free edge in maximizing the deflections is more evident when the results are compared with SSSS boundary condition.

The smallest maximum deflection values are obtained in the case of CCCC. They are very close to results obtained from CCSS, CCCF, and CCFF, which indicates the effect of clamped boundary conditions in minimizing the deflections in FGM plates. In the case of CSCS, although it also has two clamped and two simply supported edges like CCSS, the positions of the clamped edges can affect the deflection values. In CSCS, the two clamped edges are adjacent, while in CCSS, the clamped edges are opposed. It is also worth mentioning that in CCSS boundary conditions, one of the clamped edges is longer than the clamped edges in CSCS, which makes the plate more constrained, decreasing deflections. Maximum 1st principle stresses of FGM plates are presented similarly in Tables 8–10 and are compared in Figures 9–11.

As can be observed in Figures 9–11, FGM plates with SSSS boundary conditions have the lowest values of maximum 1st principle stress under both distributed loads. In contrast, the case of concentrated point load has the highest values after SSSF. This is because of the localized nature of the point load, which adds steepness to the trends in lower values of n and causes an overall increase in stress values compared to both distributed loads. Results corresponding to CCCF and CCFF boundary conditions are very close to each other in the case of uniformly distributed and concentrated point loads. By observing all three figures, it is apparent that the trends of stress values for CCCC, CCSS, CCCF, and CCFF boundary conditions converged as the load type changed from uniformly to sinusoidal distributed load and then to concentrated point load. This indicates that the two clamped edges take most of the stress. CSCS boundary condition exhibited the highest results of 1st principle stress in the plates under both distributed loads but had lower stress values than SSSF and SSSS in the case of concentrated point load.

Table 10. Maximum 1st principle stresses (MPa) of isotropic homogeneous and FGM rectangular plates under concentrated point load

Power-law index (n)	Boundary conditions						
	CCCC	SSSS	CCSS	CSCS	CCCF	SSSF	CCFF
0	37.5	43.5	37.6	39.3	37.5	44.2	37.6
0.1	21.5	25.0	21.5	22.5	21.5	25.4	21.6
0.25	23.5	27.4	23.6	24.7	23.6	27.8	23.6
0.5	26.2	30.5	26.3	27.5	26.3	31.0	26.3
0.75	28.1	32.7	28.2	29.5	28.2	33.2	28.2
1	29.5	34.3	29.6	30.9	29.5	34.8	29.6
2	31.9	37.1	32.0	33.5	32.0	37.7	32.0
5	33.3	38.8	33.4	35.0	33.4	39.4	33.4
10	34.2	39.7	34.3	35.9	34.2	40.3	34.3
15	34.8	40.4	34.9	36.5	34.8	41.0	34.9
20	35.2	40.9	35.3	36.9	35.2	41.5	35.3
∞	37.5	43.5	37.6	39.3	37.5	44.2	37.6

Table 11. Maximum Von Mises stresses (MPa) of isotropic homogeneous and FGM rectangular plates under uniformly distributed load

Power-law index (n)	Boundary conditions						
	CCCC	SSSS	CCSS	CSCS	CCCF	SSSF	CCFF
0	3.80	6.51	4.00	5.31	4.39	7.02	4.37
0.1	3.95	6.78	4.16	5.53	4.57	7.30	4.55
0.25	4.12	7.08	4.34	5.77	4.77	7.62	4.75
0.5	4.34	7.45	4.57	6.07	5.02	8.03	5.01
0.75	4.49	7.71	4.74	6.29	5.20	8.31	5.18
1	4.61	7.90	4.85	6.44	5.33	8.52	5.31
2	4.87	8.34	5.13	6.81	5.63	9.01	5.61
5	5.31	9.08	5.60	7.43	6.12	9.83	6.11
10	5.78	9.89	6.10	8.09	6.67	10.7	6.65
15	6.07	10.4	6.40	8.49	7.00	11.2	6.98
20	6.26	10.7	6.60	8.76	7.22	11.6	7.20
∞	3.80	6.51	4.00	5.31	4.39	7.02	4.37

Table 12. Maximum Von Mises stresses (MPa) of isotropic homogeneous and FGM rectangular plates under sinusoidal distributed load

Power-law index (n)	Boundary conditions						
	CCCC	SSSS	CCSS	CSCS	CCCF	SSSF	CCFF
0	2.59	3.44	2.69	3.48	2.64	3.59	2.68
0.1	2.70	3.58	2.80	3.62	2.47	3.74	2.79
0.25	2.81	3.74	2.92	3.78	2.86	3.90	2.91
0.5	2.96	3.94	3.08	3.98	3.01	4.11	3.07
0.75	3.07	4.08	3.19	4.12	3.12	4.26	3.17
1	3.14	4.18	3.27	4.22	3.20	4.36	3.25
2	3.33	4.41	3.45	4.47	3.38	4.60	3.44
5	3.63	4.80	3.77	4.87	3.69	5.01	3.75
10	3.95	5.23	4.10	5.30	4.02	5.45	4.08
15	4.14	5.49	4.30	5.57	4.22	5.73	4.29
20	4.27	5.66	4.44	5.74	4.35	5.91	4.42
∞	2.59	3.44	2.69	3.48	2.64	3.59	2.68

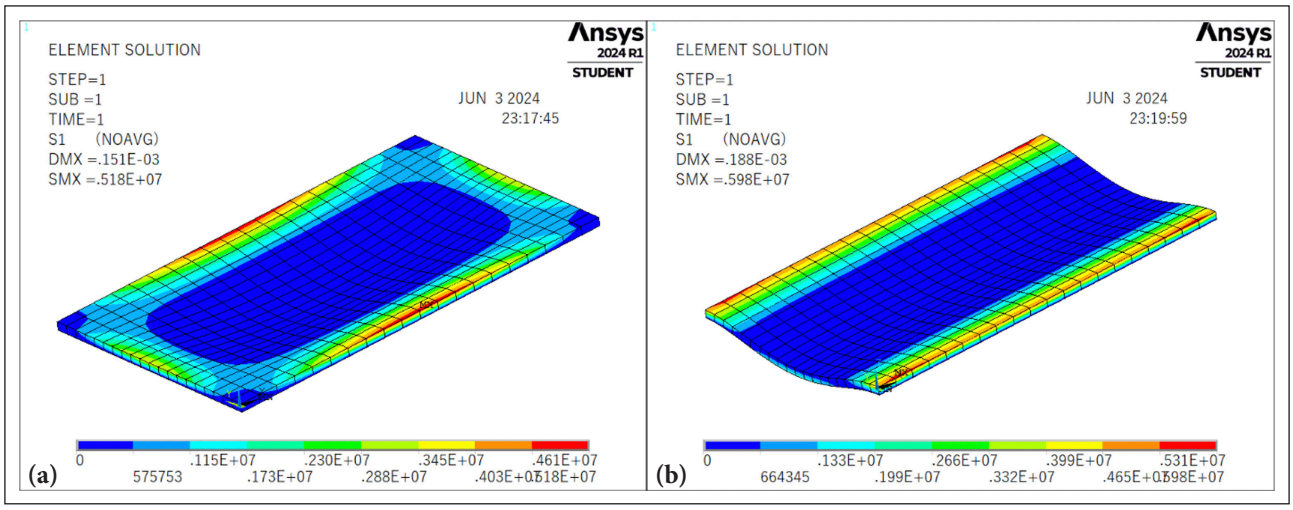

Figure 12. 1st Principle stresses in FGM rectangular plates with (a) CCCC and (b) CCFF boundary conditions.

Table 13. Maximum Von Mises stresses (MPa) of isotropic homogeneous and FGM rectangular plates under concentrated point load

Power-law index (n)	Boundary conditions						
	CCCC	SSSS	CCSS	CSCS	CCCF	SSSF	CCFF
0	35.6	41.1	35.6	37.3	35.6	41.4	35.6
0.1	37.0	42.8	37.0	38.8	37.0	43.1	37.0
0.25	38.6	44.6	38.7	40.5	38.6	44.9	38.7
0.5	40.7	47.0	40.7	42.7	40.7	47.3	40.7
0.75	42.1	48.7	42.2	44.2	42.1	49.0	42.1
1	43.2	49.9	43.2	45.3	43.2	50.2	43.2
2	45.7	52.8	45.7	47.9	45.7	53.2	45.7
5	49.8	57.6	49.9	52.3	49.8	58.0	49.9
10	54.2	62.7	54.3	56.9	54.2	63.1	54.3
15	56.9	65.8	57.0	59.7	56.9	66.2	56.9
20	58.7	67.8	58.7	61.5	58.7	68.3	58.7
∞	35.6	41.1	35.6	37.3	35.6	41.4	35.6

Moreover, the trends show an increase in stress values for all boundary conditions as the power-law index increases. This is a result of the transition of materials from alumina to steel, affecting the stiffness of the plate. At higher values of n, the ductile nature of steel decreases the steepness of the trends. Figure 12 shows the formation of 1st principle stresses in the FGM plates (n=1) subjected to uniformly distributed load with CCCC and CCFF boundary conditions.

Maximum Von Mises stresses of the FGM rectangular plates with different boundary conditions for all three types of loads are tabulated in Tables 11–13 and are compared in Figures 13–15.

As can be seen in Figures 10–12, FGM plates with SSSF and SSSS boundary conditions have higher maximum Von Mises stress values under all types of loads compared to other boundary conditions, except plates subjected to sinusoidal distributed load, where stress values of CSCS boundary condition surpassed those of SSSS. In the case of CCCF and CCFF, when the plates are subjected to uniformly distributed load, there is a very small difference in stress values, and their trends are nearly coincident. Under sinusoidal distributed load, these trends diverged enough to be observed. The maximum Von Mises stress values for FGM plates subjected to concentrate point load with CCCC,

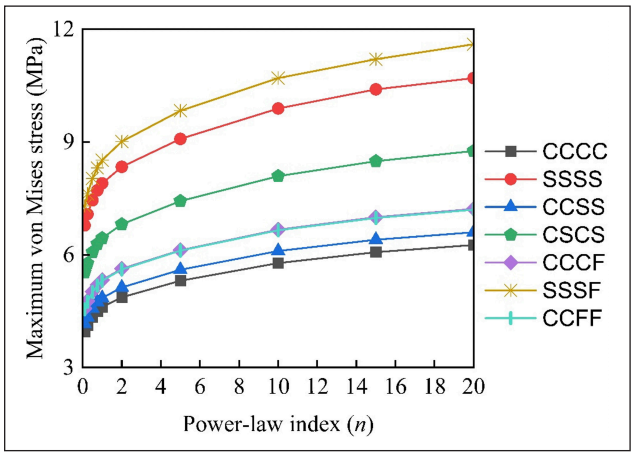

Figure 13. Maximum Von Mises stresses of FGM rectangular plates under uniformly distributed load.

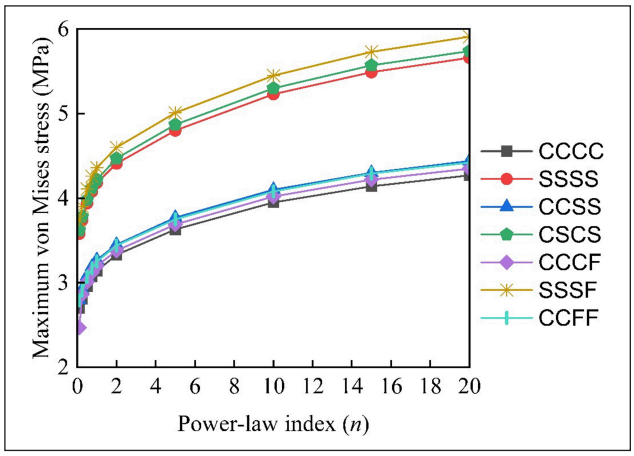

Figure 14. Maximum Von Mises stresses of FGM rectangular plates under sinusoidal distributed load.

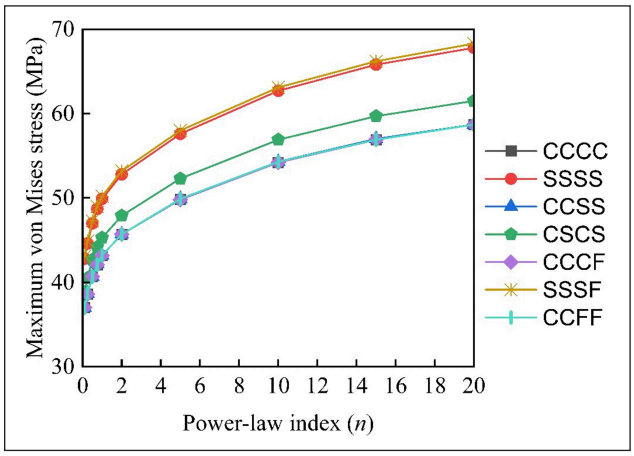

Figure 15. Maximum Von Mises stresses of FGM rectangular plates under concentrated point load.

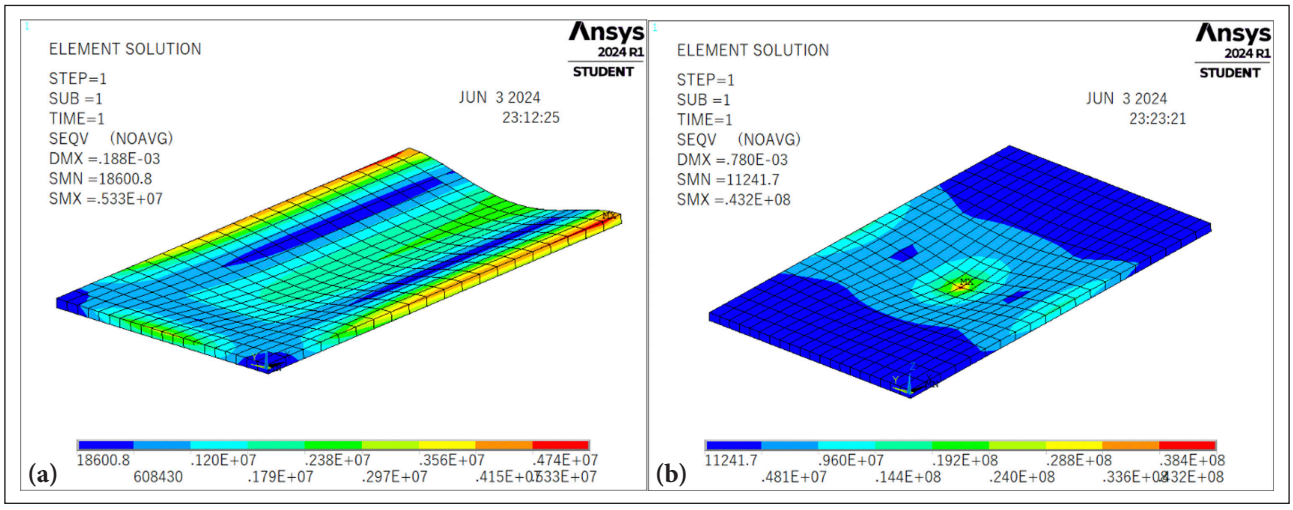

Figure 16. Von Mises stresses in FGM rectangular plates; **(a)** Subjected to uniformly distributed load with CCCF boundary condition **(b)** Subjected to concentrated point load with CCCC boundary condition.

CCSS, CCCF, and CCFF are very close and have small differences that can be neglected. The common factor between these four boundary conditions is the presence of clamped supports at the two long edges of the plate. CSCS boundary conditions also have two clamped edges, but one of them is the short edge of the plate, resulting in higher stress values than others. This indicates the clamped boundary condition's significance and position around the plate. In the case of point load, the maximum Von Mises stress values corresponding to SSSF and SSSS were very close at small values of *n*, but the trends diverged smoothly at greater values of *n*. Across all load types, the power-law index n influenced the maximum Von Mises stress values similarly, with an initial increase due to higher deflections from introducing steel-like properties. At higher n values, the rate of increase in stress values decreased as the plate gained more ductility due to the high content of steel in the composition. Figure 16 shows the formation of Von Mises stresses in FGM rectangular plates (n=1) subjected to uniformly distributed load with CCCF boundary condition and concentrated point load with CCCC boundary condition.

4. CONCLUSIONS

This paper investigates the effect of the material property gradient on the deflection and stress responses of FGM plates with various boundary conditions, subjected to three different types of loads, using the finite element method. Ten FGM plates, whose top and bottom layers are composed of alumina and steel, respectively, have intermediate layers with material properties varying based on the power-law indexes considered in this study. After obtaining numerical results from ANSYS Mechanical APDL and comparing them, the following conclusions can be drawn:

- The number of layers and mesh size significantly influence the actual behavior of FGM plates. While an increase in the number of layers and mesh size leads to more precise and accurate numerical results, no significant change in results was observed when the number of layers increased from 101 to 201 or when the mesh size was refined beyond 20 x 20.
- The type of load plays a crucial role in determining the deflections and stress formation within the FGM plates.

A sinusoidally distributed load resulted in the least deflections and stress values compared to uniformly distributed and concentrated point loads.

- Boundary conditions have a significant impact on deflections in FGM plates. Under all types of loads, plates with CCCC (all clamped) boundary conditions exhibited the least maximum deflection, while plates with SSSF (three simply supported, one free) boundary conditions showed the highest maximum deflection.
- The highest values of maximum first principal stress were observed in plates with CSCS (clamped-simply supported-clamped-simply supported) boundary conditions when subjected to distributed loads. These highest values shifted to plates with SSSF boundary conditions under concentrated point loads. In the case of distributed loads, the lowest stress was recorded in plates with SSSS (all simply supported) boundary conditions, while the lowest values under concentrated point loads were seen in plates with CCCC boundary conditions.
- For all types of loads, the highest maximum von Mises stress values in all FGM plates were recorded under SSSF boundary conditions. The lowest maximum von Mises stress values were observed in plates with CCCC boundary conditions when subjected to uniformly distributed and concentrated point loads. Under sinusoidal distributed loads, the lowest stress value was observed in plates with CCCF (three clamped, one free) boundary conditions.
- The positioning of clamped edges greatly influences the deflections and stress formation within FGM plates.
- Generally, increasing the steel content in the composition of the plates, thereby increasing the power-law index (n), resulted in higher deflections and maximum first principal and von Mises stresses in all the plates.
- At smaller values of n, the rate of increase in deflections, maximum first principal stress, and von Mises stress is higher than at larger values of n, where the plates exhibit more steel-like properties.

The results of this study are in strong agreement with the existing literature consensus, emphasizing the impact of the material gradient index and boundary conditions on the bending and stress responses of FGM plates.

ETHICS

There are no ethical issues with the publication of this manuscript.

DATA AVAILABILITY STATEMENT

The authors confirm that the data that supports the findings of this study are available within the article. Raw data that support the finding of this study are available from the corresponding author, upon reasonable request.

CONFLICT OF INTEREST

The authors declare that they have no conflict of interest.

FINANCIAL DISCLOSURE

The authors declared that this study has received no financial support.

USE OF AI FOR WRITING ASSISTANCE

Not declared.

PEER-REVIEW

Externally peer-reviewed.

REFERENCES

[1] Zhang, N., Khan, T., Guo, H., Shi, S., Zhong, W., & Zhang, W. (2019). Functionally graded materials: An overview of stability, buckling, and free vibration analysis. *Adv Mater Sci Eng, 2019*(1), 1354150. [CrossRef]

[2] Edwin, A., Anand, V., & Prasanna, K. (2017). Sustainable development through functionally graded materials: An overview. *Rasayan J Chem, 10*(1), 149–152.

[3] Torelli, G., Fernández, M. G., & Lees, J. M. (2020). Functionally graded concrete: Design objectives, production techniques and analysis methods for layered and continuously graded elements. *Constr Build Mater, 242*, 118040. [CrossRef]

[4] Chan, R., Hu, T., Liu, X., Galobardes, I., Moy, C. K., Hao, J. L., & Krabbenhoft, K. (2019). Sustainability analysis of functionally graded concrete produced with fibres and recycled aggregates. *In Sustainable Buildings and Structures: Building a Sustainable Tomorrow* (pp. 38–44). CRC Press. [CrossRef]

[5] Shamoon, A., Haleem, A., Bahl, S., Javaid, M., Prakash, C., & Budhhi, D. (2022). Understanding the role of advanced materials for energy infrastructure and transmission. *Mater Today Proc, 62*, 4260–4266. [CrossRef]

[6] Koizumi, M., & Niino, M. (1995). Overview of FGM research in Japan. *MRS Bull, 20*(1), 19–21. [CrossRef]

[7] Sobczak, J., & Drenchev, L. (2008). Functionally graded materials - Processing and modeling. *Motor Transport Inst Warsaw Foundry Res Inst*, Cracow.

[8] Chaabani, H., Mesmoudi, S., Boutahar, L., & El Bikri, K. (2023). A high-order finite element continuation for buckling analysis of porous FGM plates. *Eng Struct, 279*, 115597. [CrossRef]

[9] Moita, J. S., Correia, V. F., Soares, C. M. M., & Herskovits, J. (2019). Higher-order finite element models for the static linear and nonlinear behaviour of functionally graded material plate-shell structures. *Compos Struct, 212*, 465–475. [CrossRef]

[10] Afzali, M., Farrokh, M., & Carrera, E. (2022). Thermal buckling loads of rectangular FG plates with temperature-dependent properties using Carrera unified formulation. *Compos Struct, 295*, 115787. [CrossRef]

[11] Kazemzadeh-Parsi, M. J., Ammar, A., & Chinesta, F. (2023). Parametric analysis of thick FGM plates based on 3D thermo-elasticity theory: A proper generalized decomposition approach. *Mater, 16*(4), 1753. [CrossRef]

[12] Kargarnovin, M. H., Pouladvand, M., & Najafizadeh, M. M. (2023). Study of thermal stability of thin rectangular plates with variable thickness made of functionally graded materials. *J Mech Res Appl, 13*(3), 1–28.

[13] Saad, M., & Hadji, L. (2022). Thermal buckling analysis of porous FGM plates. *Mater Today Proc, 53*, 196–201. [CrossRef]

[14] Slimani, R., Menasria, A., Ali Rachedi, M., Mourad, C., Refrafi, S., Nimer, A. A., & Mamen, B. (2024). A novel quasi-3D refined HSDT for static bending analysis of porous functionally graded plates. *J Comput Appl Mech, 55*(3): 519–537.

[15] Rebai, B., Mansouri, K., Chitour, M., Berkia, A., Messas, T., Khadraoui, F., & Litouche, B. (2023). Effect of idealization models on deflection of functionally graded material (FGM) plate. *J Nano Electron Phys, 15*(1), 01022. [CrossRef]

[16] Hamza Madjid, B., & Bouderba, B. (2023). Buckling analysis of FGM plate exposed to different loads conditions. *Mech Based Des Struct Mach, 51*(12), 6798–6813. [CrossRef]

[17] Hong, N. T. (2020). Nonlinear static bending and free vibration analysis of bidirectional functionally graded material plates. *Int J Aerosp Eng, 2020*, 1–16. [CrossRef]

[18] Talha, M., & Singh, B. (2010). Static response and free vibration analysis of FGM plates using higher order shear deformation theory. *Appl Math Model, 34*(12), 3991–4011. [CrossRef]

[19] Singh, D., & Gupta, A. (2024). Influence of microstructural defects on vibration characteristics of sandwich double FGM layer under mixed boundary conditions. *Int J Interact Des Manuf, 2024*, 1–18. [CrossRef]

[20] Alghanmi, R. A., & Aljaghthami, R. H. (2024). A four-variable shear deformation theory for the static analysis of FG sandwich plates with different porosity models. *Math Comput Appl, 29*(2), 20. [CrossRef]

[21] Nguyen, T. T., Le, T. S., Tran, T. T., & Pham, Q. H. (2024). Buckling analysis of functionally graded porous variable thickness plates resting on Pasternak foundation using ES-MITC3. *Lat Am J Solids Struct, 21*, e524. [CrossRef]

[22] Elkafrawy, M., Alashkar, A., Hawileh, R., & AlHamaydeh, M. (2022). FEA investigation of elastic buckling for functionally graded material (FGM) thin plates with different hole shapes under uniaxial loading. *Buildings, 12*(6), 802. [CrossRef]

[23] Alashkar, A., Elkafrawy, M., Hawileh, R., & AlHamaydeh, M. (2022). Buckling analysis of functionally graded materials (FGM) thin plates with various circular cutout arrangements. *J Compos Sci, 6*(9), 277. [CrossRef]

[24] Alashkar, A., Elkafrawy, M., Hawileh, R., & AlHamaydeh, M. (2024). Elastic buckling behaviour of skew functionally graded material (FGM) thin plates with circular openings. *Buildings, 14*(3), 572. [CrossRef]

[25] Kumar, R., Sharma, H. K., Gupta, S., Malguri, A., Rajak, B., Srivastava, Y., & Pandey, A. (2024). Initial buckling behavior of elastically supported rectangular FGM plate based on higher order shear deformation theory via spline RBF method. *Mech Adv Compos Struct, 11*(1), 59–72.

[26] Shehab, M. B., Taima, M. S., Sayed, H., & El-Sayed, T. A. (2023). An investigation into the free vibration of intact and cracked FGM plates. *J Fail Anal Prev, 23*(5), 2142–2168. [CrossRef]

[27] Hu, Z., Shi, Y., Xiong, S., Zheng, X., & Li, R. (2023). New analytic free vibration solutions of non-Lévy-type porous FGM rectangular plates within the symplectic framework. *Thin-Walled Struct, 185*, 110609. [CrossRef]

[28] Peng, L. X., Chen, S. Y., Wei, D. Y., Chen, W., & Zhang, Y. S. (2022). Static and free vibration analysis of stiffened FGM plate on elastic foundation based on physical neutral surface and MK method. *Compos Struct, 290*, 115482. [CrossRef]

[29] Lim, J., Amir, M., Kim, S. W., & Lee, S. Y. (2024). Static analysis of FGM porous cooling plates with cutouts: A multilayered approach. *Adv Compos Mater, 2024*(2303947), 1–24. [CrossRef]

[30] Ramu, I., & Mohanty, S. C. (2014). Modal analysis of functionally graded material plates using finite element method. *Procedia Mater Sci, 6*, 460–467. [CrossRef]

[31] Srivastava, M. C., & Singh, J. (2023). Assessment of RBFs based meshfree method for the vibration response of FGM rectangular plate using HSDT model. *Mech Adv Compos Struct, 10*(1), 137–150.

[32] Kumar, Y. (2022). Effect of elastically restrained edges on free transverse vibration of functionally graded porous rectangular plate. *Mech Adv Compos Struct, 9*(2), 335–348.

[33] Kumaravelan, R. *Thermo mechanical analysis of functionally graded material plates* [Thesis, Anna University].

[34] Smaine, A., Mokhtari, M., Telli, F., Khiari, M. E. A., Bouchetara, M., & Habib, B. (2024). Using FGM concept in fiber-matrix coupling laws to predict the damage in carbon-epoxy graded composite application in notched plate under thermo-mechanical loading. *Mech Adv Mater Struct*, 1–15. [CrossRef]

[35] Asemi, K., & Salami, S. J. (2015). A study on low velocity impact response of FGM rectangular plates with 3D elasticity based graded finite element modeling. *J Theor Appl Mech, 53*(4), 859–872. [CrossRef]

[36] Rani, P., Verma, D., & Ghangas, G. (2023). Modeling and stress analysis of rounded rectangular inclusion enclosed by FGM layer. *Int J Math Eng Manag Sci, 8*(2), 282. [CrossRef]

[37] Yildirim, S. (2020). Hydrogen elasticity solution of functionally-graded spheres, cylinders and disks. *Int J Hydrogen Energy, 45*(41), 22094–22101. [CrossRef]

[38] Feri, M., Krommer, M., & Alibeigloo, A. (2023). Three-dimensional static analysis of a viscoelastic rectangular functionally graded material plate embedded between piezoelectric sensor and actuator layers. *Mech Based Des Struct Mach, 51*(7), 3843–3867. [CrossRef]

[39] Bendenia, N., Zidour, M., Bousahla, A. A., Bourada, F., Tounsi, A., Benrahou, K. H., & Tounsi, A. (2020). Deflections, stresses and free vibration studies of FG-CNT reinforced sandwich plates resting on Pasternak elastic foundation. *Comput Concr Int J, 26*(3), 213–226.

[40] Noori, A. R., Aslan, T. A., & Temel, B. (2018). An efficient approach for in-plane free and forced vibrations of axially functionally graded parabolic arches with nonuniform cross section. *Compos Struct, 200*, 701–710. [CrossRef]

[41] Noori, A. R., Aslan, T. A., & Temel, B. (2021). Dynamic analysis of functionally graded porous beams using complementary functions method in the Laplace domain. *Compos Struct, 256*, 113094. [CrossRef]

[42] Aslan, T. A., Noori, A. R., & Temel, B. (2023, December). An efficient approach for free vibration analysis of functionally graded sandwich beams of variable cross-section. *In Struct* (Vol. 58, p. 105397). Elsevier. [CrossRef]

[43] Doori, S. G. M., Noori, A. R., & Etemadi, A. (2024). Static response of functionally graded porous circular plates via finite element method. *Arab J Sci Eng, 49*, 14167–14181. [CrossRef]

[44] Özer, A. P., Noori, A. R., & Aygörmez, Y. (2023, November 23-25). *Effect of mesh size on finite element analysis of functionally graded porous domes*. International Conference on Engineering Technologies (ICENTE23), Konya, Türkiye.

[45] Al-ıtbı, S. K., & Noori, A. R. (2022). Influence of porosity on the free vibration response of sandwich functionally graded porous beams. *J Sustain Constr Mater Technol, 7*(4), 291–301. [CrossRef]

[46] Lee, J. K., & Lee, B. K. (2019). Free vibration and buckling of tapered columns made of axially functionally graded materials. *Appl Math Model, 75*, 73–87. [CrossRef]

[47] Huang, Y., & Li, X. F. (2010). Buckling of functionally graded circular columns including shear deformation. *Mater Des, 31*(7), 3159–3166. [CrossRef]

[48] Yildirim, S. (2020). Free vibration analysis of sandwich beams with functionally-graded-cores by complementary functions method. *AIAA J, 58*(12), 5431–5439. [CrossRef]

[49] Menasria, A., Kaci, A., Bousahla, A. A., Bourada, F., Tounsi, A., Benrahou, K. H., & Mahmoud, S. R. (2020). A four-unknown refined plate theory for dynamic analysis of FG-sandwich plates under various boundary conditions. *Steel Compos Struct Int J, 36*(3), 355–367.

[50] Rabhi, M., Benrahou, K. H., Kaci, A., Houari, M. S. A., Bourada, F., Bousahla, A. A., & Tounsi, A. (2020). A new innovative 3-unknowns HSDT for buckling and free vibration of exponentially graded sandwich plates resting on elastic foundations under various boundary conditions. *Geomech Eng, 22*(2), 119–132.

[51] Matouk, H., Bousahla, A. A., Heireche, H., Bourada, F., Bedia, E. A., Tounsi, A., & Benrahou, K. H. (2020). Investigation on hygro-thermal vibration of P-FG and symmetric S-FG nanobeam using integral Timoshenko beam theory. *Adv Nano Res, 8*(4), 293–305.

[52] Hassan, A. H. A., & Kurgan, N. (2019). Modeling and buckling analysis of rectangular plates in ansys. *Int J Eng Appl Sci, 11*(1), 310–329. [CrossRef]

[53] Liu, Y., & Glass, G. (2013, April 16-18). *Effects of mesh density on finite element analysis*. SAE Tech Pap, Detroit, USA. [CrossRef]

[54] More, S. T., & Bindu, R. S. (2015). Effect of mesh size on finite element analysis of plate structure. *Int J Eng Sci Innov Technol, 4*(3), 181–185.

[55] ANSYS Inc. (2024). Gain greater engineering and product life cycle perspectives: 2024 product releases & updates. *ANSYS 2024 R1*. Canonsburg, PA. https://www.ansys.com/products/release-highlights

[56] Singha, M. K., Prakash, T., & Ganapathi, M. (2011). Finite element analysis of functionally graded plates under transverse load. *Finite Elem Anal Des, 47*(4), 453–460. [CrossRef]

[57] Delale, F., & Erdogan, F. (1983). The crack problem for a nonhomogeneous plane. *ASME J Appl Mech, 50*(3), 609–614. [CrossRef]

[58] ANSYS Mechanical APDL Element Reference. (2013). *Mechanical APDL element reference*. Pennsylvania: ANSYS Inc.

Journal of Sustainable Construction Materials and Technologies
Web page info: https://jscmt.yildiz.edu.tr
DOI: 10.47481/jscmt.155516

JSCMT
Journal of Sustainable Construction Materials and Technologies

Research Article

High temperature performance of geopolymer: Contribution of boron tincal waste

Zinnur ÇELİK[1], Emrah TURAN*[2], Meral OLTULU[2]

[1]*Atatürk University, Pasinler Vocational School, Erzurum, Türkiye*
[2]*Department of Civil Engineering, Atatürk University Faculty of Engineering, Erzurum, Türkiye*

ARTICLE INFO

Article history
Received: 19 July 2024
Revised: 31 August 2024
Accepted: 01 September 2024

Key words:
Boron, geopolymer, high temperature, tincal waste, strength

ABSTRACT

The world's largest boron deposits are in Türkiye, Russia, and the U.S.A. Türkiye holds about 73% of the world's reserves of oil. The tincal mineral accounts for approximately 25.3% of Türkiye's boron reserves. Annually, around 900,000 tons of boron-derived waste are produced to obtain 1 million tons of borax pentahydrate from the tincal mine. This waste is stored in pools, causing considerable environmental issues. This study investigates the potential use of tincal waste, an environmental problem, in cement and concrete applications. Tincal waste (T.W.) was utilized to produce geopolymer mortar. Geopolymer samples were created by replacing ground blast furnace slag (G.B.F.S.) with 10%, 20%, 30%, and 40% tincal waste (T.W.) by weight. The mixture samples were cured at room temperature and 60 °C. After curing, the samples were exposed to high temperatures of 200 °C, 400 °C, and 600 °C. The samples' unit weight, compressive strength, ultrasonic pulse velocity (U.P.V.), and mass loss values were measured. A mathematical model was also developed to describe the relationship between compressive strength and U.P.V. before and after high temperatures. The samples underwent Fourier Transform Infrared Spectroscopy (FTIR) microstructural analysis. The results showed that using up to 20% T.W. enhanced the properties of the samples before and after high-temperature exposure. A strong correlation was found between compressive strength and U.P.V. These findings suggest that T.W. has potential as a novel material for use in geopolymer technology.

Cite this article as: Çelik, Z., Turan, E., & Oltulu, M. (2024). High temperature performance of geopolymer: Contribution of boron tincal waste. *J Sustain Const Mater Technol*, 9(3), 255–267.

1. INTRODUCTION

Global warming and climate change are recognized worldwide as significant environmental problems of our time [1]. CO_2 emissions are among the most important reasons for this situation. Literature studies report that an essential part of the CO_2 emission occurs during the production phase of O.P.C. [2–4]. It has been reported that producing O.P.C., the primary material for concrete and mortar production, contributes to approximately 5–7% of CO_2 emissions [5]. For decades, researchers have made efforts to reduce the CO_2 load on the planet by producing environmentally responsible concrete, using additional supplementary materials in concrete production [6]. However, supplementary cement materials can partially replace O.P.C., usually 20–30% by weight, due to their adverse effects on concrete workability and early age strength [7].

Geopolymer composites were first named by Davidovits in 1978. The primary material of these three-dimensional amorphous products is aluminosilicates [8, 9]. Geopolymeric cement is called green material because it reduces CO_2 emissions by about 6 times compared to O.P.C., which provides

*Corresponding author.
*E-mail address: emrah.turan@atauni.edu.tr

large energy consumption and carbon dioxide emissions in its production [10]. In addition, geopolymers are an essential part of inorganic polymeric materials with their superior mechanical and thermal properties, low permeability, prominent high-temperature resistance, excellent chemical corrosion resistance, and low density [11–14]. For these reasons, geopolymers in recent years offer an excellent opportunity to replace O.P.C. as cementitious binder material [15]. Recently, geopolymers have been used in ceramics exposed to high temperatures, in coatings, binders, and adhesives for heat-resistant building materials, and as cementing components of concrete and mortar [16]. The most common geopolymers used nowadays are obtained by activating alumino-silicate materials such as fly ash (F.A.), metakaolin, and granulated blast furnace slag (G.B.F.S.) using alkalis such as sodium hydroxide (NaOH), potassium hydroxide (K.O.H.) and sodium silicate (Na_2SiO_3) [17]. The development of mechanical performance in geopolymers depends on the formation of three-dimensional networks consisting of Si-O-Al and Si-O-Si units and the obtained calcium aluminate silicate hydrate (C-A-S-H) and sodium aluminate silicate hydrate (N-A-S-H) gels which depends on the binder composition, curing temperature, activator type and concentration [18–20]. In alkali-aluminosilicate (A.A.S.), calcium-bearing C-(A)-S-H gels predominate with N-A-S-H gels [11].

OPC-based concrete and mortars have low thermal conductivity and are known as non-combustible building materials [21]. Although concrete produced with O.P.C. has significant resistance to high temperatures, $Ca(OH)_2$ decomposes at approximately 400 °C. This phenomenon causes substantial decreases in the strength of OPC-based concrete at temperatures above 400 °C [22, 23]. Geopolymers are considered to have good high-temperature resistance due to their ceramic-like properties [24]. Moreover, the different nature of the hydration products formed in O.P.C. and A.A.S. is the reason for the significant difference in the elevated temperature resistance of geopolymer and regular concrete [25–27]. Guerrieri et al. [28] investigated the residual compressive strength of A.A.S. and O.P.C. paste after being subjected to high temperatures. The study indicates that the residual strength of A.A.S. exposed to 600 °C is similar to O.P.C. Contrary to this study, Türker et al. [29] reported in their research that A.A.S. exposed to 600 °C lost more strength than the O.P.C. specimen. Pan et al. [27] observed the post-high temperature strength values of alkaline activated materials containing G.B.F.S. and Class F F.A. An increase in strength was observed in FA-based samples after 600 °C.

On the contrary, significant decreases in strength occurred in GBFS-based samples at 300 °C compared to O.P.C. binder-based samples. These strength differences reveal substantial differences in the bonding structures of different binder materials at high temperatures. The better behavior of F.A. after high temperature compared to G.B.F.S. was due to the binding phase, N-A-S-H. In recent years, high-temperature performances have been investigated by adding materials such as red mud [30], ferrochrome slag [31, 32], rice husk ash [33] to F.A. and G.B.F.S. based mixtures, as well as the combined use of F.A. and G.B.F.S. binders.

Approximately 73% of the world's stock on reserves is in Türkiye. Türkiye's most important boron ores are tincal, ulexite, and colemanite. The most essential components of boron compounds are boron oxide (B_2O_3) and boric acid (H_2BO_3). These components are called colemanite when bound with calcium, ulexite when bound with calcium-sodium, and tincal when present with sodium [34]. 25.3% of the boron reserve in Türkiye is tincal ore and is located in the Eskişehir Kırka region. To obtain 1 million tons of borax pentahydrate ($Na_2O.\ 2B_2O_3.\ 5H_2O$) from the Tinkal mine, approximately 900000 tons of solid boron derivative waste is generated annually. These wastes are stored in pools and cause significant environmental problems [35–38]. Tinkal waste (T.W.) has been used in many fields, such as ceramics, insulation, and construction, since the 20th century. The use of tincal ore waste as an additional supplementary material in ordinary cement is available in the literature. Kula et al. [39] investigated the usability of T.W., C.B.A., and F.A. as additional cement materials in concrete. Abali et al. [35] studied using tincal waste as a supplementary cement material. As a result, it was stated that as the tincal waste rate increased, the 2-day compressive strength decreased, but at the end of 28 days, the strength approached the reference sample. Boncukcuoğlu et al. [40] used the sieve wastes obtained during borax production from tincal as an additive in the production of O.P.C. They investigated the mechanical properties of the doped O.P.C. Within the scope of the research. It was stated that using 25% by weight of sieve waste as cement additive material would be appropriate.

This study focuses on using tincal ore waste in GBFS-based geopolymer mortars. For this purpose, compressive strength and ultrasonic pulse velocity (U.P.V.) tests were conducted on the 3rd, 7th, and 28th days on geopolymer mortars obtained by replacing G.B.F.S. with tincal waste at rates of 10%, 20%, 30%, and 40%. The prepared mortar samples were either kept at ambient conditions or cured in an oven at 60°C for 24 hours and then kept at ambient conditions until the test day. The produced specimens were subjected to temperatures of 200, 400, and 600°C, and mass loss, compressive strength, and U.P.V. values were investigated. Additionally, a mathematical model was created between compressive strength and U.P.V. before and after high temperature, and the microstructure of the samples was analyzed using FTIR.

1. MATERIALS AND METHODS

1.2. Materials

Within the scope of this research, G.B.F.S. and F.A. were used as binder materials in the reference mixture. G.B.F.S. material was supplied from the Ereğli Iron and Steel Factory, and F.A. material was provided from Çatalağzı power plant. The specific gravity of F.A. and G.B.F.S. are 2.33 and 2.86, and the specific surface area is 2475 cm^2/g and 3824 cm^2/g, respectively. Since the total $SiO_2 + Al_2O_3 + Fe_2O_3$ in the F class F.A. chemical composition is 87.36% and the amount of CaO is 2.44%, it complies with ASTM C 618 [36]. SiO_2/Al_2O_3 by mass of F.A. and G.B.F.S. are 2.91 and

Table 1. Chemical compositions of G.B.F.S., F.A., and T.W.

Oxide (%)	SiO_2	Al_2O_3	Fe_2O_3	CaO	MgO	Na_2O	SO_3	B_2O_3	LOI
GBFS	33.60	11.40	1.10	41.20	6.10	0.40	2.10	–	1.05
FA	60.61	20.81	7.36	2.44	1.64	0.56	0.51	–	2.71
TW	14.12	2.03	0.76	15.87	22.19	8.12	0.53	9.83	23.26

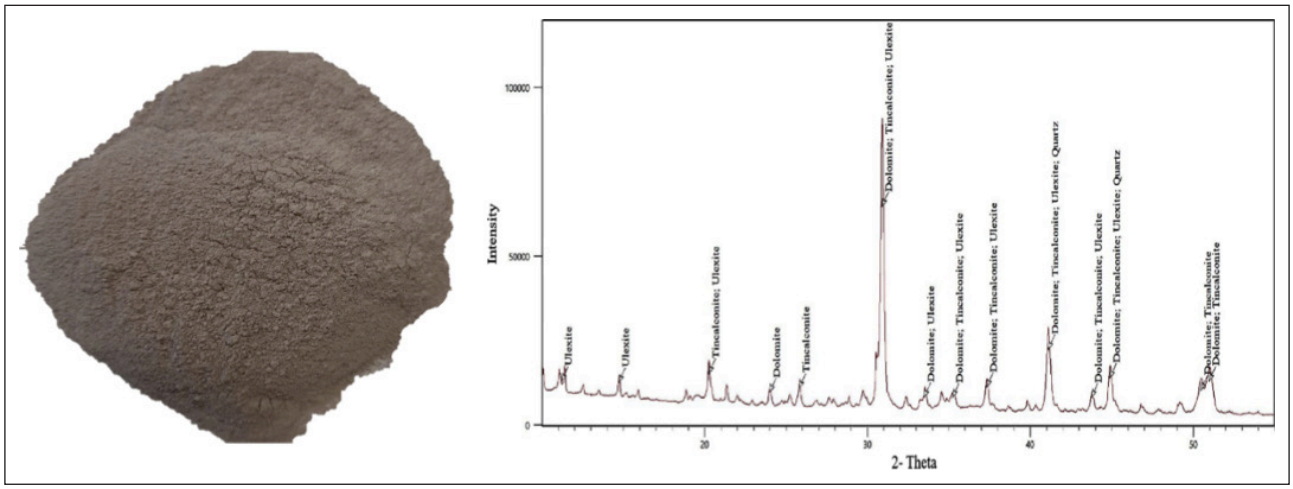

Figure 1. Image and XRD pattern of tincal waste [36].

2.95, respectively. Additionally, tincal waste (T.W.) used in this study was obtained from the Etibank Borax Plant (Kirka, Eskisehir). The specific gravity of tincal waste is 2.48, and the B.E.T. surface area is 65000 cm^2/g. The chemical properties of G.B.F.S., F.A., and T.W. are given in Table 1. According to XRF results (Table 1), the most dominant compounds in the tincal waste sample are magnesium oxide, quartz, and calcium oxide.

The XRD spectrum of tincal waste is shown in Figure 1. The most dominant phases observed in the XRD pattern are dolomite, tincal, quartz, and ulexite.

River sand with the largest grain size of 4 mm and a specific gravity of 2.70 was used to prepare geopolymer mortar samples. The study used sodium hydroxide (NaOH) and sodium silicate (Na_2SiO_3) solution as alkaline activators. The silicate modulus in sodium silicate was equal to 3.18. NaOH solution with a concentration of 12 M, prepared 24 hours in advance, was used to prepare the mixtures. The chemical properties of alkaline activators are given in Table 2.

Table 2. Chemical properties of Na_2SiO_3 and NaOH

Properties	Sodium silicate (Na_2SiO_3)	Sodium hydroxide (NaOH)
Density (g/cm^3)	1.38	2.13
Molecular weight (g/mol)	122.1	40
Color	White	White
pH		13–14
Na_2O (%)	8.9	
SiO_2 (%)	28.3	
H_2O (%)	64.3	

2.2. Mixture Proportions and Test Methods

The mixing ratios of geopolymer mortar samples are given in Table 3. The sand: binder: alkali solution ratio in geopolymer mortar mixtures was 3:1:0.50. Na_2SiO_3 / NaOH solution ratio 2. G.B.F.S. replaced T.W. by 0%, 10%, 20%, 30% and 40%. G.B.F.S., T.W., and F.A. were mixed for 90 s during the mortar preparation. After the first mixing process, 12 M NaOH solution and Na_2SiO_3 prepared the day before were added to the mixture and mixed for another 3 min. Finally, river sand was added to the mixture, and after mixing for another 4 minutes, the mortar was prepared. The prepared mortar mixtures were filled into 50 x 50 x 50 cube samples, and vibration was applied. A group of cube samples prepared by filling molds was kept in ambient cure until the test day. The other group was cured in a laboratory oven at 60 °C for 24 hours. After the specimens were cured for 24 hours, they were stored at room conditions until the test day. The compressive strengths of the samples in both cure groups on the 3rd, 7th, and 28th days were determined according to ASTM C109 [38]. Additionally, U.P.V. and dry unit weights on the 28th day were determined. All mixture series were exposed to 200, 400, and 600 °C temperatures in the oven with a temperature regime of 5 °C/min for 28 days [41]. Compressive strength, U.P.V. value, and mass losses of the mixtures after high temperature were determined.

3. RESULTS AND DISCUSSION

3.1. Dry Unit Weight

The effects of T.W., ambient curing (20 °C), and heat curing (60 °C) for 28 days on the unit weight of the geopolymer mortar specimen are presented in Figure 2. The

Table 3. Mixing ratios of geopolymer mortars

Specimen codes	G.B.F.S. (g)	T.W. (g)	F.A. (g)	Sand (g)	Na_2SiO_3 solution (g)	NaOH solution (g)
Control	405		45	1350	150	75
TW-10	360	45	45	1350	150	75
TW-20	315	90	45	1350	150	75
TW-30	270	135	45	1350	150	75
TW-4	225	180	45	1350	150	75

unit weights of the samples kept in the ambient cure ranged from 2120 to 2223 kg/m^3. The lowest unit weight value was obtained from the TW-40 series, and the highest was obtained from the TW-10 series. Substitution of 10% and 20% T.W. increased the unit weights by 2.82% and 1.94%, respectively, compared to the reference sample. Unit weights were decreased as the T.W. ratio increased to 30% and 40%.

The unit weights of the samples cured at 60 °C ranged between 2138 and 2250 kg/m^3. Similar to the samples in ambient cure, the highest unit weight was calculated in the TW-10 series with 2250 kg/m^3. This value was 2.74% higher than the control sample. The unit weight of the TW-40 mixture was approximately 2.34% less than the control sample. The values obtained from heat curing were higher than those obtained in the ambient cure. This can be attributed to heat curing accelerating the hydration reaction and higher bulk density. In the control and TW-10 series, 1.30% and 1.21% increase in unit weights was calculated as the curing rate increased by 60 °C compared to the ambient cure.

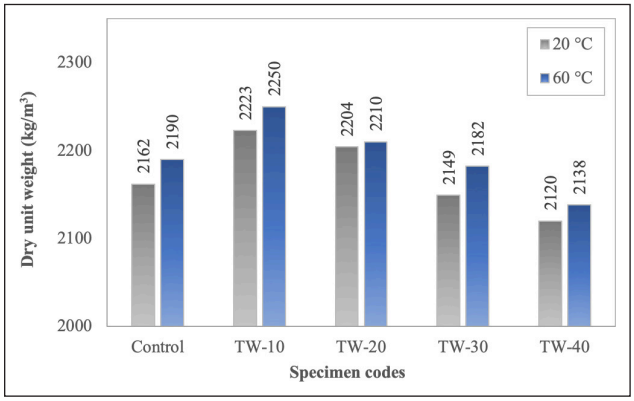

Figure 2. Dry unit weight of geopolymer mortars.

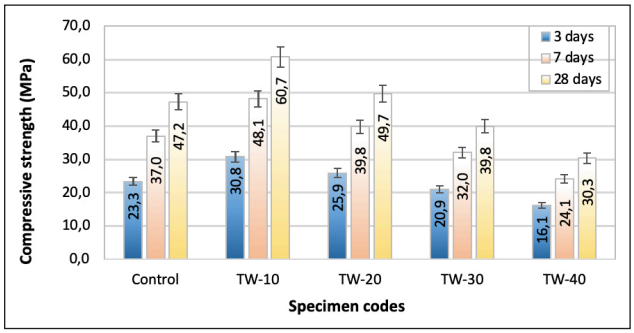

Figure 3. Compressive strength of specimens cured at ambient temperature.

3.2. Compressive Strengths

3.2.1. Curing at Ambient Temperature

The compressive strength test results of the mixtures at ambient temperature conditions on 3, 7, and 28 days are given in Figure 3. The 3 days compressive strength of the mixture samples varies between 16.09 MPa and 30.75 MPa. The highest 3-day compressive strength was obtained from the TW-10 series with 30.75 MPa. As a result of increasing curing time, compressive strength improved significantly. The highest 7-day compressive strength was obtained in the mortar mixture using 10% T.W. An improvement of 30.25% and 7.65%, respectively, was detected in the compressive strengths of mixtures using 10% and 20% T.W. compared to the control specimen.

The strength results of the mixtures on the 28th day were also compatible with the 3 and 7-day strength values. The strength results on the 28th day showed that the mixtures varied between 30.30 MPa and 60.70 MPa. The highest compressive strength value was detected in the TW-10 series. According to the reference mixture, substituting 10% T.W. increased the strength by 28.60%. Although mixtures containing 30% and 40% T.W. showed a particular strength improvement, their performance was lower than the control sample. Compared to the control mixture, a decrease of 15.67% and 35.8% was achieved in the compressive strengths obtained from the TW-30 and TW-40 series. As a result, 10% and 20% T.W. substitution increased the series' strength at all ages. This increase in compressive strength can be attributed to the development of geopolymerization and the production of additional sodium aluminosilicate hydrate (NASH) gel due to the Na_2O contained in T.W. Additionally, unlike G.B.F.S., which is high in calcium, T.W. contains high amounts of magnesium. This is one of the most critical factors causing the improvement in compressive strength, attributable to the high magnesium content, which behaves similarly to calcium and forms a new hydrate gel called a hydrotalcite-like phase or magnesium-containing silicate hydrates M-S-H and C-M-S-H [42, 43]. Bouaissi et al. [42] produced geopolymer mortars using different substitutes of high magnesium nickel slag (H.M.N.S.), F.A. and G.B.F.S. The research reported that the 14-day compressive strength of mixtures containing 10% H.M.N.S. increased by 29% compared to the reference series. Zhang et al. [43] stated that the strength of geopolymer mortars is 20% and 40% H.M.N.S. Replacement was higher

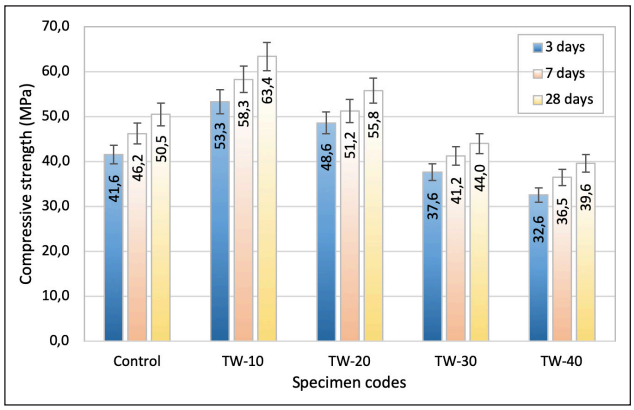

Figure 4. Compressive strength of specimens heat curing at 60° C.

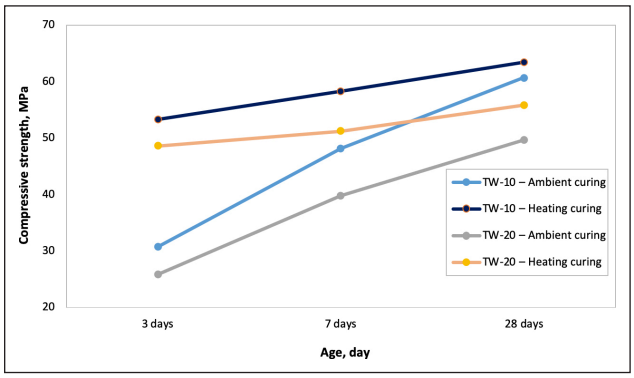

Figure 5. Effect of room temperature and heat curing on TW-10 and TW-20 series.

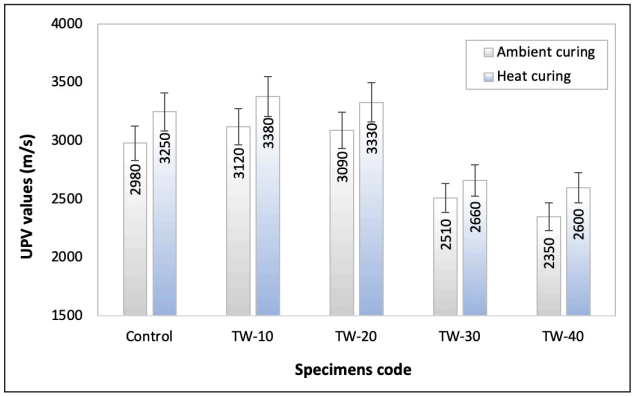

Figure 6. Ultrasonic pulse velocity values of geopolymer mortars.

than the mixture containing 100% FA. Ben Haha et al. [44] stated that slag containing high amounts of MgO increases the formation of a hydrotalcite-like phase due to hydration and reduces Al uptake by C-S-H. Uysal et al. [45] investigated using colemanite, another type of boron mineral, to produce geopolymer mortar. As a result of the study, it was determined that the use of 10% colemanite waste increased the compressive strength by 2.02%, while its substitution at 20% decreased the strength by 20.74%.

3.2.2 Heat Curing at 60 °C

Compressive strength data of specimens heat cured at 60° C are presented in Figure 4. 3 days of compressive strength of mortars ranged between 32.56 and 53.32 MPa. The highest strength value was obtained from the TW-10 series, with an increase of approximately 28.32% compared to the control specimen. Curing at 60°C remarkably affected the strength of mortars containing G.B.F.S. and T.W at an early age. The 3-day compressive strength of specimens cured at high temperatures was higher, in the range of approximately 73%–102%, compared to specimens cured at ambient temperature. Görhan et al. [46] stated that high-temperature curing did not have a remarkable effect on the physical properties of geopolymer mortars but caused an increase in compressive strength. There was an increase in strength as the cure period increased to 7 days. While the highest compressive strength was calculated from the TW-10, the lowest strength value was observed in the TW-40 series. Using 10% and 20%, T.W. improved the compressive strength by about 26% and 10.8%, compared to the control mixture.

The 28-day strength of mixtures cured at 60 °C gave similar results to the three and 7-day strengths. The highest 28-day strength result was observed in the TW-10 series, with 63.40 MPa. This value was 25% higher than the control specimen. It was observed that 30% and 40% T.W. substitution reduced the compressive strength by 12.87% and 21.58%, compared to the reference mixture. According to the results of these studies, it can be reported that the 28-day strength of specimens kept at room temperature approaches the results of samples cured at 60 °C (Fig. 5). This result is consistent with the results of previous studies in the literature [47]. It was determined that the compressive strength of heat-cured specimens after 28 days varied between approximately 4% and 30% compared to specimens cured at ambient temperature.

3.3. Ultrasonic Pulse Velocity (U.P.V.)

Ultrasonic pulse velocity test (U.P.V.) is a non-destructive testing method to examine the homogeneity of the geopolymer mortar matrix and the presence of any defects. U.P.V. results of geopolymer mortars at 28 days are given in Figure 6. U.P.V. values of 10% and 20% T.W. mixture mortars increased compared to the control sample in ambient and Heat cured. The U.P.V. value of the ambient cured TW-10 series was 4.69% higher than the control mixture. This value is determined as 4% in the heat-cured TW-10 series. As the T.W. ratio in the mixtures increased, U.P.V. values tended to decrease, similar to the compressive strength results. The velocity values of the 30% T.W. substituted mortar series after curing with the environment, and Heat decreased by approximately 15% and 18% compared to the reference specimen.

3.4. FT-IR Analysis

Fourier transform infrared spectroscopy (FTIR) is an effective method to detect the presence of chemical bonds and products formed during geopolymerization. FTIR spectra of geopolymer mortars are given in Figure 7. The broad band centered at 3360 cm^{-1} arises from the overlap of symmetric

Table 4. Changes of geopolymer mortars subjected to ambient cured after elevated temperature

Specimen code	Change in compressive strength, %			Change in U.P.V., %		
	200 °C	400 °C	600 °C	200 °C	400 °C	600 °C
Control	-3.60	-22.03	-49.36	-12.75	-29.53	-62.42
TW-10	-2.14	-17.13	-43.00	-6.41	-27.56	-59.62
TW-20	-6.44	-12.27	-47.69	-9.39	-28.16	-61.17
TW-30	-13.07	-27.39	-43.47	-12.35	-23.51	-60.96
TW-40	-24.75	-47.85	-68.32	-14.89	-31.91	-67.66

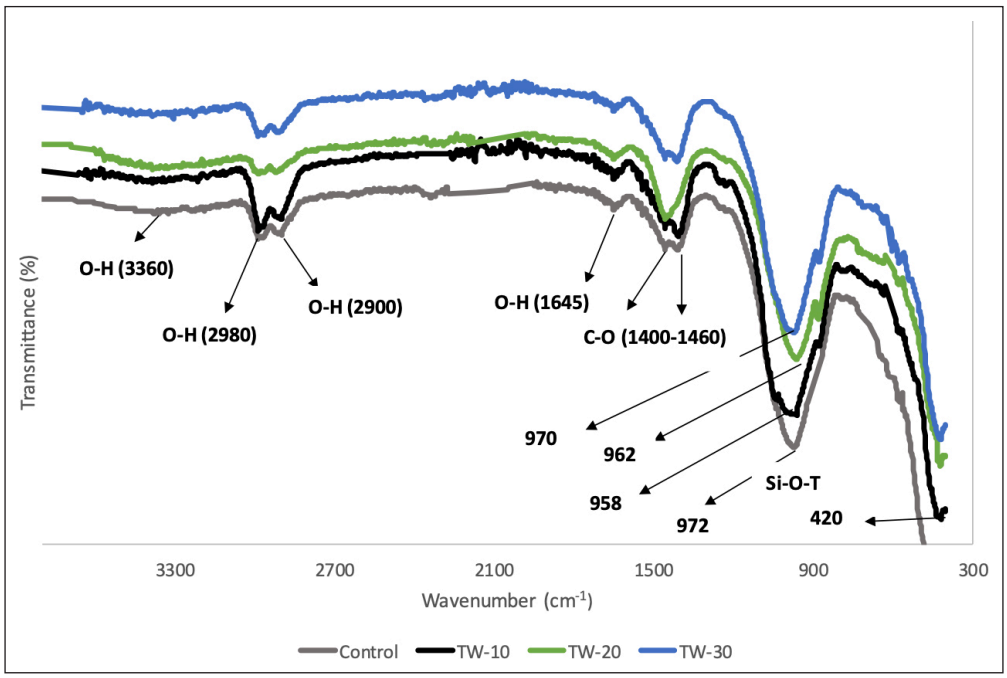

Figure 7. FTIR spectra of geopolymer mortars.

and asymmetric stretching of the O-H bending of absorbed water in the bands at 3300–3600 cm^{-1} [42, 43]. The peak of the wave number at 2980 cm^{-1} indicates the stretching vibration of the hydrogen-bonded O-H group, and the peak at 2900 cm^{-1} indicates the bending vibration of the O-H group [44, 45]. O-H bending vibrations associated with hydrated products are represented by the band determined at approximately 1645 cm^{-1}. These O-H groups refer to structural and entrapped water in sodium aluminosilicate (N-A-S-H) gels [44, 48]. The peaks at 1460 and 1400 cm^{-1}, which characterize the stretching vibration of the C-O bond, are associated with sodium bicarbonate (Na_2CO_3) [47, 49, 50].

Approximately 958–972 cm^{-1} bands are an essential point of the geopolymer, showing the asymmetric stretching vibration of the Si-O-T (T=Al or Si) bond. With the addition of T.W. to geopolymer mortars, the reference sample's 972 cm^{-1} Si-O-T stretching vibration was determined as 958 cm^{-1} and 962 cm^{-1} from the TW-10 and TW-20 series, respectively. Shifts in this band cause geopolymerization acceleration, structure strengthening, and strength improvement [48]. This shift in Si-O-T asymmetric vibration can be attributed to incorporating Al and Mg into the content of silicate hydrate gels [43].

As a result of the use of materials containing high amounts of MgO in geopolymer production, it has been proven in previous studies that Mg^{2+}, such as Al^{3+}, can replace Si^{4+} and the formation of gels such as Na-Al (Mg)-Si-O-H [43, 51]. Moreover, the formation of a broad band with a strong shoulder of approximately 860 cm^{-1} with the addition of T.W., except for the reference sample, indicates the sizeable stretching area of the O-Si bond resulting from the addition of Mg to the silicate network [43, 52]. Another indication of Mg presence can be associated with the band vibration at approximately 420 cm^{-1} [53]. Mg^{++} content in the geopolymeric chain contributes to the matrix's chemical stability or interatomic bonding by forming different connections, such as Si-O-Mg, Si-O-Al, Ca-O-Si, and Si-O-Si [42].

3.5. Properties After Elevated Temperature Exposure

The compressive strength results of geopolymer mortars subjected to ambient cured after high temperature are shown in Figure 8, and the compressive strength and U.P.V. changes are given in Table 4.

The compressive strengths of control, TW-10, and TW-20 mixtures cured in the ambient did not show a remarkable decrease at 200 °C. As a result of exposure of the reference

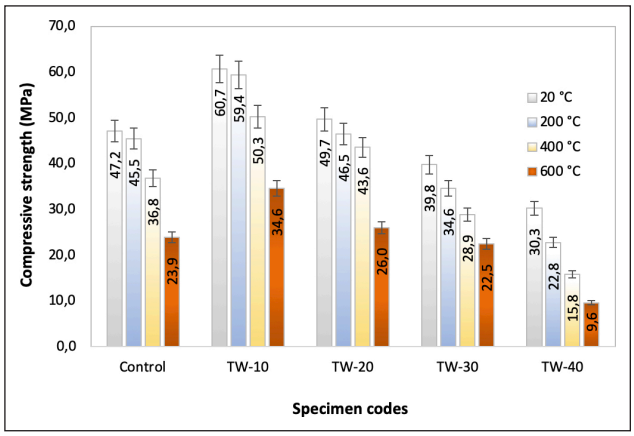

Figure 8. Compressive strengths of mortar samples in ambient cured after high temperature.

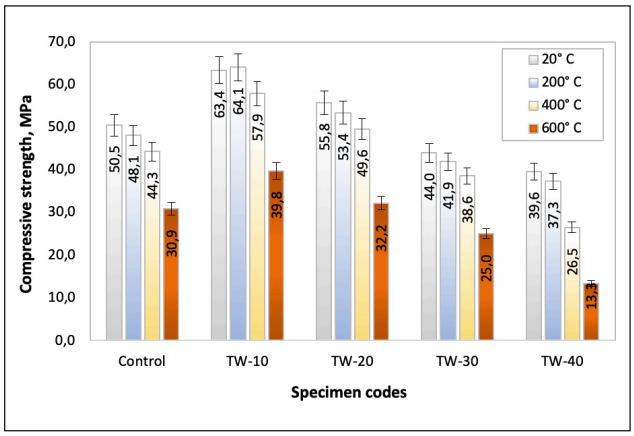

Figure 9. Compressive strength of heat-cured mortar samples after high temperature.

specimen kept in ambient cured to 200 °C, there was a 3.60% decrease in compressive strength. The lowest reduction of compressive strength at 200 °C was obtained from the TW-10 series with 2.14%. As the T.W. ratio used in the mixtures increased to 30% and 40%, a decrease of 13.07% and 24.75% in strength was observed, respectively. The compressive strength of geopolymer mortar specimens subjected to ambient curing tended to decrease as the temperature increased. In their study, Zhang et al. [54] reported that geopolymer mortars' flexural and compressive strengths increased at 100 °C and decreased with increased temperatures.

As the temperature increased to 400 °C, the decreases in strength became more evident. The compressive strength of the control sample decreased by 22.03%. The reduction in strength of mixtures using 10% and 20% T.W. was determined as 17.13% and 12.27%, respectively. Although the decreases in the strength of TW-10 and TW-20 were lower compared to the reference sample, the strength losses increased with the increase in the T.W. ratio. The reduction in strength of geopolymer mortar samples exposed to 600 °C ranged from 43.00% to 68.32%. The decrease in strength of the control sample was determined as 49.36%. Substitution of 40% T.W. reduced the strength at 600 °C by 68.32% compared to the initial strength. This is because when geopolymer mortars were exposed to high temperatures, the free water in the matrix evaporated, and the strength decreased due to dehydration [55–58]. Evaporation in the matrix increased with the increase in temperature, causing internal pressure. After the internal pressure reached a specific limit, the resistance of the composite to thermal effects decreased, causing cracks on the surfaces.

Moreover, high temperatures created thermal mismatches by creating microcracks at the interface transition area between aggregate and paste [58, 59]. However, the decrease in the strength of the mixtures using 10%, 20%, and 30% T.W. at 600 °C was less than the reference specimen. The least strength loss was reported in the TW-10 series, at 43%. Geopolymers are believed to have excellent bonding ability due to the formation of a three-dimensional N-A-S-H type gel, which is a network [Q^4(Al)] composed of SiO_4 and AlO_4 tetrahedral, which form a bonding structure between each other with shared O atoms. This structure gives geopolymer mortars significant high-temperature resistance [27, 60]. The T.W. used in this study contains Na_2O. This component may have formed an additional N-A-S-H structure in the geopolymer mortar structure. This may be one of the reasons why the high-temperature resistance of mixtures containing T.W. loses less strength compared to the reference sample.

Additionally, Lee et al. [61] investigated the effect of G.B.F.S. addition on the structure of FA-based geopolymers. They reported that the C-(A)-S-H structure formed in mixtures containing G.B.F.S. is vulnerable to thermal structure degradation. Contrary to this situation, the increase in the high-temperature resistance of the mixtures in this study can be attributed to the addition of T.W. producing the N-A(M)-S-H gel phase by containing high amounts of Mg. Yang et al. [62] stated that F.A. mixtures with nickel slag containing high amounts of magnesium produced N-A(M)-S-H, which improved the mixtures' thermal stability. However, they reported that the mechanism causing this situation is still unclear.

The U.P.V. results of the mortars are presented in Table 4. The reduction in U.P.V. values of the specimens was between 6.41% and 14.89% at 200 °C. The lowest loss in U.P.V. value was obtained in the TW-10 series, similar to the results in compressive strength. Additionally, using 10% and 20%, T.W. caused less decrease in U.P.V. values compared to the control sample. The reduction in U.P.V. results continued as the temperature increased to 400 °C. While the reduction of the reference sample was 29.53%, the decrease in the TW-10 and TW-20 series was calculated as 27.56% and 28.16%. As the temperature increased to 600 °C, a significant decrease was observed in the U.P.V. values of geopolymer mortars. 10% and 20% T.W. substitution reduced U.P.V. values by 59.62% and 61.17%. This rate was measured as 62.42% in the reference sample. Although there is a proportional difference between compressive strength and U.P.V. results, they are similar in trend.

The compressive strength results of geopolymer mortars subjected to Heat cured after high temperature are shown in Figure 9, and the compressive strength and U.P.V. changes

Table 5. Changes of geopolymer mortars subjected to Heat cured after elevated temperature

Specimen code	Change in compressive strength, %			Change in U.P.V., %		
	200 °C	400 °C	600 °C	200 °C	400 °C	600 °C
Control	-4.75	-12.28	-38.81	-11.08	-27.38	-59.38
TW-10	1.10	-8.68	-37.22	-5.33	-25.44	-57.10
TW-20	-4.30	-11.11	-42.29	-8.11	-24.92	-57.06
TW-30	-4.77	-12.27	-43.18	-8.27	-21.80	-49.62
TW-40	-5.81	-33.08	-66.41	-9.23	-26.92	-63.08

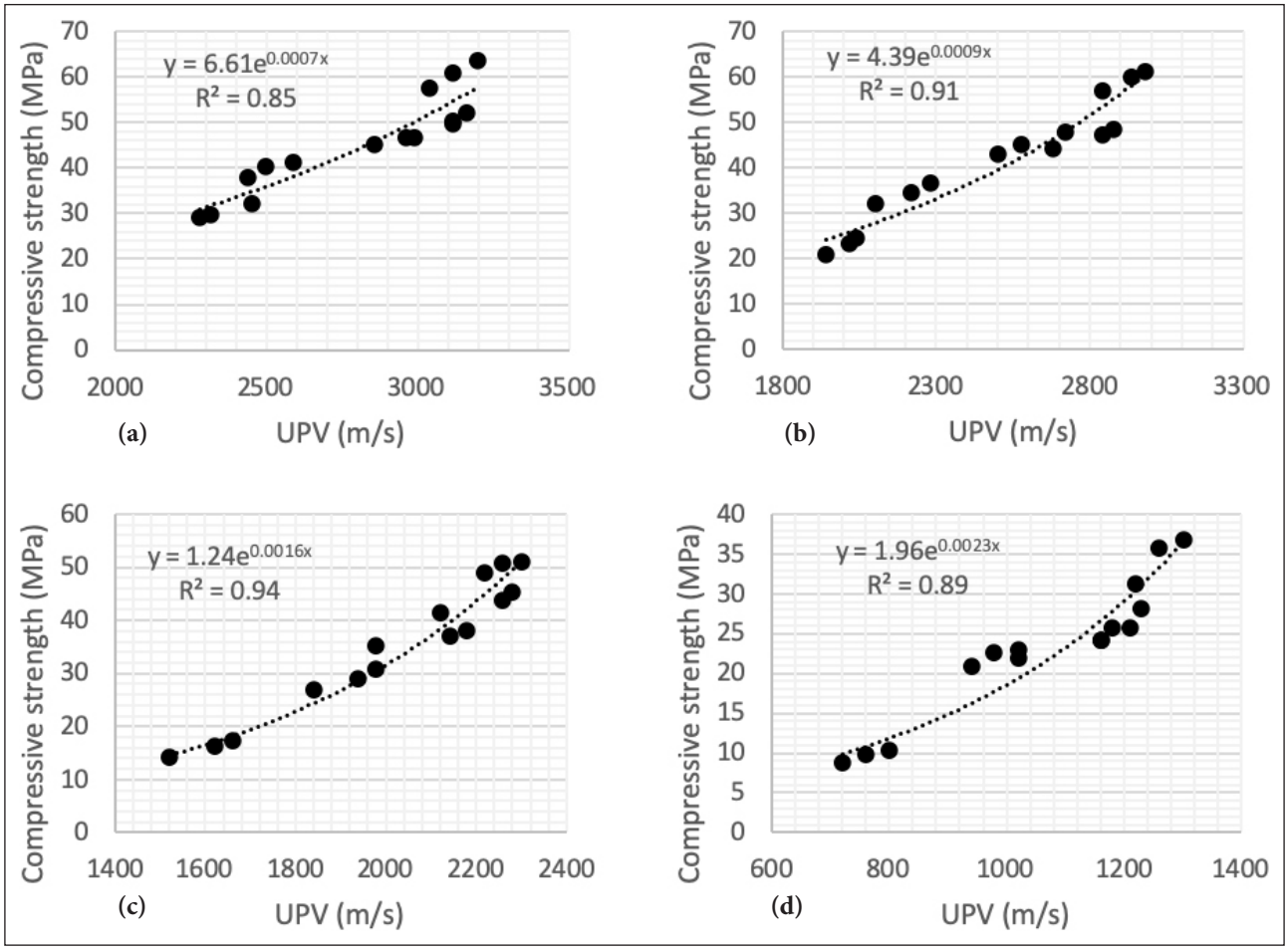

Figure 10. Compressive strength and U.P.V. relationship of samples kept in ambient cured **(a)** before high-temperature **(b)** after 200 °C temperature **(c)** after 400 °C temperature **(d)** after 600 °C temperature.

are shown in Table 5. Except for the TW-10 mixture, decreases in strength were detected at 200 °C for all mixtures cured at 60 °C. At 200 °C, a change in the compressive strength of all mixture series was observed between -5.81% and 1.10%. Similar to 200 °C, the least strength decreases at 400 °C and 600 °C were obtained from mixtures with 10% T.W. replacement. Mixtures using 20% T.W. lost less strength than the control sample, similar to the TW-10 series. The weakest performance at all temperatures was observed in the TW-40 series. In this series, as the temperature increased from 200 to 600 °C, the compressive strength decreased from 5.81% to 66.41%. Heat-cured mixtures gave approximately the same results as mixtures kept in ambient cured. However, the decrease in strength after high temperature in heat-cured samples was less than that in ambient cured.

The reduction in U.P.V. results of specimens cured at 60 °C was between 5.33% and 11.08% at 200 °C. As the temperature increased to 400 °C, there was a significant decrease in U.P.V. values. While the highest decrease was obtained from the control sample with 27.38%, the lowest decrease was calculated in the TW-30 series with 21.80%. At 600 °C, the reduction in U.P.V. values continued and ranged between 49.62% and 63.08%.

In their studies, [54] and [55] obtained a relationship between compressive strength and U.P.V. values based on experimental results using Equation (1) given below.

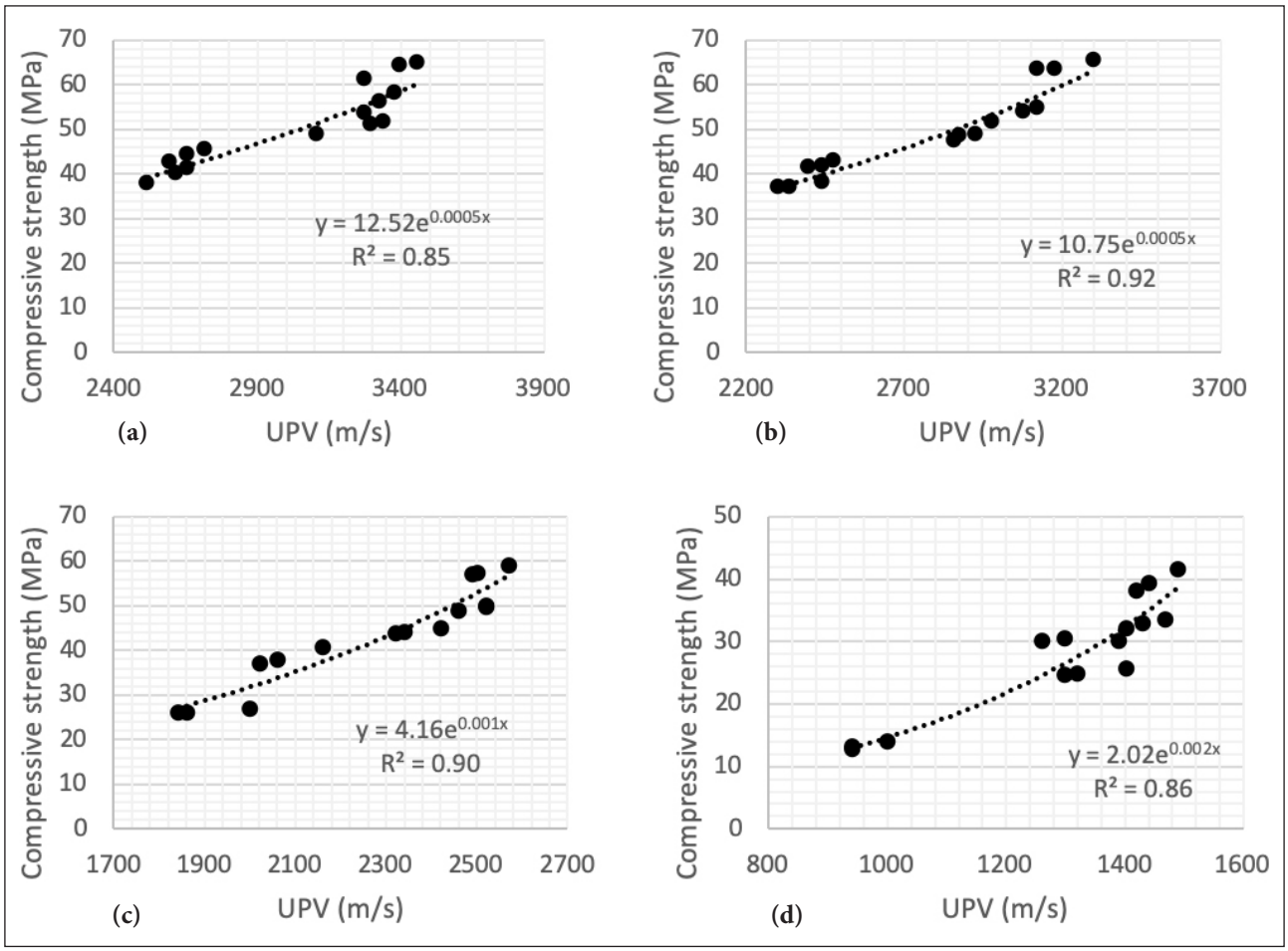

Figure 11. Compressive strength and U.P.V. relationship of samples kept in Heat cured **(a)** before high-temperature **(b)** 200 °C temperature **(c)** 400 °C temperature **(d)** 600 °C temperature.

$f_c = ae^{bV_c}$) (1)

where f_c is the compressive strength, a and b are constants, and Vc is the U.P.V. value.

The relationship between the compressive strength and U.P.V. of the specimens subjected to ambient cured before and after high temperature is given in Figure 10a–d. The relationships between compressive strength and U.P.V. were made using three specimens tested in each mixture. The coefficient of determination (R^2) of the mixture series subjected to ambient cure was approximately 0.87, 0.91, 0.96, and 0.90, respectively. The equations related to the temperature relationship at 23, 200, 400, and 600 °C are given in Equations (2), (3), (4) and (5), respectively.

$f_{c(23\ ^oC)} = 6.61e^{0.0007V_c}$ (2)

$f_{c(200\ ^oC)} = 4.39e^{0.0009V_c}$ (3)

$f_{c(400\ ^oC)} = 1.24e^{0.0016V_c}$ (4)

$f_{c(600\ ^oC)} = 1.96e^{0.0023V_c}$ (5)

The relationship between the compressive strength and U.P.V. of the samples subjected to Heat cured before and after high temperature is presented in Figure 11a–d. The coefficients of determination of heat-cured mixtures at 23, 200, 400, and 600 °C were calculated as 0.87, 0.92, 0.90 and 0.91, respectively. The following equations were determined for 23, 200, 400, and 600 °C, respectively.

$f_{c(23\ ^oC)} = 12.52e^{0.0005V_c}$ (6)

$f_{c(200\ ^oC)} = 10.75e^{0.0005V_c}$ (7)

$f_{c(400\ ^oC)} = 4.16e^{0.001V_c}$ (8)

$f_{c(600\ ^oC)} = 2.02e^{0.002V_c}$ (9)

3.5.1. Mass Loss

The mass loss results of geopolymer mortar mixture samples kept in ambient cured and subjected to high temperatures are given in Figure 12a, and the results of heat-cured samples are shown in Figure 12b. In ambient cure, control sample mass loss ranged from 5.90 to 11.86% in mixtures subjected to ambient cure. The lowest mass loss at 200 °C was obtained from the TW-10 series. The highest mass loss was calculated from thranging, ranging from 9.10% to 13.22%. Significant increases in mass losses occurred after 400 °C. The lowest loss was calculated for all estimated TW-20 series at 7.61%. At 600 °C, the mass loss of all mixtures was more than 10%. At 600 °C, mass loss ranged from 10.64 to 13.22%. The weight loss in geopolymer mortars was due to evaporation of absorption water in the temperature range of 30–210 °C, deterioration of side chains in the temperature range of 210–400 °C, and degradation of leading polymer chains at 400–500 °C. Also, weakening the bond between aggregate and paste at high temperatures increased weight losses [63, 64].

The mass losses of the samples cured at 60 °C decreased compared to those in the ambient cure. The lowest mass

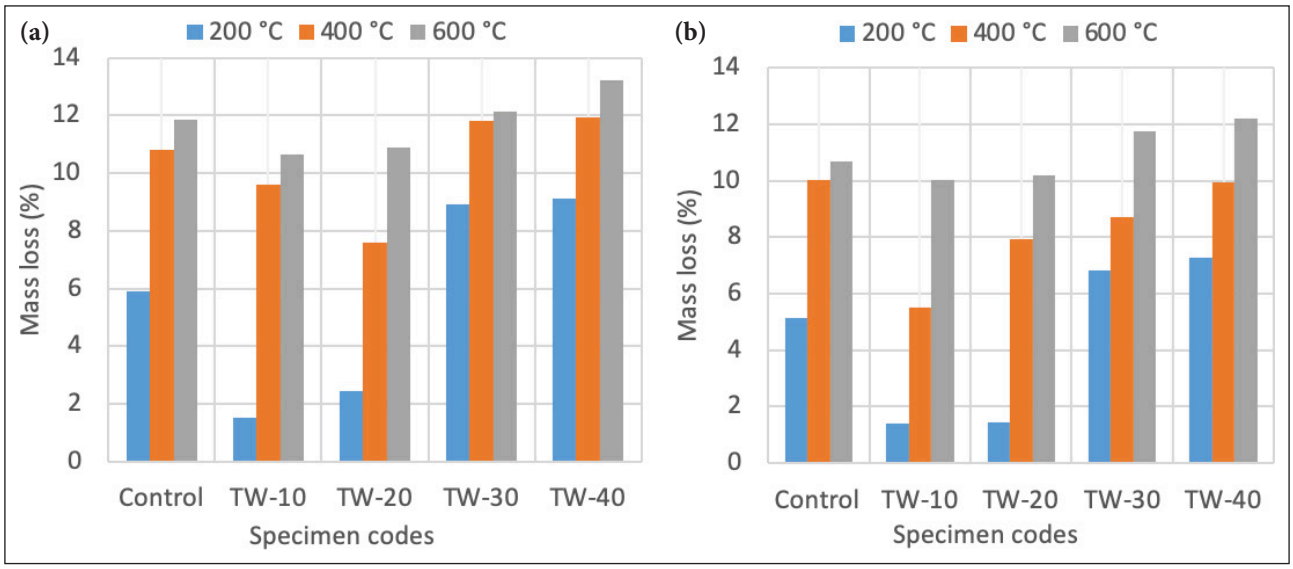

Figure 12. Mass loss of **(a)** ambient and **(b)** 60 °C cured specimens after elevated temperature.

loss at 200 °C was calculated in the TW-10 series at 1.41%. An increase in mass losses was observed with increasing temperature. At 400 °C, mass losses ranged from 5.50% to 12.20%. At 600 °C, as in other temperatures, the lowest mass loss was determined in the TW-10 series.

Within the scope of this study, the use of tincal waste in the production of geopolymer concrete, as an innovative industrial by-product that can be used both to reduce the amount of environmentally harmful waste materials and to replace cement, was examined. Study results show that T.W. is promising in geopolymer concrete production. Future studies should discuss it with different materials, curing temperatures, and alkali silicate activator ratios. In addition, both in this study and in the literature, it is clear that the microstructural properties of the N-A(M)-S-H structure, a vital gel phase especially for high-temperature resistance, require further study.

4. CONCLUSION

In this study, 10%, 20%, 30%, and 40% T.W. was replaced by slag in geopolymer production. The properties of mixtures before and after high temperatures were examined. Information about the results obtained is summarized below.

- The highest 7-day compressive strength in the ambient cured was obtained in the mortar mixture using 10% T.W. An improvement of 30.25% and 7.65%, respectively, was detected in the compressive strength of the mixtures using 10% and 20% T.W. compared to reference mixture.
- The 28th-day strength results of the samples kept in ambient cured vary between 30.30 MPa and 60.70 MPa. The highest pressure values were obtained from the TW-10 series, 28.60% higher than the control sample. Similar to the ambient cured, the highest strength in heat-cured samples was calculated in the TW-10 series.
- The difference in strength between ambient-cured and heat-cured samples at the early ages of cure decreased significantly on the 28th day.
- Using T.W. in samples kept in ambient cure increased the high-temperature resistance. TW-10 and TW-20 series were the mixture series that suffered the least compressive strength loss at 400 °C and 600 °C.
- Except for the TW-10 mixture, decreases in strength were detected at 200 °C for all mixtures at 60 °C. In specimens at 60 °C, the strength losses of TW-10 and control series at 400 °C and 600 °C were determined as 8.68%–37.22% and 12.28%–38.81%, respectively.
- The exponential relationship between compressive strength and U.P.V. before and after exposure to high temperatures, with strong R2 values, reported a sufficient approximation to compare the two.
- Similar to the compressive strength results, the least mass loss was determined in the TW-10 and TW-20 series. The mass loss of heat-cured specimens was less than that of specimens kept in ambient cure.

ETHICS

There are no ethical issues with the publication of this manuscript.

DATA AVAILABILITY STATEMENT

The authors confirm that the data that supports the findings of this study are available within the article. Raw data that support the finding of this study are available from the corresponding author, upon reasonable request.

CONFLICT OF INTEREST

The authors declare that they have no conflict of interest.

FINANCIAL DISCLOSURE

The authors declared that this study has received no financial support.

USE OF AI FOR WRITING ASSISTANCE

Not declared.

PEER-REVIEW

Externally peer-reviewed.

REFERENCES

[1] Schneider, M., Romer, M., Tschudin, M., & Bolio, H. (2011). Sustainable cement production present and future. *Cem Concr Res, 41*, 642–650. [CrossRef]

[2] Benhelal, E., Zahedi, G., Shamsaei, E., & Bahadori, A. (2013). Global strategies and potentials to curb CO2 emissions in cement industry. *J Clean Prod, 51*, 142–161. [CrossRef]

[3] He, Z., Zhu, X., Wang, J., Mu, M., & Wang, Y. (2019). Comparison of CO2 emissions from O.P.C. and recycled cement production. *Constr Build Mater, 211*, 965–973. [CrossRef]

[4] Çelik, Z. (2023). Investigation of the use of ground raw vermiculite as a supplementary cement materials in self-compacting mortars: Comparison with class C fly ash. *J Build Eng, 65*, 105745. [CrossRef]

[5] Gartner, E. (2004). Industrially interesting approaches to "low-CO2" cements. *Cem Concr Res, 34*, 1489–1498. [CrossRef]

[6] Zakka, W. P., Lim, N. H. A. S., & Khun, M. C. (2021). A scientometric review of geopolymer concrete. *J Clean Prod, 280*, 124353. [CrossRef]

[7] Bellum, R. R., Muniraj, K., Indukuri, C. S. R., & Madduru, S. R. C. (2020). Investigation on performance enhancement of fly ash-GGBFS based graphene geopolymer concrete. *J Build Eng, 32*, 101659. [CrossRef]

[8] Prud'homme, E., Michaud, E., Joussein, S., & Rossignol, S. (2012). Influence of raw materials and potassium and silicon concentrations on the formation of a zeolite phase in a geopolymer network during thermal treatment. *J Non-Cryst Solids, 358*, 1908–1916. [CrossRef]

[9] Sahin, F., Uysal, M., Canpolat, O., Cosgun, T., & Dehghanpour, H. (2021). The effect of polyvinyl fibers on metakaolin-based geopolymer mortars with different aggregate filling. *Constr Build Mater, 300*, 124257. [CrossRef]

[10] Mehta, A., & Siddique, R. (2016). An overview of geopolymers derived from industrial by-products. *Constr Build Mater, 127*, 183–198. [CrossRef]

[11] Lin, H., Liu, H., Li, Y., & Kong, X. (2021). Properties and reaction mechanism of phosphoric acid activated metakaolin geopolymer at varied curing temperatures. *Cem Concr Res, 144*, 106425. [CrossRef]

[12] Masi, G., Rickard, W. D. A., Bignozzi, M. C., & Van Riessen, A. (2015). The effect of organic and inorganic fibres on the mechanical and thermal properties of aluminate activated geopolymers. *Compos Part B Eng, 76*, 218–228. [CrossRef]

[13] Wu, Y., Lu, B., Bai, T., Wang, H., Du, F., Zhang, Y., Cai, L., Jiang, C., & Wang, W. (2019). Geopolymer, green alkali activated cementitious material: Synthesis, applications and challenges. *Constr Build Mater, 224*, 930–949. [CrossRef]

[14] Bai, T., Song, Z., Wang, H., Wu, Y., & Huang, W. (2019). Performance evaluation of metakaolin geopolymer modified by different solid wastes. *J Clean Prod, 226*, 114–121. [CrossRef]

[15] Yang, K. H., Song, J. K., & Song, K. I. (2013). Assessment of CO2 reduction of alkali-activated concrete. *J Clean Prod, 39*, 265–272. [CrossRef]

[16] Yang, T., Han, E., Wang, X., & Wu, D. (2017). Surface decoration of polyimide fiber with carbon nanotubes and its application for mechanical enhancement of phosphoric acid-based geopolymers. *Appl Surf Sci, 416*, 200–212. [CrossRef]

[17] Qaidi, S. M. A., Atrushi, D. S., Mohammed, A. S., Ahmed, H. U., Faraj, R. H., Emad, W., Tayeh, B. A., & Najm, H. M. (2022). Ultra-high-performance geopolymer concrete: A review. *Constr Build Mater, 346*, 128495. [CrossRef]

[18] Ismail, I., Bernal, S. A., Provis, J. L., San Nicolas, R., Hamdan, S., & van Deventer, J. S. J. (2014). Modification of phase evolution in alkali-activated blast furnace slag by the incorporation of fly ash. *Cem Concr Compos, 45*, 125–135. [CrossRef]

[19] Gao, X., Yu, Q. L., & Brouwers, H. J. H. (2015). Reaction kinetics, gel character and strength of ambient temperature cured alkali activated slag–fly ash blends. *Constr Build Mater, 80*, 105–115. [CrossRef]

[20] Omur, T., Miyan, N., Kabay, N., Birol, B., & Oktay, D. (2023). Characterization of ferrochrome ash and blast furnace slag based alkali-activated paste and mortar. *Constr Build Mater, 363*, 129805. [CrossRef]

[21] Zhang, H. Y., Qiu, G. H., Kodur, V., & Yuan, Z. S. (2020). Spalling behavior of metakaolin-fly ash based geopolymer concrete under elevated temperature exposure. *Cem Concr Compos, 106*, 103483. [CrossRef]

[22] Mendes, A., Sanjayan, J. G., Gates, W. P., & Collins, F. (2012). The influence of water absorption and porosity on the deterioration of cement paste and concrete exposed to elevated temperatures, as in a fire event. *Cem Concr Compos, 34*, 1067–1074. [CrossRef]

[23] Kuri, J. C., Majhi, S., Sarker, P. K., & Mukherjee, A. (2021). Microstructural and non-destructive investigation of the effect of high temperature exposure on ground ferronickel slag blended fly ash geopolymer mortars. *J Build Eng, 43*, 103099. [CrossRef]

[24] Davidovits, J. (1991). Geopolymers: inorganic polymeric new materials. *J Therm Anal Calorim, 37*, 1633–1656. [CrossRef]

[25] Kong, D. L. Y., & Sanjayan, J. G. (2010). Effect of elevated temperatures on geopolymer paste, mortar and concrete. *Cem Concr Res, 40*, 334–339. [CrossRef]

[26] Lemougna, P. N., Adediran, A., Yliniemi, J., Ismailov, A., Levanen, E., Tanskanen, P., Kinnunen, P., Roning, J., & Illikainen, M. (2020). Thermal stability of one-part metakaolin geopolymer composites containing high volume of spodumene tailings and glass wool. *Cem Concr Compos, 114*, 103792. [CrossRef]

[27] Pan, Z., Tao, Z., Cao, Y. F., Wuhrer, R., & Murphy, T. (2018). Compressive strength and microstructure of alkali-activated fly ash/slag binders at high temperature. *Cem Concr Compos, 86*, 9–18. [CrossRef]

[28] Guerrieri, M., Sanjayan, J., & Collins, F. (2010). Residual strength properties of sodium silicate alkali activated slag paste exposed to elevated temperatures. *Mater Struct, 43*, 765–773. [CrossRef]

[29] Türker, H. T., Balçikanli, M., Durmuş, İ. H., Özbay, E., & Erdemir, M. (2016). Microstructural alteration of alkali activated slag mortars depend on exposed high temperature level. *Constr Build Mater, 104*, 169–180. [CrossRef]

[30] Yang, Z., Mocadlo, R., Zhao, M., Sisson, R.D., Jr., Tao, M., & Liang, J. (2019). Preparation of a geopolymer from red mud slurry and class F fly ash and its behavior at elevated temperatures. *Constr Build Mater, 221*, 308–317. [CrossRef]

[31] Türkmen, İ., Karakoç, M. B., Kantarcı, F., Maraş, M. M., & Demirboğa, R. (2016). Fire resistance of geopolymer concrete produced from Elazığ ferrochrome slag. *Fire Mater, 40*, 836–847. [CrossRef]

[32] Karakoç, M. B., Türkmen, İ., Maraş, M. M., Kantarcı, F., Demirboğa, R., & Toprak, M. U. (2014). Mechanical properties and setting time of ferrochrome slag based geopolymer paste and mortar. *Constr Build Mater, 72*, 283–292. [CrossRef]

[33] Nuaklong, P., Jongvivatsakul, P., Pothisiri, T., Sata, V., & Chindaprasirt, P. (2020). Influence of rice husk ash on mechanical properties and fire resistance of recycled aggregate high-calcium fly ash geopolymer concrete. *J Clean Prod, 252*, 119797. [CrossRef]

[34] Bideci, Ö. S. (2016). The effect of high temperature on lightweight concretes produced with colemanite coated pumice aggregates. *Constr Build Mater, 113*, 631–640. [CrossRef]

[35] Abali, Y., Bayca, S. U., & Targan, S. (2006). Evaluation of blends tincal waste, volcanic tuff, bentonite and fly ash for use as a cement admixture. *J Hazard Mater, 131*, 126–130. [CrossRef]

[36] Turan, E. (2020). *The engineering properties of boron waste clays and its usability in stabilisation of high plasticity clay* [MS thesis, Ataturk University].

[37] Kurt Albayrak, Z.N., & Turan, E. (2019). Kestelek Bor Atık Kili Katkılı Yüksek Plastisiteli Bir Kilin Mukavemet Özelliklerinin Araştırılması. *Iğdır Univ Fen Bil Enst Der, 9*, 890–899. [CrossRef]

[38] Albayrak, Z. N. K., & Turan, E. (2021). The use of boron waste clay to improve the geotechnical properties of a high plasticity clay. *Arab J Geosci, 14*, 1002. [CrossRef]

[39] Kula, I., Olgun, A., Sevinc, V., & Erdogan, Y. (2002). An investigation on the use of tincal ore waste, fly ash, and coal bottom ash as Portland cement replacement materials. *Cem Concr Res, 32*, 227–232. [CrossRef]

[40] Boncukcuoğlu, R., Kocakerim, M. M., Tosunoğlu, V., & Yilmaz, M. T. (2002). Utilization of trommel sieve waste as an additive in Portland cement production. *Cem Concr Res, 32*, 35–39. [CrossRef]

[41] Kürklü, G. (2016). The effect of high temperature on the design of blast furnace slag and coarse fly ash-based geopolymer mortar. *Compos Part B Eng, 92*, 9–18. [CrossRef]

[42] Bouaissi, A., Li, L., Abdullah, M. M. A. B., & Bui, Q. B. (2019). Mechanical properties and microstructure analysis of FA-GGBS-HMNS based geopolymer concrete. *Constr Build Mater, 210*, 198–209. [CrossRef]

[43] Zhang, Z., Zhu, Y., Yang, T., Li, L., Zhu, H., & Wang, H. (2017). Conversion of local industrial wastes into greener cement through geopolymer technology: A case study of high-magnesium nickel slag. *J Clean Prod, 141*, 463–471. [CrossRef]

[44] Haha, M. B., Lothenbach, B., Le Saout, G. L., & Winnefeld, F. (2011). Influence of slag chemistry on the hydration of alkali-activated blast-furnace slag - Part I: Effect of MgO. *Cem Concr Res, 41*, 955–963. [CrossRef]

[45] Uysal, M., Al-mashhadani, M. M., Aygörmez, Y., & Canpolat, O. (2018). Effect of using colemanite waste and silica fume as partial replacement on the performance of metakaolin-based geopolymer mortars. *Constr Build Mater, 176*, 271–282. [CrossRef]

[46] Görhan, G., & Kürklü, G. (2014). The influence of the NaOH solution on the properties of the fly ash-based geopolymer mortar cured at different temperatures. *Compos Part B Eng, 58*, 371–377. [CrossRef]

[47] Shill, S.K., Al-Deen, S., Ashraf, M., & Hutchison, W. (2020). Resistance of fly ash based geopolymer mortar to both chemicals and high thermal cycles simultaneously. *Constr Build Mater, 239*, 117886. [CrossRef]

[48] Al-Majidi, M. H., Lampropoulos, A., Cundy, A., & Meikle, S. (2016). Development of geopolymer mortar under ambient temperature for in situ applications. *Constr Build Mater, 120*, 198–211. [CrossRef]

[49] Criado, M., Palomo, A., & Fernández-Jiménez, A. (2005). Alkali activation of fly ashes. Part 1: Effect of curing conditions on the carbonation of the reaction products. *Fuel, 84*, 2048–2054. [CrossRef]

[50] Swanepoel, J. C., & Strydom, C. A. (2002). Utilisation of fly ash in a geopolymeric material. *Appl Geochem, 17*, 1143–1148. [CrossRef]

[51] Yang, T., Yao, X., Zhang, Z., & Wang, H. (2012). Mechanical property and structure of alkali-activated fly ash and slag blends. *J Sustain Cem Based Mater, 1*, 167–178.

[52] Bobrowski, A., Kmita, A., Starowicz, M., Hutera, B., & Stypuła, B. (2012). Effect of magnesium oxide nanoparticles on water glass structure. *Arch Foundry Eng, 12*(3), 9–12. [CrossRef]

[53] Mihailova, I., Radev, L., Aleksandrova, V., Colova, I., Salvado, I. M. M., & Fernandes, M. H. V. (2015). Carbonate-apatite forming ability of polyphase glass-ceramics in the CaO-MgO-SiO. *J Chem Technol Metall, 50*, 502–511.

[54] Zhang, H. Y., Kodur, V., Wu, B., Cao, L., & Wang, F. (2016). Thermal behavior and mechanical properties of geopolymer mortar after exposure to elevated temperatures. *Constr Build Mater, 109*, 17–24. [CrossRef]

[55] Ali, N., Canpolat, O., Aygörmez, Y., & Al-Mashhadani, M. M. (2020). Evaluation of the 12–24 mm basalt fibers and boron waste on reinforced metakaolin-based geopolymer. *Constr Build Mater, 251*, 118976. [CrossRef]

[56] Aygörmez, Y., Canpolat, O., Al-mashhadani, M. M., & Uysal, M. (2020). A survey on one year strength performance of reinforced geopolymer composites. *Constr Build Mater, 264*, 120267. [CrossRef]

[57] Aygörmez, Y., Canpolat, O., Al-mashhadani, M. M., & Uysal, M. (2020). Elevated temperature, freezing-thawing and wetting-drying effects on polypropylene fiber reinforced metakaolin based geopolymer composites. *Constr Build Mater, 235*, 117502. [CrossRef]

[58] Şahin, F., Uysal, M., Canpolat, O., Aygörmez, Y., Cosgun, T., & Dehghanpour, H. (2021). Effect of basalt fiber on metakaolin-based geopolymer mortars containing rilem, basalt and recycled waste concrete aggregates. *Constr Build Mater, 301*, 124113. [CrossRef]

[59] Jiang, X., Xiao, R., Zhang, M., Hu, W., Bai, Y., & Huang, B. (2020). A laboratory investigation of steel to fly ash-based geopolymer paste bonding behavior after exposure to elevated temperatures. *Constr Build Mater, 254*, 119267. [CrossRef]

[60] Li, C., Sun, H., & Li, L. (2010). A review: The comparison between alkali-activated slag (Si+ Ca) and metakaolin (Si+ Al) cements. *Cem Concr Res, 40*, 1341–1349. [CrossRef]

[61] Lee, N. K., Koh, K. T., An, G. H., & Ryu, G. S. (2017). Influence of binder composition on the gel structure in alkali activated fly ash/slag pastes exposed to elevated temperatures. *Ceram Int, 43*, 2471–2480. [CrossRef]

[62] Yang, T., Wu, Q., Zhu, H., & Zhang, Z. (2017). Geopolymer with improved thermal stability by incorporating high-magnesium nickel slag. *Constr Build Mater, 155*, 475–484. [CrossRef]

[63] He, P., Jia, D., Lin, T., Wang, M., & Zhou, Y. (2010). Effects of high-temperature heat treatment on the mechanical properties of unidirectional carbon fiber reinforced geopolymer composites. *Ceram Int, 36*, 1447–1453. [CrossRef]

[64] Kong, D. L. Y., Sanjayan, J. G., & Sagoe-Crentsil, K. (2007). Comparative performance of geopolymers made with metakaolin and fly ash after exposure to elevated temperatures. *Cem Concr Res, 37*, 1583–1589. [CrossRef]

Journal of Sustainable Construction Materials and Technologies
Web page info: https://jscmt.yildiz.edu.tr
DOI: 10.47481/jscmt.1536080

JSCMT
Journal of Sustainable Construction Materials and Technologies

Research Article

Replacement of conventional aggregates and fillers with steel slag and palm kernel shell ash in dense-graded asphalt mixtures

Collins A. NKETIAH[*1], Kenneth A. TUTU[1], Ebenezer D. A. BARNOR[2], David A. AZONG-BIL[2]

[1]*Regional Transport Research and Education Centre Kumasi, Kwame Nkrumah University of Science and Technology, Kumasi, Ghana*
[2]*Department of Civil Engineering, Kwame Nkrumah University of Science and Technology, Kumasi, Ghana*

ARTICLE INFO

Article history
Received: 08 March 2024
Revised: 07 May 2024
Accepted: 22 July 2024

Key words:
Fatigue cracking, granite aggregates, industrial waste, palm kernel shell ash, rutting, steel slag

ABSTRACT

Large quantities of steel slag and palm kernel shell ash (PKSA) – waste products from steel production and palm oil milling, respectively – are generated annually in several countries, and their disposal is challenging. Meanwhile, the over-reliance on conventional rock aggregates for asphalt mixture production poses increasing sustainability challenges. This study investigated the potential of entirely replacing granite aggregates with steel slag and PKSA in a dense-graded asphalt mixture. Two sets of asphalt mixtures were prepared; the control mixture contained crushed granite aggregate and hydrated lime, while the other set incorporated steel slag as coarse aggregate and PKSA as fine aggregate and filler. Both mixture types utilized AC-30 viscosity-graded asphalt binder. The properties of the waste materials met the quality standards required for aggregates in asphalt mixture production. Both mixture types were designed according to the Marshall design procedure and were evaluated for durability (Cantabro abrasion loss), fatigue cracking Resistance, rutting Resistance, and moisture damage susceptibility. The Cantabro abrasion loss test indicated that the waste-based mixture was 3% less durable than the control. However, the cracking Resistance of the waste-based mixture was approximately twice that of the control. Even though the rapid rutting test indicated that the control mixture was slightly superior in rutting Resistance, the Marshall quotient suggested otherwise. Both mixture types exhibited similar moisture damage resistance. Overall, the steel slag and PKSA samples have shown high potential to replace virgin granite aggregates and lime in asphalt mixtures fully and are, thus, recommended for field performance evaluation and possible adoption.

Cite this article as: Nketiah, C. A., Tutu, K. A., Barnor, E. D. A., & Azong-bil, D. A. (2024). Replacement of conventional aggregates and fillers with steel slag and palm kernel shell ash in dense-graded asphalt mixtures. *J Sustain Const Mater Technol*, 9(3), 268–279.

1. INTRODUCTION

Aggregates must satisfy strict quality standards for asphalt mixture production, which often prevents using available marginal-quality aggregates. Apart from the challenge of obtaining high-quality aggregates, adverse environmental impacts associated with aggregate mining could be significant, including landscape alteration, land-use conversion, noise and air pollution, habitat loss, erosion, and sedimentation of water bodies. Dwindling high-quality aggregate reserves and sustainability concerns have warranted

*Corresponding author.
*E-mail address: nacollins4u@gmail.com

the exploration of alternative aggregate sources to meet the growing demand for durable pavements. Waste material recycling can enhance sustainable pavement engineering by minimizing virgin material use, reducing landfill space demand, conserving energy, and reducing greenhouse gas emissions associated with extracting and transporting virgin aggregates [1]. Steel slag and palm kernel shell ash are industrial waste materials from steel manufacturing and palm oil milling, respectively.

Steel slag has high strength and abrasive properties and has been found to improve the stability and moisture damage resistance of asphalt mixtures [2, 3]. Sorlini et al. [4] observed that slag-containing asphalt mixtures exhibited mechanical characteristics similar to or better than an asphalt mixture produced with natural aggregates. Kim et al. [5] observed significant improvements in rutting Resistance, tensile strength, and toughness in an asphalt mixture containing slag compared to a mixture with granite aggregate. The slag-containing mixture exhibited 121%, 110%, and 114% in rutting Resistance, tensile strength, and toughness, respectively, compared with the granite aggregate mixture. The relatively high dynamic modulus of the slag-containing mixture was attributed to the strong aggregate interlock and the rough surface texture of the steel slag aggregates. Kehagia [6] and Asi [7] observed that the high strength and irregular shape of steel slag aggregate contribute to improving the skid resistance of asphalt mixtures. Oluwasola et al. [8] found that replacing granite with steel slag (as fine and coarse aggregates) as well as copper mine tailings (as fine aggregate) in hot-mix asphalt improved rutting resistance, resilient modulus, moisture damage susceptibility, Marshall stability, and flow. Díaz-Piloneta et al. [9] noted that carbon emission savings associated with adding steel slag to asphalt mixtures could exceed 14%, compared with asphalt mixtures containing virgin aggregates.

Palm kernel shell ash (PKSA), also referred to as palm oil clinker (POC) or palm oil fuel ash (POFA), results from the incineration of palm kernel shells and other parts of the palm tree when used as fuel for steam generation at oil mills. The pyrolysis residue is typically described as palm kernel shell ash if the biomass fuel comprises predominantly palm kernel shells. PKSA accumulation in the furnace reduces its efficiency, lifespan, and maintenance cost [10]. Several researchers, including [11–14], have explored various engineering applications of PKSA. For instance, Usman [15] investigated the performance of refined dense-graded cold mix asphalt that incorporated PKSA as a filler and observed improved mechanical properties over conventional cold mix asphalt. POFA-modified binder improved Marshall stability and rutting resistance [16, 17], and when POFA was utilized as a filler, volumetric and Marshall properties improved [18, 19] - according to Maleka et al. [20], utilizing POFA as a filler improved durability, Marshall stability, flow, and indirect tensile strength compared with the control mixture which contained 1% Ordinary Portland Cement and 5% mineral filler. Incorporating POFA as a filler at 3% by aggregate weight yielded a mixture with optimum resilient modulus and Marshall stability [21]. Borhan et al. [22] noticed an improvement in the rutting Resistance of PKSA-containing asphalt mixtures when PKSA was used as a filler. Babalghaith et al. [23] concluded that PKSA could fully serve as a fine aggregate in stone matrix asphalt (SMA) mixture for improved rutting and fatigue resistance.

With increasing urbanization and population growth, coupled with the growing demand for steel and palm oil products, slag and PKSA generation is expected to rise, with their accompanying disposal difficulties [10, 24–26], while dwindling quality-aggregate sources for asphalt mixture production and the sustainability issues surrounding their acquisition pose challenges to road agencies.

1.1. Aim and Scope

This study aimed to investigate the feasibility of completely substituting granite aggregate and hydrated lime, traditionally used in the production of dense-graded asphalt (DGA) mixtures, with steel slag and palm kernel shell ash to enhance the sustainability of asphalt mixtures. While prior research has individually examined the benefits of either steel slag or PKSA in asphalt mixtures, this study took a unique approach by concurrently incorporating both waste materials. To achieve the stated aim, lumps of steel slag and PKSA were collected from industry dump sites, crushed into desirable-size fractions using a laboratory device, and characterized to ascertain their suitability as asphalt mixture aggregates. Following the Marshall mixture design procedure, they were then utilized to produce DGA. The control DGA mixture utilized granite aggregate and hydrated lime. Both mixtures used the same grade of asphalt binder. Mixture characterization tests included Marshall stability and flow, moisture susceptibility, Cantabro abrasion loss (durability), indirect tensile cracking, and rutting. Presented in Figure 1 is a flow chart of the experimental program.

2. MATERIALS AND METHODS

2.1. Materials

Granite aggregates obtained from a local quarry in the Ashanti region of Ghana were used to produce a conventional dense-grade asphalt (DGA) mixture designated in this study as the control mixture. Steel slag and PKSA lumps were obtained from dump sites of a steel manufacturer and an oil mill, respectively, in their raw lumps. These lumps were crushed into desirable sizes using a laboratory crusher. The slags had undergone natural aging in a humid environment for several years, experiencing an average annual rainfall of approximately 750mm and daily ambient temperatures ranging between 25°C and 30°C. Subsequently, the crushed aggregates were washed to eliminate dust particles and then oven-dried at a temperature of 105°C. The steel slag served as coarse aggregate in the waste-based mixture, while the PKSA functioned as fine aggregate and filler. Several physical tests were performed on the aggregates to ascertain their suitability for asphalt mixture production. Also, an X-ray fluorescence (XRF) analysis was conducted to determine the chemical composition of the materials. AC-30 viscosity-graded asphalt binder was used in both mixtures; its

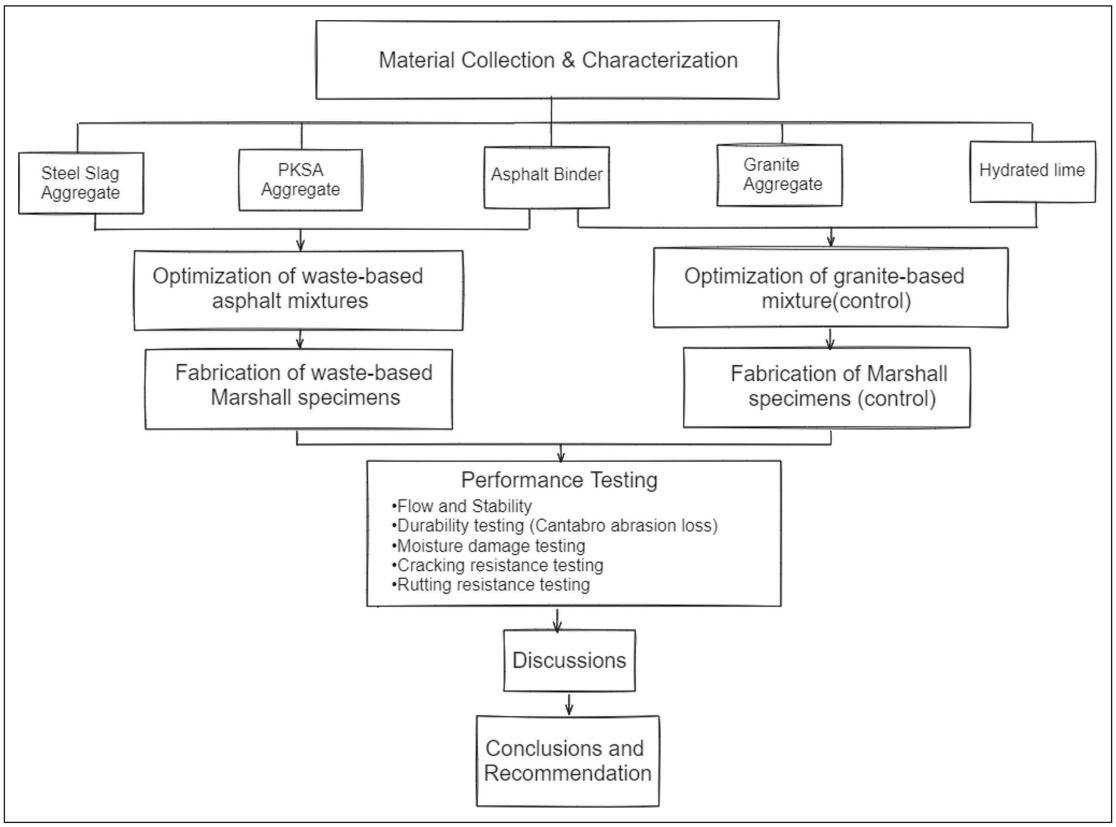

Figure 1. Flow chart of an experimental program.

Table 1. Asphalt binder properties

Property	Procedure (ASTM)	Value	Specification (ASTM D3381)
Penetration at 25°C, 100g, 5s	D5 [27]	65	30 (min)
Flash Point (Cleveland Open Cup)	D92 [28]	332°C	230°C (min)
Kinematic Viscosity at 135°C	D3381 [29]	370 mm^2/s	250 mm^2/s (min)
Viscosity at 60°C	D4402 [30]	322 Pa.s	240–360 Pa.s
Specific Gravity at 25°C	D70 [31]	1.04	–

Table 2. Aggregate blend composition

Aggregate fraction	Waste-based mixture		Control mixture	
	Material	Composition (%)	Material	Composition (%)
Coarse	Slag	45.5	Granite	46.3
Fine	PKSA	47.6	Granite	46.6
Filler	PKSA	6.9	Granite + Lime	6.1+1.0

properties are provided in Table 1. The aggregate test results are presented under the results and discussion section.

2.2. Mixture Design

The aggregate fractions were blended to conform to the Wearing Course Type I gradation envelope (Fig. 2) specified by the Ministry of Roads and Highways' Standard Specification for Road and Bridge Works [32]. As shown in Table 2, the waste-based aggregate blend comprised 45.5% steel slag aggregates (coarse aggregate) and 54.5% of PKSA (including 6.9% PKSA as filler). The control mixture com-

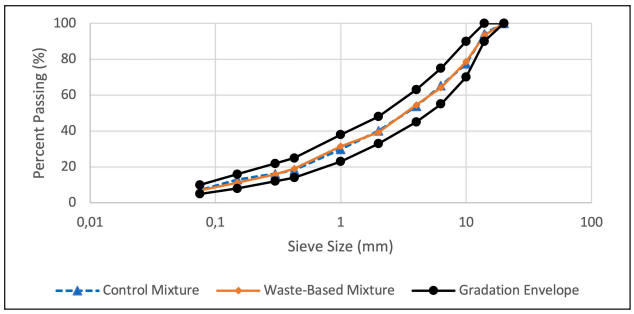

Figure 2. Aggregate gradations of the mixtures.

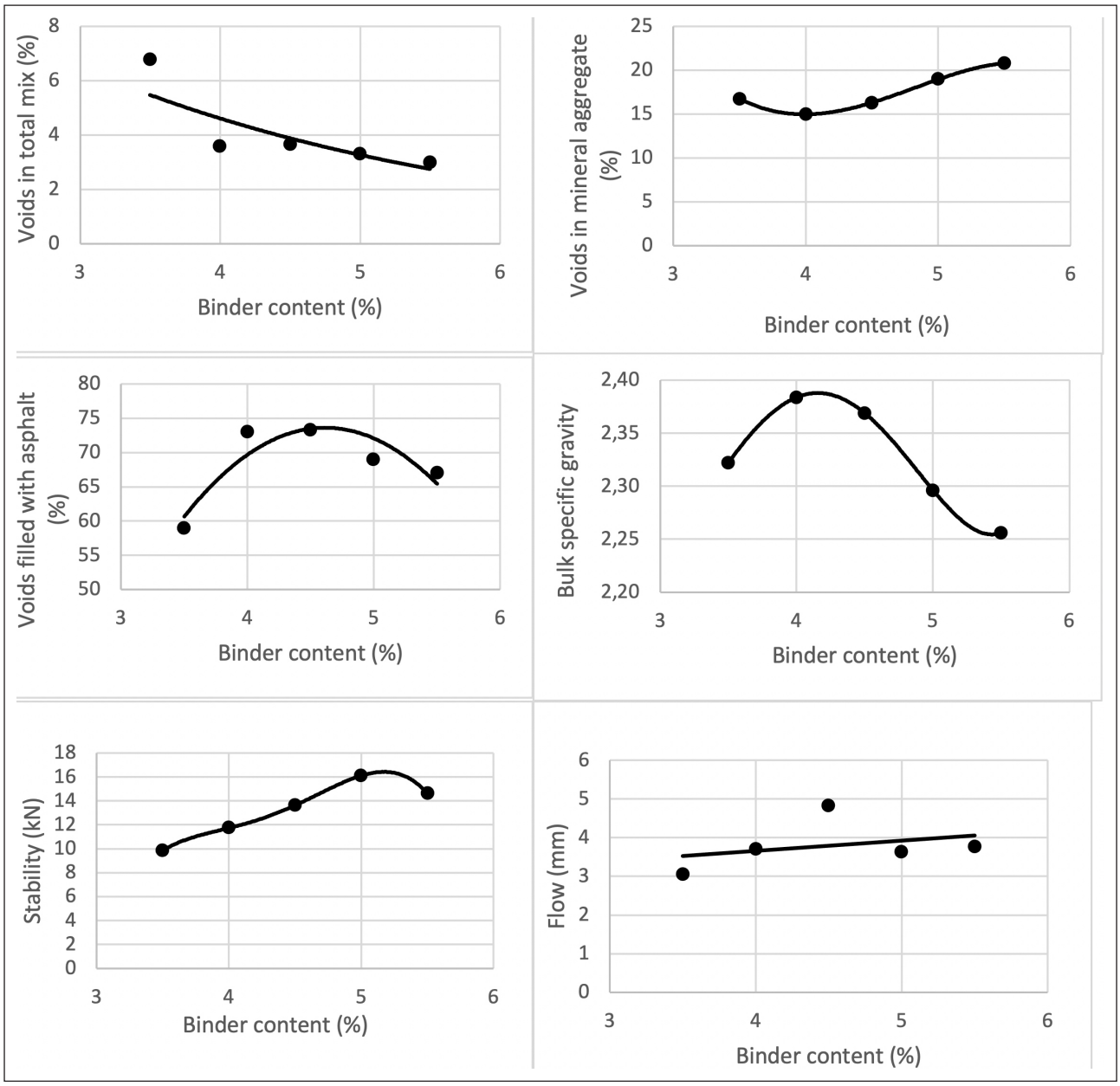

Figure 3. Marshall test results for the control mixture.

prised 99% granite aggregate (including 6.1% mineral filler) and 1% hydrated lime.

The asphalt mixtures were designed per the Marshall procedure [33] to conform to the Standard Specification for Road and Bridge Works [32]. Trial asphalt mixtures were prepared at 3.5% to 5.5% binder contents. The mixtures were produced at 160°C, aged for two hours per [34], and compacted at 130°C, with 75 blows per face. Figures 3 and 4 show asphalt binder content versus the properties of the control and waste-based mixtures, respectively. Following the Asphalt Institute method [35], the optimum binder content corresponding to 4% air voids was determined as 4.5% and 5% for the control and waste-based mixtures, respectively. The effective binder content, which refers to the amount of asphalt binder in an asphalt mixture that is available to coat and bind the aggregate particles together effectively, was, however, found to be 4.3% and 4.2%, respectively, for the control and waste-based mixtures. Table 3 shows the mixture properties at the respective optimum binder contents.

To cast samples at 7% air voids, trial mixtures were fabricated at different numbers of Marshall blows (i.e., 30, 45, and 60). Forty-eight (48) Marshall blows corresponded to 7±1% air voids for both mixtures.

2.3. Mixture Performance Testing

2.3.1. Durability

The Cantabro abrasion loss test [36] was employed to assess the durability of the mixtures. Traditionally utilized for characterizing Open Graded Friction Course (OGFC) mixtures, this test has undergone validation for its applicability to dense graded mixtures [37]. It has proven effective in distinguishing

Table 3. Mixture properties and specification requirements at optimum binder contents [32]

Mixture property	Mixture type		Specification
	Control (P_b=4.5%)	Waste-based (P^b=5.0%)	
Marshal Stability (2×75 blows) (kN)	13.8	11.0	9–18
Marshal Flow (mm)	3.7	2.8	2–4
VTM (%)	3.8	4.2	3–5
VFA (%)	73	69	65–75

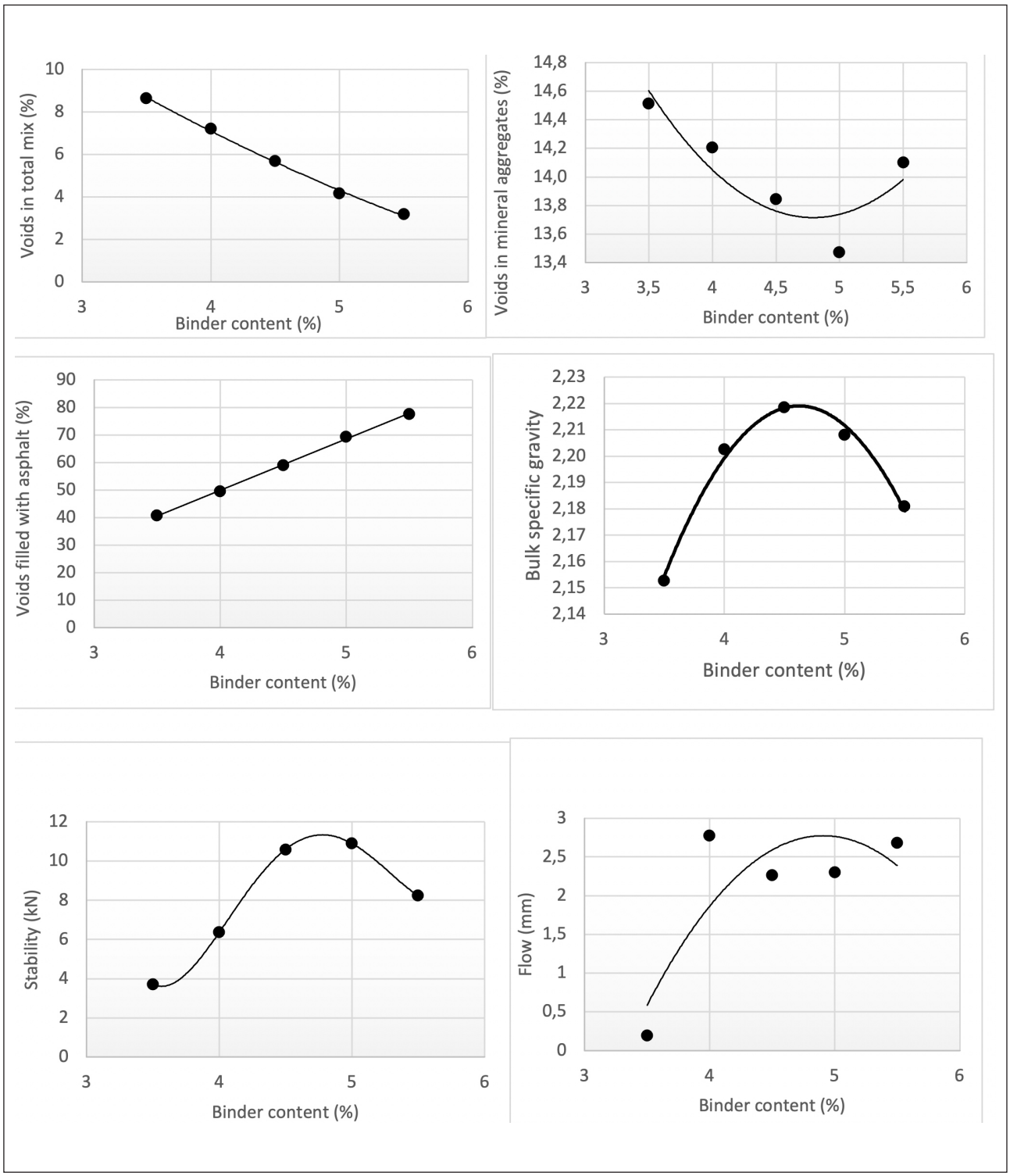

Figure 4. Marshall test results for the waste-based mixture.

Table 4. Aggregate test results

Property	Procedure	Value			MRH (2007) Specification
		Granite	Steel Slag	PKSA	
Los Angeles Abrasion (%)	ASTM C131 [52]	25	37	–	40 (max)
Ten Percent Fines (kN)	BS 812 [53]	211	234	–	160 (min)
Flakiness Index (%)	ASTM D4791 [54]	9	25	–	25 (max)
Coarse aggregate angularity (%)	ASTM D5821 [55]	100	100	–	[2]90–100
Fine aggregate angularity (%)	ASTM C1252 [56]	47	51	29	[3]45 min.
Plasticity index (%)	AASHTO T90 [57]	NP	NP	NP	NP
Moisture Absorption (%)	ASTM C127 [58]	0.11	0.60	7.2	1.0 (max)*
Aggregate Crushing Value (%)	BS 812 [53]	18	20	–	30 (max)[1]
Aggregate Impact Value (%)	BS 812 [53]	12	15	–	30 (max)[1]
Elongation Index (%)	ASTM D4791 [54]	14	10	–	15 (max)[1]
Specific Gravity	ASTM C127 [58]	2.692	2.835	1.903	–
Sodium Sulphate Soundness (%)	ASTM C88 [59]	0.9	1.2	1.8	15 (max)[2]

Source: [1][60], [2][61]; [3][62]; NP – Nonplastic; *: Not applicable to PKSA.

various mixture characteristics that play a role in durability, encompassing factors such as binder type and content, aggregate type, air void content, binder absorption, and aging [38, 39].

Three Marshall specimens for each mixture type were prepared at the 4.5% and 5.0% optimum binder content for the control and waste-based mixtures, respectively. The loose mixtures were short-term aged [34] and then compacted to 7% air voids. Having measured the initial mass of the Marshall-compacted specimens, each was subjected to abrasion in the Los Angeles abrasion machine for 300 revolutions (without steel balls). The final specimen mass was measured, and the Cantabro abrasion loss index (CALindex) was computed using Equation 1.

$$CAL_{index} = \left(\frac{\text{Initial Specimen Mass} - \text{Final Specimen Mass}}{\text{Initial Specimen Mass}}\right) \times 100 \quad (1)$$

2.3.2. Moisture Damage Resistance

The modified Lottman test [40] was performed to evaluate the moisture damage susceptibility of the mixtures. Six Marshall specimens for each mixture type were fabricated at 7% air voids using the optimum binder contents of 4.5% and 5.0% for the control and waste-based mixtures, respectively. A subset (three of the specimens) of each mixture type was conditioned per [40] (except for the freeze-thaw cycle), while the other subgroup was unconditioned. Both sets of specimens were subjected to monotonic loading at a rate of 50 mm/min, and the failure load was used to calculate the tensile strength using Equation 2. The tensile strength ratio (TSR) was calculated as the ratio of the average tensile strength of the conditioned specimens to that of the unconditioned specimens.

$$S_t = \frac{2000P}{\pi tD} \quad (2)$$

where,
S_t=tensile strength (kPa)
P=maximum load (N)
t=specimen thickness (mm)
D=specimen diameter (mm)

Table 5. XRF analysis results

Oxide	Percent composition by mass			
	Granite	Steel slag	PKSA	Hydrated lime
SiO_2	84.4	52.4	70.8	43.9
Al_2O_3	13.0	15.0	6.6	12.4
K^2O	0.8	0.0	7.3	2.0
Fe_2O_3	0.4	11.8	3.8	3.9
CaO	0.1	5.3	3.9	31.6
MnO	0.0	9.7	0.0	0.1
MgO	0.0	1.2	3.7	4.7
Traces	1.3	4.6	3.9	1.4
Total	**100.0**	**100.0**	**100.0**	**100.0**

2.3.3. Cracking Resistance

The indirect tensile cracking test [41] was employed to evaluate the cracking susceptibility of the mixtures. The efficacy of the test has been confirmed through the analysis of pavement performance data gathered from various experimental facilities. It has effectively predicted fatigue, reflective, top-down, and thermal cracking [42]. To add to its practicality, laboratory specimens, and field cores, prepared using Marshall or Gyratory compactors, can be readily utilized in this test, eliminating the need for additional procedures such as notching, drilling, instrumentation, or cutting [43–45].

The control and waste-based compacted specimens (three each) were produced at 4.5% and 5.0% optimum binder content, respectively. Similarly, the loose mixtures were short-term aged [34] and compacted to 7% air voids. The specimens were loaded in a universal testing machine at a constant rate of 50 mm/min at 25°C until failure. The cracking tolerance index (CT_{index}), a fracture mechanics-based parameter, was computed using Equation 3 [41] to evaluate the cracking Resistance of the mixtures. A higher C.T. index denotes higher cracking resistance.

$$CT_{index} = \frac{t}{62} \times \frac{l_{75}}{D} \times \frac{G_f}{|M_{75}|} \times 10^6 \quad (3)$$

where:
CT_{index}=cracking tolerance index
Gf=failure energy (Joules/m^2)
$|M_{75}|$=absolute value of the post-peak slope (N/m)
l_{75}=displacement at 75% of the peak load after the peak (mm)
D=specimen diameter (mm)a
t=specimen thickness (mm)

2.3.4. Rutting Resistance

The rapid rutting test [46] was performed to assess the rutting Resistance of the mixtures, except that Marshall-compacted specimens were used instead of 150-mm diameter gyratory-compacted specimens. Additionally, a concave supporting cradle with a curvature radius equal to the nominal radius of the test specimen was not used. This omission proved inconsequential in the comparative assessment of rutting Resistance between the two mixture types, given the absence of a standard RT_{index} criterion for asphalt mixtures at the time of the study. This simple test – which is repeatable, reproducible, and sensitive to asphalt mixture components such as binder type and content, aggregate type and gradation, additives, and mixture aging – has shown good correlation with well-established simulative and fundamental rutting tests and field performance [47–49].

The mixtures were produced at 4.5% and 5.0% binder content for the control and waste-based mixtures, respectively. They were short-term aged [34] and compacted to 7% air voids. The specimens were then conditioned in a 60°C water bath for 45 minutes and loaded at 50 mm/min until failure. The failure loads were used to calculate the shear strengths of the mixtures (Equation 4), which were subsequently used to determine rutting tolerance indices (RT_{index}) using Equation 5. The rutting tolerance index is a performance indicator where higher values indicate higher rutting Resistance.

$$\tau_f = 0.356 \times \frac{P_{max}}{t \times w} \quad (4)$$

where:
τ_f=shear strength (Pa)
P_{max}=maximum load (N)
T=specimen thickness (m)
W=width of upper loading strip (=0.0191 m)

$$RT_{Index} = 6.618 \times 10^{-5} \times \frac{\tau_f}{1P_a} \quad (5)$$

where:
RT_{Index}=rutting tolerance index
τ_f=shear strength calculated from Equation 4.

2.3.5. Marshall Quotient

Marshall quotient, computed as the ratio of stability to flow, is a recognized indicator of asphalt mixture rutting resistance [2, 50]. The Marshall stability and flow were measured per [51]. Three Marshall-compacted specimens (4% air voids) for each mixture type produced at the optimum binder content (4.5% and 5.0% for the control and waste-based mixtures) were conditioned in a 60°C water bath for 30 minutes. The conditioned samples were loaded at a 50.8 mm/minute rate until failure. The failure load was recorded as the stability, and the total plastic deformation was recorded as the flow. A higher Marshall quotient indicates higher asphalt mixture rutting Resistance.

3. RESULTS AND DISCUSSION

3.1. Aggregate Characteristics

Tables 4 and 5 show the physical and chemical properties of the aggregates, respectively. Although higher for steel slag, the Los Angeles Abrasion (LAA) values met specification requirements [32]. The granite and steel slag passed water absorption specifications [32]. PKSA had the highest water absorption value, which may be explained by the presence of a significant proportion of the deliquescent compound K_2O, as the XRF analysis results in Table 5 show. While binder absorption and water absorption are not equal in value, higher water absorption of the steel slag and PKSA aggregates indicates higher porosity, which could result in increased binder absorption.

Both steel slag aggregates and granite demonstrated similar characteristics in coarse aggregate angularity. However, steel slag aggregates showed a higher fine aggregate angularity (FAA) than granite. The angularity of aggregates plays a crucial role in determining mixture stability, with higher angularity values contributing to increased strength. The high FAA of steel slag has the potential to counterbalance the low FAA associated with PKSA to improve overall mixture stability. The steel slag aggregates generally exhibited comparable or better mechanical strength characteristics to the granite. The steel slag aggregates were denser and less elongated but flakier than the granite aggregates. Considering their Resistance to sodium sulfate deterioration, all three aggregates could withstand weathering.

The X-ray Fluorescence (XRF) analysis revealed the presence of CaO, Al_2O_3, Fe_2O_3, and MgO in significant proportions in the steel slag and PKSA, indicating their inherent pozzolanic properties. Pozzolanic property has the potential to improve the strength and durability of asphalt mixtures [63]. However, volume instability failures have been found to be typical of slag due to the presence of free lime (f-CaO) and MgO [64, 65]. The f-CaO, or free calcium oxide, refers explicitly to an unhydrated form of CaO in a material. High levels of f-CaO in materials like slag can lead to delayed ettringite formation in asphalt concrete, causing expansion and potential durability issues. One recommended approach, as suggested by Juckes [66], involves subjecting CaO-containing aggregates to an aging process. This method has proven effective in promoting the complete hydration of f-CaO. Wu et al. [67] noted that after three years of aging, the f-CaO content of steel slag aggregates fell below 6%, which posed an insignificant threat to deleterious expansion. According to the XRF results in Table 5, both steel slag and PKSA aggregates have CaO contents of 5.3% and 3.9%, respectively – suggesting low levels of f-CaO and adequate aging of both materials. The relatively low levels of f-CaO in these aggregates suggest a diminished threat of volume instability.

Furthermore, the dominant presence of silica (Si_2O) in all three aggregates (ranging from 52% to 84% by mass) indicates remarkable similarities, positioning them as viable alternatives to granite aggregate in asphalt mixtures. In essence, both the waste-based aggregates (steel slag and PKSA) and natural aggregates (granite) characterized in this study met the criteria for asphalt mixture production, emphasizing steel slag and PKSA aggregates' suitability and potential contribution to sustainable asphalt construction practices.

3.2. Mixture Performance

Figure 5 shows the average values for the mixture performance indicators: tensile strength ratio (TSR), rutting tolerance index (CT_{index}), Cantabro abrasion loss index, cracking tolerance index (CT_{index}), and Marshall quotient.

3.2.1. Moisture Damage Resistance

Although hydrated lime was absent in the waste-based mixture, it exhibited similar moisture damage resistance as the control, which contained 1% hydrated lime. Hydrated lime improves moisture damage resistance [68, 69]. Even without lime, the waste-based mixture's comparable performance may have been influenced by the low acidity and high porosity observed in steel slag and PKSA aggregates. Adequate adhesion within a bitumen-aggregate system enhances moisture damage resistance [70]. The mechanical interlocking theory [71] provides insights into the formation of a strong bond between bitumen and aggregate. This bond arises from the interlocking when hot bitumen permeates aggregate pores and air voids, coating irregularities on the aggregate surface. Subsequent cooling establishes and forms robust mechanical forces. A higher number of pores, a rough texture with angularity, and microstructures such as pores, voids, and microcracks contribute to mechanical interlocking [72]. In contrast, aggregates with high silica content (>65% by mass) tend to be geologically acidic, resulting in a weaker bond with asphalt binder. Conversely, a rough aggregate surface and fine microstructures increase the adsorptive surface available for binder adhesion [73]. It is worth noting that while the standard specification for Road and Bridge Works [32] currently does not incorporate the moisture damage test as a criterion for the mixture design of the wearing course, it is commonly recommended to adhere to a minimum tensile strength ratio of 0.8 as a best practice, which both mixtures exceeded.

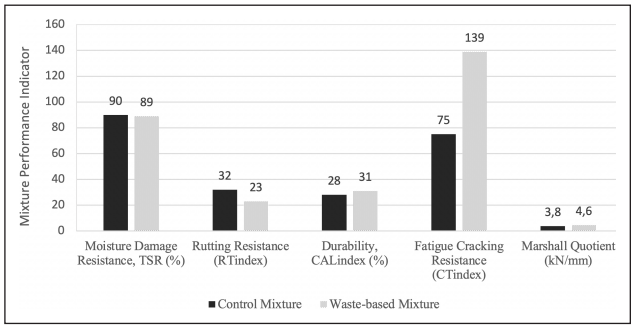

Figure 5. Performance testing results of the control and waste-based asphalt mixtures.

Analyzing the X-ray fluorescence (XRF) results from Table 5, it becomes evident that the waste-based mixture aggregate exhibited low acidity (weighted silica content of 62.43%) compared to the control mixture aggregate (weighted silica content of 84%). Looking closely at the steel slag and PKSA aggregates, conspicuous permeable pores were observed on their surfaces. Notably, the steel slag aggregate particles exhibited a more angular morphology than the granite aggregates. These physical characteristics may have influenced the moisture damage resistance of the waste-based mixture. Several studies have also reported improved asphalt moisture damage resistance when palm oil fuel ash (and its variants including PKSA) [19, 20, 74] and steel slag aggregates [2, 8] were utilized separately in asphalt mixtures, in some cases better than hydrated lime.

3.2.2. Cracking Resistance

The waste-based mixture exhibited a higher cracking resistance performance, with a CT_{index} 85% higher than the control. Several studies have also reported improved cracking resistance of mixtures by incorporating steel slag [75–78] and PKSA (and its variants) [22, 74] into asphalt mixtures. The frequently cited reasons have been the strong, angular, rough-textured steel slag aggregates, which provide better interlocking, contributing to improved cracking resistance [79], as well as the pozzolanic cementing nature of PKSA which improves aggregate-binder adhesion and overall durability. The better-cracking Resistance of the waste-based mixture, despite its lower effective binder content of 4.2% compared to 4.3% of the control, suggested that the PKSA-based mastic better tolerated cracking than the mastic of the control mixture, which contained mineral filler and hydrated lime. There is no established standard criterion for DGA mixtures based on the C.T. index. However, it is reported that poorly performing DGA mixtures typically exhibit CT_{index} values below 70, while well-performing ones usually yield values exceeding 100 [80].

3.2.3. Rutting Resistance

The rapid rutting test results showed that the waste-based mixture possessed slightly lower rutting Resistance. However, this finding was inconsistent with the Marshall quotient, which indicated that the waste-based mixture had higher rutting Resistance. This inconsistency between the two test results suggests that factors other than those captured by the Marshall quotient may influence the waste-based mixture's rutting behavior. The RT_{index} is a shear strength-based rutting performance indicator. Since rutting is considered a shear failure, it is reasonable to suggest that the RT_{index} better characterizes the rutting Resistance of asphalt mixtures. Thus, it is logical to infer that the rapid rutting test is sensitive to specific characteristics of the waste-based mix that are not fully reflected in the Marshall Stability and Flow test. Therefore, further analysis and investigation may be needed to understand better the factors contributing to the rutting behavior observed in the waste-based mixture. The Marshall testing protocol involves the application of a monotonic compressive loading along the circumference of a fully, laterally confined specimen, causing shear or deformation failure.

The rapid rutting test, on the other hand, applies monotonic compressive loading; however, as is done in the indirect tensile test, the specimen is placed in a supporting concave cradle before loading. Due to the three-point bending, this process creates two separate shear planes along the specimen's diametral surface. In this study, only one shear plane was developed since the supporting cradle was not used. It is worth noting that the RT_{index} in this study serves as indicative metrics to compare the rutting Resistance of the waste-based and control mixtures. They should not be interpreted outside the scope of this study.

3.2.4. Durability

The Cantabro abrasion loss test indicated that the control mixture was marginally better than the waste-based mixture. While there is no widely accepted criterion of Cantabro abrasion loss for dense graded asphalt mixtures, for open-graded friction course mixtures, [81] specifies an average Cantabro abrasion loss of 20% and 30% for unaged and aged compacted specimens, respectively. In comparison, the maximum loss for an individual specimen is 50%. The better abrasion resistance performance of the control mixture over the waste-based mixture may be attributed to the synergetic effect of the higher effective binder content and 1% active filler (hydrated lime) of the control mixture. Binder cohesion is crucial for abrasion loss resistance [82]. Hydrated lime has a high surface area and can absorb fines present in the asphalt mixture. This absorption can lead to a uniform distribution of fines within the binder, promoting better cohesion in the asphalt mortar. Higher Cantabro values indicate less Resistance to material loss due to abrasion, as the Los Angeles Abrasion Machine simulated.

4. CONCLUSIONS AND RECOMMENDATIONS

This study investigated the potential of entirely replacing granite aggregates with steel slag and palm kernel shell ash (PKSA) in a dense-graded asphalt mixture. The control mixture incorporated granite aggregate and 1% hydrated lime as an active filler, while the waste-based mixture utilized steel slag and palm kernel shell ash. The following conclusions and recommendations are provided based on the findings from this study:

- Steel slag and PKSA passed aggregate quality requirements for use in asphalt mixtures.
- XRF analysis identified silica (SiO_2) as the dominant compound in the steel slag and PKSA, which is also prevalent in granite aggregate. The steel slag and PKSA also contained the cementitious compounds CaO, MgO, and K_2O, which might have benefited the moisture damage resistance of the asphalt mixture.
- Despite the absence of hydrated lime in the waste-based mixture, it exhibited similar moisture damage resistance as the control mixture, which contained hydrated lime.
- The rapid rutting test and Marshall quotient predicted contradictory rutting performance of the mixtures. While the rapid rutting test suggested the control mixture had higher rutting Resistance, the Marshall quotient indicated otherwise. This inconsistency underscores the need to diversify asphalt mixture rutting performance characterization.
- The waste-based mixture exhibited cracking Resistance approximately twice as the control. The higher asphalt binder content of the waste-based mixture might have contributed to this observation.
- The Cantabro abrasion loss suggested that the control mixture was slightly durable; however, the difference is insignificant. Hence, both mixtures could have similar durability in service.
- Overall, steel slag and PKSA have shown high potential to replace conventional aggregates in asphalt mixtures thoroughly and are, thus, recommended for field performance evaluation to confirm the observed laboratory performance and possible implementation on real-life projects.

ACKNOWLEDGMENTS

The authors wish to acknowledge the Regional Transport Research and Education Centre Kumasi (TRECK) of the Department of Civil Engineering at the Kwame Nkrumah University of Science and Technology (KNUST) for their financial support in this study.

ETHICS

There are no ethical issues with the publication of this manuscript.

DATA AVAILABILITY STATEMENT

The authors confirm that the data that supports the findings of this study are available within the article. Raw data that support the finding of this study are available from the corresponding author, upon reasonable request.

CONFLICT OF INTEREST

The authors declare that they have no conflict of interest.

FINANCIAL DISCLOSURE

The authors declared that this study has received no financial support.

USE OF AI FOR WRITING ASSISTANCE

Not declared.

PEER-REVIEW

Externally peer-reviewed.

REFERENCES

[1] Langer, W. H. (2002). *Managing and protecting aggregate resources*. US Geological Survey. [CrossRef]

[2] Ahmedzade, P., & Sengoz, B. (2009). Evaluation of steel slag coarse aggregate in hot mix asphalt concrete. *J Hazard Mater, 165*(1-3), 300–305. [CrossRef]

[3] Motz, H., & Geiseler, J. (2001). Products of steel slag an opportunity to save natural resources. *Waste Manag, 21*(3), 285–293. [CrossRef]

[4] Sorlini, S., Sanzeni, A., & Rondi, L. (2012). Reuse of steel slag in bituminous paving mixtures. *J Hazard Mater, 209*, 84–91. [CrossRef]

[5] Kim, K., Jo, S. H., Kim, N., & Kim, H. (2018). Characteristics of hot mix asphalt containing steel slag aggregate according to temperature and void percentage. *Constr Build Mater, 188*, 1128–1136. [CrossRef]

[6] Kehagia, F. (2009). Skid resistance performance of asphalt wearing courses with electric arc furnace slag aggregates. *Waste Manag Res, 27*(3), 288–294. [CrossRef]

[7] Asi, I. M. (2007). Evaluating skid resistance of different asphalt concrete mixes. *Build Environ, 42*(1), 325–329. [CrossRef]

[8] Oluwasola, E. A., Hainin, M. R., & Aziz, M. M. A. (2015). Evaluation of rutting potential and skid resistance of hot mix asphalt incorporating electric arc furnace steel slag and copper mine tailing. *Indian J Eng Mater Sci, 22*(5), 550–558.

[9] Díaz-Piloneta, M., Terrados-Cristos, M., Álvarez-Cabal, J. V., & Vergara-González, E. (2021). Comprehensive analysis of steel slag as aggregate for road construction: Experimental testing and environmental impact assessment. *Materials, 14*(13), 3587. [CrossRef]

[10] Baidoo, M. F. (2022). Characterization of Palm Kernel Shell Ash (PKSA) generated from a furnace at Juaben Oil Mills. *KEEP Bull, 3*(2), 22–23.

[11] Osei, D. Y., & Jackson, E. N. (2012). Experimental study on palm kernel shells as coarse aggregates in concrete. *Int J Sci Eng Res, 3*(8), 1–6.

[12] Mahlia, T. M. I., Ismail, N., Hossain, N., Silitonga, A. S., & Shamsuddin, A. H. (2019). Palm oil and its wastes as bioenergy sources: A comprehensive review. *Environ Sci Pollut Res, 26*, 14849–14866. [CrossRef]

[13] Bonsu, B. O., Takase, M., & Mantey, J. (2020). Preparation of charcoal briquette from palm kernel shells: A case study in Ghana. *Heliyon, 6*(10), E05266. [CrossRef]

[14] Nyamful, A., Nyogbe, E. K., Mohammed, L., Zainudeen, M. N., Darkwa, S. A., Phiri, I., Mohammed, M., & Ko, J. M. (2020). Processing and characterizing activated carbon from coconut shell and palm kernel shell waste by H3PO4 activation. *Ghana J Sci, 61*(2), 91–104. [CrossRef]

[15] Usman, K. R., Hainin, M. R., Satar, M. K. I. M., Warid, M. N. M., Kamarudin, S. N. N., & Abdulrahman, S. (2021). Palm oil fuel ash application in cold mix dense-graded bituminous mixture. *Constr Build Mater, 287*, 123033. [CrossRef]

[16] Yaro, N. S. A., Sutanto, M. H., Habib, N. Z., Napiah, M., Usman, A., Jagaba, A. H., & Al-Sabaeei, A. M. (2023). Modeling and optimization of asphalt content, waste palm oil clinker powder and waste rice straw ash for sustainable asphalt paving employing response surface methodology: A pilot study. *Cleaner Mater, 8*, 100187. [CrossRef]

[17] Bujanga, M., Bakiea, N. A., Bujanga, U. H., Kiana, L. S., Juslia, E. A., & Azahara, W. N. A. W. (2023). Characteristics of oil palm fruit ash as binder in asphaltic concrete. *J Kejuruteraan, 35*(4), 913–921. [CrossRef]

[18] Olayemi, O. R., & Olaiya, R. A. (2023). Optimization of palm oil fiber ash in asphalt mixture. *Int J Res Publ Rev, 4*(4), 5262–5267.

[19] Yaro, N. S. A., Sutanto, M. H., Habib, N. Z., Napiah, M., Usman, A., Jagaba, A. H., & Al-Sabaeei, A. M. (2023). Modeling and optimization of asphalt content, waste palm oil clinker powder and waste rice straw ash for sustainable asphalt paving employing response surface methodology: a pilot study. *Cleaner Mater, 8*, 100187. [CrossRef]

[20] Maleka, A. M., Alkali, I. A., & Jaya, R. P. (2014). The indirect tensile strength of palm oil fuel ash (POFA) modified asphaltic concrete. *Appl Mech Mater, 587–589*, 1270–1275. [CrossRef]

[21] Ahmad, J. B., Yunus, K. N. B. M., Kamaruddin, N. H. B. M., & Zainorabidin, A. B. (2012). The practical use of palm oil fuel ash as a filler in asphalt pavement. In *Proceedings of International Conference of Civil and Environmental Engineering for Sustainability (IconCEES)*, Johor Bahru, Malaysia, 3–5.

[22] Borhan, M. N., Ismail, A., & Rahmat, R. A. (2010). Evaluation of palm oil fuel ash (POFA) on asphalt mixtures. *Aust J Basic Appl Sci, 4*(10), 5456–5463.

[23] Babalghaith, A. M., Koting, S., Sulong, N. H. R., Karim, M. R., Mohammed, S. A., & Ibrahim, M. R. (2020). Effect of palm oil clinker (POC) aggregate on the mechanical properties of stone mastic asphalt (SMA) mixtures. *Sustainability, 12*(7), 2716. [CrossRef]

[24] Khajuria, A., Yamamoto, Y., & Morioka, T. (2010). Estimation of municipal solid waste generation and landfill area in Asian developing countries. *J Environ Biol, 31*(5), 649–654.

[25] Han, X., Hu, C., & Lin, L. (2020). A study on the impact of China's urbanization on the quantity of municipal solid waste produced. *Waste Manag Res, 38*(2), 184–192. [CrossRef]

[26] Juckes, L. M. (2003). The volume stability of modern steelmaking slags. *Miner Process Extr Metall, 112*(3), 177–197. [CrossRef]

[27] American Society for Testing and Materials. (2006). *Standard test method for penetration of bituminous materials (D5)*. ASTM International.

[28] American Society for Testing and Materials. (2018). *Standard test method for flash and fire points by Cleveland open cup tester (D92)*. ASTM International.

[29] American Society for Testing and Materials. (2009). *Standard specification for viscosity-graded asphalt cement for use in pavement construction (D3381)*. ASTM International.

[30] American Society for Testing and Materials. (2006). *Standard test method for viscosity determination of asphalt at elevated temperatures using a rotational viscometer (D4402)*. ASTM International.

[31] American Society for Testing and Materials. (2018). *Standard test method for density of semi-solid asphalt binder (Pycnometer method) (D70)*. ASTM International.

[32] Ministry of Roads and Highways (MRH). (2007). *Ministry of Transportation Standard Specification for Road and Bridge Works*. Accra.

[33] American Society for Testing and Materials. (1999). *Standard practice for preparation of bituminous specimens using Marshall apparatus (D6926)*. ASTM International.

[34] American Association of State Highway and Transportation Officials. (2015). *Standard practice for mixture conditioning of hot mix asphalt (R30)*. AASHTO.

[35] Asphalt Institute. (2009). *Asphalt mix design methods (MS-2 7th Edition)*. ASTM International.

[36] Texas Department of Transportation. (2014). *Test procedure for Cantabro abrasion loss (Tex-245-F)*. https://ftp.dot.state.tx.us/pub/txdot-info/cst/TMS/200-F_series/archives/245-1104.pdf

[37] Doyle, J., & Howard, I. (2016). Characterization of dense-graded asphalt with the Cantabro test. *J Test Eval, 44*(1), 77–88. [CrossRef]

[38] Doyle, J. D., & Howard, I. L. (2011). Evaluation of the Cantabro durability test for dense graded asphalt. In *Geo-Frontiers 2011: Advances in Geotechnical Engineering* (pp. 4563–4572). [CrossRef]

[39] Cox, B. C., Smith, B. T., Howard, I. L., & James, R. S. (2017). State of knowledge for Cantabro testing of dense graded asphalt. *J Mater Civ Eng, 29*(10), 04017174. [CrossRef]

[40] American Association of State Highway and Transportation Officials. (2014). *Resistance of compacted asphalt mixtures to moisture-induced damage (T283)*. https://www.intertekinform.com/en-us/standards/aashto-t-283-2014-1349_saig_aashto_aashto_3417/

[41] American Society for Testing and Materials. (2019). *Standard test method for determination of cracking tolerance index of asphalt mixture using the indirect tensile cracking test at intermediate temperature (D8225)*. https://onlinepubs.trb.org/onlinepubs/nchrp/nchrp_rpt_987E.pdf

[42] Texas Transportation Researcher (TTR). (2021). IDEAL-CT – Simple, reliable, efficient, repeatable, cost effective. *Tex Transp Res, 57*(1), 10–11.

[43] Chowdhury, P. S., Noojilla, S. L. A., & Reddy, M. A. (2022). Evaluation of fatigue characteristics of asphalt mixtures using Cracking Tolerance index (CTIndex). *Constr Build Mater, 342*, 128030. [CrossRef]

[44] Newcomb, D., & Zhou, F. (2018). *Balanced design of asphalt mixtures (No. MN/RC 2018-22)*. Minnesota Department of Transportation.

[45] Yan, C., Zhang, Y., & Bahia, H. U. (2020). Comparison between SCB-IFIT, un-notched SCB-IFIT and IDEAL-CT for measuring cracking resistance of asphalt mixtures. *Constr Build Mater, 252*, 119060. [CrossRef]

[46] American Society for Testing and Materials. (2022). *Standard test method for determination of rutting tolerance index of asphalt mixture using the Ideal Rutting Test (D8360)*. https://cdn.standards.iteh.ai/samples/113516/4102b8bc605447fba3cd471927c7cc16/ASTM-D8360-22.pdf

[47] Zhou, F., Crockford, B., Zhang, J., Hu, S., Epps, J., & Sun, L. (2019). Development and validation of an Ideal Shear Rutting Test for asphalt mix design and QC/QA. *J Assoc Asph Pav Technol, 88*, 719–750.

[48] Zhou, F., Hu, S., & Newcomb, D. (2020). Development of a performance-related framework for production quality control with Ideal Cracking and Rutting Tests. *Constr Build Mater, 261*(3), 120549. [CrossRef]

[49] Zhou, F., Steger, R., & Mogawer, W. (2021). Development of a coherent framework for balanced mix design and production quality control and quality acceptance. *Constr Build Mater, 287*, 123020. [CrossRef]

[50] Zhang, W., Khan, A., Huyan, J., Zhong, J., Peng, T., & Cheng, H. (2021). Predicting Marshall parameters of flexible pavement using support vector machine and genetic programming. *Constr Build Mater, 306*, 124924. [CrossRef]

[51] Liu, C., & Wu, X. W. (2011). Factors influencing municipal solid waste generation in China: A multiple statistical analysis study. *Waste Manag Res, 29*(4), 371–378. [CrossRef]

[52] American Society for Testing and Materials. (2003). *Standard test method for resistance to degradation of small-size coarse aggregate by abrasion and impact in the Los Angeles machine (C131)*. https://cdn.standards.iteh.ai/samples/105858/245bf79852bf-4d3aaadf0404f8524423/ASTM-C131-C131M-20.pdf

[53] British Standard Institution (BS 812). (1975). *Testing aggregates*. https://storethinghiem.vn/uploads/files/BS%20812-3-75.pdf

[54] American Society for Testing and Materials. (2010). *Standard test method for flat particles, elongated particles, or flat and elongated particles in coarse aggregate (D4791)*. https://cdn.standards.iteh.ai/samples/75008/534478c0f43f40959d8d06e02751a64a/ASTM-D4791-10.pdf

[55] American Society for Testing and Materials. (2017). *Standard test method for determining the percentage of fractured particles in coarse aggregate (D5821)*. https://www.nicet.org/nicetorg/assets/file/public/performance_examination_checklists/aggregate/astm_d5821-13-17.pdf

[56] American Society for Testing and Materials. (2017). *Standard test methods for uncompacted void content of fine aggregate (as influenced by particle shape, surface texture, and grading) (C1252)*. https://cdn.standards.iteh.ai/samples/97023/94801c3943a94944a-caf4d1717025704/ASTM-C1252-17.pdf

[57] American Association of State Highway and Transportation Officials. (2022). *Standard method of test for determining the plastic limit and plasticity index of soils (T90)*. https://www.studocu.com/vn/document/dai-hoc-nha-trang/dong-luc-hoc-may-va-ket-cau-co-khi/aashto-t-90-22-determining-the-plastic-limit-and-plasticity-index-of-soils/84524957

[58] American Society for Testing and Materials. (2001). *Standard test method for specific gravity and water absorption of coarse aggregate (C127)*. https://cdn.standards.iteh.ai/samples/16248/d3b8da9eacbe4132bbfd396713e84689/ASTM-C127-88-2001-.pdf

[59] American Society for Testing and Materials. (1999). *Test method for soundness of aggregates by use of sodium sulfate or magnesium sulfate (C88)*. https://cdn.standards.iteh.ai/samples/1524/9c76b77219974fdc857031d16ec270d1/ASTM-C88-99a.pdf

[60] The Constructor. (2017). *Aggregate tests*. https://theconstructor.org/practical-guide/aggregate-crushing-value/2245/ (accessed 19-06-2023).

[61] American Association of State Highway and Transportation Officials. (2012). *Standard specification for stone matrix asphalt (M325)*. https://www.scribd.com/document/410673640/AASHTO-M-325-08-2012-Stone-Matrix-Asphalt-SMA-pdf

[62] NAPA. (2002). *Designing and constructing SMA mixtures: State-of-the-practice (Quality Improvement Series 122)*. National Asphalt Pavement Association.

[63] Murana, A. A., Olowosulu, A. T., & Ahiwa, S. (2014). Performance of metakaolin as partial replacement of cement in hot mix asphalt. *Niger J Technol, 33*(3), 387–393. [CrossRef]

[64] Grubeša, I. V., Barišić, I., Fucic, A., & Bansode, S. S. (2016). *Characteristics and uses of steel slag in building construction*. Woodhead Publishing.

[65] Amelian, S., Manian, M., Abtahi, S. M., & Goli, A. (2018). Moisture sensitivity and mechanical performance assessment of warm mix asphalt containing by-product steel slag. *J Clean Prod, 176*, 329–337. [CrossRef]

[66] Juckes, L. M. (2003). The volume stability of modern steelmaking slags. *Miner Process Extr Metall, 112*(3), 177–197. [CrossRef]

[67] Wu, S., Xue, Y., Ye, Q., & Chen, Y. (2007). Utilization of steel slag as aggregates for stone mastic asphalt (SMA) mixtures. *Build Environ, 42*(7), 2580–2585. [CrossRef]

[68] Zaidi, S. B. A. (2018). *The influence of hydrated lime on moisture susceptibility of asphalt mixtures* (Doctoral dissertation, University of Nottingham).

[69] Al-Marafi, M. N. I. (2021). Effects of hydrated lime on moisture susceptibility of asphalt concrete. *Adv Sci Technol Res J, 15*(2), 13–17. [CrossRef]

[70] Omar, H. A., Yusoff, N. I. M., Mubaraki, M., & Ceylan, H. (2020). Effects of moisture damage on asphalt mixtures. *J Traffic Transp Eng, 7*(5), 600–628. [CrossRef]

[71] McBain, J. W., & Hopkins, D. G. (2002). On adhesives and adhesive action. *J Phys Chem, 29*(2), 188–204. [CrossRef]

[72] Kiggundu, B. M., & Roberts, F. L. (1988). *Stripping in HMA mixtures: State-of-the-art and critical review of test methods*. NCAT Report No. 88-2.

[73] Shell. (2015). *The Shell Bitumen Handbook*. ICE Publishing.

[74] Nwaobakata, C., & Agunwamba, J. C. (2014). Effect of palm kernel shells ash as filler on the mechanical properties of hot mix asphalt. *Arch Appl Sci Res, 6*(5), 42–49.

[75] Pasetto, M., & Baldo, N. (2011). Mix design and performance analysis of asphalt concrete with electric arc furnace slag. *Constr Build Mater, 25*(8), 3458–3468. [CrossRef]

[76] Xie, J., Chen, J., Wu, S., Lin, J., & Wei, W. (2013). Performance characteristics of asphalt mixture with basic oxygen furnace slag. *Constr Build Mater, 38*, 796–803. [CrossRef]

[77] Kavussi, A., & Qazizadeh, M. J. (2014). Fatigue characterization of asphalt mixes containing electric arc furnace (EAF) steel slag subjected to long-term aging. *Constr Build Mater, 72*, 158–166. [CrossRef]

[78] Chen, Z., Wu, S., Xiao, Y., Zeng, W., Yi, M., & Wan, J. (2016). Effect of hydration and silicone resin on basic oxygen furnace slag and its asphalt mixture. *J Clean Prod, 112*, 392–400. [CrossRef]

[79] Yildirim, I. Z., & Prezzi, M. (2015). Geotechnical properties of fresh and aged basic oxygen furnace steel slag. *J Mater Civ Eng, 27*(12), 04015046. [CrossRef]

[80] Zhou, F., Im, S., Sun, L., & Scullion, T. (2017). Development of an IDEAL cracking test for asphalt mix design and QC/QA. *Road Mater Pavement Des, 18*(sup4), 405–427. [CrossRef]

[81] American Society for Testing and Materials. (2017). *Standard practice for open-graded friction course (OGFC) mix design (AD7064)*. ASTM International.

[82] Arrieta, V. S., & Maquilón, J. E. C. (2014). Resistance to degradation or cohesion loss in Cantabro test on specimens of porous asphalt friction courses. *Procedia Soc Behav Sci, 162*, 290–299. [CrossRef]

Journal of Sustainable Construction Materials and Technologies
Web page info: https://jscmt.yildiz.edu.tr
DOI: 10.47481/jscmt.1554809

JSCMT
Journal of Sustainable Construction Materials and Technologies

Research Article

Experimental investigation of mechanical and physical properties of glass fiber reinforced concretes produced with different magnetized waters

Serkan SUBAŞI[1], Doğu RAMAZANOĞLU[2], Muhammed MARAŞLI[2], Volkan ÖZDAL[2], Yasemin HATİPOĞLU[2], Heydar DEHGHANPOUR*[3]

[1]*Department of Civil Engineering, Düzce University Faculty of Engineering, Düzce, Türkiye*
[2]*Fibrobeton Company, Department of R&D, Düzce, Türkiye*
[3]*Department of Civil Engineering, İstanbul Aydın University Faculty of Engineering and Architecture, İstanbul, Türkiye*

ARTICLE INFO

Article history
Received: 21 May 2024
Revised: 03 July 2024
Accepted: 30 August 2024

Key words:
Fracture mechanics, GFRC, magnetized water, microstructure, UPV

ABSTRACT

Magnetized water may act as a thickener in cementitious mixtures due to its slippery effect. Therefore, it can be beneficial for the mixture to settle easily and to improve its strength. This study investigated the effects of magnetized water passing through pipes with magnetic field intensity (MFI) 8 and 10 on glass fiber reinforced concrete (GFRC). Three different mixtures, the GFRC mixture produced with regular tap water, were obtained, and the properties of the produced GFRC samples, such as 7, 14, and 28 days H-Leeb hardness, density, Ultrasonic pulse velocity (UPV), flexural strength, compressive strength, and fracture mechanics were investigated. In addition, SEM, EDS, FTIR, and TGA analyses were carried out to investigate the change in surface tension in the internal structures of GFRCs produced with magnetized water. Overall, the results were promising. Results showed a proportional H-Leep hardness increase with curing time and density variations. Magnetized water reduced air voids, enhancing sound transmission speeds. Flexural and compressive strength improved with magnetic water. The study suggests significant contributions to energy savings and reduced production costs, highlighting the efficient use of energy resources.

Cite this article as: Subaşı, S., Ramazanoğlu, D., Maraşlı, M., Özdal, V., Hatipoğlu, Y. & Dehghanpour, H. (2024). Experimental investigation of mechanical and physical properties of glass fiber reinforced concretes produced with different magnetized waters. *J Sustain Const Mater Technol*, 9(3), 280–293.

1. INTRODUCTION

Concrete is a composite with a wide area of use as a building material due to its high compressive strength, hardness, and durability [1]. At the same time, concrete is brittle and weak in tension. Low tensile and tensile strength is the weakest aspect of plain concrete. These deficiencies can be eliminated by retrofitting. Fiber-reinforced concrete (FRC) is a relatively new concrete material made from hydraulic cement, aggregates, and reinforcing fibers. It is a composite containing a dispersion of natural or artificial tiny fibers with high tensile strength. The fibers in its matrix increase the cracking strength of concrete [2]. There is nothing new in this technique, as using fibers in concrete is very ancient [3]. At the beginning of the 20th century, there were developments in the production of glass fibers, mainly of the borosilicate type (E-glass). The first production of Glass Fiber Reinforced Cement dates back to the late 1950s when E-glass fibers were combined with non-alkaline matrices. It was understood then that the al-

***Corresponding author.**
*E-mail address: heydar.dehghanpour@yahoo.com / haydardehgan@aydin.edu.tr

kaline environment of hardened ordinary Portland cement caused corrosion and loss of tensile strength of E-glass fibers. Therefore, Glass fiber reinforced concrete (GRC) production required unusual cement and was very limited. Unique alkaline-resistant glasses were only developed and produced on a commercial scale in the late 1960s [3, 4]. Glass fiber reinforced concrete (GFC) is a material that has contributed significantly to the economy, technology, and aesthetics of the construction industry worldwide for nearly 40 years [5].

Water that is exposed to a magnetic field is called magnetized water. At the end of this exposure, the physical properties of the water change [6]. The main difference between regular water and magnetized water is the hydrogen bonding. In normal water, water molecules behave in clusters that slide over each other, resulting from hydrogen bonding. As the hydrogen bond between these clusters and groups is broken in the water entering the magnetic field, the number of water molecules moving collectively decreases. Thus, the activity of the water increases [7, 8]. Magnetized water's electromagnetic properties, thermodynamic bond angle, dielectric constant, electrical conductivity, pH, solubility, viscosity, surface tension, boiling point, and freezing point differ from normal water [9]. Even if the magnetic field effect disappears, this change in the water shows its impact for a long time [10]. Applying the magnetic field causes a significant increase in the ultraviolet absorption of water. The exposure time of water to the magnetic field increases the absorption intensity of UV rays. In addition, magnetic water, which has a lower surface tension than pure water, turns into a more hydrophilic structure [11].

Surface tension in water is important for concrete's hydration and hardening process. During hydration, cement particles and water molecules react, forming a thin layer, which prevents the reaction from progressing. Because of this inhibition, the cement partially accompanies the reaction. Therefore, the strength values of the cement particles relative to the final concrete cannot be precisely obtained. Using magnetized water instead of regular water in the hydration process of concrete prevents the hydrate residue from forming around the cement particles since the surface tension is lower than regular water, thus allowing more cement to mix with water. Therefore, an improvement is observed in the strength values of the concrete to be formed [11–13].

This study examines the effects on the mechanical and physical parameters of GFRC concretes produced using magnetized water obtained from equipment with two magnetic fields with magnetic field intensity (MFI) of 8 and 10.

2. MATERIALS AND METHODS

2.1. Materials

In this study, Mk37 Silver (1.222 Kg. / 5 cm x 5 cm x 36 cm. / 8 magnetic fields. / 16 magnets) and Mk37 Gold (1.490 Kg. / 5 cm x 5 cm x 45 cm. / 10 magnetic fields. / 20 magnets), which outer surfaces are aluminum anodized and inner surfaces are chrome steel, with a diameter of ¾ inch and a minimum pressure strength of 2 Bar, were used to obtain magnetized water (Fig. 1). CEM II/B-L 42,5R Portland cement was the binder material. Silica sand with a diameter of less than 1 mm was used as filling material, and Calcined kaolin (2.52 g/cm^3) was used as pozzolanic. Fibro WR-78 was chosen as the superplasticizer. Alkaline-resistant glass fibers (AR-GF) with a length of 12 mm and a diameter of 14 µm were used as the fiber. The chemical components of cement, calcined kaolin, and silica sand used in GRC production are summarized in Table 1. Sample views of the materials used in the study are shown in Figure 2.

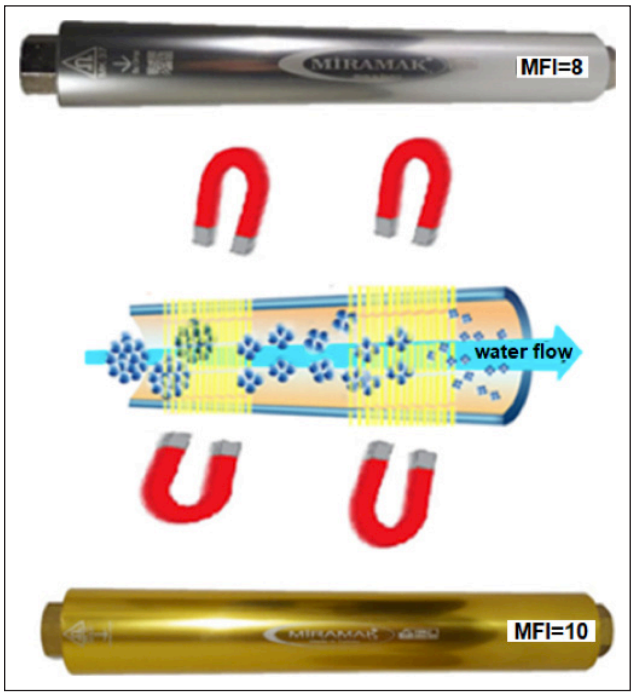

Figure 1. The divergence of water molecules from each other by the effect of the magnetic field.

Table 1. Chemical components of mineral materials used in the construction of GRC

components (wt.%)	Cement	Silica sand	Calcined kaolin
SiO_2	17.46	98.57	59.78
$A1_2O_3$	3.27	0	10.23
Fe_2O_3	0.21	0.17	0.44
CaO	63.04	0.29	9.91
MgO	1.67	0	1.59
K_2O	0.34	0.16	0.9
Na_2O	0.3	0	0.05
SO_3	3.02	0	1.25
P_2O_5	0.04	0.01	0.04
TiO_2	0.09	0.12	0.15
Cr_2O_3	0.0021	0.0137	0.0186
Mn_2O_3	0.0042	0.0029	0.0077
LOI	11	0.39	16.24

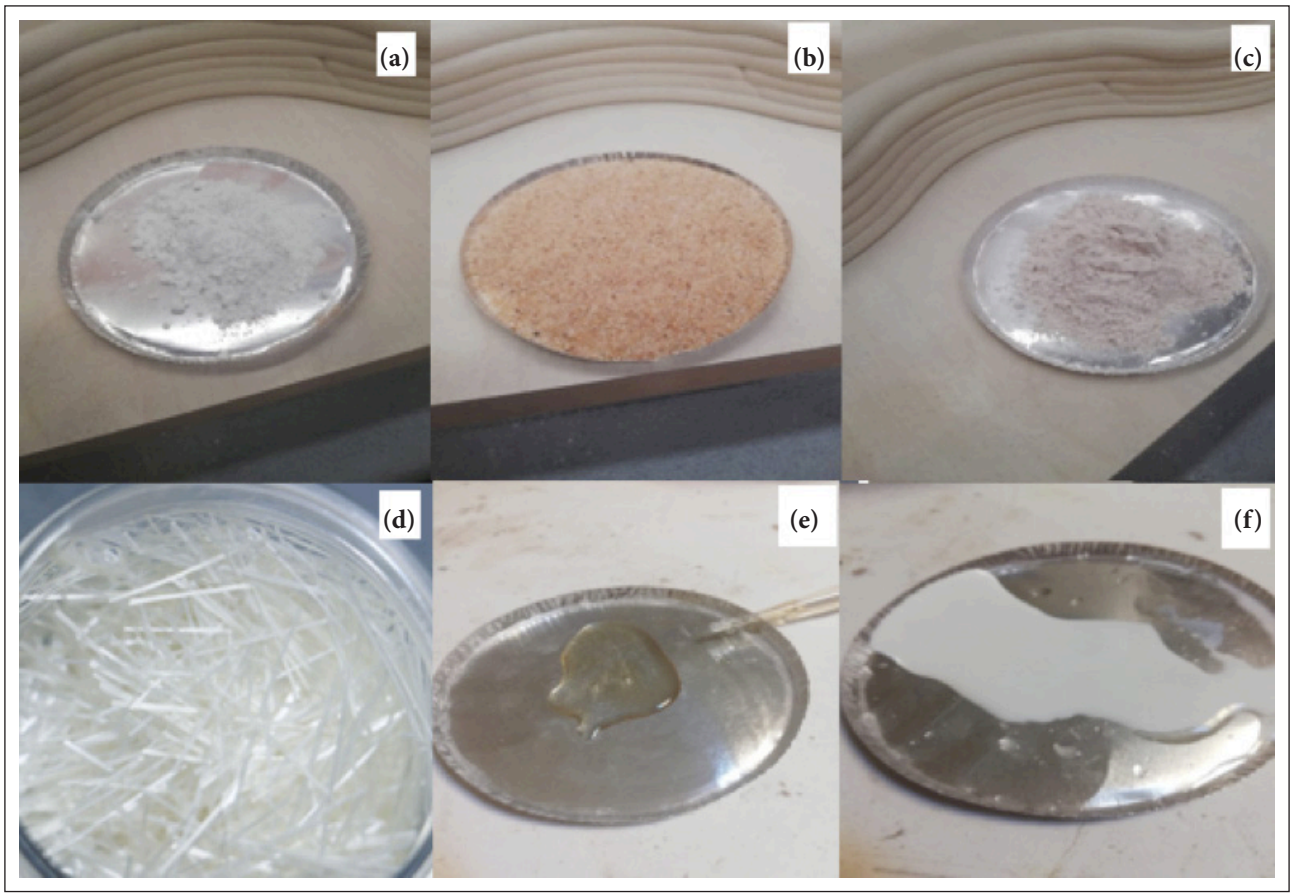

Figure 2. GRC concrete mortar components; CEM II/B-L 42.5R Portland Cement **(a)**, Aggregate/Silica sand **(b)**, Calcined kaolin **(c)**, Alkali resistant glass fibers **(d)**, Plasticizer **(e)** and **(f)** Acrylic polymer.

Table 2. Type and proportions of materials used

No	Material	Type	Amount
1	Cement	Çimsa white 42.5 R	33.75 kg
2	Silica sand	AFS NO: 30–35	37.95 kg
3	Water	Tap water/MFI8/MFI10	12.00 kg
4	Polymer	Betton Bettolatex	1.23 kg
5	Plasticizer	Fibro WR-78	90.00 g
6	Mineral additive	Calcined Kaolin	3.75 kg
7	Fiber	Alkaline-resistant glass fibers 32 mm	3.27 kg

2.2. Method

Spray and premix methods are generally used in GRC production [14, 15]. In this study, the premix method was preferred. The GRC mixture of cement, aggregate, calcined kaolin, and glass fibers was mixed in dry form for about 3 minutes. Then, acrylic polymer, superplasticizer, and magnetized water were added and mixed for 2 minutes. All mixes were produced with a single design component specified in Table 2.

For compressive strength, cube samples of 50 mm^3 were prepared, and their 7, 14, and 28-day strengths were tested according to the TS EN 196-1 standard [16]. Before the compressive strength tests, the density values of the 7, 14, and 28-day-old concrete samples were determined. In addition, Leeb hardness tests of cube samples were carried out according to ASTM-A956 [17]. To determine the flexural strength of the composites, the tests of 270 × 50 × 12 mm samples at 7, 14, and 28 days were carried out according to the TS EN 1170-4 standard [18]. Ultrasonic pulse velocity (UPV) tests were carried out according to ASTM C 597 standard [19] to determine the ultrasonic sound transmission velocity of GRC concrete samples. The morphologies of GFRC samples were analyzed by scanning electron microscopy (SEM) on an FEI model Quanta FEG 250 in secondary electron mode at 10 keV. Fourier Transform Infrared Spektrofotometre (FT-IR) analyses were performed to examine the molecular bond properties of the samples. Thermogravimetric analysis (TGA) and differential scanning calorimetry (DSC) measurements were performed with Shimadzu DTG

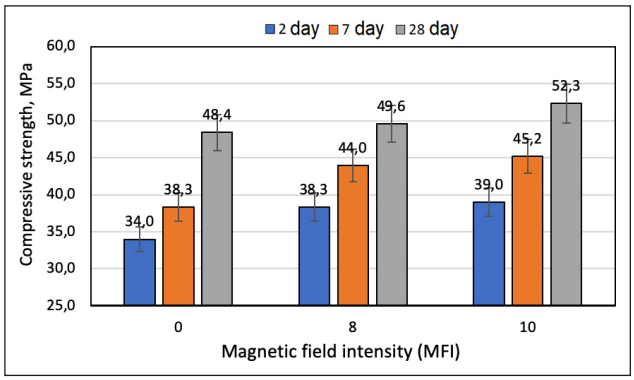

Figure 3. Compressive strengths of GRC composites produced with different magnetic waters.

60H - DSC 60 Thermal Gravimetric Analyzer with high purity nitrogen and 50 mL/min flow rate.

3. RESULTS AND DISCUSSION

3.1. Compressive Strength of GRC Composites

The compressive strengths of GRC concrete prepared with water magnetized in different magnetic fields are given graphically in Figure 3 according to different curing times and magnetized areas. As evident in the graph and other test results, curing periods have positively influenced the compressive strength of concrete, and the use of magnetized water in mortar production is observed to enhance the compressive strength performance of specimens compared to those produced with normal water. The performances at early curing periods, considered as 2 and 7 days, in GRC specimens produced with water exposed to 8 magnetic fields have shown increases of 12.4% and 14.9%, respectively. The ratio of compressive strength performance at 28 days is 2.48%, indicating a relatively lower increase compared to the early ages. In GRC specimens produced with water passing through 10 independent magnetic fields, the compressive strength performances for early periods were 14.7% and 18.0%, and a subsequent increase of 8.05% was observed in the long-term aging at 28 days. An increase in NMF enhances the mechanical strengths of GRC concrete material.

Magnetized water is a type of water that has been treated under the influence of a magnetic field, which organizes the water molecules and changes the physical properties of the water [20]. This water can affect reactions and material properties in the concrete mixture. Various studies [21–24] show that magnetized water can positively affect concrete strength. Magnetized water is thought to help arrange the water molecules in the concrete mixture and hydrate the cement particles more effectively. This can increase the early strength of concrete and improve its overall mechanical properties. However, these effects can vary depending on many factors, so obtaining specific results for each concrete mix and type of magnetized water is essential. The impact of magnetized water on the strength of concrete will depend on a number of factors, including various parameters such as mixing proportions, type of cement used, strength, and duration of the magnetic field [25].

In an experimental study, Ghorbani et al. [21] investigated that using magnetized water can positively affect concrete mixtures, especially its effects on foam stability, compressive strength, tensile strength, water absorption, and microstructure of foam concrete. Tests conducted on 9 different mixtures prepared with water passed through a constant magnetic field at various flow rates and in different numbers showed that using magnetized water increases foam stability and improves foam concrete's compressive and tensile strength. However, a slight decrease in the water absorption of the hardened foam concrete was observed. The high compressive strength of samples with magnetized water can be attributed to the high specific field compared to normal water. The activity of magnetized water increases, and the interaction with cement particles increases, which can increase the compressive strength and split tensile strength. Su et al. [22] have investigated the compressive strength and workability of mortar and concrete mixed with magnetic water. The study reveals a 9–19% increase in compressive strength for mortar samples using 0.8–1.35 T magnetic water and a 10–23% increase for concrete samples. Additionally, magnetic water has improved the mortar and concrete's flowability, slump, and hydration degree.

Keshta et al. [23] examined the impact of magnetized water on the compressive strength of concrete. The results indicate that the use of magnetized water increased the pH value. The magnetic field was determined to raise pH by 12.6%, possibly due to a decrease in hydrogen ion concentration. Additionally, the polarization of water molecules and a reduction in hydrogen ions enhance the organization of water molecules, improving the hydration process. This results in greater cohesive forces applied to cement-based material particles, enhancing concrete properties. The post-use increase in pH due to magnetized water reduces corrosion rates and increases compressive strength. Acidic water negatively affects concrete's compressive strength. From a workability perspective, a higher pH positively influences concrete workability; using magnetized water can reduce slump values by causing minimal excess cement and fine particles. Therefore, increasing the pH value of the water used can improve concrete properties.

3.2. Flexural Strength of GRC Composites

The flexural strengths of GRC concrete samples produced with magnetic water appear to be higher than the reference sample (Fig. 4). The direct relationship between the number of magnetic fields and the magnetic effect of water on homogeneous hydration in the flexural strength tests has been observed. In the early-age flexural strengths, the GRC concrete sample produced with water exposed to 8 magnetic fields exhibited a flexural strength trend of 18.3% compared to the reference sample in 7-day specimens. However, despite an increase in the 14-day strengths, it demonstrated an 11.4% lower performance than the reference sample. Similar to other tests, magnetic water tends to enhance the strength properties of the sample at early ages. Although the strength property of the same sample increased compared to the reference after 28 days, there

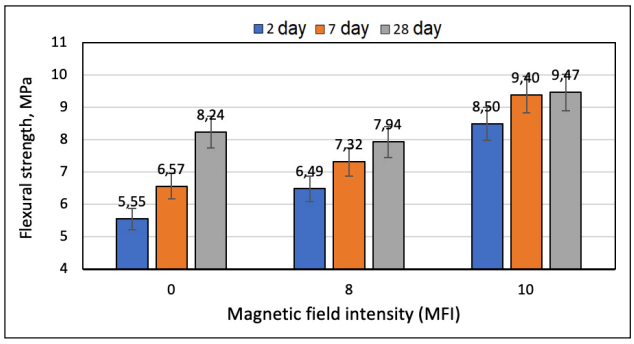

Figure 4. Flexural strengths of GRC composites produced with different magnetic waters.

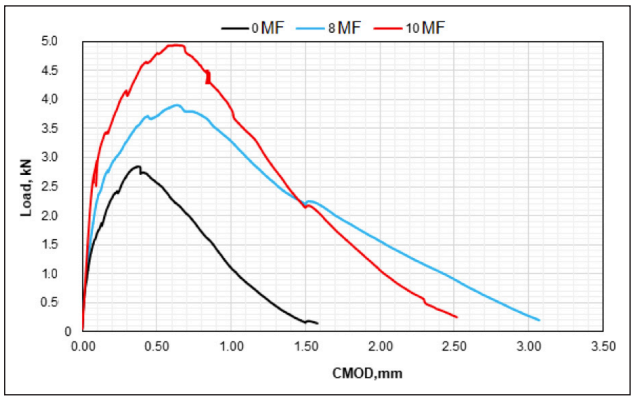

Figure 5. Fracture mechanics curves of GRC beams produced with different magnetic waters.

was a 3.64% increase in the reference sample. In GRC samples produced with water exposed to 10 magnetic fields, an increase in sound conductivity was observed, with higher percentages of 53.1%, 43.1%, and 14.9% in 7, 14, and 28-day curing times, respectively, demonstrating a tendency for a decrease in increase proportional to the curing periods compared to the reference sample.

Using magnetized water can cause cement particles to interact more strongly with water molecules. This may contribute to the cement matrix creating a stronger structure and increasing its bending strength. Also, the positive effects of magnetized water on the flexural strength of cement can be attributed to the C-S-H development in the cement paste. There is no definitive information about how magnetized water affects the C-S-H (calcium silicate hydrate) gel of cement because there are very few scientific studies on this subject. However, some research suggests that magnetized water organizes water molecules, changing the molecular structure of water, and these changes may impact cement hydration [26–28]. Cement hydration involves the formation of C-S-H gel due to the reaction of cement particles with water [29]. It is thought that using magnetized water may contribute to water molecules binding more effectively to cement particles and creating a more ordered structure in the process [30]. This may lead to the forming of a more solid and ordered structure of the C-S-H gel.

In addition to the effect of magnetized water, which is the primary purpose of this study, the most crucial factor affecting flexural strength is the glass fiber used in the mixtures. Glass fibers improve the flexural strength of cementitious composites by increasing their tensile strength. This ensures that the structural elements have a greater load-carrying capacity [31]. Glass fibers can limit the formation of cracks in concrete. This prevents cracks from propagating and ensures more consistent performance of the material [32]. Glass fibers can help make concrete more resistant to environmental influences (for example, freeze-thaw cycles), thus ensuring the longevity of the material [33]. Glass fibers can provide better shaping of the concrete mixture. This will be advantageous in accommodating bending and tensile loads, especially for architectural elements with complex or fine details [34]. In glass fiber reinforced concretes, the interaction of glass fiber with C-S-H gel during the hydration process with cement plays an important role [35]. Glass fibers can form a network surrounding the C-S-H gel, which can reduce crack formation [36]. Additionally, the surface properties of glass fibers enable hydration products to bind and form a strong bond. This interaction can increase the durability and mechanical properties of glass fiber-reinforced concrete, significantly improving tensile strength and crack resistance [37].

3.3. Fracture Mechanics of GRC Composites

Within the scope of fracture mechanics, the amount of energy absorbed by cementitious materials against fracture is examined through the three-point bending test. This test method creates a notch (crack) at one-third of the beam cross-sectional height in the middle of pre-cast cementitious beam specimens. Notched specimens are subjected to loading until a fracture occurs [38]. This test can usually be controlled by increased crack mouth opening displacement (CMOD). The load-CMOD curves of GRC concrete samples obtained using water exposed to two different numbers of magnetic fields are given in Figure 5. Considering the load values in the graph, and it is observed that the maximum fracture load increases with the increase in the number of MF. The maximum fracture load of GRC produced with water passed through NMF 8 increased by 39% compared to the reference, while the maximum fracture load of GRC produced with water passed through NMF 10 increased by 75% compared to the reference.

On the other hand, the magnetic field also positively affected the samples' flexibility. Crack opening corresponding to maximum load values was measured as 0.4, 0.62, and 0.66 mm for samples with NMF numbers of 0, 8, and 10, respectively. Also, the increase in total CMOD values proves magnetized water's positive effect on the samples' elastic properties. The positive effect of magnetized water on fracture mechanics can be attributed to the C-S-H development and the compressive and bending strength results. In addition, since the most important factor affecting the fracture mechanics of fibrous concrete is the shape of the fibers, it can be said that magnetized water also causes the homogeneous distribution of the fibers.

Aligning steel fibers is an effective way to improve the mechanical properties of steel fiber cement composites

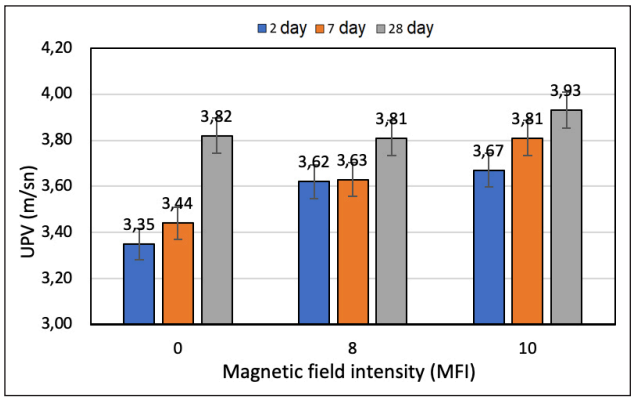

Figure 6. UPV results of GRC composites produced using water with different magnetic properties.

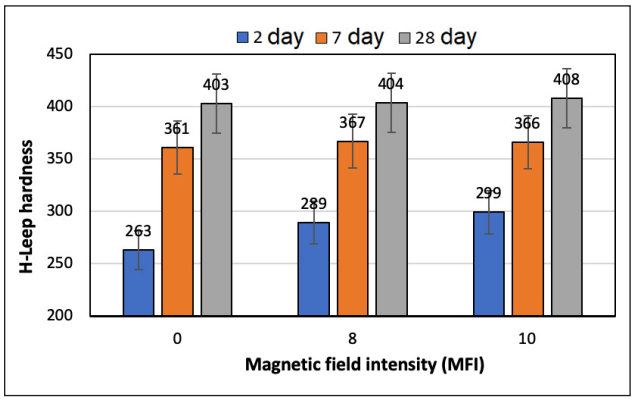

Figure 7. Effect of water exposed to different magnetic fields on H-Leep hardness values of GRC composites.

(SFRC). Some studies have investigated creating a magnetized field to align the fibers in steel fiber-reinforced concrete. However, no specific research has been found regarding creating a magnetized field in synthetic fiber-reinforced cementitious materials or the mechanical behavior of cementitious products produced with magnetized water. Khan et al. [39] investigated the preparation and fracture behavior of aligned hooked-end steel fiber cement-based composites (ASFRC) using the magnetic field method. The mixture's rheology and the magnetic induction of the electromagnetic field for aligning steel fibers were theoretically analyzed. The results demonstrated that the cracking load and ultimate load of ASFRC increased by approximately 24–55% and 51–86%, respectively, compared to SFRC. The tensile strength and residual flexural strength of ASFRC increased by 105% and 100%, respectively. ASFRC exhibited 56–70% higher fracture energy than SFRC, indicating that the reinforcing effect of hooked-end steel fibers was superior to straight steel fibers.

3.4. UPV Test Results of GRCs

The most common method for assessing the strength quality of concrete is the compressive strength test. Alternatively, the ultrasonic pulse velocity (UPV) test can be applied as a non-destructive method to obtain information about the durability of concrete [40]. Figure 6 presents the UPV test results for GRC concretes produced with magnetized water. The GRC matrix provides sound insulation within the structure, consequently reducing the transmission speed of sound waves. The increased sound speed indicates the composite has a homogeneous and solid structure. An increase in the speed of sound indicates that the composite is in a homogeneous and robust state. The voids within the structure change inversely with density. For GRC composites produced with water exposed to 8 magnetic fields, the sound wave transmission ratios on the early ages of the 2nd and 7th days have increased by 8.06% and 5.52%, respectively, compared to the reference sample. In the GRC composites produced with water exposed to 10 magnetic fields, the speed of sound has increased by 9.55% and 10.7%, respectively. It can be inferred that water with a higher MFI number has facilitated the formation of a more

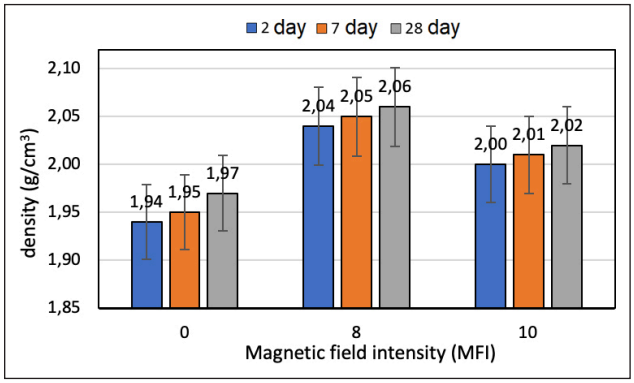

Figure 8. Density values of GRC composites produced using water with different magnetic properties.

homogeneous structure with lower surface tension in the cement-based composite, resulting in a structure with more voids. Therefore, sound transmission has been accelerated in the early stages due to the rapid transmission of magnetic water. In the later stage of aging, on the 28th day, the sound transmission speed of the concrete produced with magnetic water exposed to 8 magnetic fields was observed to be 0.26% less than the reference sample. However, the sound transmission speed of the GRC sample produced with water magnetized by 10 magnetic fields continued to increase by 2.88% compared to the reference sample. The increase in MFI has ensured a more homogeneous hydration reaction between cement and water in the GRC matrix, maintaining the magnetic effect of water for a more extended period and resulting in a structure with fewer voids.

When UPV values are compared with density values in terms of the use of magnetized water and regular water, it is evident that there is a parallel relationship between them. However, both UPV and density values did not yield significantly different results using magnetized water. In their experimental study, Yousry et al. [41] investigated the mechanical properties and UPV values of cement-based mortar using magnetic water. According to the results obtained, while there were profound differences between the strength values, the UPV results did not show a trend that could be followed or trusted. UPV values are generally inversely proportional to the void ratio within the material. Gaps make it

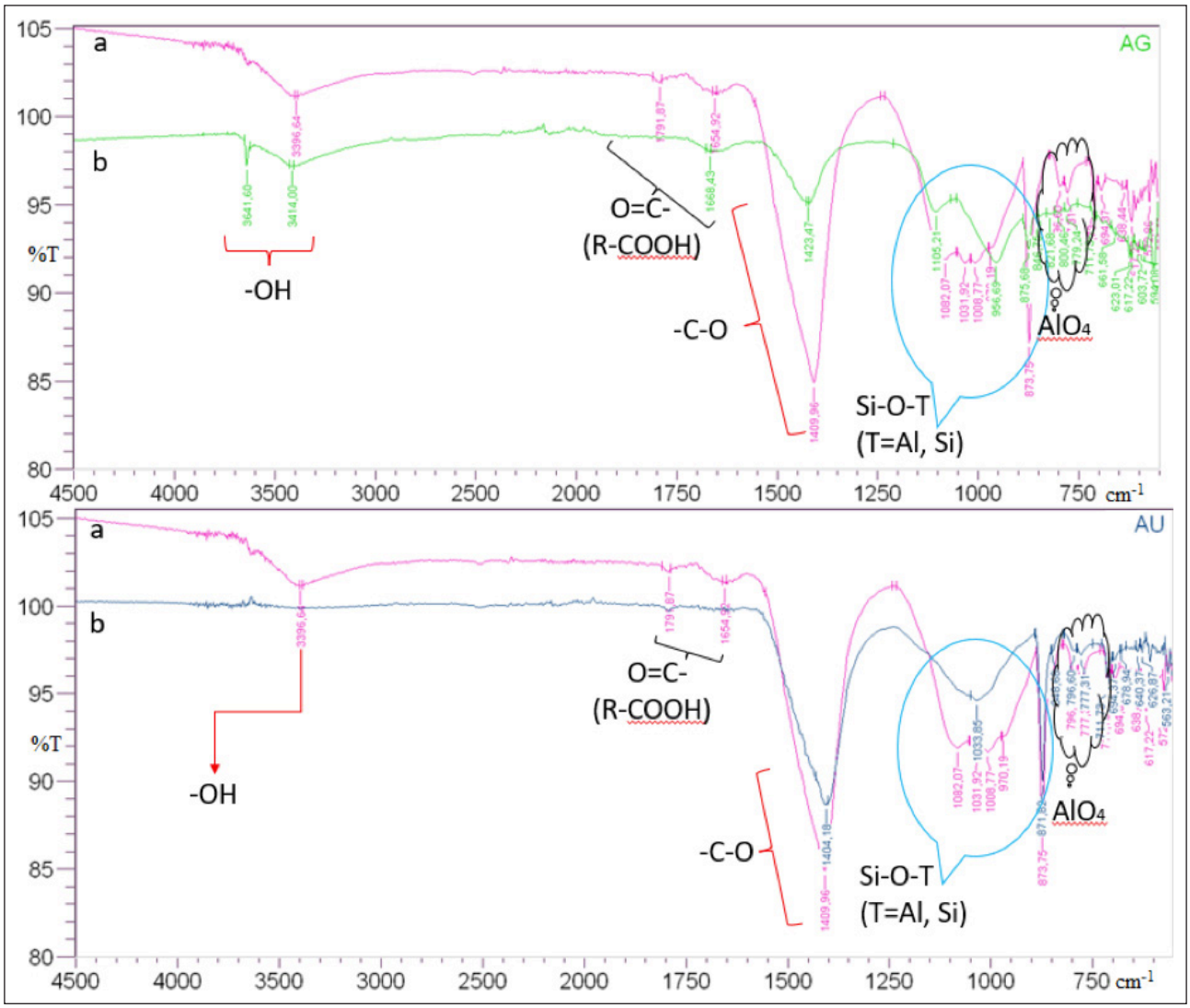

Figure 9. FTIR spectra of GRC composites produced with different magnetic waters.

difficult for sound waves to propagate, resulting in low UPV values, and a cement mat hasvoid ratio will generally have higher UPV values [42]. UPV values are directly proportional to the density of the material. A dense material allows sound waves to be transmitted more quickly and effectively, leading to high UPV values [43].

3.5. H-Leep Hardness Tests of GRC Compo

Hardness tests are a type ofprovidetructive testing that provides information about the surface hardness of cement-based structural composite materials [44]. Figure 7 shows the effects of magnetic field and curing times on Leep hardness values. The increase in curing periods has resulted in a proportional increase in hardness values for reference and other magnetized specimens. The rise in MFI has facilitated faster initial increases in Leeb values compared to the reference, with lower contribution rates throughout the curing period. The increase in the specimen left for 2 days under exposure to 8 magnetic fields is observed to be 9.88%, while for the specimen exposed to 10 magnetic fields, this ratio is 13.6%. After a curing period of 7 days, a decrease in percentage increases in Leeb values is evident, with rates of 1.66% and 1.38% for samples exposed to 8 and 10 magnetic fields, respectively. For specimens with a curing period of 28 days, the increases in Leeb hardness values are 0.24% and 1.24%, respectively. According to these values, it is observed that the magnetic water accelerates early curing periods in H-Leeb values; however, as the curing period increases, this effect diminishes.

The Schmidt hammer is the most commonly used testing tool to estimate the compressive strength of concrete non-destructively. However, few studies are in the literature on applying the Leeb hardness test to estimate concrete strength. The Leeb rebound hammer is a dynamic hardness test method and instrument developed initially for testing metallic materials. On the other hand, the Schmidt rebound hammer showed different correlations with compressive strength for concretes with different w/c ratios. The authors also discussed factors influencing the hardness value, such as surface moisture conditions and concrete carbonation. They observed that the Leeb rebound numbers were higher for older concretes and weaker concrete compositions at higher w/c ratios due to faster carbonation rates in more porous systems.

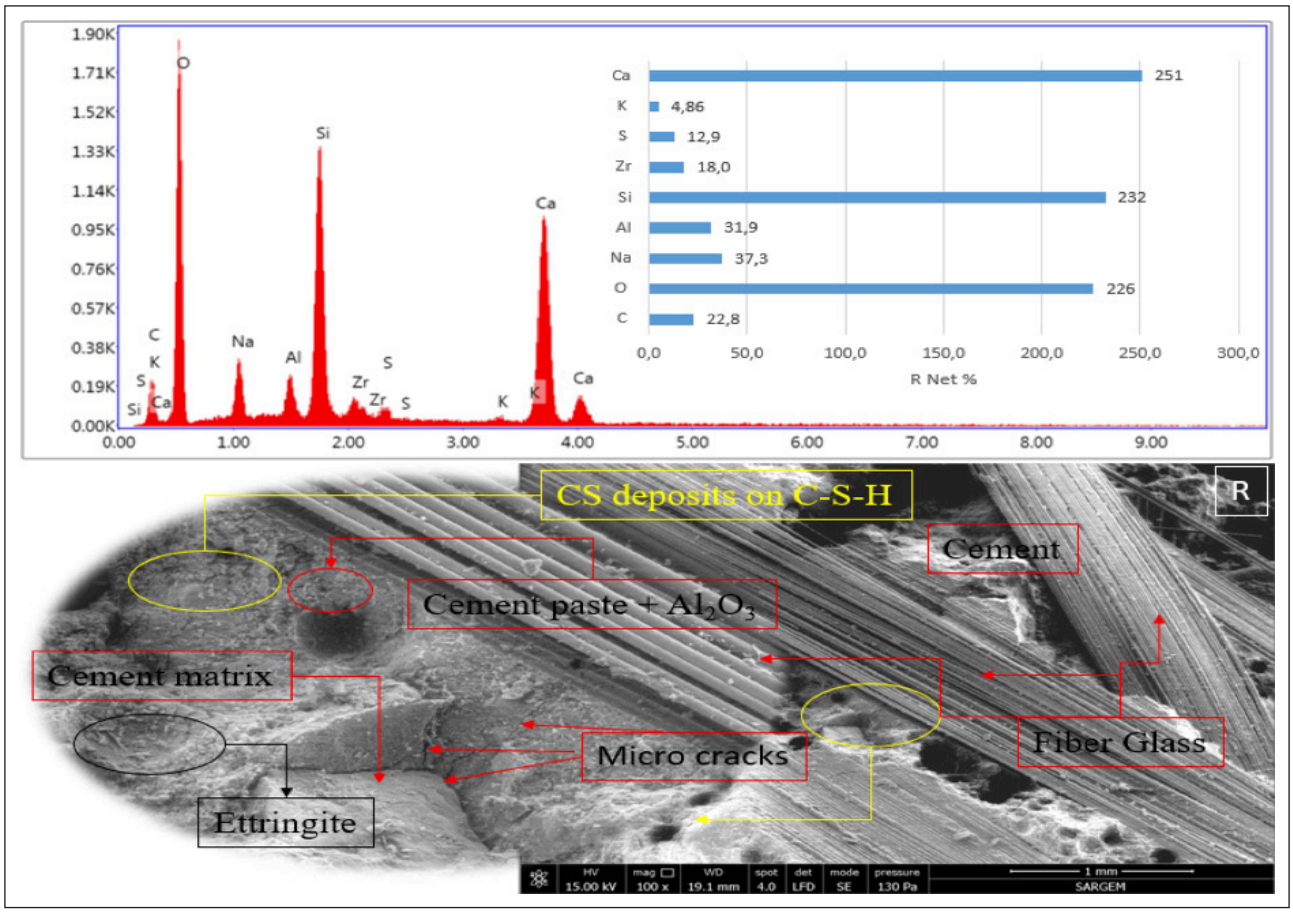

Figure 10. SEM image and EDS spectrum of reference GRC composite.

Dehghanpour et al. [38] examined the hardness properties of Ultra High Strength Concrete (UHPC) structural elements produced for facade elements. The results of the Leeb and Schmidt hammer hardness of PVA, GF, and SF-reinforced UHPC samples were compared and evaluated. A linear relationship was observed between Leeb and Rebound number values for all mixtures, and it was stated that these two hardness test methods were used to verify the values obtained from each other. While Leeb hardness values decreased in samples with PVA added, a decrease was observed in samples with GF added; There was an increase and decrease in samples with SF added. Similar changes were detected in Schmidt hardness values. The results showed that SF-reinforced samples had the highest hardness values. Compared with the literature, it was concluded that the hardness values obtained were suitable for high-strength concretes.

3.6. Density Values of GRC Composites

Before compressive strength evaluations, density measurements of GRC samples were made. The values are summarized in Figure 8. By the Archimedes principle, and these measurements explored the variations in the density values of GRC samples subjected to curing periods of 2, 7, and 28 days, as well as exposure to two different magnetic drinks of water, one at 8 and the other at 10 magnetic fields. Density differences were observed within the specified curing periods for reference samples, ranging between 1.94 and 1.97 g/cm^3. Samples produced with water obtained from 8 magnetic fields exhibited density values between 2.04–2.06 g/cm^3, while those made with water passing through 10 magnetic fields showed a distribution between 2.01–2.07 g/cm^3. In cement-based materials, density values are correlated with the water-to-binder ratio, where the binder component is typically cement [45]. In this study, as the water-to-cement ratio was kept constant, the variations in density values were found to be dependent on both the age of the concrete and the magnetic field.

The variation in density values of GRC concrete samples is generally directly associated with the curing period. The interaction of water in the mortar with cement hydration and water's subsequent evaporation from porous structures significantly influences density [46]. The magnetized water ratio resulted in a decrease in density increase compared to the reference sample, with a reduction of 5.07% on the 2nd day, 4.87% on the 7th day, and 4.83% on the 28th day. In other words, the magnetized water may have acted as a catalyst, accelerating the early curing period but losing its magnetic effect relatively quickly.

3.7. FTIR Analysis Results

FT-IR (Fourier Transform Infrared) analysis in cementitious composites is a technique used to understand the material's chemical composition and molecular structure [47]. Since polymer binders are frequently used, especial-

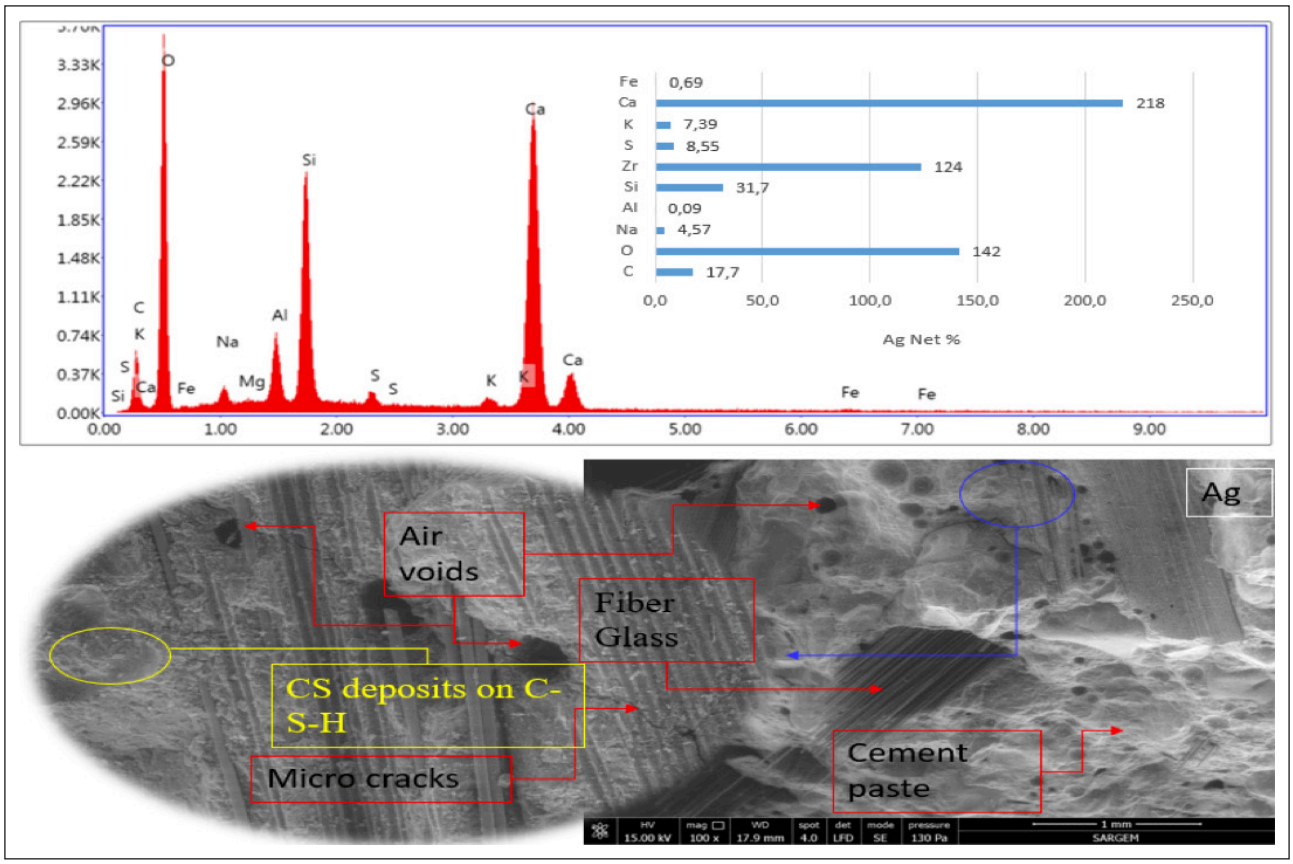

Figure 11. SEM image and EDS spectrum of GRC composite produced with water magnetized in eight magnetic fields.

ly in cementitious composites, this analysis can effectively determine the polymer's type and molecular structure. Because cementitious composites react with water during the hardening process, FT-IR analysis provides information on water content and hydration products [48]. This can affect the durability and structural properties of the material. FT-IR spectrum can identify various chemical bonds and functional groups. This gives information about the polymer material and additives or other ingredients within the composite material [49]. Cementitious composites often contain mineral additives. FT-IR analysis can help determine the presence and amount of mineral inclusions (e.g., quartz, calcite). FT-IR analysis can monitor chemical changes when cementitious composites are subjected to aging, environmental influences, or chemical attack [50].

FTIR spectra of GRC samples produced with magnetized water are given in Figure 9. The absorption bands observed at 3341.60 cm^{-1} and 3414.00 cm^{-1} in the spectrum with a magnetic field strength of 8 (Ag) are attributed to the vibrations of hydroxyl (-O-H) bonds in water molecules. These bands are also present at 3396.64 cm^{-1} in the reference spectrum. No hydroxyl band is observed in the spectrum with a magnetic field strength of 10 (Au). Previous studies [51, 52] have suggested that this band is associated with water molecules absorbed in voids formed on the surface or during copolymerization.

The bands around 1400 cm^{-1} are attributed to carbonate groups (O-C-O) formed due to the atmosphere's reaction between alkali metal hydroxides and carbon dioxide [47, 49]. The irregular strains associated with the (Si-O-X) bond encompass all vibrations around 1050 cm^{-1}. X represents silicon (Si) and aluminum (Al) atoms in a tetrahedral structure. The (Si-O-X) bond supports the geopolymerization process with the phases of the formed amorphous aluminosilicates. Studies indicate that the sharp absorption band is related to the number of tetrahedrally coordinated aluminum in the geopolymer gel [53, 54]. Peaks between 750 cm^{-1} and 800 cm^{-1} are attributed to vibrations from AlO4, while strong tension and vibration peaks between 950 cm^{-1} and 1050 cm^{-1} belong to Si-O-T (T= Al, Si). AlO4 represents a chemical group in which aluminum forms a tetrahedral structure with four oxygen atoms [55]. This may be due to amorphous aluminosilicate phases present in the cementitious composite, and these peaks provide information about the aluminum content of the material. Si-O-T represents tetrahedral structures formed by silicon bonding with oxygen and other elements [56]. These peaks offer information about the bonding pattern of silicon and aluminum in the cementitious composite.

3.8. Characterization of SEM and EDS Analysis

The Figure 10, Figure 11, and Figure 12, respectively, describe the physicochemical changes in the structure of the reference GRC sample and GRC concrete produced with water exposed to eight and ten magnetic fields, illustrating alterations during the hydration process. It has been observed that water exposure to a magnetic field leads to an increase in conductivity and a decrease in surface tension. This indi-

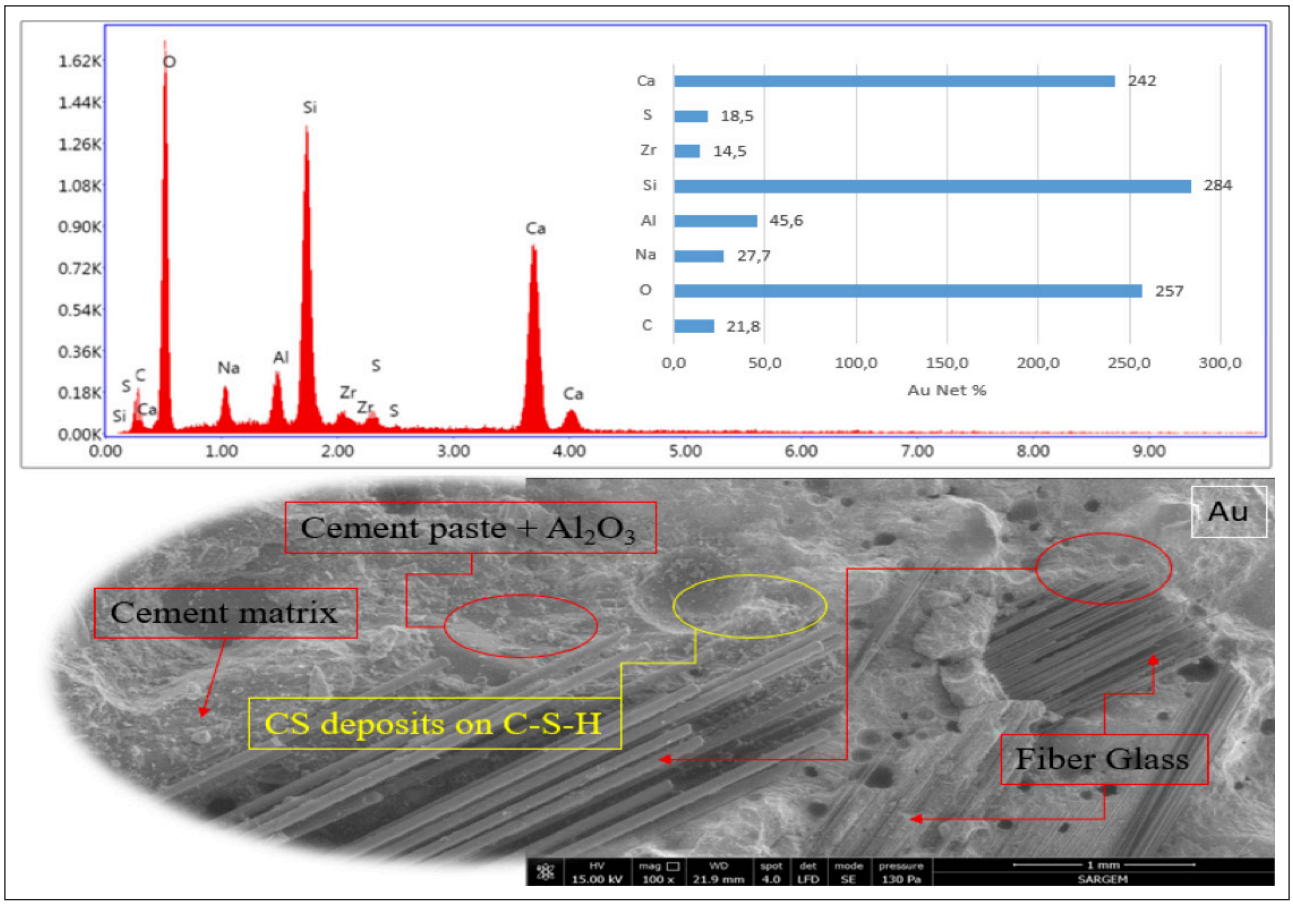

Figure 12. SEM image and EDS spectrum of GRC composite produced with water magnetized in ten magnetic fields.

cates the influence of the magnetic field on the structure of water molecules. Following exposure to the magnetic field, water molecules exhibit changes in their bonding angles, decreasing from 104.5° to 103° and forming single or more minor groups rather than clusters. The reduced surface tension allows for more homogeneous water hydration with cement, reducing the required water-to-cement ratio for setting. The quality and type of raw materials used determine the physicochemical and mechanical properties of the concrete.

Additionally, the quality and quantity of water play a significant role in determining the strength of the concrete. In the literature, although detailed explanations of how magnetic fields affect the structure of water are not explicitly mentioned, it is observed that magnetized water disperses cement particles more effectively compared to regular water. Regarding the hydration of cement, the net percentages of Ca, Al, and O elements, allowing for interpretations, have been measured as 251%, 31.9%, and 226%, respectively (Fig. 10).

According to the results of Energy Dispersive Spectroscopy (EDS) in Figure 11, the chemical element contents of the examined samples have been considered. In comparison to the reference sample, the GRC sample exposed to a magnetic field shows the presence of 218% calcium (Ca), 0.09% aluminum (Al), and 142% carbon (C) elements. This indicates a decrease in these elements compared to the reference sample. Similarly, in the EDS spectrum of the GRC sample produced with water passed through 10 identical magnetic fields (Fig. 12), 242% calcium (Ca), 45.6% aluminum (Al), and 257% oxygen (O) elements were detected. In other words, the increase in the number of magnetic fields has led to an overall increase in the percentage of aluminum, carbon, and oxygen elements. These results demonstrate that the magnetic field influences the chemical composition of GRC samples produced with water, causing significant changes in element contents.

The microstructure of cement mortar produced with water exposed to a magnetic field can be examined using various analytical techniques. Electron microscopes, X-ray scanning microscopes, and other relevant methods can be employed to assess the microstructural properties of the mortar. Water exposed to a magnetic field can influence the crystal structures of the cement mortar [57]. This can lead to changes in the crystal sizes, shapes, and distributions of cement mineral phases. The impact of the magnetic field on the water's structure can affect the porosity of the cement mortar. Achieving a more regular microstructure or reducing porosity can enhance the material's durability. Water exposed to a magnetic field can also influence the hydration process of the cement mortar, leading to the formation of different hydration products [26]. This can impact the mechanical properties of the material. This type of water can affect the homogeneous distribution of minerals in the cement mortar. This condition can determine whether the material has homogeneous mechanical properties.

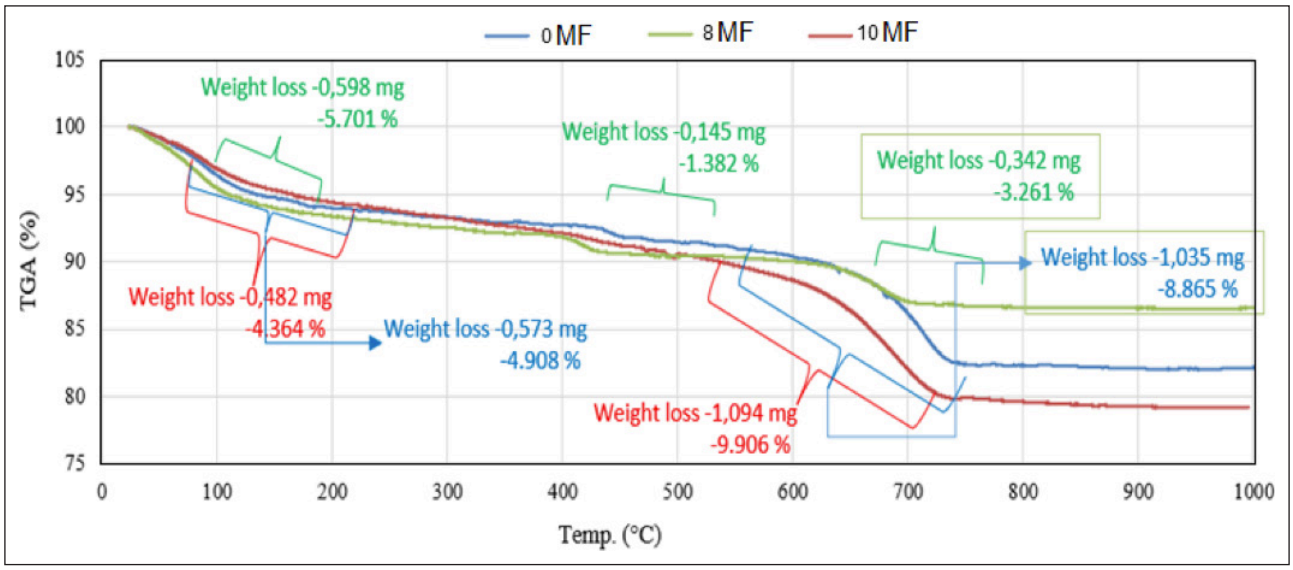

Figure 13. TGA spectrum curves of GRC composites produced with different magnetic waters.

3.9. TGA Analysis

Figure 13 shows the TGA analysis spectra of GRC samples prepared using water exposed to different numbers of magnetic fields. The amount of C-S-H increases with hydration and reaches its maximum level during heating. It is possible to predict the amount of C-S-H by measuring the water loss from C-S-H through TGA analysis. This is because the dehydration and decomposition of C-S-H and Aft (trisulfoaluminate-4CaO.3Al_2O_3.3$_2H_2O$) phases occur between 25 °C and 200 °C. However, the exact decomposition temperature of C-H-S, i.e., the range of departure of physically and chemically bound water content, is unknown. For instance, Taylor and colleagues have determined this range as 115–125 °C, while Odelson and his group have predicted a 200–400 °C range for water loss in C-S-H [58]. The water mass loss observed at 26.98–90.29 °C in the reference sample is 0.573 mg, accounting for 4.908%. For sample b with a magnetic field number (NMF) of 8, the mass loss is measured as 0.598 mg at 83.98 °C–269.0 °C, corresponding to 5.701%. In sample c with NMF = 10, the amount of lost water mass is determined as 0.482 mg at 30.01 °C–86.44 °C, accounting for 4.364%. The sample obtained with magnetic water and an NMF of 8 shows that the hydration amount is higher compared to the reference. This is because the lost water amount is directly proportional to the amount of C-S-H. Compared to the reference sample, a higher cement hydration of 4.36% is observed. The increase in the number of magnetic fields is evident in the TGA graph of sample c, showing a more precise water mass loss. The lost water amount measured as 0.482 mg in sample C, produced with water passed through 10 magnetic fields, is 15.9% higher than the reference sample.

It occurs between 105–130 °C. Some researchers say this limit can be close to 100 °C or 145 °C [59]. A similar explanation has been expressed for analyzing reactive powder concrete [60]. The amount of bound water in reactive powder concrete can be related to cement hydration through the classical Powers equation (1).

$$\alpha\% = Wne(t).Wne(t\infty)*100 \quad (1)$$

Here, Wne(t) represents the amount of bound water at time t, and Wne(t∞) is the required amount of water for complete cement hydration according to the calculation by Czernin [61]. In this study, Wne(t∞) is determined to be 0.25. Thermogravimetry can also be used to predict the pozzolanic reaction of silica fume. The content of calcium hydroxide ($Ca(OH)_2$) can be calculated from the peaks observed in the DTG curve between 400 °C and 500 °C. The peak between 500 °C and 750 °C represents the decarbonization of $CaCO_3$. The decarbonization of calcium carbonate was found to be 1.035 mg with 8.865% in sample (a), 0.342 mg with 3.261% in sample (b), and 1.094 mg with 9.906% in sample (c). An increase in the amount of calcium carbonate is observed proportionally with magnetized water. Between 105 °C and 1000 °C, the dehydration and decomposition of C-S-H gel, C-H, and other hydrated products occur as water loss [62–64].

4. CONCLUSION

This study examined the changes in the physical and mechanical properties of GRC (Glass Fiber Reinforced Concrete) specimens produced with magnetic water obtained by exposing them to 8 and 10 different numbers of magnetic fields. According to the data, the H-Leep hardness value increased proportionally with the curing time. The increase in the number of magnetic fields resulted in a 9.88% and 13.6% increase in H-Leep values during 2-day intervals, 1.66% and 1.38% during 7-day curing, and 0.24% and 1.24% during 28-day curing.

While the density values of GRC specimens increased with curing periods, a decrease in density values over time was observed in specimens prepared using magnetic water. It was determined that magnetic waters reduced the air voids in the composite structure, leading to an increase in sound transmission speeds. In samples produced with magnetic water, an increase of 8.06% and 5.52% on the 2nd and 7th days, respectively,

was observed with 8 magnetic fields, and with 10 magnetic fields, these increase rates reached 9.55% and 10.7%.

In bending strength tests, a proportional increase with the curing period was observed in all GRC samples. Magnetic water increased the bending strengths of GRC samples by 18.3%, 11.4%, and 3.64% during the 7, 14, and 28 days of curing, respectively. The impact of magnetic water on compressive strength resulted in a 12.4% and 14.9% increase in the early stages and a 2.48% increase at the end of the 28 days.

In fracture mechanics analysis, a sample magnetized with 8 magnetic fields reduced the fracture strength of the GRC concrete beam by 37.1%, while increasing the number of magnetic fields by 20% resulted in a 26.5% improvement in fracture strength. In FTIR analysis, a 20% increase in magnetic fields did not show hydroxyl (-OH) and carboxyl peaks (R-COOH). SEM-EDS analysis revealed that the increase in the number of magnetic fields caused an increase in the percentages of Ca, Al, and O elements. TGA analysis indicated that a 20% increase in the magnetic field increased the amount of lost water, thereby enhancing cement hydration.

In conclusion, positive results were achieved in the physical and mechanical properties of GRC specimens produced with magnetized water. The primary reasons for this positive effect are the reduction of surface tension in magnetized water and its contribution to better hydrolysis with cement, resulting in a more homogeneous composite structure. In future studies, the effects of magnetized water on different cement composites can be investigated in more detail. This study can contribute significantly to energy savings and reduced production costs, especially considering global issues related to the efficient use of energy resources.

ACKNOWLEDGEMENTS

This study was carried out in Fibrobeton R&D Center Laboratory. We are grateful to Fibrobeton company for their support.

ETHICS

There are no ethical issues with the publication of this manuscript.

DATA AVAILABILITY STATEMENT

The authors confirm that the data that supports the findings of this study are available within the article. Raw data that support the finding of this study are available from the corresponding author, upon reasonable request.

CONFLICT OF INTEREST

The authors declare that they have no conflict of interest.

FINANCIAL DISCLOSURE

The authors declared that this study has received no financial support.

USE OF AI FOR WRITING ASSISTANCE

Not declared.

PEER-REVIEW

Externally peer-reviewed.

REFERENCES

[1] Kim, K., & Milstein, F. (1987). Relation between hardness and compressive strength of polymer concrete. *Constr Build Mater, 1*(4), 209–214. [CrossRef]

[2] Chandramouli, K., Rao, P. S. R., Narayanan, P., Tirumala, S. S., & Sravana, P. (2010). Strength properties of glass fiber concrete. *ARPN J Eng Appl Sci*, 5, 1–6.

[3] Bartos, P. J. M. (2017). Glassfibre reinforced concrete: A review. *IOP Conf Ser Mater Sci Eng, 246*, 012002. [CrossRef]

[4] Lalinde, L. F., Mellado, A., Borrachero, M. V., Monzó, J., & Payá, J. (2022). Durability of glass fiber reinforced cement (GRC) containing a high proportion of pozzolans. *Appl Sci, 12*(7), 3696. [CrossRef]

[5] Karimipour, A., Ghalehnovi, M., & de Brito, J. (2020). Mechanical and durability properties of steel fibre-reinforced rubberised concrete. *Constr Build Mater, 257*, 119463. [CrossRef]

[6] Babaloo, F., Majd, A., Arbabian, S., Sharifnia, F., & Ghanati, F. (2018). The effect of magnetized water on some characteristics of growth and chemical constituent in rice (Oryza sativa L.)Var Hashemi. *EurAsian J Biosci, 12*, 129–137.

[7] Cai, R., Yang, H., He, J., & Zhu, W. (2009). The effects of magnetic fields on water molecular hydrogen bonds. *J Mol Struct, 938*(1–3), 15–19. [CrossRef]

[8] Inaba, H., Saitou, T., Tozaki, K., & Hayashi, H. (2004). Effect of the magnetic field on the melting transition of H2O and D2O measured by a high resolution and supersensitive differential scanning calorimeter. *J Appl Phys, 96*(11), 6127–6132. [CrossRef]

[9] Shukla, S. K., Barai, S. V., & Mehta, A. (2020). *Advances in sustainable construction materials and geotechnical engineering* (Vol. 35). Springer Singapore. [CrossRef]

[10] Kimura, T. (2003). Study of the effect of magnetic fields on polymeric materials and its application. *Polym J, 35*(11), 823–843. [CrossRef]

[11] Ahmed, H. I. (2017). Behavior of magnetic concrete incorporated with Egyptian nano alumina. *Constr Build Mater, 150*, 404–408. [CrossRef]

[12] Gholhaki, M., Kheyroddin, A., Hajforoush, M., & Kazemi, M. (2018). An investigation on the fresh and hardened properties of self-compacting concrete incorporating magnetic water with various pozzolanic materials. *Constr Build Mater, 158*, 173–180. [CrossRef]

[13] Wei, H., Wang, Y., & Luo, J. (2017). Influence of magnetic water on early-age shrinkage cracking of concrete. *Constr Build Mater, 147*, 91–100. [CrossRef]

[14] Marasli, M., Subasi, S., & Dehghanpour, H. (2022). Development of a maturity method for GFRC shell concretes with different fiber ratios. *Eur J Environ Civ Eng, 26*(10):1–19. [CrossRef]

[15] Subasi, S., Dehghanpour, H., & Marasli, M. (2022). Production and characterization of GRC-SWCNT composites for shell elements. *Mater Sci, 28*(4), 423–433. [CrossRef]

[16] TS EN 196-1. (2005). *Methods of testing cement–Part 1: Determination of strength*. Turkish Standards.
[17] ASTM A956. (2006). *Standard test method for Leeb hardness testing of steel products*. ASTM International.
[18] TS EN 1170-4. (1999). *Precast concrete products-test method for glass-fibre reinforced cement-part 4: Determination of flexural strength*. Turkish Standards.
[19] ASTM C597. (2009). *Standard test method for pulse velocity through concrete*. ASTM International.
[20] Guo, Y. Z., Yin, D. C., Cao, H. L., Shi, J. Y., Zhang, C. Y., Liu, Y. M., Huang, H. H., Liu, Y., Wang, Y., Guo, W. H., Qian, A. R. & Shang, P. (2012). Evaporation rate of water as a function of a magnetic field and field gradient. *Int J Mol Sci, 13*(12), 16916–16928. [CrossRef]
[21] Ghorbani, S., Ghorbani, S., Tao, Z., de Brito, J., & Tavakkolizadeh, M. (2019). Effect of magnetized water on foam stability and compressive strength of foam concrete. *Constr Build Mater, 197*, 280–290. [CrossRef]
[22] Su, N., Wu, Y. H., & Mar, C. Y. (2000). Effect of magnetic water on the engineering properties of concrete containing granulated blast-furnace slag. *Cem Concr Res, 30*(4), 599–605. [CrossRef]
[23] Keshta, M. M., Yousry Elshikh, M. M., Kaloop, M. R., Hu, J. W., & ELMohsen, I. A. (2022). Effect of magnetized water on characteristics of sustainable concrete using volcanic ash. *Constr Build Mater, 361*, 129640. [CrossRef]
[24] Ghorbani, S., Gholizadeh, M., & de Brito, J. (2020). Effect of magnetized mixing water on the fresh and hardened state properties of steel fibre reinforced self-compacting concrete. *Constr Build Mater, 248*, 118660. [CrossRef]
[25] Hu, H. X., & Deng, C. (2021). Effect of magnetized water on the stability and consolidation compressive strength of cement grout. *Mater Basel, 14*(2), 275. [CrossRef]
[26] Ramalingam, M., Narayanan, K., Masilamani, A., Kathirvel, P., Murali, G., & Vatin, N. I. (2022). Influence of magnetic water on concrete properties with different magnetic field exposure times. *Mater Basel, 15*(12), 4291. [CrossRef]
[27] Elkerany, A. M., Yousry Elshikh, M. M., Elshami, A. A., & Youssf, O. (2023). Effect of water magnetization technique on the properties of metakaolin-based sustainable concrete. *Constr Mater, 3*(4), 434–448. [CrossRef]
[28] Ghorbani, S., Gholizadeh, M., & de Brito, J. (2018). Effect of magnetized water on the mechanical and durability properties of concrete block pavers. *Mater Basel, 11*(9), 1647. [CrossRef]
[29] Kong, D., Huang, S., Corr, D., Yang, Y., & Shah, S. P. (2018). Whether do nano-particles act as nucleation sites for C-S-H gel growth during cement hydration? *Cem Concr Compos, 87*, 98–109. [CrossRef]
[30] Mohammadnezhad, A., Azizi, S., Sousanabadi, H. F., Tashan, J., & Habibnejad, A. K. (2022). Understanding the magnetizing process of water and its effects on cementitious materials: A critical review. *Constr Build Mater, 356*, 129076. [CrossRef]
[31] Al-Gemeel, A. N., Zhuge, Y., & Youssf, O. (2018). Use of hollow glass microspheres and hybrid fibres to improve the mechanical properties of engineered cementitious composite. *Constr Build Mater, 171*, 858–870. [CrossRef]
[32] Shafei, B., Kazemian, M., Dopko, M., & Najimi, M. (2021). State-of-the-art review of capabilities and limitations of polymer and glass fibers used for fiber-reinforced concrete. *Mater Basel, 14*(2), 409. [CrossRef]
[33] Yan, F., Lin, Z., Zhang, D., Gao, Z., & Li, M. (2017). Experimental study on bond durability of glass fiber reinforced polymer bars in concrete exposed to harsh environmental agents: Freeze-thaw cycles and alkaline-saline solution. *Compos Part B Eng, 116*, 406–421. [CrossRef]
[34] Marasli, M., Subasi, S., & Dehghanpour, H. (2022). Development of a maturity method for GFRC shell concretes with different fiber ratios. *Eur J Environ Civ Eng, 26*(10), 1–19. [CrossRef]
[35] Wu, C., He, X., Zhao, X., He, L., Song, Y., & Zhang, X. (2022). Effect of fiber content on mechanical properties and microstructural characteristics of alkali resistant glass fiber reinforced concrete. *Adv Mater Sci Eng, 2022*, 1–19. [CrossRef]
[36] Chen, H., Wang, P., Pan, J., Lawi, A. S., & Zhu, Y. (2021). Effect of alkali-resistant glass fiber and silica fume on mechanical and shrinkage properties of cement-based mortars. *Constr Build Mater, 307*, 125054. [CrossRef]
[37] Balea, A., Fuente, E., Monte, M. C., Blanco, Á., & Negro, C. (2021). Fiber reinforced cement based composites. *In Fiber reinforced composites* (pp. 597–648). Elsevier. [CrossRef]
[38] Dehghanpour, H., Subasi, S., Guntepe, S., Emiroglu, M., & Marasli, M. (2022). Investigation of fracture mechanics, physical and dynamic properties of UHPCs containing PVA, glass and steel fibers. *Constr Build Mater, 328*, 127079. [CrossRef]
[39] Khan, S., Qing, L., Ahmad, I., Mu, R., & Bi, M. (2022). Investigation on fracture behavior of cementitious composites reinforced with aligned hooked-end steel fibers. *Mater Basel, 15*(2), 542. [CrossRef]
[40] Kim, W., & Lee, T. (2023). A study to improve the reliability of high-strength concrete strength evaluation using an ultrasonic velocity method. *Mater Basel, 16*(20), 6800. [CrossRef]
[41] Yousry, O. M. M., Abdallah, M. A., Ghazy, M. F., Taman, M. H., & Kaloop, M. R. (2020). A study for improving compressive strength of cementitious mortar utilizing magnetic water. *Mater Basel, 13*(8), 1971. [CrossRef]
[42] Constantinides, G., & Ulm, F. J. (2004). The effect of two types of C-S-H on the elasticity of cement-based materials: Results from nanoindentation and micromechanical modeling. *Cem Concr Res, 34*(1), 67–80. [CrossRef]
[43] Lafhaj, Z., Goueygou, M., Djerbi, A., & Kaczmarek, M. (2006). Correlation between porosity, permeability and ultrasonic parameters of mortar with variable water/cement ratio and water content. *Cem Concr Res, 36*(4), 625–633. [CrossRef]

[44] Mishra, D. A., & Basu, A. (2013). Estimation of uniaxial compressive strength of rock materials by index tests using regression analysis and fuzzy inference system. *Eng Geol, 160*, 54–68. [CrossRef]

[45] Tassew, S. T., & Lubell, A. S. (2014). Mechanical properties of glass fiber reinforced ceramic concrete. *Constr Build Mater, 51*, 215–224. [CrossRef]

[46] Amran, Y. H. M., Farzadnia, N., & Abang Ali, A. A. (2015). Properties and applications of foamed concrete: A review. *Constr Build Mater, 101*, 990–1005. [CrossRef]

[47] Yusuf, M. O. (2023). Bond characterization in cementitious material binders using Fourier-transform infrared spectroscopy. *Appl Sci, 13*(5), 3353. [CrossRef]

[48] Sun, H., Ding, Y., Jiang, P., Wang, B., Zhang, A., & Wang, D. (2019). Study on the interaction mechanism in the hardening process of cement-asphalt mortar. *Constr Build Mater, 227*, 116663. [CrossRef]

[49] Cosentino, A. G. M., Silva, F. C., da Silva, G., Sciamareli, J., & da Costa Mattos, E. (2020). A short review about aerospace materials characterization – Bonding agents and thermal insulation. *Propellants Explos Pyrotech, 45*(8), 1175–1184. [CrossRef]

[50] Muthu, M., Yang, E. H., & Unluer, C. (2021). Effect of graphene oxide on the deterioration of cement pastes exposed to citric and sulfuric acids. *Cem Concr Compos, 124*, 104252. [CrossRef]

[51] Ng, C., Alengaram, U. J., Wong, L. S., Mo, K. H., Jumaat, M. Z., & Ramesh, S. (2018). A review on microstructural study and compressive strength of geopolymer mortar, paste and concrete. *Constr Build Mater, 186*, 550–576. [CrossRef]

[52] Caggiani, M. C., Occhipinti, R., Finocchiaro, C., Fugazzotto, M., Stroscio, A., Mazzoleni, P., & Barone, G. (2022). Diffuse reflectance infrared Fourier transform spectroscopy (DRIFTS) as a potential on site tool to test geopolymerization reaction. *Talanta, 250*, 123721. [CrossRef]

[53] Benavent, V., Steins, P., Sobrados, I., Sanz, J., Lambertin, D., Frizon, F., Rossignol, S., & Poulesquen, A. (2016). Impact of aluminum on the structure of geopolymers from the early stages to consolidated material. *Cem Concr Res, 90*, 27–35. [CrossRef]

[54] Duxson, P., Provis, J. L., Lukey, G. C., Separovic, F., & van Deventer, J. S. J. (2005). 29Si NMR study of structural ordering in aluminosilicate geopolymer gels. *Langmuir, 21*(7), 3028–3036. [CrossRef]

[55] Schroeder, R. A., & Lyons, L. L. (1966). Infra-red spectra of the crystalline inorganic aluminates. *J Inorg Nucl Chem, 28*(5), 1155–1163. [CrossRef]

[56] Qu, J., Zhang, J., Li, H., Li, S., Hou, Z., Chang, R., & Zhang, Y. (2024). Coal gasification slag-derived highly reactive silica for high modulus sodium silicate synthesis: Process and mechanism. *Chem Eng J, 479*, 147771. [CrossRef]

[57] Wang, Y., Liu, Z., He, F., Zhuo, W., Yuan, Q., Chen, C., & Yang, J. (2021). Study on water instability of magnesium potassium phosphate cement mortar based on low-field 1H nuclear magnetic resonance. *Measurement, 180*, 109523. [CrossRef]

[58] Blanc, P., Bourbon, X., Lassin, A., & Gaucher, E. C. (2010). Chemical model for cement-based materials: Temperature dependence of thermodynamic functions for nanocrystalline and crystalline C–S–H phases. *Cem Concr Res, 40*(6), 851–866. [CrossRef]

[59] Deboucha, W., Leklou, N., Khelidj, A., & Oudjit, M. N. (2017). Hydration development of mineral additives blended cement using thermogravimetric analysis (TGA): Methodology of calculating the degree of hydration. *Constr Build Mater, 146*, 687–701. [CrossRef]

[60] Kim, J. J., Foley, E. M., & Reda Taha, M. M. (2013). Nano-mechanical characterization of synthetic calcium–silicate–hydrate (C–S–H) with varying CaO/SiO2 mixture ratios. *Cem Concr Compos, 36*, 65–70. [CrossRef]

[61] Loukili, A., Khelidj, A., & Richard, P. (1999). Hydration kinetics, change of relative humidity, and autogenous shrinkage of ultra-high-strength concrete. *Cem Concr Res, 29*(4), 577–584. [CrossRef]

[62] Heikal, M. (2016). Characteristics, textural properties and fire resistance of cement pastes containing Fe2O3 nano-particles. *J Therm Anal Calorim, 126*(3), 1077–1087. [CrossRef]

[63] Saraya, M. E. S. I. (2014). Study physico-chemical properties of blended cements containing fixed amount of silica fume, blast furnace slag, basalt and limestone, a comparative study. *Constr Build Mater, 72*, 104–112. [CrossRef]

[64] Zhang, Q., & Ye, G. (2011). Microstructure analysis of heated Portland cement paste. *Procedia Eng, 14*, 830–836. [CrossRef]

Journal of Sustainable Construction Materials and Technologies
Web page info: https://jscmt.yildiz.edu.tr
DOI: 10.47481/jscmt.1535527

JSCMT
Journal of Sustainable Construction Materials and Technologies

Research Article

Optimizing seismic performance: Integrating friction dampers into spherical liquid tanks

Yunus UÇAR*[1], Mehmet Fatih ALTAN[2]

[1]*Department of Civil Engineering, İstanbul Aydın University, İstanbul, Türkiye*
[2]*Department of Civil Engineering, İstanbul Arel University, İstanbul, Türkiye*

ARTICLE INFO

Article history
Received: 28 March 2024
Revised: 10 May 2024
Accepted: 02 July 2024

Key words:
Earthquake resilience, friction dampers, LNG tank, retrofit, seismic performance, sloshing effect

ABSTRACT

This study addresses the vital challenge of ensuring the safe storage of Liquid Natural Gas (LNG) in spherical tanks during seismic events, focusing on the crucial balance between meeting seismic performance criteria and mitigating economic losses due to potential operational disruptions from necessary retrofitting efforts. In response to this challenge, we present a case study on retrofitting an LNG tank near the North Anatolian Fault (NAF) line of Türkiye. Through a comprehensive seismic evaluation, this study reveals inadequacies in the existing case's compliance with seismic criteria. It suggests a remedy involving the increased stiffness of lateral force-resisting members coupled with the utilization of friction dampers. Following the proposed stiffness increase achieved through retrofitting, our approach is fundamental to exploring alternative damping mechanisms designed to enhance the steel column-brace support structure. One of the key design challenges is the unique dynamic behavior of LNG, especially its sloshing during earthquakes, which necessitates a comprehensive understanding of fluid-structure interaction for accurate modeling and analysis. Through a series of transient analyses incorporating actions, we evaluate the effectiveness of the proposed retrofitting measures on the structure. Our findings introduce a feasible and efficient retrofitting strategy, marked by minimal operational interruption, primarily by avoiding the extensive demolition and reconstruction typically required.

Cite this article as: Uçar, Y., & Altan, M. F. (2024). Optimizing seismic performance: Integrating friction dampers into spherical liquid tanks. *J Sustain Const Mater Technol*, 9(3), 294–304.

1. INTRODUCTION

As lifeline structures of strategic importance, liquid storage tanks are extensively used in the petroleum industry, urban water resources management, and nuclear power facilities [1]. During an earthquake, LNG storage tanks may experience significant gas pressure, potentially causing damage and permanent deformation to the steel structure [2]. Damage to liquid storage tanks can disrupt essential infrastructure and may result in fires or environmental pollution due to leaks of flammable substances or hazardous chemicals [1]. These tanks must comply with high seismic performance standards, given the risk of explosions or fires from LNG leaks. Therefore, conducting an extensive seismic assessment of these tanks is essential. If an LNG tank fails to satisfy the required seismic performance criteria, retrofitting with either conventional or advanced solutions becomes necessary. However, the prolonged downtime and disruption in confined spaces often render traditional retrofitting methods impractical. Additionally, seismic forces tend to increase as the structure's stiffness increases, necessitating foundation expansions [3]. Therefore, exploring alternative solutions to introduce additional damping to these structures is sensible, aiming to limit seismic drifts without significantly increasing stiffness.

***Corresponding author.**
*E-mail address: yunusucar@stu.aydin.edu.tr, yucar@ipkb.gov.tr

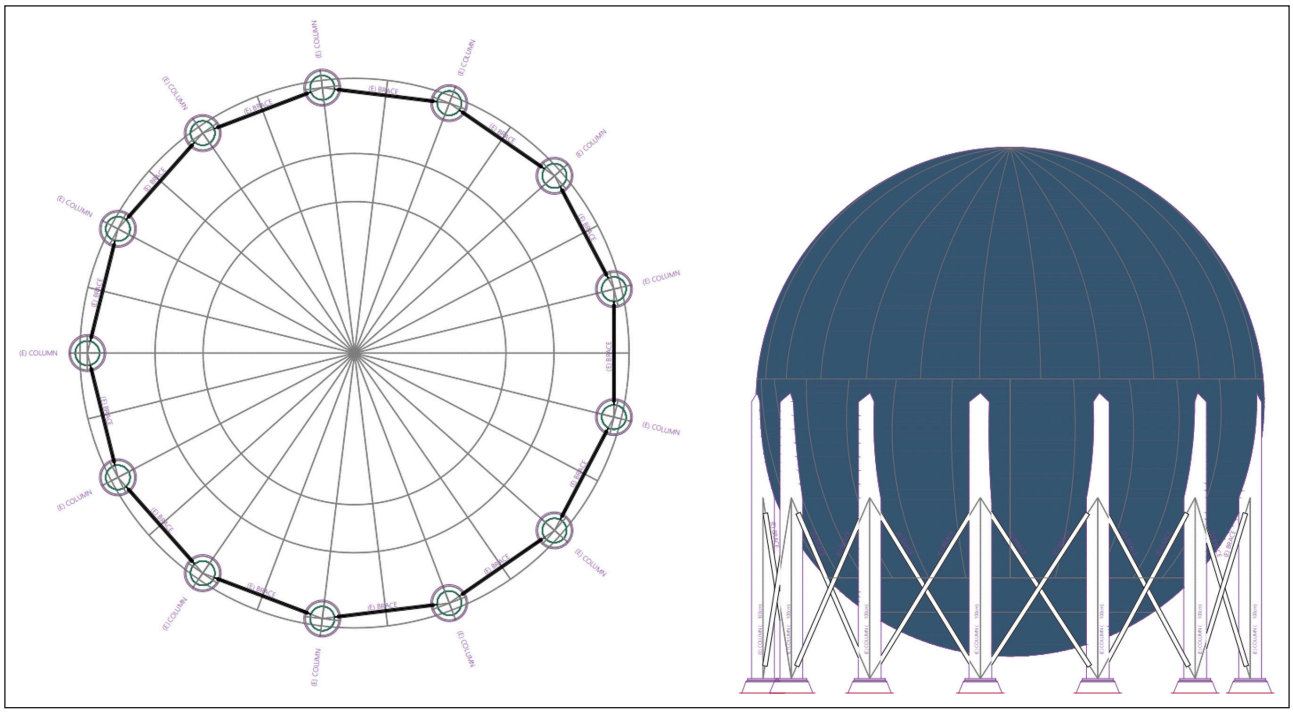

Figure 1. Plan and elevation view of the LNG tank.

Previous studies have investigated the seismic performance of LNG tank structures using seismic energy-dissipating devices such as seismic isolators and dampers. Seismic isolators, positioned at the base to isolate the superstructure from earthquakes, exhibit low horizontal stiffness but substantial vertical stiffness and strength to support structural weight without differential movement. While isolators significantly reduce acceleration, their horizontal flexibility increases horizontal displacements [1]. Gregoriou et al. [4] conducted dynamic analyses of LNG tanks with seismic isolators, resulting in considerable reductions in base shear and maximum strains. Jadhav et al. [5] explored the impact of different isolator settings on the seismic response of base-isolated fluid storage tanks. However, structures located in near-fault areas may experience increased displacement demands due to large-pulse ground motions [6]. Saha et al. [7] investigated the seismic behavior of liquid storage tanks equipped with sliding systems and elastomer bearings near fault lines. Based on the findings of the study by Çerçevik et al. [8], it can be inferred that base-isolated structures in near-fault locations may require additional damping devices such as viscous or friction dampers. Structural dampers with passive control systems operate through various mechanisms, including metallic, friction-based, viscous, and viscoelastic. In Çalım et al. [9] and Güllü et al. [10], the advantages and disadvantages of various structural dampers with passive control systems are discussed. Notably, friction dampers are commonly favored due to their affordability, effectiveness, and compatibility with multiple bracing types [11]. Furthermore, the stability and rigidity offered by friction dampers make them particularly appealing [12].

The sloshing effect has also been a focal point in prior research. Housner [13] used two lumped mass models for storage tanks, assuming complete rigidity of the tank walls and ideal liquid dynamics. Haroun and Housner [14] introduced a simplified mechanical model that considers both the liquid-solid interaction and the elastic deformation of the tank walls when subjected to stress. This approach to modeling LNG storage tanks incorporates various assumptions and simplifications to navigate the complexities of fluid-structure interaction.

In this case study, we assessed the seismic performance of an existing steel LNG tank, considering the fluid-structure interaction and proposing retrofitting measures that include the utilization of friction dampers. The study is organized into several sections: Part 2 is an overview of the existing structure, including structural details, soil conditions, and regional seismicity. Part 3 focuses on the methodology for modeling and analysis. The seismic assessment process and retrofitting design are discussed in Parts 4 and 5, respectively. Finally, our concluding remarks are summarized in Part 6.

2. MATERIALS AND METHODS

2.1. Existing Structure

This section presents an overview of the spherical LNG tank's structural properties, corresponding site conditions, and regional seismicity.

2.1.1. Structural Details

Considering that the LNG tank in question was designed in 1990 and is located in a region of high seismic activity, it has become necessary to evaluate the structure against current performance-based design codes and specifications. The plan and elevation view of the structure are depicted in Figure 1.

Table 1. Structural member properties

Diameter of LNG Tank	21.2 m
Column section	CHS1000/10.1
Column height	12.1 m
Spherical tank wall thickness	Varies
Brace section	205x43 mm

Table 2. Site condition parameters

Shear Wave Velocity (average) (V_{s30})	400–450 m/s
Soil Class (ASCE7-16)	C
Allowable Soil Bearing (σ_{all})	200 kPa
Vertical Subgrade Modulus (K_V)	75000 kN/m^3
Horizontal Subgrade Modulus (K_H)	35000 kN/m^3
Average Shear Strength of Soil (S)	140 kPa
Ground Water Level	–

Thirteen steel columns support the tank, and steel braces are utilized as lateral load-resisting members. Table 1 provides a summary of structural member properties.

2.1.2. Site Conditions

The LNG Tank is located on a site featuring a 1-meter-thick layer of fill soil. Beneath this layer lies clayey sand soil mixed with gravel at specific points. There were no indications of groundwater presence throughout six boring operations conducted on the site. The parameters detailing the site conditions are summarized in Table 2.

2.1.3. Seismicity

The exact location of the site is marked in red in Figure 2. Regarding regional seismicity, the LNG tank is in the Marmara region of Türkiye, a region rich in history as the cradle of numerous civilizations and the epicenter of several destructive earthquakes [15]. The area's seismotectonic characteristics, fault segments, and the related seismic source parameters have been the research focus for many years, accompanied by earthquake catalogs covering historical and instrumental periods. As a result, various studies have been conducted to analyze the seismic sources of this region. In our research, source parameters were adopted from Erdik et al. [15], and the SHARE project model [16] was also employed. While deterministic and probabilistic seismic hazard analyses were carried out for the site, they are not detailed in this study as they fall outside its scope. Still, we provide the peak ground acceleration (PGA=0.96g) and the spectral values (Ss=2.41g and S1=1.24g) obtained for the considered event (with a 2% probability of exceedance in 2475 years).

The site is within 15 km of an active fault, necessitating the consideration of near-fault effects. For this purpose, CALTRANS (2013) near-fault model [17] has been employed in this study (Fig. 3). By deriving site-specific acceleration values and near-fault amplification factors, we constructed the simplified target design spectrum curve by ASCE 7–10 [18]. Figure 4 demonstrates the MCER spectrum, which aligns with the DD-1 design level for the Turkish Seismic Code (TSC) (2018) [19].

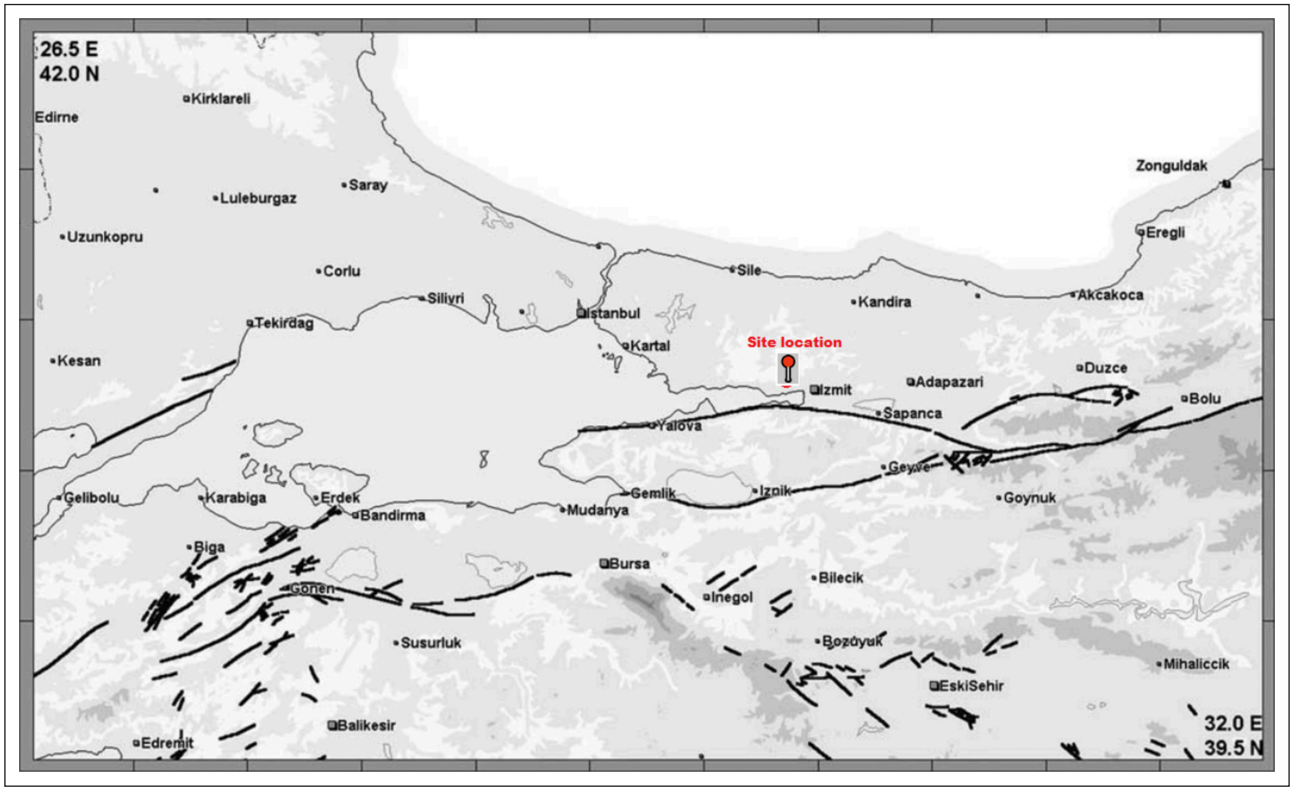

Figure 2. Site location illustrated on the active fault map of the region [15].

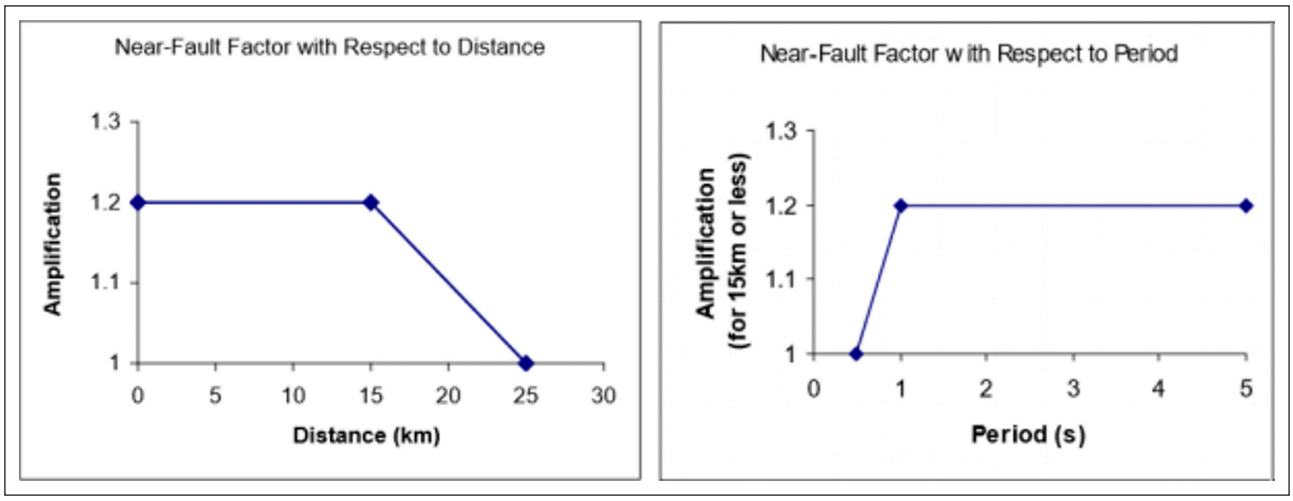

Figure 3. Near-fault effect by CALTRANS (2013) [15].

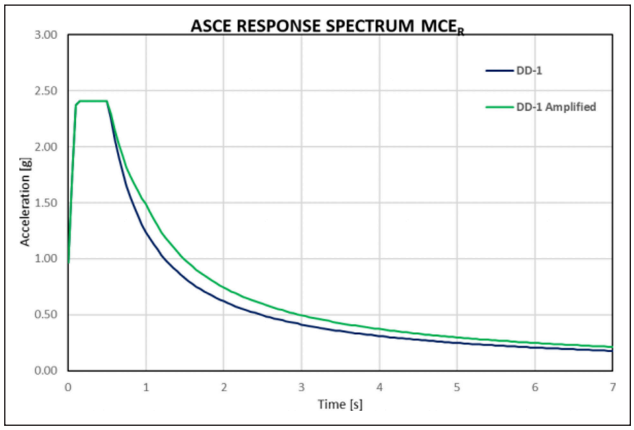

Figure 4. Simplified design spectrum.

2.2. Structural Modelling and Analysis

Analyses of the structural behavior of the LNG storage tank under seismic loads were conducted utilizing the fluid-structure interaction (FSI) approach, which integrates finite element analysis (FEA) and computational fluid dynamics (CFD) models within ANSYS.

2.2.1. Analysis Model of the Existing Structure

The development of the structural analysis model commenced with specifying the sheet thicknesses for the shell elements. These thicknesses, applied across the entire structure, are depicted visually in Figure 5. A minimum sheet thickness of 5mm was applied to the lamellae in the 13 steel columns, while the base plates featured the thickest sheet metal, with a wall thickness of 51mm, as shown in Figure 5.

The mesh necessary for the finite element analysis was generated using linear SHELL181 elements for the sheet metal components. The model comprises 65,000 nodes and 55,000 elements. Connections across all components are established through contact elements, with sourced connections defined as edge-to-edge or edge-to-surface types, depending on the requirements. The contact elements employed include CONTA172, CONTA175, and TARGE170.

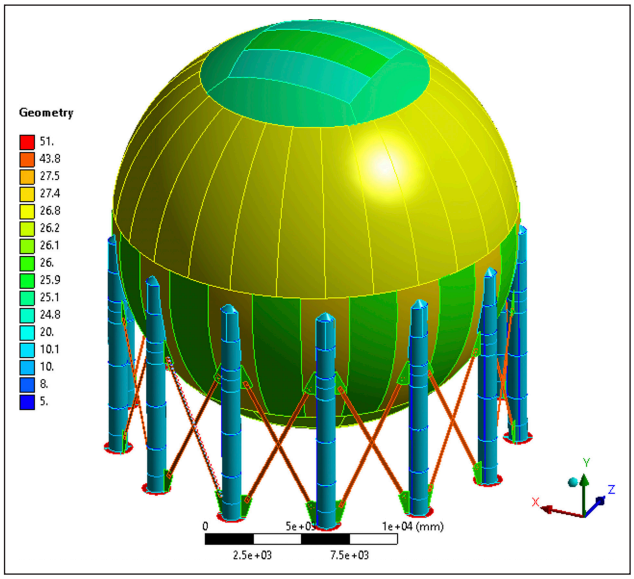

Figure 5. FEA model of the tank-sheet thickness- isometric view.

The adequacy of the mesh's resolution was confirmed through natural frequency analyses conducted on an empty tank, ensuring the mesh's reliability for the study. A mesh convergence study was undertaken using three distinct mesh sizes: 600 mm, 300 mm, and 150 mm, as depicted in Figure 6. The study's findings determined that the optimal mesh size for the main shell components is 300 mm, while 150 mm is suitable for the other parts. The final configuration of the meshed model is demonstrated in Figure 7.

2.2.2. LNG Mass Modeling and Fluid-Structure Interaction: Simulating Hydrostatic Pressure and LNG Mass

The fluid-structure interaction (FSI) method allows for accurate simulations of structural and fluid components. This approach effectively models the hydrostatic pressure induced by LNG and its mass inertia and dynamic behavior with high precision and without numerical issues. Due to the requirement for iterative data exchange between the

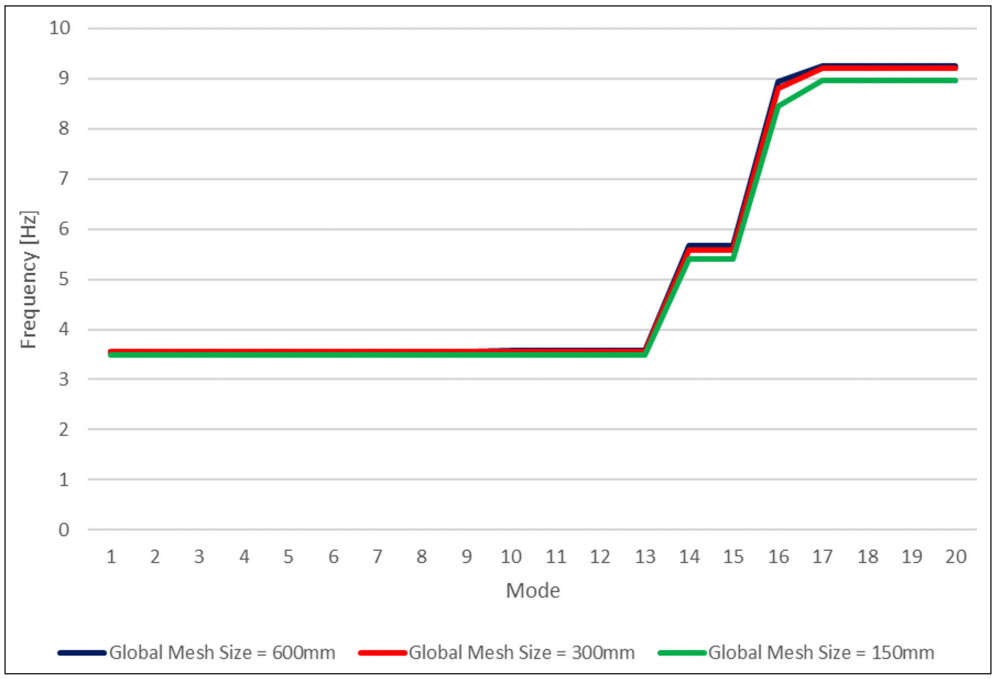

Figure 6. Mesh convergence analysis- comparison of natural frequencies of an empty tank.

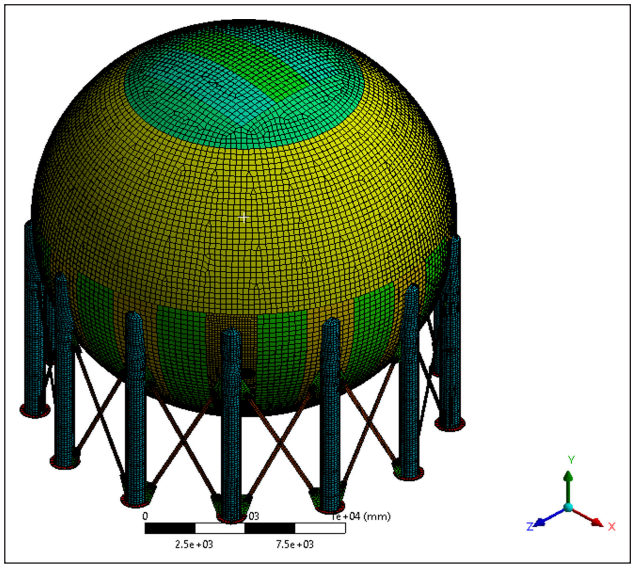

Figure 7. Analysis model with meshes for structural analysis- isometric view.

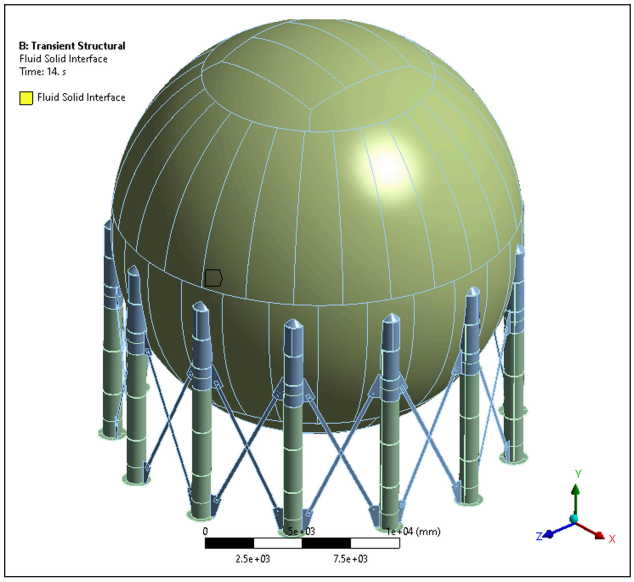

Figure 8. Pressure deformation definition for FSI analysis.

structural and fluid model solvers, this type of analysis tends to have relatively longer resolution times.

In the finite element analysis model, movement in all translational directions is restricted to zero at the joint points on the 13 baseplate surfaces.

Standard gravity acceleration, directed vertically in the Y-axis, is applied as 9.8066m/s^2 for the entire structure.

The pressure load data, derived from the CFD solution, is assigned for the shell surfaces. In solving the FSI problem, the deformations occurring on these surfaces are relayed to the CFD solver. Subsequently, both hydrostatic and dynamic pressure values calculated by the CFD solver are transferred back to these surfaces as a pressure load, as illustrated in Figure 8.

The CFD model was developed with a mesh featuring an element size of 300 mm to accommodate various solvers. This mesh comprises 220,000 elements, as illustrated in Figure 9. The model configures the interface between LNG and air for the volume-of-fluid (VOF) method. The liquid level within the tank is determined using the software's volumetric ratio functions. By employing the values of 366,400 kg for the empty weight and 3,216,400 kg for the operating weight, the volume of LNG was calculated to be 4913.79 m^3. The specific Gravity of LNG is taken as 580 kg/m^3.

The model characterizes LNG and air as two distinct immiscible fluids through the multi-phase analysis method. The Volume of Fluid (VOF) method determines the

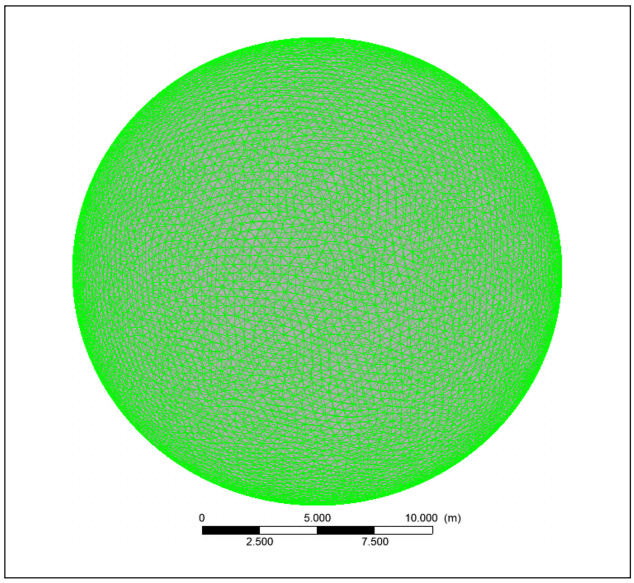

Figure 9. Mesh size for CFD analysis – 300 mm element size with 220,000 elements.

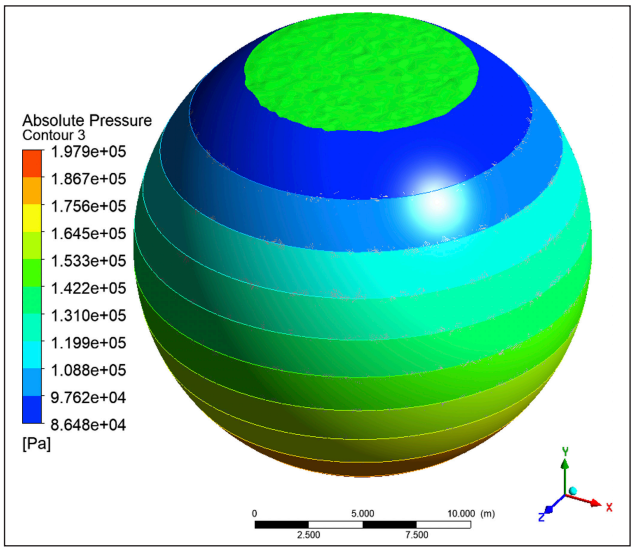

Figure 10. Free LNG surface (green color) and hydrostatic pressure distribution.

fluid interface. At each iteration of the solution, hydrostatic and dynamic pressures derived from the CFD model are transferred to the structural model (Fig. 10). The material properties considered in the analysis of these fluids are detailed in Table 3.

The model's accuracy was verified by comparing the reaction force values derived from static analysis. The total reaction force was anticipated to be 31.54MN, and the study yielded a result of 31.50MN. This indicates a mere 0.23% discrepancy between the numerical model and the engineer's calculations, demonstrating a high level of agreement.

2.3. Seismic Assessment

The objective is to achieve the Life Safety (LS) performance level under the Maximum Considered Earthquake (MCE_R) conditions.

To assess the structure's seismic performance, 11 pairs of earthquake ground motions presented in Table 4 were selected and scaled to align with the target spectrum for an earthquake level corresponding to a return period of 2475 years (2% probability of exceedance in 50 years). Another Yarımca record from the Kocaeli Earthquake has also been used in the retrofitted case analysis to examine the structure's response to pulse actions.

Although recent studies have shown that energy spectra should be used for earthquake record scaling, simple scaling was used in this study [20]. Studies have also shown that the site-dominant period is an essential criterion for scaling [21, 22].

The scaling process involved adjusting both components of the seismic records to RotD100, as the most critical impact on such structures often results from maximum ground motion in a single direction. A com-

Table 3. Material properties of fluids

Material	Specific gravity (kg/m³)	Viscosity (kg/ms)
LNG	580	0.00113
Air	1.185	1.831e-5

Table 4. Selected ground motion records for time history analysis

Record name	Earthquake name	Magnitude	Joyner-Boore distance (km)	Vs30 (m/s)	Style of faulting
RSN6	Imperial Valley-02	6.95	6.09	213.44	Strike-slip
RSN26	Hollister-01	5.6	19.55	198.77	Strike-slip
RSN30	Parkfield	6.19	9.58	289.56	Strike slip
RSN95	Managua, Nicaragua-01	6.24	3.51	288.77	Strike-slip
RSN99	Hollister-03	5.14	8.85	198.77	Strike-slip
RSN102	Northern Calif-07	5.2	8.2	219.31	Strike-slip
RSN147	Coyote Lake	5.74	8.47	270.84	Strike-slip
RSN158	Imperial Valley-06	6.53	0.0	259.86	Strike-slip
RSN214	Livermore-01	5.8	15.19	377.51	Strike slip
RSN233	Mammoth Lakes-02	5.69	2.91	382.12	Strike slip
RSN236	Mammoth Lakes-03	5.91	2.67	382.12	Strike slip

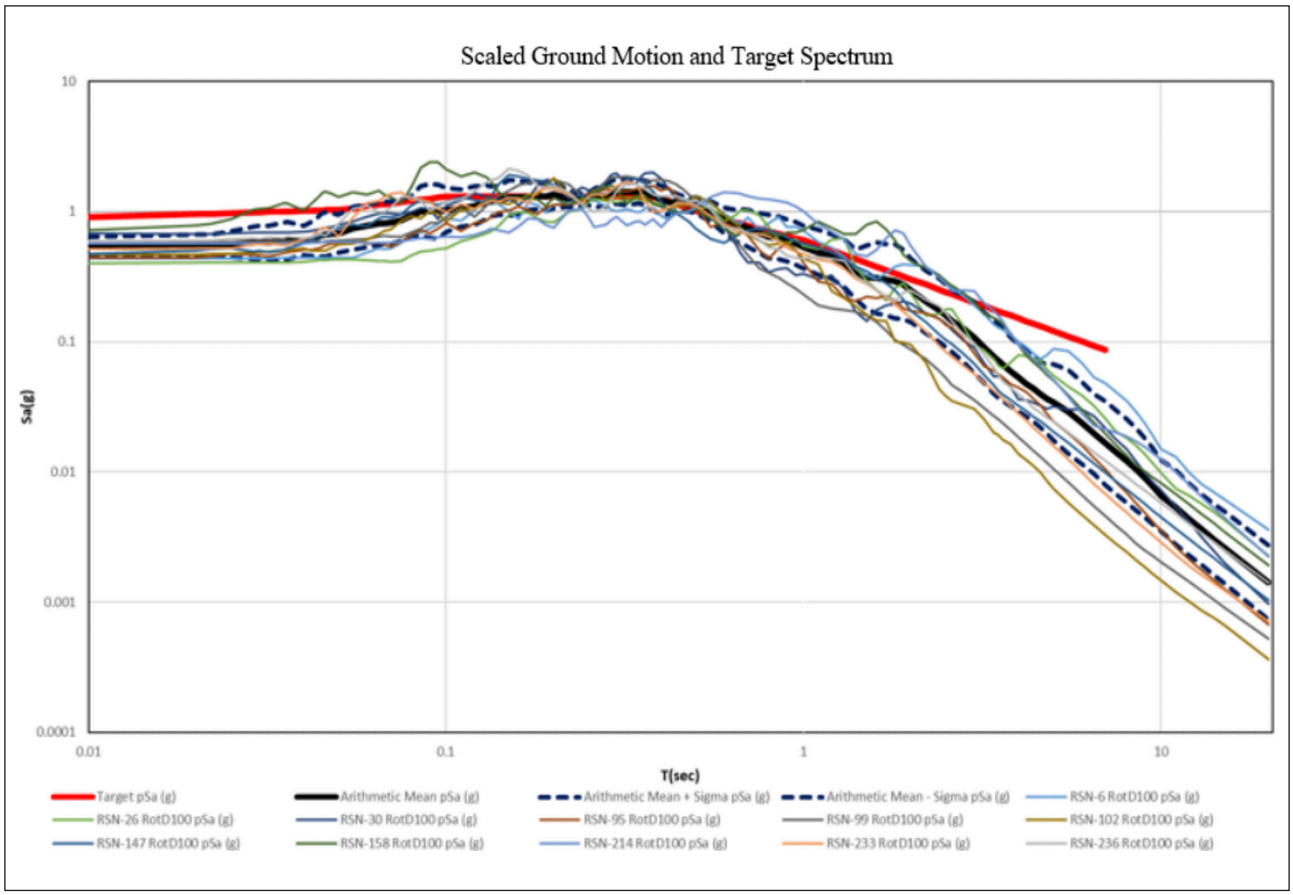

Figure 11. Scaled ground motions vs. specific target response spectrum (semi-log scale).

Table 5. Analysis results for friction dampers with different yield strengths and base shear reduction

		Yield strength [kN]				
	Existing	**100**	**200**	**350**	**500**	**1000**
Base Shear [kN]	27359.73	8711.09	8777.27	8623.73	8918.18	11286.09
Top Column Displacement [cm]	12.55	17.98	14.42	12.41	11.16	8.37
P [kN]	4799.91	3043.55	3204.27	3184.73	3234.36	3543.73
M2 [kNm]	1297.91	2127.55	1546.64	1796.45	1643.09	1313.73
M3 [kNm]	2441.55	2997.91	3225.82	2303.55	1986.91	1679.18
Link Displacement [cm]	–	5.51	4.05	3.26	2.75	1.60

parison between the target spectrum and the spectra of scaled ground motions is displayed in Figure 11, utilizing a semi-logarithmic scale.

During seismic performance assessment, steel columns and brace elements have been checked against criteria provided in ASCE41. Accordingly, the columns' total rotation and brace axial deformations have been calculated. The shell stresses have also been monitored. Key results from the seismic performance assessment include the columns' rotation and braces' axial deformation, as shown in Figure 12. Finally, the maximum top displacement values were calculated for each ground motion. The top displacement values and the seismic-induced deformation of the LNG tank are also visualized in Figure 13.

After assessing the existing structure, it was determined that it failed to meet the necessary criteria, indicating a need for retrofitting. The failing mechanism starts with compression failure and subsequent buckling of the brace elements, followed by the exceedance of the plastic rotation capacity of the column elements.

2.4. Seismic Retrofit Design

Various retrofit options have been researched, including (A) conventional retrofitting using larger columns and brace sections, (B) seismic isolation, (C) viscous dampers, and (D) friction dampers. Conventional retrofit alternatives have been eliminated due to the extended construction downtime and foundation retrofit requirement, which prevent access to critical nearby facilities.

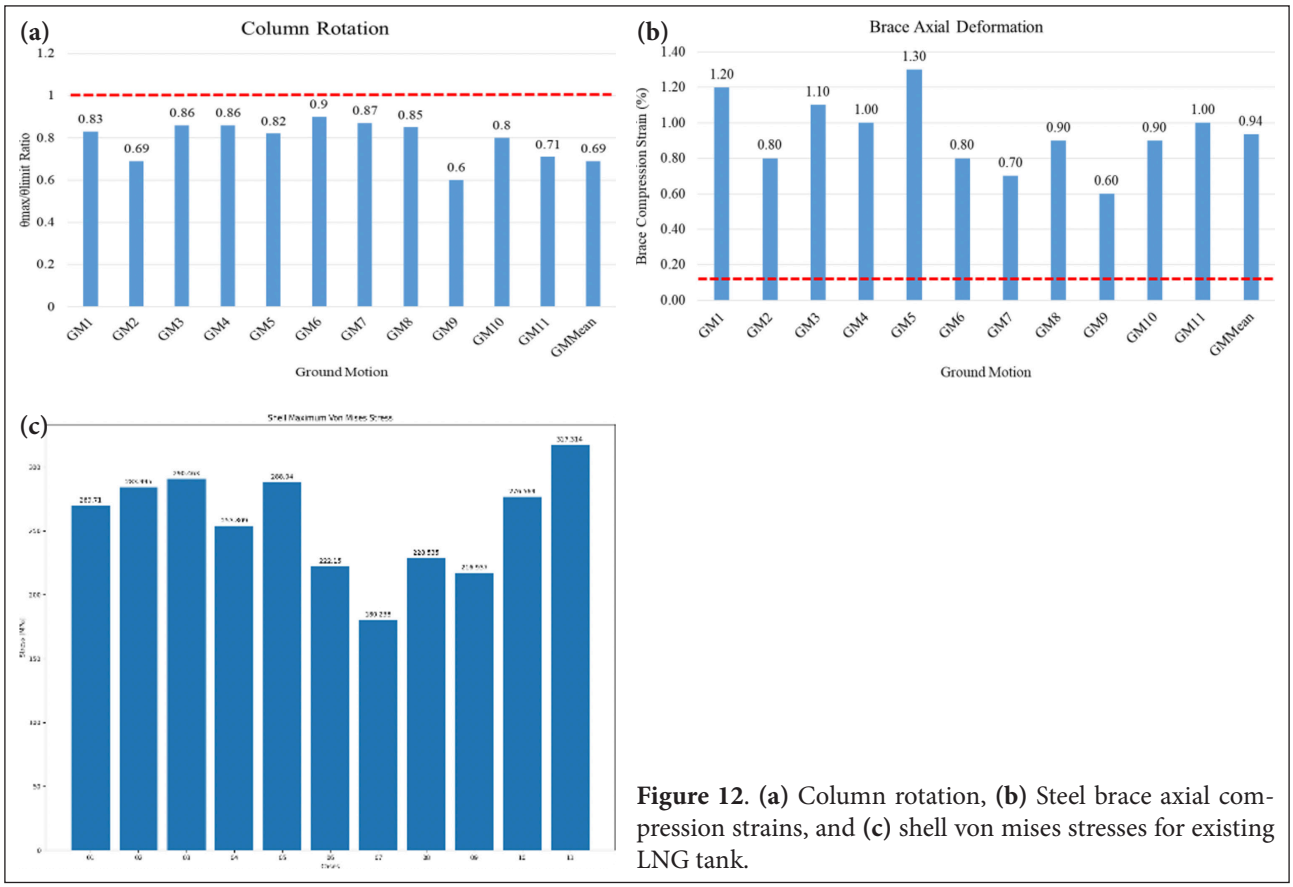

Figure 12. **(a)** Column rotation, **(b)** Steel brace axial compression strains, and **(c)** shell von mises stresses for existing LNG tank.

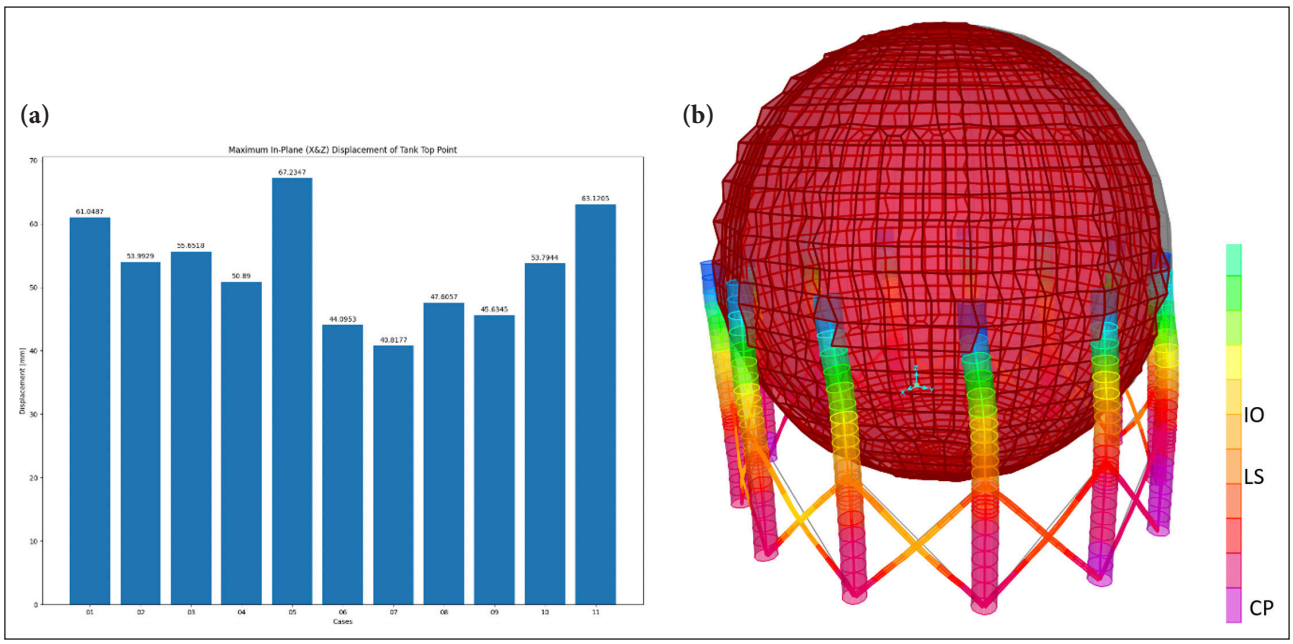

Figure 13. **(a)** Top displacement values and **(b)** Deformed shape of LNG Tank*.

*CP stands for Collapse Prevention, LS for Life Safety, and IO for Immediate Occupancy performance levels.

The seismic isolation option is eliminated due to the high displacement demands, which require the replacement of many pipelines. Viscous and Friction damper retrofit solutions, were found rational; however, due to stricter drift values, friction-type dampers (Fig. 14) emerged as the preferable solution.

The primary motivation for selecting friction-type dampers was to enhance the structure's damping and diminish the base shear forces experienced during seismic events. For this case, linear friction dampers have been used.

The retrofitting model is presented in Figure 15.

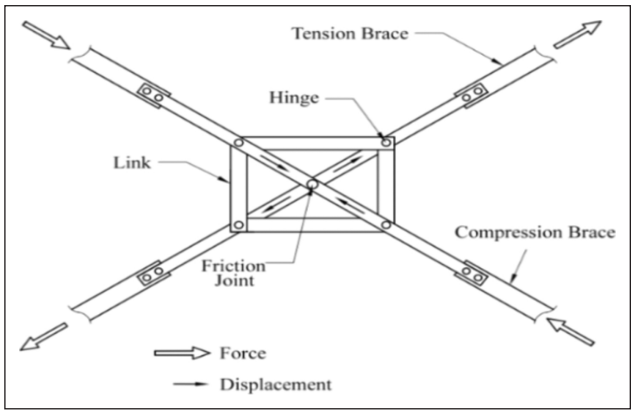

Figure 14. Friction damper type.

Analysis revealed that the current braces were operating beyond their capacity, necessitating their replacement with CHS 219.1/16 pipe profiles in conjunction with the introduction of friction-type dampers. The newly added braces were chosen based on their ability to exceed the axial compression load capacity of the dampers. This retrofitting strategy eliminates the need for further modifications to the existing structure.

Friction dampers featuring varying yield strengths were evaluated to identify the optimal retrofit configuration (Table 5).

Typical base shear and top deformation plots have been provided in Figure 16.

As demonstrated in Table 5, the friction damper with a yield strength of 350kN offers the optimal solution. This is because an increase in yield strength directly increases earthquake demands, thus increasing the base shear and potentially necessitating foundation retrofitting. The hysteresis curve of friction damper with 350kN yield strength and 5 cm target displacement is provided in Figure 17.

Analysis results with friction damper having 350kN yield strength indicate that the average displacement at the top of the columns, relative to the foundation, is 12.41cm, corresponding to 1% of the column height.

Based on the obtained rotation values, capacity evaluations of the columns showed that the Immediate Occupancy limit, as specified by ASCE 41–13 [23], was not exceeded on average. It was noted that columns, which previously partially exceeded their capacities, remained within their

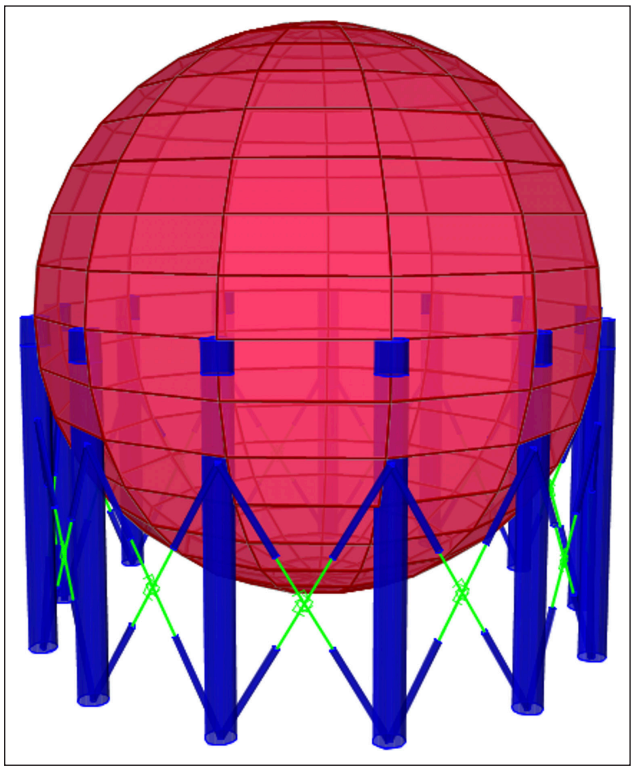

Figure 15. Model of retrofitted LNG tank with friction damper.

capacity values after strengthening. The deformed shape of the retrofitted LNG tank is depicted in Figure 18.

The rotation demands of the steel column for the retrofitted structure decreased by 10% compared to the existing LNG tank. Furthermore, the axial strain demand of braces in the retrofitted LNG tank structure remains within the strain capacity, as shown in Figure 19. Based on the updated FSI analyses, it has been determined that a reduction in the velocity response reduced the inertial and sloshing forces of the included viscous materials by as much as 70%.

3. RESULT AND DISCUSSION

This study focused on the seismic performance assessment and retrofitting of an existing steel LNG Tank near the North Anatolian Fault (NAF) line. The evaluation revealed that the structure's column rotations and the axial deforma-

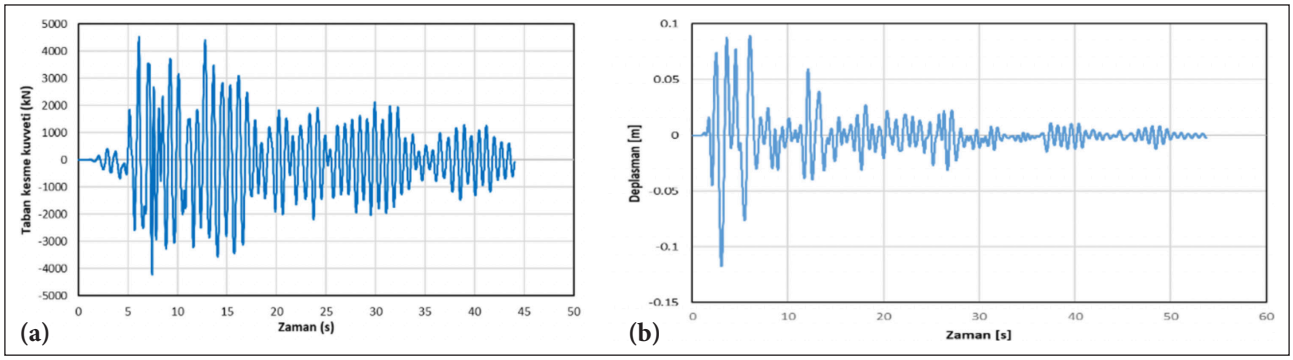

Figure 16. **(a)** RSN6 record base shear plot and **(b)** RNS6 record top displacement plot.

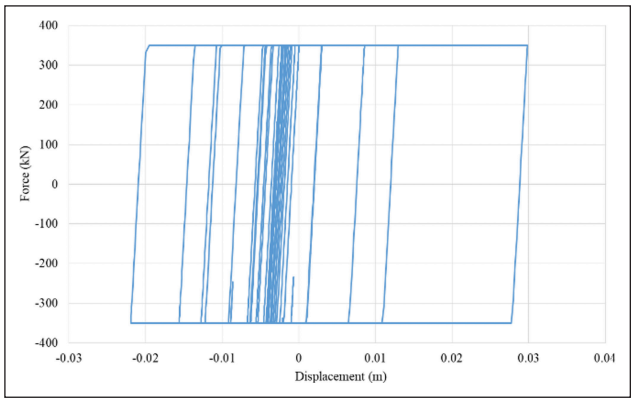

Figure 17. Hysteresis behavior of friction damper (yield strength 350 kN).

tions of the braces did not satisfy the desired seismic performance criteria. Consequently, a retrofitting approach was proposed, incorporating friction dampers alongside new steel braces. The primary aim of introducing additional damping was to minimize operational downtime during the retrofit process and to eliminate the need for foundation retrofitting.

4. CONCLUSION

Implementing friction dampers successfully reduced the inertial, sloshing seismic loads and the total base shear demand on the structure, eliminating the necessity for foundation retrofitting. The total base shear reduction is approximately 68%, the increase in the top displacement is approximately 3%, and the decrease in the column axial forces is approximately 34%. The expected nominal displacement of the link elements is approximately 35 mm. Since the yield force of the links is constant, the member results are not significantly affected by ground motions, including pulse behavior; however, a slight increase in the link and top displacement is observed. This study does not address the long-term effects due to heat, dust, stick-slip, or other maintenance-related factors, which will be that's for future research together with instrumentation of the retrofitted structure to collect data from actual seismic events, enhancing the understanding and validation of retrofitting strategies.

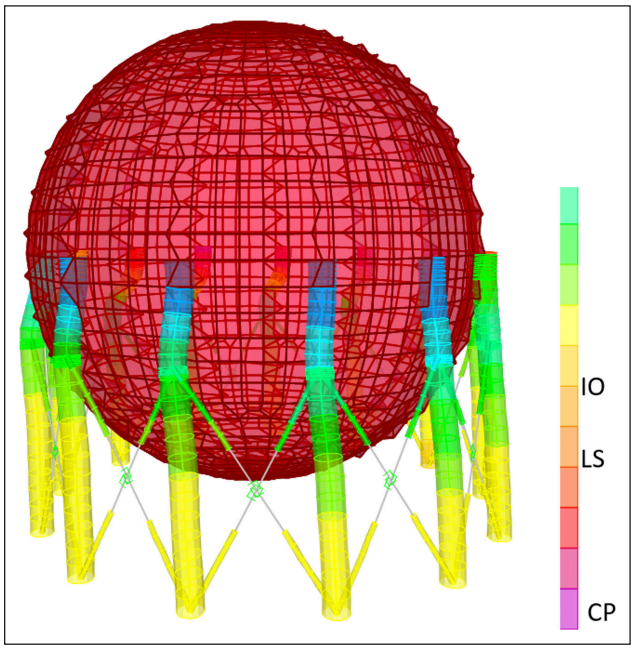

Figure 18. Deformed shape of retrofitted LNG tank.

ETHICS

There are no ethical issues with the publication of this manuscript.

DATA AVAILABILITY STATEMENT

The authors confirm that the data that supports the findings of this study are available within the article. Raw data that support the finding of this study are available from the corresponding author, upon reasonable request.

CONFLICT OF INTEREST

The authors declare that they have no conflict of interest.

FINANCIAL DISCLOSURE

The authors declared that this study has received no financial support.

USE OF AI FOR WRITING ASSISTANCE

Not declared.

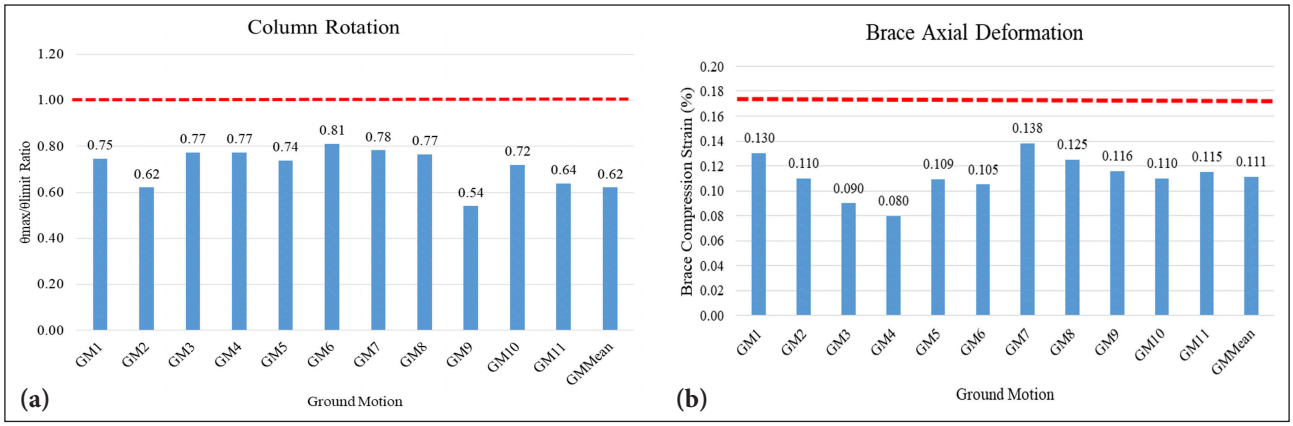

Figure 19. **(a)** Column rotation and (b) Steel brace axial compression strain for retrofitted LNG tank.

*CP stands for Collapse Prevention, LS for Life Safety, and IO for Immediate Occupancy performance levels.

PEER-REVIEW

Externally peer-reviewed.

REFERENCES

[1] Shekari, M. R., Khaji, N., & Ahmadi, M. T. (2010). On the seismic behavior of cylindrical base-isolated liquid storage tanks excited by long-period ground motions. *Soil Dyn Earthq Eng*, 30, 968–980. [CrossRef]

[2] Niwa, A., & Clough, R. W. (1982). Buckling of cylindrical liquid-storage tanks under earthquake loading. *Earthq Engng Struct Dyn*, 10, 107–122. [CrossRef]

[3] Shaban, N., Ozdemir, S., Caner, A., & Akyüz, U. (2017, June 15-17). *Seismic retrofit of buildings with backbone dampers*. In Proceedings of the ECCOMAS Thematic Conference—COMPDYN 2017: 6th International Conference on Computational Methods in Structural Dynamics and Earthquake Engineering: An IACM Special Interest Conference, Programme, Rhodos Island, Greece. [CrossRef]

[4] Gregoriou, V. P., Tsinopoulos, S. V., & Karabalis, D. L. (2011, May 25-28). *Dynamic analysis of liquefied natural gas tanks seismically protected with energy dissipating base isolation systems*. In Proceedings of the ECCOMAS Thematic Conference—COMPDYN 2011: 3rd International Conference on Computational Methods in Structural Dynamics and Earthquake Engineering: An IACM Special Interest Conference, Programme, Corfu, Greece.

[5] Jadhav, M. B., & Jangid, R. S. (2006). Response of base-isolated liquid storage tanks to near-fault motions. *Struct Eng Mech*, 23, 615–634. [CrossRef]

[6] Ozbulut, O. E., Bitaraf, M., & Hurlebaus, S. (2011). Adaptive control of base-isolated structures against near-field earthquakes using variable friction dampers. *Eng Struct*, 33, 3143–3154. [CrossRef]

[7] Saha, S. K., Matsagar, V. A., & Jain, A. K. (2014). Earthquake response of base-isolated liquid storage tanks for different isolator models. *J Earthq Tsunami, 8*, 1450013. [CrossRef]

[8] Çerçevik, A. E., Avsar, Ö., & Hasançebi, O. (2020). Optimum design of seismic isolation systems using metaheuristic search methods. *Soil Dyn Earthq Eng, 131*, 106012. [CrossRef]

[9] Çalım, F., Güllü, A., Soydan, C., & Yüksel, E. (2023). State-of-the-art review for lead extrusion dampers: Development, improvement, characteristics, application areas, and research needs. *Structures, 58*, 105477. [CrossRef]

[10] Güllü, A., Smyrou, E., Khajehdehi, A., Ozkaynak, H., Bal, I. E., Yuksel, E., & Karadogan, F. (2019). Numerical modeling of energy dissipative steel cushions. *Int J Steel Struct*, 19, 1331–1341. [CrossRef]

[11] Balazic, J., Guruswamy, G., Elliot, J., Pall, R. T., & Pall, A. (2011). *Seismic rehabilitation of justice headquarters building*. 12th WCEE 2000.

[12] Soli, B., Baerwald, D., Krebs, P., & Pall, R. T. (2004, August 1-6). *Friction Dampers for Seismic Control of Ambulatory Care Center, Sharp Memorial Hospital, San Diego*, CA. 13th World Conference on earthquake Engineering, Paper No. 1953.

[13] Housner GW. (1957). Dynamic pressure on accelerated fluid containers. *Bull Seismol Soc Am, 47*(1):15–35. [CrossRef]

[14] Haroun, M.A., & Housner, G.W. (1981). Earthquake response of deformable liquid storage tanks. *J Appl Mech, 48*, 411–418. [CrossRef]

[15] Erdik, M., Demircioglu, M., Sesetyan, K., Durukal, E., & Siyahi, B. (2004). Earthquake hazard in Marmara Region, Turkey. *Soil Dyn Earthq Eng*, 24(8), 605–631. [CrossRef]

[16] Giardini, D., Woessner J., & Danciu L. (2014). SHARE Project: Mapping Europe's Seismic Hazard. *EOS, 95*(29): 261–262. [CrossRef]

[17] Caltrans. (2013). *Caltrans seismic design criteria, version 1.7*. California Department of Transportation.

[18] ASCE. (2010). *Minimum design loads for buildings and other structures*. ASCE Standart, ASCE 7- 10.

[19] Turkish Building Earthquake Code. (2018). *Specification for buildings to be built in seismic areas*. Ministry of Public Works and Housing, Ankara, Türkiye.

[20] Hasanoğlu, S., Güllü, A., Dindar, A. A., Müderrisoğlu, Z., Özkaynak, H., & Bozer, A. (2024). Optimal selection and scaling of ground motion records compatible with input energy and acceleration spectra. *Earthq Eng Struct Dyn, 53*(7), 2382–2404. [CrossRef]

[21] Güllü, A. (2023). A compendious review on the determination of fundamental site period: Methods and importance. *Geotechnics, 3*(4), 1309–1323. [CrossRef]

[22] Güllü, A., Hasanoğlu, S., & Yüksel, E. (2022). A practical methodology to estimate site fundamental periods based on the KiK-net Borehole Velocity Profiles and its application to Istanbul. *Bullet Seismol Soc Am, 112*(5), 2606–2620. [CrossRef]

[23] ASCE. (2013). Seismic Evaluation and Retrofit of Existing Buildings. ASCE 41-13.